ADAM MICKIEWICZ UNIVERSITY
FACULTY OF PHYSICS

Correlation effects in transport through quantum dot systems

Kacper Wrześniewski

Doctoral dissertation

Supervised by
dr hab. Ireneusz Weymann

Mesoscopic Physics Division
Faculty of Physics
Adam Mickiewicz University in Poznań, Poland

Poznań 2018

Acknowlegments

I am very grateful to dr hab. Ireneusz Weymann for providing guidance and excellent support.

I would like to thank all the members of Mesoscopic Physics Division for many fruitful discussions and amazing atmosphere.

Contents

List of articles constituting the dissertation

(I) K. Wrześniewski, I. Weymann,
Spin effects in transport through triangular quantum dot molecule in different geometrical configurations,
Phys. Rev. B **92**, 045407 (2015).

(II) K. Wrześniewski, I. Weymann,
Current Suppression in Transport Through Triple Quantum Dots Coupled to Ferromagnetic Leads,
Acta Phys. Pol. A **127**, 460 (2015).
(Proceedings of the European Conference Physics of Magnetism, Poznań 2014).

(III) K. Wrześniewski, I. Weymann,
Influence of Magnetic Field on Dark States in Transport through Triple Quantum Dots,
Acta Phys. Pol. A **132**, 109 (2017).
(Proceedings of the Twelfth International School on Theoretical Physics - Symmetry and Structural Properties of Condensed Matter Rzeszãşw, Poland, September 5-10, 2016).

(IV) K. Wrześniewski, I. Weymann,
Dark states in spin-polarized transport through triple quantum dot molecules,
Phys. Rev. B **97**, 075425 (2018).

(V) K. Wrześniewski, P. Trocha, I. Weymann,
Current cross-correlations in double quantum dot based Cooper pair splitters with ferromagnetic leads,
J. Phys.: Cond. Matter **29**, 195302 (2017).

(VI) P. Trocha, K. Wrześniewski,
Cross-correlations in a quantum dot Cooper pair splitter with ferromagnetic leads,
J. Phys.: Cond. Matter **30**, 305303 (2018).

(VII) K. Wrześniewski, I. Weymann,
Kondo physics in double quantum dot based Cooper pair splitters,
Phys. Rev. B **96**, 195409 (2017).

Abstract

This PhD thesis concerns theoretical studies of charge and spin transport through the systems consisting of coupled quantum dots attached to external leads. The considered structures exhibit many interesting physical properties, not observed in bulk materials, resulting from various quantum effects and correlations, as well as different geometrical arrangements. With recent progress in nanofabrication techniques, it has become possible to implement nanostructures composed of coupled quantum dots in a fully tunable manner. In consequence, such systems can have very promising applications as novel nanoelectronic devices, where both electron charge and spin are exploited.

The focus of this dissertation is on various correlation effects and their influence on transport through quantum dot systems. In particular, the quantum interference effects in triangular quantum dots responsible for the appearance of *dark states* are extensively studied. This quantum mechanical phenomenon reveals itself with non-trivial transport properties: current suppression, negative differential conductance, enhanced shot noise and coherent electron population trapping. The underlying mechanism, conditions and parameters necessary for the emergence of dark states, possible schemes for manipulation and exploitation of such states are the subject of the comprehensive theoretical analysis in further part of the thesis.

Another important class of considered systems are quantum dot based Cooper pair splitters. The proximity of superconductor induces pairing correlations in quantum dots and gives rise to the formation of Andreev bound states for energies smaller than the superconducting energy gap. The Andreev transport is analyzed with an emphasis on the current cross-correlations in order to optimize the parameters for obtaining high Cooper pair splitting efficiency. The transport properties of double quantum dot based Cooper pair splitters are also studied in the Kondo regime. The interplay of Kondo and superconducting correlations are thoroughly analyzed, both in the $SU(2)$ and $SU(4)$ Kondo regimes, and differences in transport behavior in these cases are discussed.

The thesis begins with an introductory part consisting of motivation and aim of the work, description of the methodology, including an outline of the real-time diagrammatic technique and the numerical renormalization group method, and the discussion of basic concepts in transport through quantum dot systems. Subsequently, a set of seven papers, containing the theoretical studies of introduced problems and constituting this dissertation, is presented.

Chapter 1

Introduction

1.1 Motivation and aim

For over three decades [1] quantum dot systems have been extensively studied experimentally and theoretically [2,3]. Due to the manifestation of many quantum effects and correlations at the nanoscale, quantum dots are attractive for applications in the fields of nanoelectronics, spintronics [4,5] and quantum information processing [6], among many others. High tunability of experimental realizations of such systems is another important feature stimulating extensive research in this area. Finally, quantum dot systems provide a great playground for testing fundamental correlations between single charges and spins and examining their role in quantum transport [7–11].

An accurate theoretical study of transport properties of quantum dot systems is a broad and challenging task belonging to the field of mesoscopic physics. It combines the classical and quantum mechanics and demands one to confront with difficult quantum many-body problems [12]. To tackle this task a variety of analytical and numerical methods and approaches have been proposed. Many of them are computationally demanding and, in order to capture the physics more and more accurately, under the constant development. The rich and beautiful physics awaiting to be unraveled, the intellectual challenge and scientific adventure in this modern and active field, and, last but not least, the prospect of soon-to-be applications in common technology, are all igniting the curiosity and strong motivation across the physics community. Considering all of the above, the author devoted himself to follow this path.

This thesis is focused on the investigations of transport properties of coupled quantum dot systems and the examination of the influence of various correlations on their transport behavior. The analysis is divided into two parts. The first one addresses systems built of three quantum dots arranged in a triangular geometry. This is a prominent example resembling a simple planar molecular system. The triple quantum dot systems have a complex electronic structure and a vast space of tunable parameters, which result in compelling and non-trivial transport phenomena. In particular, the quantum interference effects leading to the formation of dark states [13–16] are thoroughly analyzed and discussed. The second part of conducted studies is devoted to quantum dot based Cooper pair splitters [17–20]. The Andreev transport [21] in such hybrid structures is analyzed for wide range of transport parameters, both in the weak- and strong-coupling regimes. In the former regime, the focus is put on examining the current cross-correlations [22] and their dependencies on various system's parameters. Strong positive cross-correlations are associated with high splitting efficiency, which is a desired feature

of Cooper pair splitters. The negative current cross-correlations are also predicted and the underlying mechanism is explained. In the strong coupling regime, the interplay of superconducting and Kondo [23–25] correlations is the prime objective of the research. The $SU(2)$ and $SU(4)$ [26] Kondo regimes are considered in the case of double quantum dot based Cooper pair splitters. The influence of superconducting correlations on the Kondo physics is studied along with the Andreev transport properties of the system.

The main aim of this dissertation is to deepen the understanding of transport phenomena at the nanoscale and in correlated quantum dot systems in particular. The presented theoretical results can be confronted with experimental data with up-to-date nanofabrication technology and measurements techniques [26–30]. The analysis of fundamental quantum effects in considered systems may also stimulate further research and progress in this broad and rapidly developing field of contemporary physics.

The dissertation has a form of a series of seven publications preceded by the essential introduction. Therefore, the thesis is divided into three chapters. The present Chapter 1 carries forward with a brief description of the theoretical framework and discussion of basic concepts in quantum transport through systems of coupled quantum dots, fundamental for understanding the following research. The introduction is concluded with a short summary. Chapter 2 is the most important part of the dissertation, where the results of theoretical studies performed by the author, in the form of seven papers published in peer-reviewed international journals, are presented. Finally, Chapter 3 includes appropriate appendices.

1.2   Theoretical framework

This section presents a brief introduction to the methodology used for the conducted research. The description of a general coupled quantum dot system in the Hamiltonian approach is presented, followed by an outline of employed numerical and analytical methods for studies of quantum transport. The real-time diagrammatic method is used in order to examine the behavior of the system in the weak coupling regime, while the numerical renormalization group approach allows one to analyze the system's transport properties in the strong coupling regime.

1.2.1   Hamiltonian

A general form of the Hamiltonian describing the considered systems can be written as a sum of three parts

$$H_{Total} = H_{QD} + H_{Leads} + H_{Tun}, \tag{1.1}$$

where H_{QD} describes isolated quantum dots, H_{Leads} is the leads' Hamiltonian and H_{Tun} accounts for tunneling between the corresponding leads and quantum dots. More specifically, the studied systems are described with an extended Anderson impurity model [31] written in the second-quantized notation. The single-impurity Anderson model allows one to conveniently study the properties of a single orbital level interacting with metallic environment, however, it can be easily extended to multi-level case. In our considerations it is always assumed that every quantum dot in analyzed models has a single orbital level. This assumption can be justified by assuming a large energy spacing between consecutive levels due to the ultra-small size of quantum dots and examination of transport properties in the low temperature limit.

The Hamiltonian H_{QD} is generally given by

$$H_{QD} = \sum_i \varepsilon_i n_i + \sum_i U_i n_{i\uparrow} n_{i\downarrow} + \sum_{\langle ij \rangle} \frac{U_{ij}}{2} \sum_{\sigma\sigma'} n_{i\sigma} n_{j\sigma'} + \sum_{\langle ij \rangle} \frac{t_{ij}}{2} \sum_{\sigma} (d_{i\sigma}^\dagger d_{j\sigma} + H.c.). \tag{1.2}$$

The first term describes the orbital energy ε_i of an electron on quantum dot i, with n_i being the occupation operator $n_i = \sum_\sigma n_{i\sigma}$, where $n_{i\sigma} = d_{i\sigma}^\dagger d_{i\sigma}$ and $d_{i\sigma}^\dagger (d_{i\sigma})$ is the creation (annihilation) operator of an electron on quantum dot i with spin σ. The second term stands for the on-site Coulomb interaction U_i, while the third term relates to the interdot Coulomb correlations, U_{ij}. Finally, the last term represents spin-conserving hopping between neighboring quantum dots, with the hopping amplitude given by t_{ij}. The term $H.c.$ stands for Hermitian conjugate. The

parameters U_{ij} and t_{ij} are divided by 2 to handle the double counting.

In the following studies, there are three types of leads considered in the examined systems. The normal metallic (N) and ferromagnetic (FM) leads are both modeled as reservoirs of non-interacting quasiparticles

$$H_{NLead} = \sum_{\mathbf{k}\sigma} \varepsilon_{\mathbf{k}} c_{\mathbf{k}\sigma}^{\dagger} c_{\mathbf{k}\sigma}, \tag{1.3}$$

$$H_{FMLead} = \sum_{\mathbf{k}\sigma} \varepsilon_{\mathbf{k}\sigma} c_{\mathbf{k}\sigma}^{\dagger} c_{\mathbf{k}\sigma}, \tag{1.4}$$

where $c_{\mathbf{k}\sigma}^{\dagger} (c_{\mathbf{k}\sigma})$ is the creation (annihilation) operator of quasiparticle in a lead with momentum $\mathbf{k}$ and spin σ. It is important to note, that the distinction between these two types of metallic electrodes is in the dispersion relation, which for the ferromagnetic case is spin-dependent $\varepsilon_{\mathbf{k}\sigma}$.

In the case of Cooper pair splitters, the quantum dot system is also coupled to superconducting lead. In the proceeding analysis, the mean-field BCS Hamiltonian [32] is used to model the s-wave superconductor

$$H_{SCLead} = \sum_{\mathbf{k}\sigma} \varepsilon_{\mathbf{k}} c_{\mathbf{k}\sigma}^{\dagger} c_{\mathbf{k}\sigma} + \Delta \sum_{\mathbf{k}} (c_{\mathbf{k}\uparrow}^{\dagger} c_{-\mathbf{k}\downarrow}^{\dagger} + H.c.), \tag{1.5}$$

with Δ being the order parameter assumed to be momentum independent and real, as the phase can be discarded in the case of single superconductor present in the system. Lastly, the term H_{Leads} in Hamiltonian (1.1) is a sum of the corresponding leads' Hamiltonians discussed above, depending on the details and geometry of the considered system.

Finally, the last term of the general Hamiltonian (1.1) expresses the tunneling between quantum dots and attached leads. In all papers presented in Chapter 2, the spin conserving tunneling is assumed. Then, the tunneling Hamiltonian takes the following form

$$H_{Tun} = \sum_{ri\mathbf{k}\sigma} v_{ri\sigma} (c_{r\mathbf{k}\sigma}^{\dagger} d_{i\sigma} + H.c.). \tag{1.6}$$

Here, v_{ri} are the tunnel matrix elements between lead r and quantum dot i. The tunnel coupling for junction ri can be written as

$$\Gamma_{ri}^{\sigma} = 2\pi \rho_r^{\sigma} |v_{ri\sigma}|^2, \tag{1.7}$$

where ρ_r^{σ} is the corresponding density of states. For ferromagnetic leads it is obviously spin-dependent, for nonmagnetic leads $\rho_r^{\sigma} = \rho_r$, while for superconducting leads $\rho_r^{\sigma} = \rho_r$ denotes the density of states of superconductor in normal state. For the ferromagnetic leads, the coupling

strength is often also described by the spin polarization p_r of lead r, defined as

$$p_r = \frac{\rho_r^+ - \rho_r^-}{\rho_r^+ + \rho_r^-}. \tag{1.8}$$

With the above, one can express the couplings in the following manner

$$\Gamma_{ri}^\pm = \Gamma_{ri}(1 \pm p_r), \tag{1.9}$$

with $\Gamma_{ri} = (\Gamma_{ri}^+ + \Gamma_{ri}^-)/2$, where Γ_{ri}^+ is the coupling to the spin-majority and Γ_{ri}^- to spin-minority electron band of the lead r. In the case of normal metallic (non-ferromagnetic) leads, the spin polarization is equal to zero, i.e. $p_r = 0$.

In the analysis of transport properties of hybrid systems with a single superconducting lead presented in publications (V, VI, VII), the main focus is on the Andreev transport regime [21]. In order to rule out the normal tunneling processes and provide a clear understanding of Andreev reflection processes, the infinite superconducting energy gap limit is assumed. This assumption considerably simplifies the problem, as the limit $|\Delta| \to \infty$ can be solved exactly [33]. Integration of fermionic degrees of freedom in superconductor generates an induced action, which can be simply added to the bare action of the isolated quantum dot subsystem. Hence, the following effective Hamiltonian is obtained for the system with a single quantum dot (SQD) [34–36]

$$H_{SQD}^{Eff} = H_{SQD} - \frac{\Gamma^S}{2}(d_\uparrow^\dagger d_\downarrow^\dagger + d_\downarrow d_\uparrow), \tag{1.10}$$

where the effective pairing potential Γ^S is the coupling strength between the quantum dot and the superconducting electrode. Subsequently, for the system with a double quantum dot (DQD) coupled to superconductor [37, 38] the effective Hamiltonian can be written as

$$H_{DQD}^{Eff} = H_{DQD} - \sum_i \frac{\Gamma_i^S}{2}(d_{i\uparrow}^\dagger d_{i\downarrow}^\dagger + d_{i\downarrow} d_{i\uparrow}) + \frac{\Gamma_{LR}^S}{2}(d_{L\uparrow}^\dagger d_{R\downarrow}^\dagger + d_{R\uparrow}^\dagger d_{L\downarrow}^\dagger + d_{R\downarrow} d_{L\uparrow} + d_{L\downarrow} d_{R\uparrow}), \tag{1.11}$$

where Γ_i^S describes direct Andreev reflection processes in the system and $\Gamma_{LR}^S = \sqrt{\Gamma_L^S \Gamma_R^S}$ is responsible for non-local Andreev reflections [37].

1.2.2 Weak vs. strong coupling regime

The theoretical study of transport phenomena in mesoscopic systems is a challenging problem. The separate parts of the system, i.e. electrodes and an isolated finite subsystem with discrete spectrum, such as a quantum dot or a molecule, are all well understood and quite accurately described by the theory. However, when they are brought together into the contact, the description becomes more complicated as new issues come into play. The diversity of phenomena concerning the physics of interface, interactions between reservoirs and discrete system, non-equilibrium conditions due to applied bias voltage, screening, field effects and many more are all important effects. Nonetheless, their significance and influence on the transport behavior depend mainly on the coupling strength between the individual parts of the system. Therefore, it is convenient to study the transport in two antipodal cases: in the weak or the strong coupling regime.

In the weak coupling regime, the coupling strength between electrode and quantum dot Γ is assumed to be the lowest energy scale in the problem, $\Gamma \ll U, T$ ($k_B \equiv 1$), where Γ is the total coupling strength given by a sum of all couplings between the quantum dot and attached reservoirs. Experimentally, the couplings can be tuned by electric gates producing high tunnel barriers. When the coupling is weak, the orbital levels on the quantum dots or molecular system remain well defined, discrete states and the electronic transport takes place through a sequence of single electron tunneling events. Because the coupling strength Γ is a small parameter in the problem, the transport characteristics can be calculated with the use of perturbative methods. The results presented in articles (I, II, III, IV, V, VI) are all concerning weak coupling regime and designated quantities are found by means of the real-time diagrammatic technique, which is described in Sec. 1.2.3.

The perturbation approach cannot be applied to the strong coupling regime [39], where Γ is significantly larger compared to the weak coupling case. Strong Γ is responsible for hybridization of the relevant states of two subsystems, i.e. electrodes and coupled quantum dots, which results in a significant broadening of the corresponding energy levels and their finite lifetime. The electron transport is no longer described by a sequence of tunneling events, but by the scattering theory and Landauer approach [40, 41]. Moreover, when the system is studied in the temperatures below the so-called Kondo temperature T_K, $T < T_K$, the Kondo effect emerges with a strong zero-bias peak in the differential conductance. A more detailed description of the Kondo effect is presented in Sec. 1.3.6. Here, it is important to note that the Kondo temperature

is exponentially dependent on the coupling strength Γ, therefore, by increasing the coupling strength Γ one can enhance T_K. For the single-level Anderson model, T_K can be found from the poor man's scaling approach [42, 43], and is given by

$$T_K = \frac{\sqrt{U\Gamma}}{2} e^{\pi\varepsilon(\varepsilon+U)/\Gamma U}, \qquad (1.12)$$

where ε is the level's energy and U denotes the Coulomb on-site interaction for the single-level system. The paper (VII) presents the results for the double quantum dot based Cooper pair splitter in the strong coupling regime. The results were obtained by using the numerical renormalization group method, which is described in Sec. 1.2.4. This non-perturbative approach allows one to study transport in the strong coupling regime and precisely capture the interesting Kondo physics.

1.2.3 Real-time diagrammatic technique

In order to study the non-equilibrium transport through quantum dot systems, the real-time diagrammatic technique (RTDT) [44–46] is employed. This approach is based on the perturbation expansion of an operator of interest with respect to the parameter Γ, which is assumed to be small in the weak coupling regime. In the presented calculations, the operators of interest are the current operator along with higher order correlators, as well as the reduced density matrix of the quantum dot subsystem.

The perturbation expansion of the expectation value of an operator $O(t)$ can be written as

$$\langle O(t) \rangle = \text{Tr} \left\{ \rho_0 \sum_{n=0}^{\infty} (-i)^n \int_C d\tau_1 \int_C d\tau_2 ... \int_C d\tau_n T_C[H_T(\tau_1)_I H_T(\tau_2)_I ... H_T(\tau_n)_I O(t)_I] \right\}.$$
$$(1.13)$$

The subscript I marks the operators represented in the interaction picture of quantum mechanics. T_C is the time-ordering operator on the Keldysh contour. The operator T_C orders the time-dependent operators on the Keldysh contour accordingly, in the way described by the following conditions

$$T_C[H_T(\tau_1)_I H_T(\tau_2)_I] = \begin{cases} H_T(\tau_1)_I H_T(\tau_2)_I & \text{for } \tau_1 > \tau_2, \\ H_T(\tau_2)_I H_T(\tau_1)_I & \text{for } \tau_1 < \tau_2. \end{cases} \qquad (1.14)$$

In the RTDT approach, the tunneling is switched on adiabatically at the initial time t_0. Moreover, the initial density matrix is assumed to factorize into a simple product of density matrix

of quantum dots and density matrices of the leads, $\rho_0 = \rho_0^{QD}\rho_0^{Lead_1}\rho_0^{Lead_2}(...)$. In the case of normal metallic and ferromagnetic leads, the Fermi function describes the electron distribution. Furthermore, the Wick's theorem is applied to integrate out the leads' degrees of freedom. However, for quadratic terms of fermionic operators in quantum dots Hamiltonian H_{QD}, the Wick's theorem does not hold and an exact treatment by means of reduced density matrix is appropriate.

The time evolution of the system can be illustrated as a sequence of irreducible blocks on the Keldysh contour, see Fig. 1.1. The upper and lower branches stand for the forward and backward propagators. The tunneling lines are associated with contractions of the lead
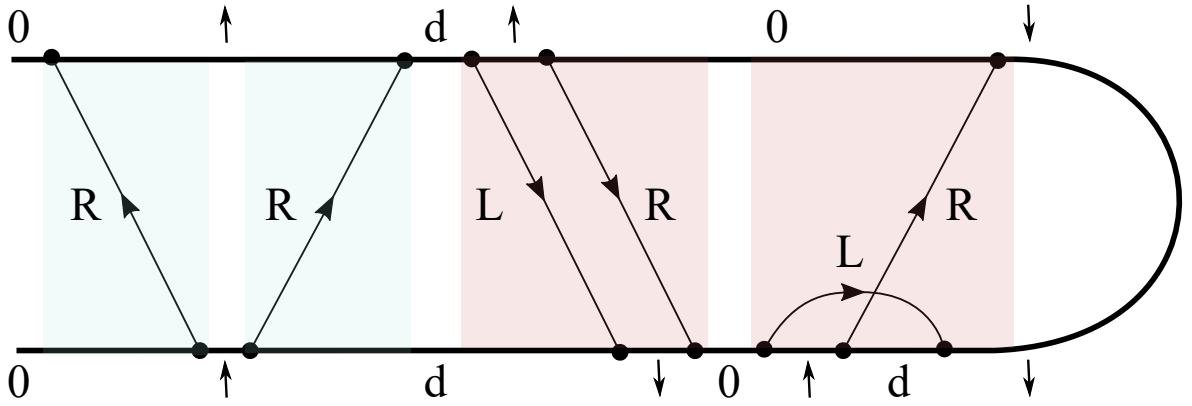

Figure 1.1: Time evolution of the reduced density matrix for a single level quantum dot with four local states: $\chi = 0, \uparrow, \downarrow, d$. The dot states are indicated on the forward (upper branch) and backward (lower branch) propagators. The light-blue/(light-red) squares highlight the irreducible diagrams of the first/(second) order. Each tunneling line represents electron leaving or entering the dot and is labeled by (L)/(R) representing left/right junction.

operators and the direction of the arrow indicates if an electron of a given spin enters or leaves the quantum dot. The vertices represent a product of lead and quantum dot operators. Fig. 1.1 also presents irreducible diagrams indicated by the color squares. An irreducible diagram is a diagram in which every possible vertical cut at a fixed time crosses at least one tunneling line. The full propagation can be written as a sequence of irreducible blocks. With every irreducible block, there is an associated self-energy $\Sigma_{\chi'\chi}(t', t)$ corresponding to the transition rate from the state χ at time t to state χ' at time t'. Areas without tunneling lines represent free propagation: $\mathbf{\Pi}^{(0)} = \mathbf{1}$. The bold characters express the matrix notation in the local states of the quantum dot subsystem. The full propagator is then given by the Dyson equation [44, 45]

$$\mathbf{\Pi}(t', t) = \mathbf{1} + \int_t^{t'} dt_2 \int_t^{t_2} \mathbf{\Sigma}(t_2, t_1)\mathbf{\Pi}(t_1, t). \tag{1.15}$$

In the long-time limit the propagator is stationary, which can be expressed as

$$\lim_{t_0 \to -\infty} \mathbf{\Pi}(t' - t_0) = \mathbf{p}^{\text{st}} \otimes \mathbf{e}^T, \tag{1.16}$$

where $\mathbf{p}^{\text{st}}$ is the probability vector of local states χ and $\mathbf{e}^T = (1, ..., 1)$. In order to determine the stationary probabilities $\mathbf{p}^{\text{st}}$, the Laplace transform of the transition rates needs to be performed and then the following equation solved

$$\mathbf{W}\mathbf{p}^{\text{st}} = \mathbf{0}, \tag{1.17}$$

along with the normalization condition $\text{Tr}\{\mathbf{p}^{\text{st}}\} = 1$. The matrix $\mathbf{W}$ consists of all transition rates $W_{\chi'\chi}$ being exactly related to self-energies, $\Sigma_{\chi\chi'} = iW_{\chi'\chi}$. The self-energy $\Sigma_{\chi\chi'}$ is given by a sum of all topologically different diagrams having the state χ at the left-side ends and the state χ' at the right-side of the diagram. The contribution of the diagram can be calculated with help of the diagrammatic rules. Below, general rules in energy space are listed:

1. Find all topologically different diagrams with $2n$ vertices connected with n tunneling lines, where n responds to the expansion order. Assign the energies E_χ to respective states on the forward and backward propagators and frequency ω_l, junction and spin to each tunneling line.

2. Add direction to each tunneling line expressing if the electron enters or leaves the quantum dot. Assign $\gamma_{ri}^{-\sigma}(\omega) = \frac{\Gamma_{ri}^{\sigma}}{2\pi}[1 - f(\omega - \mu_r)]$ to the lines going according to the Keldysh contour and $\gamma_{ri}^{+\sigma}(\omega) = \frac{\Gamma_{ri}^{\sigma}}{2\pi}f(\omega - \mu_r)$ to the lines going backward to the Keldysh contour, where $f(\omega)$ is the Fermi-Dirac distribution function and μ_r denotes the chemical potential of lead r.

3. Draw a vertical line representing resolvent $1/(\Delta E + i0^+)$ for each time interval between two adjacent vertices. Here, ΔE is an energy difference of left-going and right-going lines crossing the resolvent.

4. Add a prefactor $(-1)^{b+c}$, where b is a number of vertices on the backward propagator and c expresses the number of crossings of tunneling lines.

5. Assign appropriate matrix element to each vertex: $\langle \chi | d_\sigma^\dagger | \chi' \rangle$ or $\langle \chi | d_\sigma | \chi' \rangle$.

6. Integrate over the energies ω_l of the tunneling lines and sum over all junctions and spins.

The examples of first-order and second-order diagrams contributing to appropriate self-energies are presented in the Appendices of papers (I) and (IV).

The elements of matrix $\mathbf{W}$ and vector $\mathbf{p}^{\text{st}}$ can be determined diagrammatically order by order in Γ. A given order of the perturbation expansion corresponds to the respective number of tunneling lines in the diagrams. Accordingly, to calculate the first-order and second-order contributions, all topologically different, irreducible diagrams with one and two tunneling lines need to be evaluated. The expansion of the matrix $\mathbf{W}$ begins in the first order, while that of vector $\mathbf{p}^{\text{st}}$ in the zeroth order. The corresponding zeroth and first-order probabilities can be found by solving the equations [44, 45]:

$$\mathbf{W}^{(1)}\mathbf{p}^{\text{st}(0)} = 0 \tag{1.18}$$

and

$$\mathbf{W}^{(2)}\mathbf{p}^{\text{st}(0)} + \mathbf{W}^{(1)}\mathbf{p}^{\text{st}(1)} = 0, \tag{1.19}$$

with the normalization condition $\text{Tr}\left\{\mathbf{p}^{\text{st}(n)}\right\} = \delta_{0,n}$. In order to calculate the current, the following equation needs to be solved [44, 45]

$$I = \frac{e}{2\hbar}\text{Tr}\left\{\mathbf{W}^I\mathbf{p}^{\text{st}}\right\}, \tag{1.20}$$

where $\mathbf{W}^I$ is the self-energy matrix accounting for the number of electrons transferred through the quantum dot system. The perturbation expansion is also performed for the current, such that the first-order current can be found from

$$I^{(1)} = \frac{e}{2\hbar}\text{Tr}\left\{\mathbf{W}^{I(1)}\mathbf{p}^{\text{st}(0)}\right\}, \tag{1.21}$$

while the second-order current is given by

$$I^{(2)} = \frac{e}{2\hbar}\text{Tr}\left\{\mathbf{W}^{I(2)}\mathbf{p}^{\text{st}(0)} + \mathbf{W}^{I(1)}\mathbf{p}^{\text{st}(1)}\right\}. \tag{1.22}$$

The total current is simply given by the sum of the first and second-order contributions

$$I = I^{(1)} + I^{(2)}. \tag{1.23}$$

The description of how to calculate the shot-noise and the current cross-correlations within the

real-time diagrammatic technique framework is presented in Sec. 1.3.4.

1.2.4 Numerical renormalization group method

The equilibrium properties of correlated quantum impurity models can be studied by means of numerical renormalization group (NRG) with a very high accuracy. The NRG approach is a non-perturbative method developed originally by Kenneth G. Wilson [47] to solve the Kondo Hamiltonian and overcome the difficulties with applying the perturbative schemes, which break down in the strong coupling regime. Nowadays, Wilson's NRG is considered as one of the most accurate and versatile quantum impurity solvers [48].

The starting idea of the discussed approach is the division of the conduction band into shorter and shorter energy intervals, with increasing resolution around the Fermi level. The discretization scheme is controlled by the parameter $\Lambda > 1$ (see Fig. 1.2), where $\Lambda \to 1$ would recover the continuous limit. The consecutive intervals can be written as: $I_n^\pm = \pm D[\Lambda^{-(n+1)}, \Lambda^{-n}]$, with D expressing the half-width of the conduction band and $n \in \mathbb{N}$ denoting the interval number. Eventually, the continuum of electron states is substituted by the discrete Fourier basis with new fermionic operator for each interval.
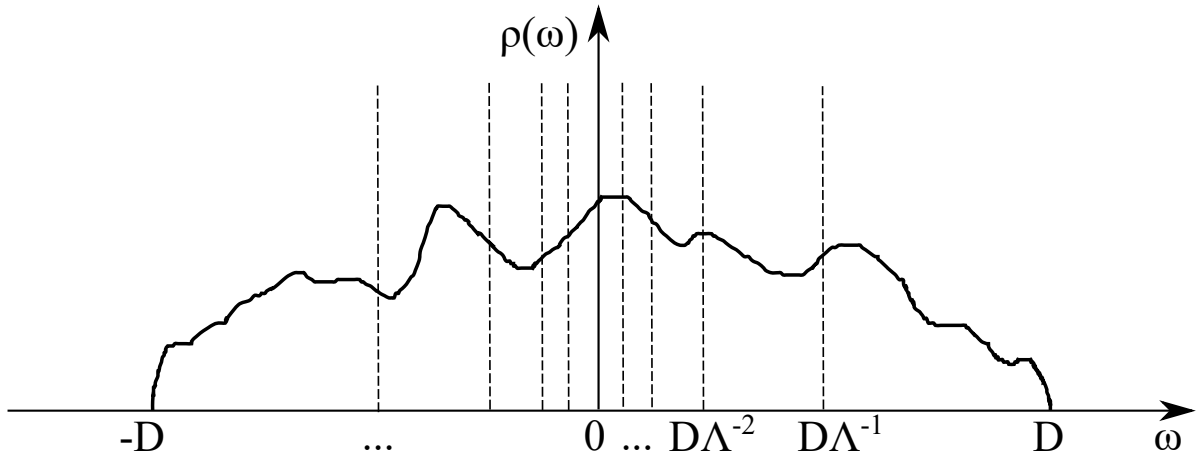

Figure 1.2: Logarithmic discretization of the conduction band controlled by the discretization parameter Λ.

After the logarithmic discretization of the conduction band, the starting Hamiltonian (1.1) is mapped onto the so-called Wilson chain, a semi-infinite tight-binding chain approximating the leads, coupled to the impurity

$$H_{NRG} = H_{QD} + H_{Tun} + \sum_{n=0}^{\infty} \sum_{\sigma} \xi_n f_{n\sigma}^\dagger f_{n\sigma} + \sum_{n=0}^{\infty} \sum_{\sigma} t_n (f_{n\sigma}^\dagger f_{n+1\sigma} + H.c.), \qquad (1.24)$$

where the impurity (quantum dot) interacts only with the zeroth site of the Wilson chain through $H_{Tun} = \sum_\sigma v_l(f^\dagger_{0\sigma} d_\sigma + H.c.)$. The operator $f^\dagger_{n\sigma}$ ($f_{n\sigma}$) is creating (annihilating) a spin-σ electron on site n of the Wilson chain. The on-site energies of the Wilson chain ξ_n and the hoppings t_n are determined by tridiagonalizing the initial Hamiltonian with the corresponding density of states $\rho(\omega)$. For a particle-hole symmetric flat band, assumed in paper (VII), the on-site energies are given by $\xi_n = 0$ and hoppings are analytically approximated by $t_n \sim \Lambda^{-n/2}$.

For the Hamiltonian (1.24) a recursive relation can be written as

$$H_{n+1} = H_n + \mathcal{E}_{n+1} + \mathcal{T}_{n,n+1}, \tag{1.25}$$

with H_n given by

$$H_n = H_{QD} + H_{Tun} + \sum_{m=0}^{n}\sum_\sigma \xi_m f^\dagger_{m\sigma} f_{m\sigma} + \sum_{m=0}^{n-1}\sum_\sigma t_m(f^\dagger_{m\sigma} f_{m+1\sigma} + H.c.) \tag{1.26}$$

and the terms describing on-site energies and hopping related to iteration n given by $\mathcal{E}_{n+1} = \xi_{n+1} \sum_\sigma(f^\dagger_{n+1\sigma} f_{n+1\sigma})$ and $\mathcal{T}_{n,n+1} = t_n \sum_\sigma(f^\dagger_{n\sigma} f_{n+1\sigma} + H.c.)$.

Whilst increasing n, the Hamiltonian H_n more and more precisely approximates Hamiltonian H_{NRG} (1.24). This observation advocates the iterative approach. The procedure starts with the numerical diagonalization of H_0, which describes the impurity coupled to the first site of the Wilson chain. In the following steps, consecutive sites are added one by one and new states are created with the help of fermionic operators $f^\dagger_{n+1\sigma}$ of the Wilson chain. This leads to a rapid growth of the Hilbert space. In order to handle this issue, a maximum number of states kept at each iteration N_{kept} is introduced to control the truncation scheme. Starting from an iteration with a size of the Hilbert space exceeding N_{kept}, after the diagonalization procedure, the states are sorted with respect to their eigenenergies and then N_{kept} lowest energy states are kept, while higher energy states are discarded. The kept states are used to build a new Hilbert space in subsequent iteration with another added site from the Wilson chain.

The transformation of the NRG: $\mathcal{R} : H_N \to H_{N+1}$, is often expected to have a fixed point, which means that there exists an effective Hamiltonian H_{fixed}, for which the following is true: $\mathcal{R}(H_{fixed}) = H_{fixed}$. Therefore, after a certain number of NRG iterations, the obtained spectrum of the Hamiltonian does not change under further transformations and the procedure can be stopped, while the low-energy spectrum is well designated, allowing to capture the low-temperature behavior of the system, including the Kondo physics.

In 2000, Walter Hofstetter proposed an extension of the traditional NRG method by calculating the expectation value of an operator using the density matrix (DM), which was built from states at the last NRG iteration [49]. Such DM-NRG allowed for the analysis of more complex systems and magnetic field effects where the splitting of the ground state is important. The next milestone in the development of NRG was the introduction of an approximate, but complete eigenbasis by Anders and Schiller in 2005 [50], which is constructed from states discarded at each iteration. An important step in building the complete Anders-Schiller basis is to supplement all the states $\{|s\rangle_n^X\}$ from the iteration n with a set of degenerate *environmental* states spanning the rest of the chain $\{|e\rangle_n = |\sigma_{n+1}\rangle \otimes ... \otimes |\sigma_N\rangle\}$, that $\{|se\rangle_n^X = |s\rangle_n^X \otimes |e\rangle_n\}$ [51]. The superscript $X = K, D$ indicates kept (K) or discarded (D) state of a given iteration. Then, the complete and orthogonal Anders-Schiller basis that spans the full Fock space of the Hamiltonian H_{NRG} is given by

$$\sum_n \sum_{se} |se\rangle_n^{DD}{}_n\langle se| = \mathbb{1}. \tag{1.27}$$

The energies of the corresponding states are given by *NRG approximation*

$$H_{NRG}|se\rangle_n^X \approx E_{ns}^X |se\rangle_n^X. \tag{1.28}$$

The construction of complete many-body eigenbasis of the full NRG Hamiltonian pave the way to the concept of full density matrix introduced by Weichselbaum and von Delft in 2007 [51]

$$\rho_{NRG} = \sum_n \sum_{se} |se\rangle_n^D \frac{e^{-\beta E_{ns}^D}}{Z}{}_n^D\langle se|, \tag{1.29}$$

with $Z = \sum_{ns} e^{-\beta E_{ns}^D}$ and $\beta = 1/T$. The full density-matrix NRG enables very accurate (sum-rule conserving) calculation of various operators of interest and correlation functions at arbitrary temperatures and magnetic fields.

In NRG calculations, for the single-impurity Anderson model, it is convenient to perform an orthogonal transformation from the left-right into the even-odd basis of the leads' operators. As a result, only the even linear combination of the lead operators couples to the quantum dot, while odd combination is decoupled. However, it was not possible to use this transformation in the calculations performed in the paper (VII) as the considered system is built of two quantum dots, each one coupled to a separate metallic lead. Therefore, the calculations were done in the two-channel fashion, i.e. the two metallic leads were modeled by two distinct Wilson's chains

attached to the corresponding quantum dots.

The calculations performed in (VII) were performed with the use of the Budapest Flexible DM-NRG code [52], which fully utilizes the concept of full density matrix. The code is available under the GNU license.

1.3 Basic concepts and effects in transport through quantum dots

The following section presents a brief introduction to basic concepts and phenomena emerging in charge and spin transport through the quantum dot systems. In general, quantum transport strongly depends on the dimensionality of considered systems, relevant energy scales and geometry, rather than on exact material properties, atomic structure or even the size. It is especially the case for the quantum dots, which are zero-dimensional systems with electrons confined in all three spatial dimensions. A quantum dot built of a few atoms can have a very similar transport properties compared to a nanometer-sized one. The effective models and employed methods used in this thesis to describe the coupled quantum dots, can also model simple molecules [11, 53–56] or even nanostructures like carbon nanotubes [28, 57–59]. Therefore, the presented results and analysis are also of great importance for molecular electronics. Additionally, the presented papers include discussions of the conditions and range of parameters, for which the relevant effects are present, which is of great value for further experiments and possible applications.

1.3.1 Sequential tunneling and cotunneling

One of the most important concepts regarding the quantum transport research in quantum dot systems is the tunneling of electrons. Quantum dots are of ultra-small size and their examination is typically done at low temperatures, which in consequence leads to the crucial role of discrete orbital levels. When the system is attached to external leads, the most common processes that can take place is that an electron can either enter or leave the quantum dot through the dot-lead tunnel barrier. When a weak coupling between quantum dot and lead is considered, most of processes transfer only one electron. Single electron tunneling refers to first-order processes in perturbation expansion, while the transport regime described by aforementioned processes is known as the sequential tunneling regime [60]. Therefore, in order to quantitatively describe sequential transport in the system by means of the real-time diagrammatic method, all first-order diagrams (with single tunneling line) have to be considered.

In articles (I) and (IV), the results also account for the second-order tunneling events known as cotunneling [61]. Such tunneling act takes place through an intermediate virtual state of the system, which is prohibited due to the energy conservation, except for a short time accessible
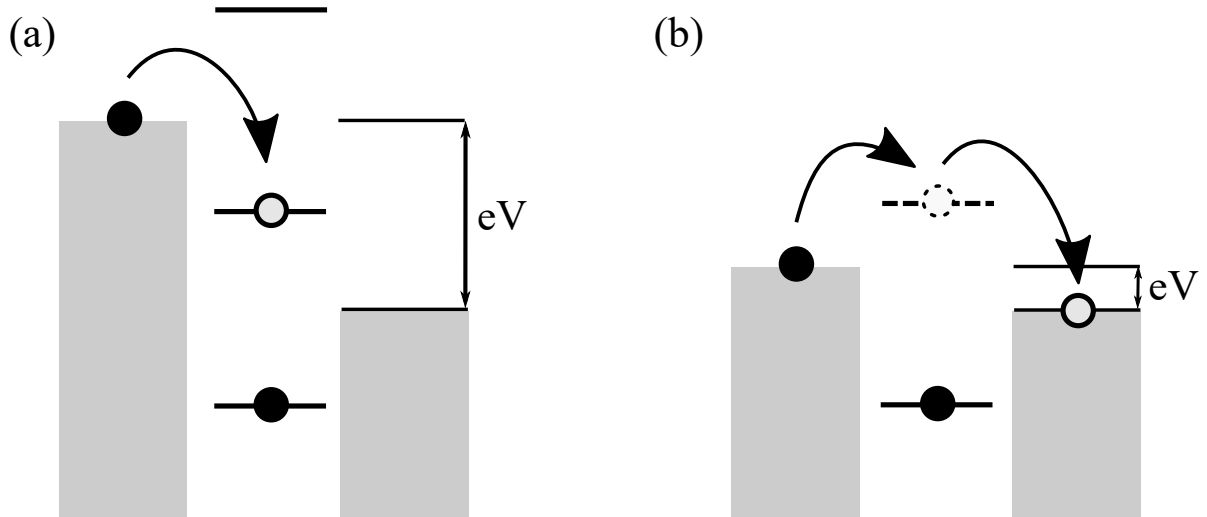
Figure 1.3: Two types of tunneling processes: (a) sequential tunneling and (b) cotunneling.

by virtue of the Heisenberg uncertainty. Cotunneling transport processes dominate the current in the Coulomb blockade regime or in dark state regime, where sequential tunneling is exponentially suppressed. In the real-time diagrammatic approach, when calculating the cotunneling contribution, one needs to evaluate all second-order diagrams (with two tunneling lines). Figure 1.3 illustrates the discussed processes.

1.3.2 Coulomb blockade

Due to the quantization of charge and electrostatic interaction between the electrons, nanoscopic systems, such as quantum dots, exhibit the *single-electron charging effects* [62]. The charging energy E_C is a classical idea responding to the capacitance in electronic circuits. The number of electrons on the isolated quantum dot is an integer number N and the total charge can be expressed as $Q = Ne$, where e is the elementary charge of the electron. The charge Q produces electric field and has associated electrostatic energy. The energy can be expressed with capacitance of a charged capacitor C as $E = \frac{Q^2}{2C} = E_C N^2$. Therefore, adding another electron to the quantum dot requires an additional energy, which is often called the *single-electron charging energy*, $E_C = \frac{e^2}{2C}$. In studied systems, the transport energy is provided by the applied bias voltage between the leads. Once more and more states enter the transport voltage window, the step-like current-voltage dependence is exposed known as the *Coulomb staircase*. However, if the energy is not provided or it is smaller than the charging energy, the transport is exponentially suppressed and this situation is known as the *Coulomb blockade* [63].

It is convenient to illustrate how the Coulomb blockade reveals itself in transport characteristics by considering a simple case of a single-level interacting quantum dot coupled to two metallic leads and assuming temperature much lower than the charging energy, $T \ll E_C$. The coupling strength is assumed as follows: $\Gamma_L = \Gamma_R = \Gamma/2$ and a symmetric bias between the left (L) and right (R) leads is applied: $\mu_L = -\mu_R = eV/2$. The following results were calculated with the aid of the real-time diagrammatic technique in sequential tunneling approximation. Figure 1.4 shows the sequential current I and differential conductance $G = dI/dV$ in density plots as a function of applied bias voltage and the position of the quantum dot's energy level ε. The current dependence presented in Fig. 1.4(a) displays three extensive black regions where
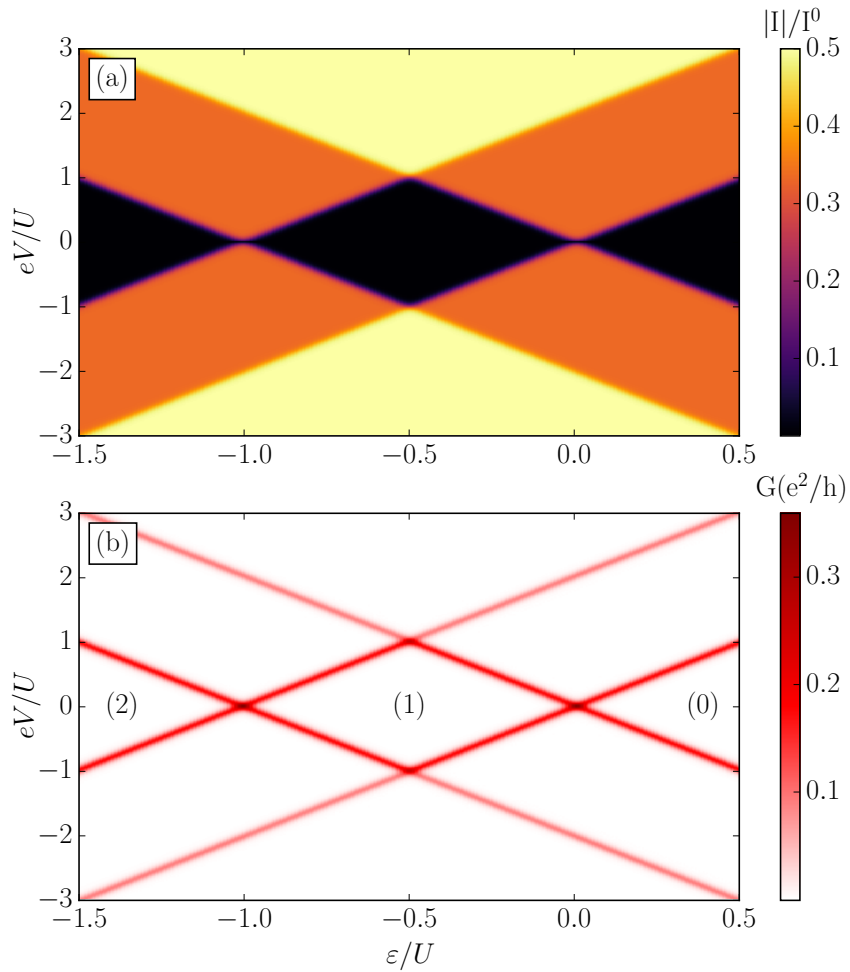

Figure 1.4: (a) The absolute value of the sequential current and (b) the differential conductance calculated as a function of bias voltage and the position of the dot's energy level ε. The parameters are $\Gamma = 0.01$, $T = 0.015$ in units of $U = 2E_C \equiv 1$. The current is plotted in units of $I_0 = e\Gamma/\hbar$. The numbers in brackets in panel (b) indicate the electron number in the dot, with Coulomb blockade for the region with (1) electron.

the net current flowing through the system is equal to zero, i.e. $I = 0$. The central black region for $-1 \leqslant \varepsilon/U \leqslant 0$, with one electron occupying the dot [see Fig1.4(b)], is corresponding

to the Coulomb blockade regime where the sequential tunneling is exponentially suppressed. The low bias voltage does not provide the electrons with energy high enough to overcome the charging energy of the singly occupied quantum dot. However, with further increase of the voltage, the consecutive quantum dot's states enter the transport window and the current starts to flow through the system. Another important observation is that the presented current-voltage dependence reveals the *Coulomb staircases*. It can be seen, that starting from $V = 0$ where obviously $I = 0$ and then observing the current value along the higher bias voltage with a fixed value of ε, the current increases in two substantial steps while reaching the maximal value of $|I|/I_0 = 0.5$, where $I_0 = e\Gamma/\hbar$. Such step-like dependence is due to the Coulomb correlations $U = 2E_C$ that energetically separate the singly and doubly occupied states of the quantum dot. In consequence, these two states enter the transport window at two different values of the bias voltage. It is important to note, that there is one exceptional point on the x-axis representing the position of the quantum dot's energy level, with cross-section exposing qualitatively different current-voltage dependence. It is for energy level $\varepsilon/U = -0.5$, which is called the particle-hole symmetric point. In such a case, the singly and doubly occupied states enter the symmetric transport window at the same time, as the excitation energies to empty and doubly occupied states are equal. As a result, there is only one step in the current-voltage dependence and the differential conductance assumes the highest value.

The dependence of the differential conductance remarkably reveals the effect of Coulomb blockade in the form of *Coulomb diamonds* pattern, see Fig. 1.4(b). In the case of an unbiased system $V = 0$, the diagram shows the stability regions with integer electron occupation number in the quantum dot (labeled with the numbers in brackets) and indicates values of ε where resonant peaks in linear conductance emerge. Furthermore, the peaks in differential conductance at finite bias voltage are associated with quantum dot states entering the transport window and, thus, with the step-like dependence of the current. In consequence, the differential conductance is a transport quantity that provides a lot of information about the electronic structure of the examined system and is a great indicator of various regimes and transport phenomena.

Finally, it is important to note that, experimentally, all presented regimes are attainable by applying appropriate bias voltage between the leads, while the position of the quantum dot energy level ε can be tuned by the electrostatic potential of the corresponding electrostatic gate [29, 64, 65].

1.3.3 Tunnel Magnetoresistance

Tunnel magnetoresistance (TMR) is a transport phenomenon taking place in tunnel junctions with ferromagnetic leads [66–69]. Due to the spin-dependent lead-dot coupling strengths, the spin degree of freedom is exploited giving rise to the TMR effect. In the papers presented in this thesis, the two co-linear configurations of leads' magnetic moments are studied, the parallel and antiparallel one, see Fig. 1.5. Such consideration allows one to designate quantitatively the TMR by finding the currents in both magnetic configurations, i.e. the current flowing in the parallel (I^P) and in the antiparallel (I^{AP}) magnetic configuration.

The theoretical model of TMR was proposed by M. Julliére [70], where the tunneling of electrons in a single ferromagnetic junction between the respective conduction subbands was analyzed. In the parallel magnetic configuration the majority (minority) electrons of the left lead tunnel to the majority (minority) states in the right lead, while in the antiparallel configuration, the majority (minority) electrons of the left lead tunnel to the minority (majority) states in the right lead, see Fig. 1.5. Julliére showed that for a single ferromagnetic tunnel junction TMR
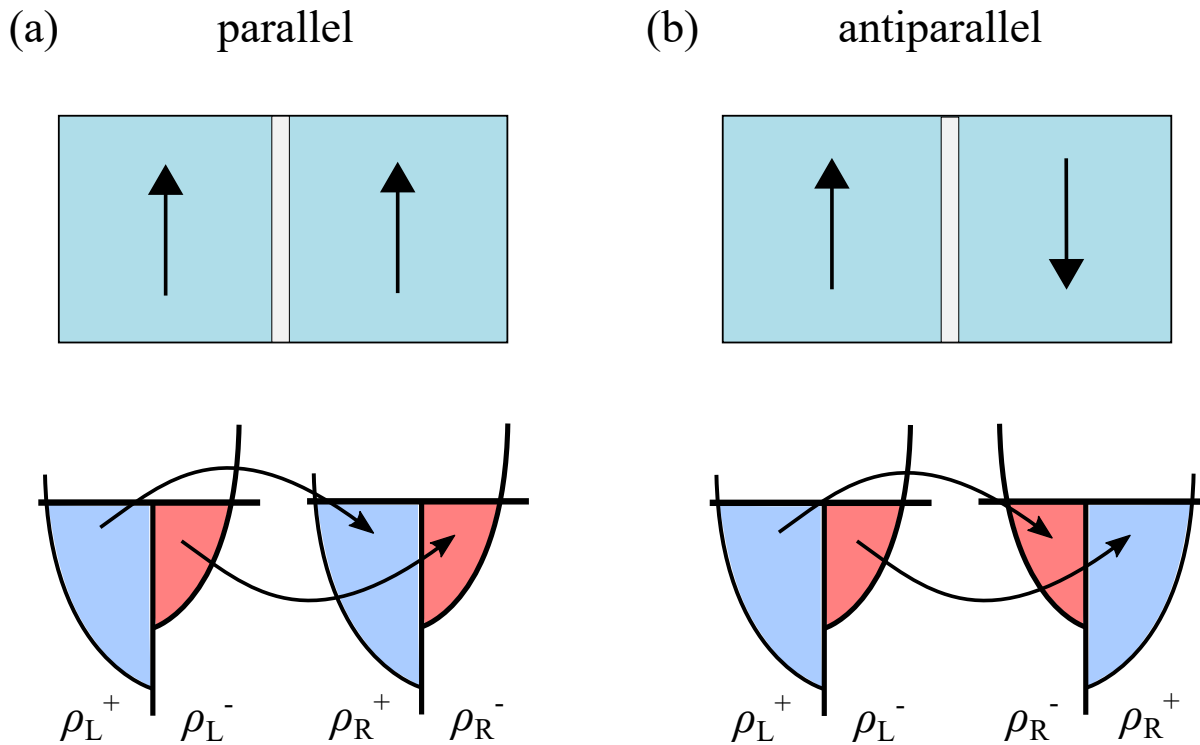

Figure 1.5: The scheme of single ferromagnetic junction presenting the system in the parallel (a) and antiparallel (b) magnetic configuration together with the corresponding densities of states for majority and minority electron bands in the left (L) and right (R) leads.

strongly depends on spin polarization of the leads, $p_r = \frac{\rho_r^+ - \rho_r^-}{\rho_r^+ + \rho_r^-}$, where $r = R, L$, and the

dependence has the following form

$$\text{TMR}^{\text{Jull}} = 2p_L p_R / (1 - p_L p_R). \tag{1.30}$$

The situation is more complex when a double ferromagnetic tunnel junction is considered, with quantum dots embedded between the ferromagnetic leads [67–69, 71]. In general, in such systems the TMR deviates from TMR^{Jull} due to the various spin-dependent transport processes, spin relaxation or partial polarization of the quantum dot. Hence, the calculation of the TMR as a function of bias and gate voltages can give valuable insight into relevant transport processes or can indicate interesting effects, such as spin accumulation, in the quantum dot.

Quantitatively, the TMR is given by [66–69]

$$\text{TMR} = \frac{I^P - I^{AP}}{I^{AP}}, \tag{1.31}$$

where $I^P(I^{AP})$ is the current flowing through the system in the parallel (antiparallel) magnetic configuration.

1.3.4 Current fluctuations

The noise is the signal is the inspiring title of the paper written by Rolf Landauer for Nature - News & Views in 1998 [72]. The conveyed idea is that the noise in electronic systems is not exclusively an unwanted part of the measured signal, but it can be used to get an additional insight into electronic transport. The most common type of noise in mesoscopic systems is the shot-noise, i.e. the noise associated with charge discreteness and current flow. It was introduced by Walter Schottky in 1918 after studying the current fluctuations in a vacuum tube [73]. The shot-noise originates from the quantization of the charge carriers and, especially in mesoscopic systems, it can become a significant part of a measured signal.

When the electrons pass the conductor with a Poissonian statistics, i.e. each tunneling act is an independent and random event, the shot-noise is then given by [73]

$$S_P(\omega) = 2|eI|, \tag{1.32}$$

where e is electron charge and I is the average current. The Poissonian noise is independent of the frequency ω. In the research presented in this thesis, the current and shot-noise are always

calculated for the zero-frequency ($\omega = 0$) as the applied bias voltage is constant in time.

The corresponding Fano factor F is introduced to describe the deviation of the measured shot-noise from the Poissonian value [74]:

$$F = \frac{S}{2|eI|}. \tag{1.33}$$

When the designated Fano factor is lower than unity ($F < 1$), the shot-noise is called sub-Poissonian and is very often associated with the antibunching of tunneling events correlated by the charging effects. When the shot-noise is super-Poissonian ($F > 1$), it is related to bunching, which can happen e.g. in the Coulomb blockade regime [22, 75, 76].

An interesting quantity to consider in multi-terminal systems is the zero-frequency cross-correlation function between the currents flowing through distinct junctions. In articles (V) and (VI), the analysis of cross-correlations between two currents flowing through the two separate arms of the device was performed. The current cross-correlations can give additional insight into transport processes and, in the case of Andreev transport and Cooper pair splitter devices, it can help to optimize the system's parameters for the efficient splitting properties. Finally, the current cross-correlations in multi-terminal systems were successfully measured in many experiments [77–79], which is always an important factor advocating for a comprehensive theoretical study of the quantity in question.

From the Wiener-Khintchine theorem, the noise can be written as the Fourier transform of the auto-correlation function, and for the zero-frequency it is given by

$$S = \int_{-\infty}^{\infty} dt \langle \delta I(t) \delta I(0) + \delta I(0) \delta I(t) \rangle, \tag{1.34}$$

with $\delta I(t) = I(t) - \langle I \rangle$. In the real-time diagrammatic approach, the total shot-noise is found from [75]

$$S = \frac{e^2}{\hbar} \mathbf{e}^T [\mathbf{W}^{II} + \mathbf{W}^I (\mathbf{P} \mathbf{W}^I + \mathbf{p}^{\text{st}} \otimes \mathbf{e}^T \partial \mathbf{W}^I)] \mathbf{p}^{\text{st}}. \tag{1.35}$$

The matrix $\mathbf{W}^{II}$ describes the contributions coming from two current operators in a single irreducible self-energy block. $\mathbf{P}$ is the so-called "decaying" propagator describing stationary part of the propagation. The propagator can be found from $\tilde{\mathbf{W}} \mathbf{P} = \mathbf{p}^{\text{st}} \mathbf{e}^T - \mathbf{1}$, with $\tilde{\mathbf{W}}$ being equal to the matrix $\mathbf{W}$ with arbitrary row replaced by $(\Gamma, ..., \Gamma)$. The matrix $\partial \mathbf{W}^I$ is the derivative of the Laplace-transformed matrix $\mathbf{W}^I$. Finally, $\mathbf{e}^T$ is a vector $\mathbf{e}^T = (1, ..., 1)$. The zero-frequency

current cross-correlations are defined as

$$S_{LR} = \int_{-\infty}^{\infty} dt \langle \delta I_L(t) \delta I_R(0) + \delta I_R(0) \delta I_L(t) \rangle, \qquad (1.36)$$

Then, the real-time diagrammatic formula for cross-correlations in the sequential tunneling approximation is given by

$$S_{LR} = \frac{e^2}{\hbar} \mathbf{e}^T [\mathbf{W}^{I_L} \mathbf{P} \mathbf{W}^{I_R} + \mathbf{W}^{I_R} \mathbf{P} \mathbf{W}^{I_L}] \mathbf{p}^{\text{st}}, \qquad (1.37)$$

where the self-energy matrix $\mathbf{W}^{I_{L(R)}}$ takes into account the electrons transferred through the left (right) junction.

More details about the mesoscopic shot-noise and the real-time diagrammatic approach can be found in [22, 75, 80].

1.3.5 Dark states

The *dark states* in mesoscopic systems [13–16, 28, 81, 82] are the electronic analogs of the well-known phenomenon from the atomic physics [83–85]. The effect arises due to a destructive interference of the electronic wavefunction effectively decoupling the system from one of the external reservoirs. In consequence, the transport through the system is suppressed, while the electrons are coherently trapped in the central part of the device. The effect reveals itself in transport characteristics through a strong current blockade, associated negative differential conductance and super-Poissonian shot-noise [14–16]. Apart from many important effects on the electronic transport, the dark states are also considered to have potential applications in quantum information technology [90, 91].

In particular, triple quantum dot systems [86, 87] are perfect playground to study the effects of *dark states* and their influence on the transport properties. Quantum dots in triangular arrangement resemble a simple planar molecule and enable the investigation of quantum interference effects, similarly like in the Aharonov-Bohm rings [88, 89].

To illustrate the idea of a dark state in a triangular system, it is convenient to consider a triple quantum dot with hopping t, in the singly occupied regime ($U_i \to \infty, U_{ij} \to \infty$). The local basis is defined as $|1\rangle, |2\rangle, |3\rangle$, where the integer i in the ket labels the state with an electron occupying the i-dot, see Fig. 1.6. In order to find a dark state in this system, a small asymmetry between the dots needs to be introduced, and in this case, it is achieved by detuning one of the

dot's (dot 2) energy level by a parameter ξ.

The Hamiltonian can be written as

$$H = \begin{pmatrix} \varepsilon & t & t \\ t & \varepsilon - \xi & t \\ t & t & \varepsilon \end{pmatrix}. \tag{1.38}$$

The exact diagonalization of the above system allows one to find the eigenspectrum. One of the eigenstates has the form

$$|\psi_{DS}\rangle = \frac{1}{\sqrt{2}}(1|1\rangle + 0|2\rangle - 1|3\rangle), \tag{1.39}$$

with eigenenergy $E_{DS} = \varepsilon - t$. The state $|\psi_{DS}\rangle$ has the electron density distributed only between dot 1 and dot 3, while the dot 2 has a vanishing amplitude. As a result, the presence of $|\psi_{DS}\rangle$
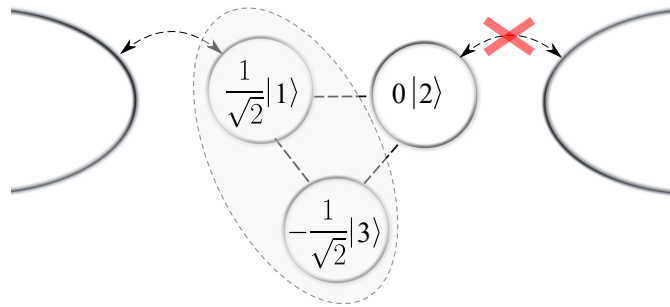

Figure 1.6: The scheme of a triangular quantum dot occupied by a dark state $|\psi_{DS}\rangle$ decoupling the system from the right lead.

state effectively decouples the triple quantum dot from the lead associated with the quantum dot 2 and in consequence blocks the current flowing through the device.

1.3.6 The Kondo effect

The first observations of a resistance minimum in some metals [92] gave the beginning to significant developments in the physics of magnetic impurities. An important progress was achieved by P. W. Anderson, who proposed the *Anderson model* [31], where the short range interaction U was introduced to explain the localized magnetic moments. Furthermore, the uppermost advance in this field was done by Jun Kondo in 1964 [23], who applied third-order perturbation theory in the coupling J to explain the problem of resistivity minimum. The magnetic impurity's exchange interaction J leads to the scattering of the conduction electrons near the Fermi level and, in consequence, provides an additional logarithmic term to the resistivity.

Unfortunately, the perturbation approach is not valid at low temperatures, as the logarithmic term diverges when T becomes of the order of T_K.

The milestone contribution was provided by K. G. Wilson (who received the Nobel prize in 1982 for his theory of critical phenomena in connection with phase transitions). Wilson took the idea of renormalization group from the quantum field theory, developed his *numerical renormalization group* [47] - a non-perturbative approach, and subsequently applied it to phase transitions, and later to the Kondo problem. This allowed to numerically solve the problem of a magnetic impurity interacting with a continuum of fermionic states.

In 1988, it was suggested that the Kondo effect should occur in small semiconductor transistor-type devices [93, 94]. Quantum dots, also known as artificial atoms, can hold a small number of electrons in a tunable fashion and seemed to be a perfect candidate as a device for testing the Kondo problem. The first successful experiments confirming the presence of the Kondo effect in quantum dots were performed at MIT by D. Goldhaber-Gordon et al. [25] and at Delft by L. P. Koewenhoven et al. [95], reported in 1998 - almost 10 years after aforementioned theoretical predictions. The papers were quickly followed by another two important experiments [96, 97], see also Fig. 1.7.
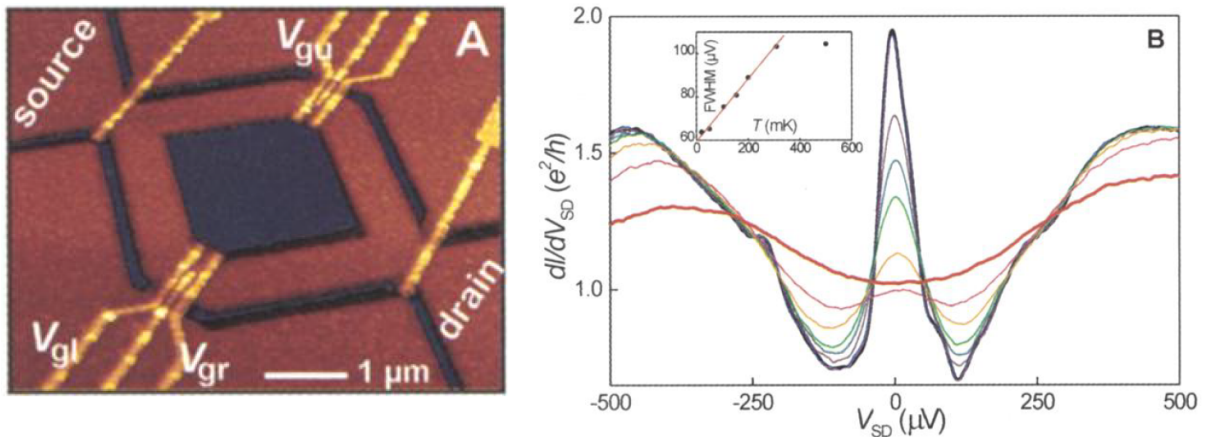

Figure 1.7: Illustration of the experiment performed by L. Kouwenhoven et al. [97] (A) Atomic force microscope image of the device - a quantum dot defined in 2DEG in AlGaAs/GaAs heterostructure. (B) Differential conductance plotted vs bias voltage for temperature from 900mK (thick red) down to 15mK (thick black).

A quantum dot attached to external leads is the system very similar to the magnetic impurity hosted in a bulk metal, with the main distinction that the Kondo effect in quantum dots increases the conductance. The electrons traveling in quantum dot setup has no other path around, than to travel through the central part between the two separate leads. The Kondo resonance mixes

the states between two distinct electrodes and thus the conductive properties are significantly enhanced, in opposite to the bulk case were resistivity is enhanced.

In the Kondo regime, similarly like in the case of resistance in bulk sample, the conductance in quantum dots depends on the Kondo temperature T_K, which is a temperature at which the conductance approximately reaches the half of its maximal value. At the lowest temperatures, the conductance dependence achieves the quantum limit of $\frac{2e^2}{h}$. In this limit, the electron transmission through the system is perfect in both spin channels. Finally, it is important to stress the advantage of tunability in quantum dots once again. All the parameters, on which Kondo temperature depends, i.e. the level energy ε, Coulomb correlations U and coupling strength Γ can be conveniently adjusted by the gate voltages [98–100].

Nowadays, the Kondo effect is incessantly a vibrant topic in the field of condensed matter physics. It includes novel, widely explored problems, such as heavy fermions, Fermi liquid theory for quantum impurities, Kondo insulators and among many others, the Kondo effect in quantum dots and molecules.

1.4 Summary

The presented PhD thesis, entitled *Correlation effects in transport through quantum dot systems*, has a form of a series containing seven papers presented in Chapter 2. The articles constitute the main part of the scientific achievement corresponding to the research performed by the author during his PhD studies. The preceding part, Chapter 1, which presents the motivation and aims, methodology and basic concepts in charge and spin transport through quantum dot systems.

Considering the examined systems, the papers are ordered in the following way. In articles (I, II, III, IV) the focus is on a triangular quantum dot setup. Subsequently, papers (V, VI, VII) deal with Cooper pair splitters based on quantum dots. The results presented in (I, II, III, IV, V, VI) were obtained by employing the real-time diagrammatic method, while the results presented in (VII) were calculated with the aid of the numerical renormalization group method. The common subject across all the papers are various correlations in the systems, their interplay and effects on the charge and spin transport. A short summary of the performed research is given below.

The presented series begins with the paper (I), entitled *Spin effects in transport through triangular quantum dot molecule in different geometrical configurations*. In this publication, comprehensive analysis of the current, differential conductance and Fano factor was performed in the parallel and the antiparallel magnetic configurations, up to the second-order of perturbation theory accounting both for sequential and cotunneling processes. Moreover, the resulting TMR and various spin effects were studied. Two geometrical configurations were analyzed in particular. In the *mirror* arrangement, the system was coupled to two external leads in symmetric manner, which in consequence resulted in symmetry of transport characteristics under the change of the bias voltage sign. The other one, i.e. the *fork* configuration, enabled the splitting of the current from the source electrode into two distinct drain electrodes. An enhanced TMR and super-Poissonian shot noise were predicted in the *mirror* geometry, while negative differential conductance and inverse TMR were found in the *fork* arrangement. The underlying mechanisms leading to the described effects were thoroughly discussed and explained.

The next article (II), entitled *Current Suppression in Transport Through Triple Quantum Dots Coupled to Ferromagnetic Leads*, presents an extension of the previous paper. By introducing the detuning parameter δ in one of the quantum dots, the symmetry of the quantum dots' energy levels was broken. In consequence, two regimes with strong current suppressions were

present in the system, along with trapping of either one or two electrons in the quantum dots. The one-electron blockade unfolded itself as a *dark state*, while the two-electron blockade was due to the Coulomb correlations. The differences between the blockades were revealed in the shot-noise and the TMR.

The paper (III), entitled *Influence of Magnetic Field on Dark States in Transport through Triple Quantum Dots*, is focused on the manipulation of dark states by means of external magnetic field. The system's parameters were tuned to allow for the formation of one- and two-electron dark states. Furthermore, the influence of the external magnetic field was considered. It was shown that magnetic field can shift the bias voltage regime dominated by the one-electron dark state. On the other hand, the bias range for the two-electron dark state can be decreased, eventually leading to complete lifting of the blockade for the strong values of applied magnetic field. The analysis of the states energetic structure and their magnetic properties allowed for the convenient explanation of presented effects.

In the last article (IV) concerning the triple quantum dot systems, *Dark states in spin-polarized transport through triple quantum dot molecules*, an extensive analysis of dark states in quantum dots and their magneto-transport properties was performed. In particular, dark states formed of one, two, four and five electrons were examined. Depending on the number of particles forming a dark state, the TMR revealed an interesting behavior: for odd number of electrons the TMR was strongly suppressed, while for an even electron number the TMR acquired negative values. The considerations included both sequential and cotunneling processes and the influence of the latter was in particular discussed by analyzing the behavior of the TMR and the Fano factor. It was shown that the cotunneling processes were dominating transport in dark states regimes, at the same time substantially modifying the TMR effect. Finally, the dark states with high number of electrons were conveniently analyzed as the states formed by the inference of holes, and it was shown that resulting transport characteristics could be understood within the hole current framework. The comparison of appropriate electron and hole dark states indicated, that the conclusions were correct and a very interesting example of the electron-hole symmetry was revealed.

In the three consecutive papers (V, VI, VII) the theoretical study of transport concerns hybrid quantum dot systems coupled to superconducting electrode. Article (V), entitled *Current cross-correlations in double quantum dot based Cooper pair splitters with ferromagnetic leads*, contains a detailed study of current cross-correlation function as well as differential conductance

for the Andreev transport. The noise analysis in mesoscopic systems can give an additional insight into the transport processes and this is exactly the case in the considered problem. The revealed enhanced positive cross-correlations are associated with high Cooper pair splitting efficiency of the device. The regimes of negative sign of cross-correlations indicate tunneling processes in opposite directions through distinct junctions. The mechanisms responsible for both effects were thoroughly explained with the help of relevant eigenstates and transition rates analysis. Moreover, it is worth to highlight the influence of the leads' spin polarization and magnetic alignment of the ferromagnetic leads on the transport properties. The results were enriched by the derivation of approximate analytical formulas to evaluate the cross-correlations in the most interesting transport regimes. Finally, the work consists of the analysis of the Coulomb correlations influence on the transport properties. The conducted study for wide parameter space allows one to identify the optimal regimes for the highly efficient splitting, which is of great importance for the experiments and future applications.

In a similar spirit, the study of single quantum dot system in paper (VI), *Cross-correlations in a quantum dot Cooper pair splitter with ferromagnetic leads*, was prepared. The differential conductance and current cross-correlations analysis was extended by considering non-magnetic electrodes, where the interesting uncorrelated transport is predicted near the particle-hole symmetry point. Moreover, the influence of external magnetic field was analyzed. The Andreev states were split exposing additional lines in differential conductance and doubling the number of corresponding excitations. The number of regimes, where negative cross-correlations were present, remained independent of magnetic field, however, negative values were diminished. On the other hand, the external magnetic field resulted in enhanced positive cross-correlations, when the bias voltage is in resonance with excitation energies of the split Andreev states.

The main aim of the last paper (VII), *Kondo physics in double quantum dot based Cooper pair splitters*, was to study the interplay of superconducting correlations and those leading to the Kondo effect. For the $SU(2)$ Kondo effect, the finite superconducting pairing potential suppresses the Kondo resonance, which can reemerge for larger values of the coupling to superconductor. On the other hand, in the $SU(4)$ Kondo regime, a crossover from the $SU(4)$ to the $SU(2)$ Kondo state was observed. The behavior was explained with the support of the spectral functions and the ground state analysis, which was also conveniently illustrated on the relevant energy diagrams. The Andreev transmission and Cooper pair splitting efficiency were studied as well, which, in consequence, allowed one to find the parameters and regimes for optimal

splitting.

To summarize, the performed theoretical research was focused on studying the correlation effects in the transport properties of coupled quantum dot systems and brought many interesting results. The origin of analyzed and explained non-trivial effects is clearly in various correlations present in the system. On the one hand, similar transport characteristics can be achieved by different means, e.g. current flow through the system can be blocked either by strong Coulomb correlations, by superconducting correlations leading to a triplet blockade, or by quantum interference resulting in formation of dark states. On the other hand, the same type of correlations can be also responsible for different effects, depending on other conditions present in the system. Finally, the interplay of certain correlations may lead to a rich and non-trivial effects, such as the suppression and reemergence of the Kondo effect in double quantum dot systems in the proximity of the superconductor. Another important conclusion is that the analyzed transport characteristics are very helpful in capturing and explaining those phenomena. In particular, the quantities that are measurable in nowadays experimental setups, i.e. current fluctuations, such as shot-noise or cross-correlations, and the TMR, can all indicate the dominant transport processes and effects present in the system.

1.5 Streszczenie (Summary of the thesis in Polish)

Zaprezentowana rozprawa doktorska, zatytułowana *Efekty korelacji w transporcie przez układy kropek kwantowych* (*ang. Correlation effects in transport through quantum dot systems*), ma formę cyklu siedmiu artykułów zamieszczonych w Rozdziale 2. Stanowią one główną część osiągnięć naukowych autora, związanych z przeprowadzonymi badaniami zjawisk transportu kwantowego w układach kropek kwantowych podczas studiów doktoranckich. Artykuły zostały poprzedzone stosownym wprowadzeniem przedstawionym w Rozdziale 1 zawierającym opis motywacji i celu dysertacji, zastosowanej metodologii oraz najważniejszych zjawisk pojawiających się w badaniach transportu ładunkowego i spinowego przez układy kropek kwantowych.

Przedstawiony cykl artykułów został uporządkowany ze względu na rodzaj badanego układu na dwie spójne tematycznie części. W artykułach (I, II, III, IV) skupiono się na analizie własności transportowych układu trzech kropek kwantowych w trójkątnej konfiguracji przestrzennej. Natomiast, pozostałe trzy prace (V, VI, VII) dotyczą badania układów typu rozdzielaczy par Coopera zbudowanych w oparciu o kropki kwantowe. Wyniki zaprezentowane w artykułach (I, II, III, IV, V, VI) otrzymane zostały przy wykorzystaniu techniki diagramowej w czasie rzeczywistym, natomiast w artykule (VII) do obliczeń użyto metody numerycznej grupy renormalizacji. Wspólnym tematem wszystkich prac są efekty korelacji występujące w badanych układach, ich współoddziaływanie oraz wpływ na transport spinowy i ładunkowy. Wprowadzenie do poszczególnych artykułów oraz podsumowanie najważniejszych wyników zamieszczone zostało poniżej.

Artykuł (I) zatytułowany *Efekty spinowe w transporcie przez molekułę opartą na trójkątnym układzie kropek kwantowych w różnych konfiguracjach geometrycznych* przedstawia kompleksową analizę spinowo sporalyzowanego transportu przez układ trzech kropek kwantowych. W pracy przeprowadzono dokładną analizę prądu, konduktancji różniczkowej oraz szumów ziarnistych dla szerokiego zakresu parametrów transportowych. W badaniach uzgędniono procesy tunelowania sekwencyjnego oraz kotunelowania. Rozważany układ potrójnej kropki kwantowej był sprzężony z elektrodami ferromagnetycznymi, co w konsekwencji umożliwiło także analizę tunelowego magnetooporu oraz innych efektów spinowych. Rozpatrzone zostały w szczególności dwie konfiguracje geometryczne różniące się sprzężeniami kropek kwantowych do zewnętrznych elektrod. W konfiguracji nazwanej *lustrzaną* układ sprzężony był symetrycznie do dwóch elektrod, co prowadzi do symetrii wszystkich charakterystyk transportowych ze względu na zmianę znaku przyłożonego napięcia. Druga zbadana konfiguracja,

rozwidlająca, polegała na przyłączeniu kropek kwantowych do trzech zewnętrznych elektrod. Napięcie transportowe było przyłożone w taki sposób, aby możliwe było rozdzielenie prądu pochodzącego z jednej elektrody – źródła, dwoma osobnymi ramionami struktury do dwóch oddzielnych elektrod – drenów. W geometrii *lustrzanej* przewidziano obszary znacznego wzmocnienia tunelowego magnetooporu oraz fluktuacji prądowych. W geometrii *rozwidlającej* pojawiły się zarówno ujemna konduktancja różniczkowa, jak i ujemny efekt tunelowego magnetooporu. Mechanizmy prowadzące do tych zjawisk zostały w pracy dokładnie omówione i wyjaśnione.

Kolejny artykuł (II) o tytule *Wygaszenia prądu w transporcie przez układ trzech kropek kwantowych sprzężonych z elektrodami ferromagnetycznymi* stanowi rozszerzenie badań z artykułu (I). W układzie trzech kropek kwantowych w konfiguracji *lustrzanej* złamano symetrię poziomów energetycznych kropek kwantowych, poprzez wprowadzenie parametru odstrojenia δ na jednej z nich. Konsekwencją tej modyfikacji było pojawienie się w charakterystykach prądowo-napięciowych dwóch obszarów, w których prąd jest silnie wygaszany, a na kropkach kwantowych spułapkowane są odpowiednio jeden i dwa elektrony. Blokada jednoelektronowa miała charakter *stanu ciemnego*, natomiast blokada dwuelektronowa wynikała z odpowiedniej konfiguracji oddziaływań kulombowskich. Różnice pomiędzy obszarami transportu z obu blokad widoczne były także w analizie fluktuacji prądu oraz tunelowego magnetooporu.

Artykuł (III) nosi tytuł *Wpływ pola magnetycznego na stany ciemne w transporcie przez układ trzech kropek kwantowych* i skupia się na badaniach możliwości manipulacji stanami ciemnymi poprzez przyłożone zewnętrzne pole magnetyczne. W pracy wyznaczono parametry układu trzech kropek kwantowych, dla których możliwe jest formowanie się stanów ciemnych, zarówno jedno- jak i dwuelektronowych. Następnie przeanalizowany został wpływ zewnętrznego pola magnetycznego na własności tych stanów ciemnych. W szczególnosci wykazano, że zakres napięć, dla którego pojawia się jednoelektronowy stan ciemny, można zmieniać polem magnetycznym. Natomiast, w przypadku dwuelektronowego stanu ciemnego, możliwe jest zmniejszenie wielkości obszaru napięć, gdzie występuje stan ciemny, a przy odpowiednio silnym polu, całkowite zniesienie blokady prądu. Przeprowadzona analiza struktury energetycznej stanów własnych układu oraz ich własności spinowe umożliwiły precyzyjne wyjaśnienie tych mechanizmów.

W ostatnim artykule (IV) dotyczącym układu trzech kropek kwantowych o tytule *Stany ciemne w spinowo-spolaryzowanym transporcie przez molekuły oparte na trzech kropkach*

kwantowych przestawiona została kompleksowa analiza zjawiska tworzenia się stanów ciemnych, ze szczególnych uwzględnieniem ich wpływu na własności magneto-transportowe. Badaniom poddano stany ciemne o różnej liczbie spułapkowanych elektronów w układzie kropek kwantowych. W zależnosci od parzystości liczby elektronów, tunelowy magnetoopór wykazuje różne zachowanie: przy nieparzystej liczbie magnetoopór ulega mocnemu wygaszeniu, natomiast przy stanach ciemnych z parzystą liczbą cząstek, efekt tunelowego magnetooporu przyjmuje ujemne wartości. W rozważaniach uwzględniono zarówno procesy tunelowania pierwszego, jak i drugiego rzędu oraz ich wpływ na prąd, tunelowy magnetoopór i fluktuacje prądu. Omówione różnice pomiędzy przybliżeniem sekwencyjnym, a uwzględnieniem kotunelowania, podkreślają istotną rolę procesów drugiego rzędu w obszarze transportu gdzie występują stany ciemne. Ponadto, w pracy przedstawiono opis stanów ciemnych o wysokiej liczbie cząstek w obrazie transportu, gdzie nośnikami są dziury elektronowe. Porównanie własności odpowiednich stanów opisanych w obu ujęciach wskazuje, że jest to trafna obserwacja manifestacji symetrii elektronowo-dziurowej.

W kolejnych trzech artykułach (V, VI, VII) przeprowadzono teoretyczne badania transportu w hybrydowych układach kropek kwantowych sprzężonych do elektrody nadprzewodzącej, będącej źródłem wstrzykiwanych do układu par Coopera. Artykuł (V) zatytułowany *Wzajemne korelacje prądu w rozdzielaczach par Coopera opartych na dwóch kropkach kwantowych sprzężonych do ferromagnetycznych elektrod* zawiera szczególową analizę funkcji wzajemnych korelacji w układzie typu *rozdzielacz* oraz konduktancji różnicznkowej dla transportu Andriejewa. Badanie szumów w układach mezoskopowych pozwala uzyskać dodatkowy wgląd w procesy opisujące transport, a w rozważanym przypadku *wzajemne korelacje* w szczególności okazują się mieć istotne znaczenie. Badania pozwoliły znaleźć obszary o dużych, dodatnich wartościach korelacji sugerujące, że układ w tym obszarze wykazuje wysoką skuteczność rozdzielania par Coopera. Omówione zostały także obszary, gdzie pojawiają się ujemne wartości wzajemnych korelacji, wskazujące na przeciwny kierunek tunelowania w rozważanych złączach. Mechanizmy odpowiedzialne za oba zjawiska zostały dokładnie wyjaśnione poprzez analizę stanów własnych układu oraz procesów dominujących w transporcie. W szczególności, należy zwrócić uwagę na wpływ polaryzacji elektrod ferromagnetycznych na transport Andriejewa i procesy rozdzielania par Coopera, oraz odpowiedni dobór konfiguracji momentów magnetycznych elektrod. Wyniki te wzbogacono o wyznaczenie przybliżonych formuł analitycznych na wartości wzajemnych korelacji w szczególnie istotnych obszarach transportu. Pon-

adto, dokonano analizy transportu w zależności od siły korelacji kulombowskich na kropkach kwantowych. Przeprowadzone badania w bardzo szerokim zakresie parametrów pozwalają na znalezienie optymalnych parametrów i obszarów transportu, co posiada istotne znaczenie z punktu widzenia eksperymentu i przyszłych zastosowań.

Badania korelacji przeprowadzono również dla układu opartego na jednej kropce kwantowej, a wyniki zaprezentowano w artykule (VI) *Wzajemne korelacje w rozdzielaczu par Coopera opartego na kropce kwantowej sprzężonej do ferromagnetycznych elektrod*. Analizę konduktancji różniczkowej oraz wzajemnych korelacji rozszerzono o przypadek układu z niemagnetycznymi elektrodami, w którym pojawił się obszar nieskorelowanego transportu w pobliżu punktu symetrii elektronowo-dziurowej. W pracy przeanalizowano także wpływ zewnętrznego pola magnetycznego, prowadzącego do rozszczepienia stanów Andriejewa, na wzajemne korelacje. Obecność pola magnetycznego prowadzi do osłabienia ujemnych oraz wzmocnienia dodatnich wartości wzajemych korelacji prądu, w stosunku do wartości wyznaczonych dla przypadku bez zewnętrznego pola magnetycznego.

Ostatni artykuł (VII), *Fizyka Kondo w rozdzielaczu par Coopera opartego na dwóch kropkach kwantowych*, przedstawia wyniki analizy transportu dla układu silnie sprzężonego z elektrodami metalicznymi, co prowadzi do pojawienia się efektu Kondo. Głownym celem było zbadanie współoddziaływania korelacji nadprzewodzących oraz tych prowadzących do zjawiska Kondo. Okazało się, że dla efektu Kondo o symetrii SU(2), włączenie oddziaływań nadprzewodzących bardzo szybko prowadzi do zniszczenia zjawiska Kondo, jednak dalsze zwiększenie siły sprzężenia do nadprzewodnika prowadzi do odbudowy tego efektu. Natomiast w przypadku, gdy układ znajduje się w obszarze efektu Kondo typu SU(4), podczas zwiększania siły sprzężenia do naprzewodnika, obserwowane jest przejście do stanu Kondo o symetrii SU(2). Zachowania te wyjaśniono poprzez dokładną analizę lokalnej gęstości stanów oraz stanu podstawowego układu, co przedstawiono w postaci odpowiednich diagramów energetycznych. Przebadano także własności transportowe, analizując transmisję Andriejewa oraz efektywność rodzielania par Coopera, co umożliwiło znalezienie optymalnych parametrów pracy badanego układu.

Podsumowując, przeprowadzone teoretyczne badania transportu przez układy sprzeżonych kropek kwantowych dostarczyły wiele interesujących wyników i obserwacji. Wyraźnie wykazano, że przeanalizowane i wyjaśnione efekty mają swoje źródło w korelacjach obecnych w omawianych układach. Z jednej strony, podobne charakterystyki transportowe można otrzy-

mać w badanym układzie na różne sposoby, np. przepływ prądu może zostać zablokowany poprzez silne oddziaływania kulombowskie, przez korelacje nadprzewodnika prowadzące do blokady trypletowej lub poprzez zjawisko kwantowej interferencji odpowiedzialnej za powstanie stanu ciemnego. Z drugiej strony, te same korelacje potrafią odpowiadać za różne efekty, w zależności od specyficznych parametrów badanego układu. Ponadto, współoddziaływanie różnych korelacji może również prowadzić do ciekawych i nietrywialnych efektów, takich jak np. wygaszenie i odbudowa efektu Kondo w układzie podwójnej kropki kwantowej sprzężonej do nadprzewodnika. Kolejnym ważnym wnioskiem płynącym z przeprowadzonych badań jest duże znaczenie i przydatność wyznaczonych charakterystyk transportowych dla zidentyfikowania i wyjaśnienia omawianych efektów. W szczególności, wielkości takie jak fluktuacje prądu i tunelowy magnetoopór, które można wyznaczyć eksperymentalnie, potrafią wyraźnie wskazać najważniejsze procesy oraz efekty w transporcie przez badany uklad. Przedstawione badania oraz uzyskane wyniki pokazują jak bogaty i ciekawy jest świat fizyki mezoskopowej, oraz w szczególności, jakie potencjalne możliwości kryją się w układach kropek kwantowych. Można oczekiwać, że przedstawiony tutaj cykl prac przyczyni się do dalszego zintensyfikowania teoretycznych i eksperymentalnych prac badawczych dotyczących różnego typu korelacji w układach niskowymiarowych takich jak kropki kwantowe.

Chapter 2

Articles constituting the dissertation

Spin effects in transport through triangular quantum dot molecule in different geometrical configurations

Kacper Wrześniewski[*] and Ireneusz Weymann[†]

Faculty of Physics, Adam Mickiewicz University, Umultowska 85, 61-614 Poznań, Poland

We analyze the spin-resolved transport properties of a triangular quantum dot molecule weakly coupled to external ferromagnetic leads. The calculations are performed by using the real-time diagrammatic technique up to the second-order of perturbation theory, which enables a description of both the sequential and cotunneling processes. We study the behavior of the current and differential conductance in the parallel and antiparallel magnetic configurations, as well as the tunnel magnetoresistance (TMR) and the Fano factor in both the linear and nonlinear response regimes. It is shown that the transport characteristics depend greatly on how the system is connected to external leads. Two specific geometrical configurations of the device are considered—the mirror one, which possesses the reflection symmetry with respect to the current flow direction and the fork one, in which this symmetry is broken. In the case of first configuration we show that, depending on the bias and gate voltages, the system exhibits both enhanced TMR and super-Poissonian shot noise. On the other hand, when the system is in the second configuration, we predict a negative TMR and a negative differential conductance in certain transport regimes. The mechanisms leading to those effects are thoroughly discussed.

I. INTRODUCTION

Quantum dot systems have been the subject of broad experimental and theoretical research for more than two decades due to their potential applications in quantum computing, spintronics, and nanoelectronics [1–6]. While the transport properties of single quantum dots are rather well understood [7–10], coupled quantum dot systems still draw a considerable attention [11–16]. This is because such artificial molecules allow one to study various interference and correlation effects in a controllable fashion. In this regard, an undoubtedly important example is a triple quantum dot (TQD) system [17–26]. Recently, many relevant effects and properties related to TQDs have been reported. In particular, quantum entanglement in such systems have been widely studied [27,28], with qubit dynamics and read-out [29], qubit encoding [30], spin-entangled currents [31], and entanglement switching via the Kondo effect [32]. Other studies of Kondo physics on TQD were reported as well [33,34], including the transport properties in the Kondo regime [35–37], the Kondo-Aharonov-Bohm effect [38], or the anisotropic charge Kondo effect [39].

Moreover, the charge and spin transport through TQD systems also undergoes extensive investigation [40,41]. The role of single-particle [42–44] and two-particle [45] dark states in transport was analyzed. Superexchange blockade [46] and various types of the Pauli spin blockade [47,48] were also studied, and the mechanism of spin blockade control by ac magnetic field was discussed [49]. Moreover, in serially coupled TQD, the tunnel magnetoresistance (TMR) [50], long-distance tunneling [51,52], dephasing-assisted transport [53], and spin-orbit effects in a TQD shuttle [54] were examined. All these indicate that there is a great, both theoretical and experimental, interest in triple quantum dot systems and, in fact, there are still some problems that need to be addressed.

In this paper, we consider spin-resolved transport properties of a triangular quantum dot molecule weakly attached to external ferromagnetic electrodes, with a special focus on the geometrical configuration of the device and its influence on transport properties. We analyze two distinct setups of coupling to electrodes and different ways the bias voltage is applied. In the first configuration, which we call the mirror one, since it possesses a reflection symmetry with respect to the current flow direction, two of the three dots are coupled to the leads. In such a setup, the system's transport characteristics are symmetric with respect to the bias reversal. On the other hand, in the second configuration, called the fork one, one of the dots is coupled to one lead and the other two dots are coupled to the second lead. In this case, the reflection symmetry is broken and consequently the current-voltage characteristics are asymmetric with respect to the bias reversal.

To perform numerical calculations, we employ the real-time diagrammatic technique [55], including the first and second-order diagrams, which enable the description of both sequential tunneling and cotunneling processes. In both geometrical arrangements of the device, we determine the current, the corresponding differential conductance, the TMR, and the Fano factor in both the linear and nonlinear response regimes. In the case of mirror geometry, we show that the TMR can be enhanced in certain Coulomb blockade regimes and we also find super-Poissonian shot noise. On the other hand, in the case of fork geometry, we predict a negative TMR and a negative differential conductance, associated with current suppression due to Coulomb correlations. The mechanisms leading to the aforementioned effects are thoroughly discussed.

The paper is organized as follows. The model Hamiltonian of the TQD and the method used in the calculations are described in Sec. II. The numerical results and their discussion for TQDs in the case of mirror geometry are presented in Sec. III, while Sec. IV is devoted to the case of fork geometry. Finally, the paper is summarized in Sec. V.

_____

[*]wrzesniewski@amu.edu.pl
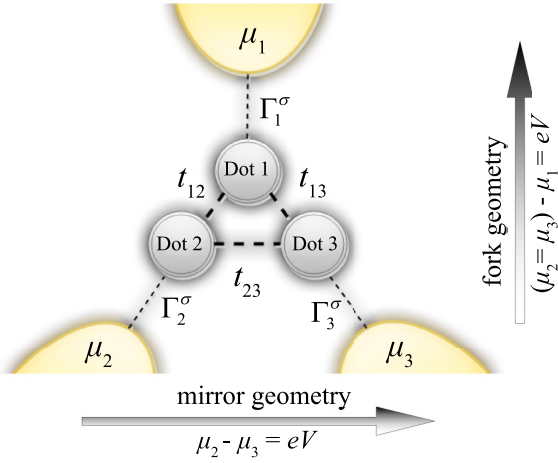
[†]weymann@amu.edu.pl

FIG. 1. (Color online) Schematic of a triple quantum dot system in triangular geometry. The ith dot is coupled to the dot j through the hopping matrix element t_{ij}. Each dot is coupled to a respective lead j, with Γ_j^σ describing the coupling strength, and μ_j denoting the chemical potential of this lead. We consider two different configurations of the device, the mirror and fork ones, as indicated by the arrows, respectively. In the mirror geometry, the current flows between the second and third lead with $\Gamma_1^\sigma = 0$, while in the fork geometry the voltage drop is applied between the first and the second-and-third lead.

II. THEORETICAL FRAMEWORK

A. Model

The schematic of the considered system is shown in Fig. 1. It consists of three single-level quantum dots in a triangular geometry. The dots are coupled to each other through the hopping matrix elements t_{ij} and attached to external leads with respective coupling strength Γ_j^σ. The leads are assumed to be ferromagnetic and their magnetizations can point either in the same direction (parallel configuration) or in opposite directions (antiparallel configuration). The Hamiltonian of the system is given by

$$H = H_{\text{Leads}} + H_{\text{TQD}} + H_{\text{Tun}},\qquad(1)$$

where H_{Leads} describes the noninteracting electrons in the leads,

$$H_{\text{Leads}} = \sum_{j=1,2,3}\sum_{k\sigma}\varepsilon_{jk\sigma}c_{jk\sigma}^\dagger c_{jk\sigma},\qquad(2)$$

with $\varepsilon_{jk\sigma}$ being the energy of an electron with spin σ, momentum k in lead j, and $c_{jk\sigma}^\dagger$ ($c_{jk\sigma}$) denoting the respective creation (annihilation) operator. The Hamiltonian of the triple dot reads

$$H_{\text{TQD}} = \sum_{j\sigma}\varepsilon_j n_{j\sigma} + U\sum_j n_{j\uparrow}n_{j\downarrow} + \frac{U'}{2}\sum_{\langle ij\rangle}\sum_{\sigma\sigma'}n_{i\sigma}n_{j\sigma'}$$
$$+ \sum_{\langle ij\rangle}\frac{t_{ij}}{2}\sum_\sigma(d_{i\sigma}^\dagger d_{j\sigma} + d_{j\sigma}^\dagger d_{i\sigma}),\qquad(3)$$

with $n_{j\sigma} = d_{j\sigma}^\dagger d_{j\sigma}$, where $d_{j\sigma}^\dagger$ ($d_{j\sigma}$) is the creation (annihilation) operator of an electron with spin σ in the jth quantum dot, and ε_j is the corresponding single-particle energy. The second

term takes into account the on-site Coulomb interaction U on dot j, U' corresponds to the interdot Coulomb correlation, and $\langle ij\rangle$ denotes the summation over the nearest-neighbor dots. The last term of H_{TQD} describes the interdot hopping, with t_{ij} being the hopping parameter between the dot i and j. The parameters U' and t_{ij} are divided by 2 to avoid double counting. We assume that the coupling between the dots is relatively large, so that there is a considerable overlap of the wave functions of neighboring dots, leading to the formation of molecular many-body states, $|\chi\rangle$, through which transport takes place. The states $|\chi\rangle$ are the eigenstates of H_{TQD}, $H_{\text{TQD}}|\chi\rangle = \varepsilon_\chi|\chi\rangle$, where ε_χ is the corresponding eigenenergy.

The last term of the Hamiltonian describes tunneling processes between TQD and leads, and can be written as

$$H_{\text{Tun}} = \sum_{j=1,2,3}\sum_{k\sigma}v_j(c_{jk\sigma}^\dagger d_{j\sigma} + d_{j\sigma}^\dagger c_{jk\sigma}),\qquad(4)$$

with v_j denoting the tunnel matrix element between the jth lead and respective quantum dot. The coupling between jth lead and jth dot is described by $\Gamma_j^\sigma = 2\pi|v_j|^2\rho_j^\sigma$, where ρ_j^σ is the spin-dependent density of states of lead j. Introducing the definition of the spin polarization of lead j, $p_j = (\rho_j^+ - \rho_j^-)/(\rho_j^+ + \rho_j^-)$, one can express the couplings as $\Gamma_j^\pm = \Gamma_j(1 \pm p_j)$, where $\Gamma_j = (\Gamma_j^+ + \Gamma_j^-)/2$. Then, Γ_j^+ (Γ_j^-) denotes the coupling of the jth dot to the spin-majority (spin-minority) electron band of lead j. In the following, we assume that the couplings are symmetric, $\Gamma_j \equiv \Gamma/2$ and $p_j \equiv p$.

While the geometry of the considered system is quite general, in this paper we will analyze two specific configurations of the device, which we henceforth call the mirror and fork ones. In the mirror geometry, the voltage drop is applied between the second and third leads, $\mu_2 - \mu_3 = eV$, with $\mu_2 = -\mu_3 = eV/2$, while the first lead is decoupled ($\Gamma_1^\sigma = 0$), see Fig. 1. In this setup, for symmetric systems, the current-voltage characteristics are symmetric with respect to the bias reversal. In the fork geometry, on the other hand, the current flows between the first (with chemical potential μ_1) and second-and-third leads, which are kept at the same chemical potential, $\mu_2 = \mu_3$, see Fig. 1, and the voltage drop is applied symmetrically, $-\mu_1 = \mu_2 = \mu_3 = eV/2$. In this case, the current symmetry with respect to the bias reversal does not hold any more and the transport characteristics are asymmetric around $V = 0$. Transport through TQDs in a similar geometry has been recently explored experimentally by Rogge and Haug [21].

B. Method

In order to calculate the spin-dependent transport properties of a triple quantum dot system, we use the real-time diagrammatic technique [55]. This method is based on a perturbation expansion of quantities of interest, such as the reduced density matrix or the current operator, with respect to the coupling strength Γ. The elements of the reduced density matrix in the steady state can be found from the following equation [55,56]:

$$\mathbf{W}\mathbf{p} = 0,\qquad(5)$$

together with the normalization condition, $\text{Tr}(\mathbf{p}) = 1$. Here, $\mathbf{W}$ is the self-energy matrix whose elements, $W_{\chi\chi'}$, describe transitions between the TQD many-body states $|\chi\rangle$ and $|\chi'\rangle$, while $\mathbf{p}$ is the probability vector. The current flowing through

the system can be found from [55,56]

$$I = \frac{e}{2\hbar}\mathrm{Tr}(\mathbf{W}^I\mathbf{p}),\tag{6}$$

where the self-energy matrix $\mathbf{W}^I$ takes into account the number of electrons transferred through the system. It can be calculated by replacing one internal vertex resulting from the expansion of tunneling Hamiltonian by the current operator. To calculate the self-energies, one can use the respective diagrammatic rules in a given order of expansion with respect to tunneling processes [55–57]. Some details of the calculations are presented in Appendix. In this paper, we determined the self-energies up to the second order of expansion, which allows us to describe both the sequential tunneling (first-order processes) and cotunneling (second-order processes). While sequential tunneling gives the dominant contribution to the current out of the Coulomb blockade regime, it becomes exponentially suppressed at low voltages where the system is in the Coulomb blockade. In this transport regime, the current can then flow due to the second-order tunneling processes [58].

Having determined the first and second-order diagrams, the zeroth- and first-order occupation probabilities can be found from the respective kinetic equations [56], $\mathbf{W}^{(1)}\mathbf{p}^{(0)} = 0$ and $\mathbf{W}^{(2)}\mathbf{p}^{(0)} + \mathbf{W}^{(1)}\mathbf{p}^{(1)} = 0$, where $\mathbf{p}^{(n)}$ and $\mathbf{W}^{(n)}$ denote the probability vector and self-energy matrix in nth order of expansion with respect to Γ. This allows one to find the first- and second-order currents from

$$I^{(1)} = \frac{e}{2\hbar}\mathrm{Tr}(\mathbf{W}^{I(1)}\mathbf{p}^{(0)}),\tag{7}$$

$$I^{(2)} = \frac{e}{2\hbar}\mathrm{Tr}(\mathbf{W}^{I(2)}\mathbf{p}^{(0)} + \mathbf{W}^{I(1)}\mathbf{p}^{(1)}).\tag{8}$$

The total current is then simply given by $I = I^{(1)} + I^{(2)}$. In addition, we also calculate the Fano factor, [59] $F = S/(2|eI|)$, where S denotes the zero-frequency shot noise. The Fano factor describes the deviation of the shot noise from its Poissonian value, $S_P = 2|eI|$ [60]. To find the shot noise, one needs to determine the self-energy matrix $\mathbf{W}^{II}$, in which two internal vertices were replaced by the current operator. The diagrammatic prescription of how to calculate the first and second-order shot noise can be found in Ref. [56].

We would like to note that the employed method relies on perturbative expansion of tunneling processes with respect to the coupling strength, which is assumed to be the smallest energy scale in the problem [55]. Thus the approximations made in these considerations allow us to study the transport properties in the weak coupling regime, but they are not sufficient to capture higher-order many-body correlations, such as the ones leading to the Kondo effect [61–63]. However, since in the weak coupling regime the Kondo temperature is usually exponentially small and the Kondo correlations are negligible [64], our calculations are reliable in the whole range of bias and gate voltages.

In the following, we present and discuss the numerical results on the current, differential conductance and shot noise in the parallel and antiparallel configurations of the device. The behavior of these quantities is studied in both the sequential and cotunneling regimes. In addition, we also calculate the tunnel magnetoresistance (TMR), which is associated with a change of magnetic configuration from parallel to antiparallel,

and can be defined as [65–68]

$$\mathrm{TMR} = \frac{I^P - I^{AP}}{I^{AP}},\tag{9}$$

where I^P and I^{AP} denote the currents flowing in the parallel and antiparallel configuration, respectively. Experimentally, the magnetic configuration of the device can be changed by sweeping through the hysteresis loop upon applying a small external magnetic field, provided the two ferromagnets have different coercive fields [69].

III. RESULTS IN THE CASE OF mirror GEOMETRY

In this section, we analyze the transport properties in the case when the current flows between the second and third lead, while the first lead is decoupled. In this geometry, the system exhibits the left-right reflection symmetry with respect to the current direction, see Fig. 1, and the current-voltage characteristics are symmetric with respect to the bias reversal. The absolute value of the current and the differential conductance in both the parallel and antiparallel configurations, together with the TMR in the case of mirror geometry are shown in Fig. 2. These quantities are plotted as a function of the bias voltage and the position of the dots' levels, which are kept the same, $\varepsilon_1 = \varepsilon_2 = \varepsilon_3 \equiv \varepsilon$. The position of the levels can be changed upon applying a gate voltage, therefore this figure effectively presents the bias and gate voltage dependence of transport characteristics.

The current and differential conductance dependencies on the bias and gate voltages reveal typical Coulomb stability diagram of the device. For voltages below a certain threshold, the sequential tunneling is exponentially suppressed due to the single-electron charging energy and the system is in the Coulomb blockade regime. The blockade can be lifted by either shifting the TQD levels to resonance or by applying a transport voltage larger than the corresponding threshold voltage. This results in a step in the current and the corresponding peak in the differential conductance, see Figs. 2(a)–2(d). By increasing the bias voltage, the next steps (peaks) occur whenever the next energy level of TQD enters the energy window provided by the bias voltage. For complex multilevel structures, as considered in the present paper, this results in a very reach Coulomb diamond pattern, which reflects various interactions and correlations in the system, see Fig. 2.

By comparing the currents in the case of parallel and antiparallel magnetic configuration, one observes that, generally, the system is more conductive in the parallel configuration compared to the antiparallel one. However, the general structure of the stability diagram is rather independent of magnetic configuration. The difference in current values in the two magnetic configurations results from the asymmetry in couplings to the leads, which occurs in the antiparallel alignment. In the parallel configuration, the majority (minority) electrons of one lead tunnel to the majority (minority) band of the second lead. On the other hand, in the antiparallel configuration, this situation is reversed and the majority (minority) electrons of a given lead tunnel to the minority (majority) subband of another lead. This implies that the current in the parallel configuration is generally larger than that in the antiparallel configuration. For the considered mirror geometry, in whole
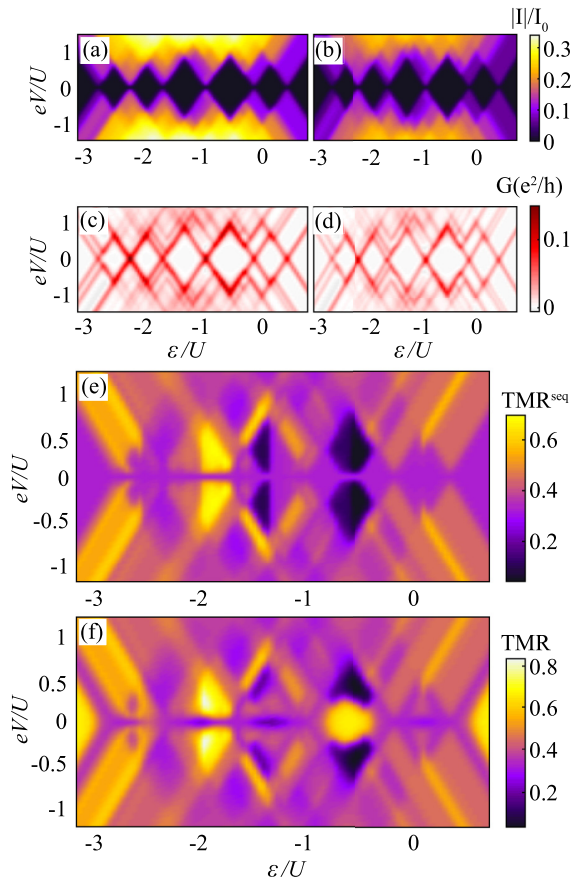
FIG. 2. (Color online) The absolute value of the current in (a) the parallel and (b) the antiparallel magnetic configuration, (c) and (d) the corresponding differential conductance, as well as (e) the sequential and (f) the total (sequential plus cotunneling) TMR calculated in the case of mirror geometry as a function of the bias voltage and the dots' levels position $\varepsilon \equiv \varepsilon_1 = \varepsilon_2 = \varepsilon_3$. The parameters are $U' = 0.4$, $t_{12} = t_{13} = -0.2$, $t_{23} = -0.1$, $\Gamma = 0.005$, $T = 0.025$, in units of $U \equiv 1$, and $p = 0.5$. The current is expressed in units of $I_0 = e\Gamma/\hbar$. To facilitate direct comparison, the same color scale is used in the following pairs of panels: (a) and (b), (c) and (d), and (e) and (f).

range of bias voltage, one always finds, $I^P > I^{AP}$, which gives rise to positive TMR, see Figs. 2(e) and 2(f).

Although in the Coulomb blockade regime the sequential tunneling processes are exponentially suppressed, the current can still flow due to cotunneling processes [58]. Such processes involve two, correlated in time, tunneling events occurring through virtual states of the system. In spite of the fact that the cotunneling current, which is $\propto \Gamma^2$, is considerably smaller than the sequential current, it gives the dominant contribution to transport in the Coulomb blockade regime. Its influence can be, however, hardly visible in the current and differential conductance dependencies shown in the full range of bias and gate voltages. Nevertheless, the effect of cotunneling is clearly evident in the TMR, which measures the relative change in the current when the magnetic configuration is varied. This is why in Fig. 2 we show both the TMR obtained using only sequential tunneling processes and the total TMR. One can immediately see that, as was to be expected, cotunneling modifies the TMR mainly in the Coulomb blockade regime,

cf. Figs. 2(e) and 2(f). Furthermore, while in the linear response regime the sequential TMR is given by [67] TMR = $\text{TMR}^{\text{Jull}}/2$, where $\text{TMR}^{\text{Jull}} = 2p^2/(1 - p^2)$ is the value of TMR obtained from the Julliere model [65], the total TMR exhibits a nontrivial dependence on both the number of electrons on the TQD and the spin of the ground state. More specifically, TMR = TMR^{Jull} ($\text{TMR}^{\text{Jull}} = 2/3$ for $p = 0.5$, as considered in this paper), in the transport regime where only elastic (spin-conserving) cotunneling processes are present. This happens when the ground state is spin singlet, which occurs for empty or fully occupied TQD as well as in the case when the TQD is occupied by two electrons, i.e., for $-1 \gtrsim \varepsilon/U \gtrsim -1/2$, see Fig. 2(f). For other occupancies, the TMR is much smaller, TMR $\lesssim \text{TMR}^{\text{Jull}}$, which is associated with inelastic cotunneling events that lead to spin relaxation in the system and, thus, decrease the TMR.

The detailed behavior of the current, differential conductance, and the TMR as a function of the bias voltage for two different values of level position ε is shown in Fig. 3. The left column of the figure corresponds to the cross-section of Fig. 2 taken at $\varepsilon/U = -0.7$. In this case, at equilibrium, the TQD is doubly occupied and the ground state is the spin singlet. In the Coulomb blockade regime, only the spin-conserving cotunneling processes are possible, therefore the TMR reaches the value predicted by the Julliere model [67], TMR = TMR^{Jull}. Note that this value is clearly different from what one obtains within the sequential tunneling approximation, see Fig. 3(e). By increasing the bias voltage above the threshold, sequential processes become possible leading to a step in the current and to a large maximum in the differential conductance, see Figs. 3(a) and 3(c). Interestingly, around the threshold voltage, the TMR becomes strongly suppressed to rise again with increasing the bias voltage further. The suppression of TMR around the threshold voltage can be understood by realizing that the sequential current starts flowing due to three-electron doublet states, which enter the bias window. The occupation of such states at the threshold voltage is comparable in both magnetic configurations and therefore the difference between the corresponding currents is relatively small. Consequently, the TMR becomes then much suppressed. Further increase of the bias voltage, however, results in spin accumulation in the antiparallel configuration, and the TMR becomes enhanced again, see Fig. 3(e).

On the other hand, in the transport regime where sequential processes are allowed, the TMR is generally below TMR^{Jull} and displays an oscillatory behavior as a function of bias voltage. This behavior is clearly related to single-electron charging effects and is associated with consecutive steps in the current and the corresponding peaks in the differential conductance, which occur whenever the next charge states become available for transport, see Figs. 3(a) and 3(c).

A similar behavior out of the Coulomb blockade regime can be observed in the case of $\varepsilon/U = -2$, which is presented in the right column of Fig. 3. Again, the TMR exhibits an oscillatory behavior as a function of the bias voltage with a period related to the energy difference between consecutive charge states being active in transport. However, interesting behavior occurs now for voltages around the threshold voltage, where the TMR becomes enhanced above the Julliere value, see Fig. 3(f). For $\varepsilon/U = -2$, at equilibrium, the TQD is occupied
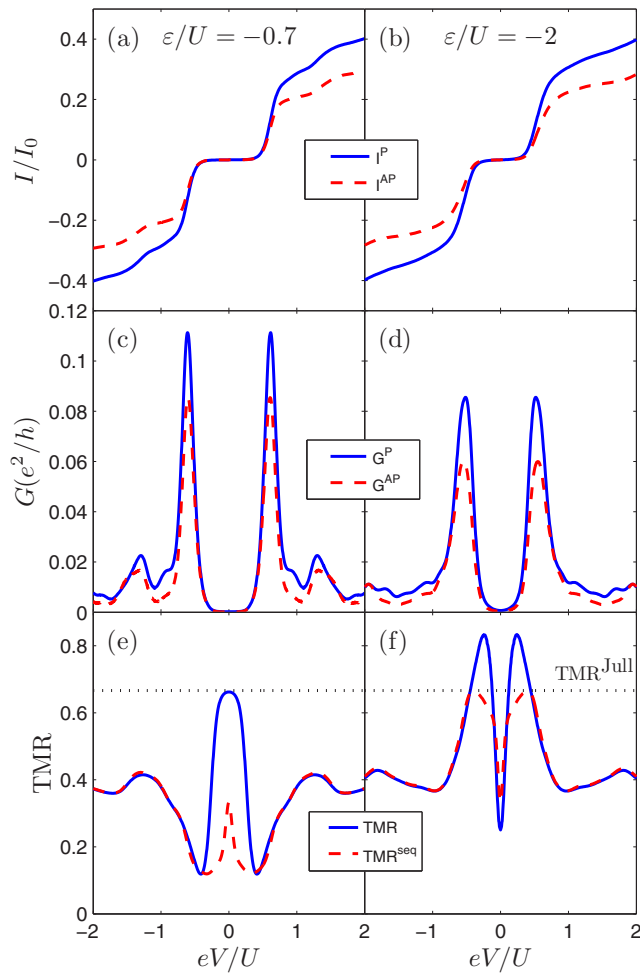
FIG. 3. (Color online) The bias dependence of [(a) and (b)] the current and [(c) and (d)] the differential conductance in both magnetic configurations, and [(e) and (f)] the TMR in the case of mirror geometry for two values of TQD level position: $\varepsilon/U = -0.7$ (left) and $\varepsilon/U = -2$ (right). The dashed line in (e) and (f) shows the TMR obtained including only sequential processes. The horizontal dotted line in (e) and (f) presents the TMR obtained from the Julliere model. The other parameters are the same as in Fig. 2.

FIG. 4. (Color online) The bias and gate voltage dependence of the Fano factor F in the parallel [(a) and (c)] and antiparallel [(b) and (d)] magnetic configuration calculated in the case of mirror geometry. The first row shows the Fano factor calculated using only sequential tunneling processes, F^{seq}, while the second row presents the total Fano factor calculated taking into account both sequential and cotunneling processes. The Fano factor is divergent in the low-bias-voltage range, $V \rightarrow 0$, therefore this regime is covered by a thick horizontal line. The parameters are the same as in Fig. 2.

by four electrons and the ground state is a spin triplet. With increasing the bias voltage, in the antiparallel configuration, the occupation of either the lowest-weight or the highest-weight triplet component is greatly enhanced, depending on the sign of the bias voltage. This gives rise to strong nonequilibrium spin accumulation, which increases the difference between the parallel and antiparallel configuration, since the spin accumulation in the parallel configuration is absent in the case of left-right symmetric systems as considered here. When the bias voltage reaches the threshold voltage, other excited states become populated and spin accumulation is decreased. Consequently, one observes a maximum in TMR for voltages around the threshold voltage, with TMR > TMR^{Jull}, see Fig. 3(f).

In addition, we have also calculated the shot noise S and the corresponding Fano factor $F = S/(2|eI|)$. Figure 4 shows the density plots of F as a function of bias and gate voltages calculated in the case of mirror geometry for parameters the same as in Fig. 2. The second row presents the total Fano
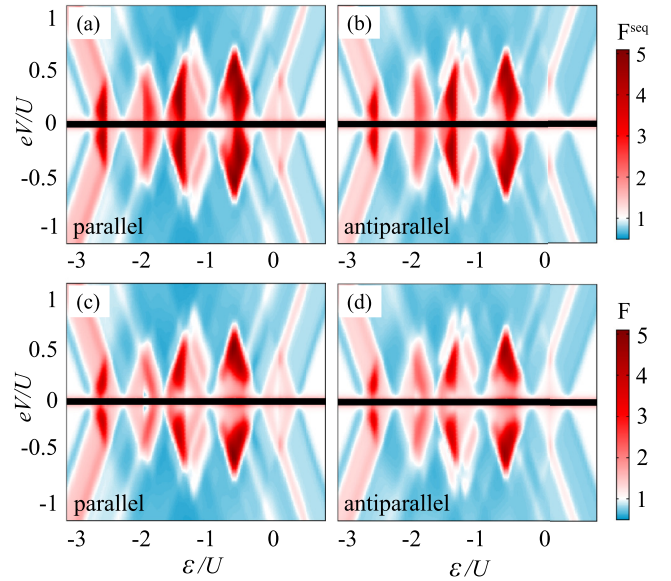
factor F, i.e., when both sequential and cotunneling processes are taken into account. To elucidate the role of cotunneling, it can be directly compared to the first row, which presents the Fano factor, F^{seq}, calculated using only sequential processes. It can be seen that the cotunneling processes modify the Fano factor mainly in the Coulomb blockade regime, however, their influence is not that spectacular as in the case of the TMR. The color scale used in Fig. 4 is adjusted in such a way that white color corresponds to $F = 1$, blue to $F < 1$, and red color corresponds to $F > 1$. When transport is due to uncorrelated tunneling events, the shot noise takes the Poissonian value, $S = 2|eI|$, and the Fano factor equals unity. On the other hand, when $F < 1$, the shot noise is sub-Poissonian, while for $F > 1$, the noise becomes super-Poissonian. Moreover, for low bias voltages, the Fano factor is divergent because of thermal noise, which gives a finite contribution to the noise, while $I \rightarrow 0$ for $V \rightarrow 0$. This transport regime is covered by a thick horizontal line in Fig. 4.

Before analyzing more detailed behavior of F, let us make some general observations. First of all, one can see that the shot noise is sub-Poissonian out of the Coulomb blockade regime. This is due to the fact that sequential tunneling events are correlated in time by the charging energy (electrons tunnel one by one through the system), which decreases the current fluctuations, yielding $F < 1$. On the other hand, in the Coulomb blockade regime the shot noise becomes super-Poissonian, which can be attributed to bunching of inelastic cotunneling processes that leads to enhanced current fluctuations. Moreover, in the case when only elastic cotunneling is present, the noise becomes Poissonian

and $F = 1$, since such processes are uncorrelated. This can be clearly seen in the case when the TQD is empty ($\varepsilon/U \gtrsim 0.5$) or fully occupied ($\varepsilon/U \lesssim -3$), see Fig. 4.

An interesting behavior can be observed in the Coulomb blockade regime with two electrons in the TQD, see Fig. 4 for $\varepsilon/U \approx -0.7$. Then, at low bias voltage, the Fano factor is slightly above 1, indicating super-Poissonian shot noise, which then becomes greatly enhanced for voltages just before the threshold for sequential tunneling. This can be understood by realizing that at low voltages the TQD is mainly occupied by the spin singlet state and transport is dominated by elastic cotunneling processes. However, while increasing the bias voltage, inelastic cotunneling events come into play, which, firstly, give rise to spin relaxation suppressing the TMR, cf. Figs. 2(f) and 3(e), and, secondly, enhance the current fluctuations by bunching of cotunneling processes. As a matter of fact, a similar enhancement of the shot noise can be observed in other Coulomb blockade regimes, indicating the role of inelastic cotunneling in transport.

Moreover, super-Poissonian shot noise can also be observed beyond the Coulomb blockade regime, see the transport region for $\varepsilon/U \approx -3$ and $|eV|/U > 1/2$ in Fig. 4. In this regime, five-electron (doublet) and six-electron (singlet) states are active in transport. As checked numerically (not shown), when the leads are nonmagnetic, the Fano factor is close to unity and sub-Poissonian. For finite spin polarization, on the other hand, F is increased and becomes larger than unity. This super-Poissonian shot noise is thus related to the spin dependence of tunneling processes. This can be understood by realizing that for ferromagnetic leads, fluctuations between tunneling through singlet and doublet states are enhanced, which generally leads to larger current fluctuations and, consequently, to enhanced Fano factor.

Finally, we note that the bias and gate voltage dependence of the Fano factor in the two magnetic configurations is qualitatively similar, and the main difference is associated with the magnitude of F, cf. the left and right column of Fig. 4. In the parallel configuration, the shot noise is generally larger than in the antiparallel configuration due to an additional factor related with the difference between the currents flowing in a given spin channel. More specifically, the majority-spin channel is more conductive than the minority-spin channel, which generally increases the fluctuations of the current.

IV. RESULTS IN THE CASE OF fork GEOMETRY

The bias and gate voltage dependence of the current, differential conductance in both parallel and antiparallel configurations, and the TMR in the case of fork geometry is shown in Fig. 5. This geometry is realized by setting $\Gamma_1 = \Gamma_2 = \Gamma_3$ and applying the bias voltage as follows: $(\mu_2 = \mu_3) - \mu_1 = eV$, with $-\mu_1 = \mu_2 = \mu_3 = eV/2$, see Fig. 1.

In general, one observes similar transport characteristics as in the case of the mirror geometry, i.e., Coulomb staircases for current characteristics and diamonds for differential conductance as a function of bias and gate voltages. However, a closer analysis reveals important differences. First of all, now the system no longer responds identically to a sign change of the bias voltage. Moreover, one can see that the diamonds are now somewhat distorted, which is especially visible for
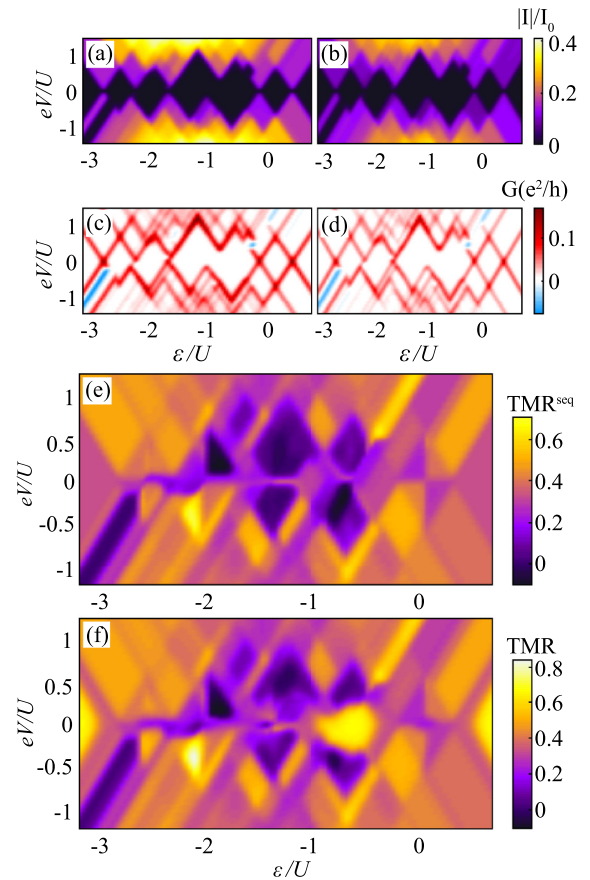

FIG. 5. (Color online) The absolute value of the current in (a) the parallel and (b) antiparallel magnetic configuration, [(c) and (d)] the corresponding differential conductance, and (e) the sequential and (f) the total TMR in the case of fork geometry as a function of the bias voltage and the dots' levels position $\varepsilon \equiv \varepsilon_1 = \varepsilon_2 = \varepsilon_3$. The other parameters are as in Fig. 2.

two large Coulomb blockade regions with two and three electrons, see Figs. 5(c) and 5(d) for $-3/2 \gtrsim \varepsilon/U \gtrsim -1/2$. More specifically, the resonant peak in the linear conductance as a function of ε associated with the degeneracy between two and three-electron states is hardly visible. Instead, one observes a gap in the diamonds around $\varepsilon/U \approx -1$, which opens for positive bias voltage. Note that since the eigen-spectrum of TQD does not depend on how the leads are attached, the difference between conductances directly reveals the difference between the mirror and fork geometry. In the case of fork geometry, some of the transitions between the TQD eigenstates are suppressed, which is visible as quenching of certain Coulomb blockade lines, cf. Figs. 2 and 5.

Another interesting feature that occurs in the case of fork geometry is associated with the nonmonotonic dependence of the current on the bias voltage. In the bias and gate voltage dependence of the current, there are three regions where the current is suppressed, despite the increase of the bias voltage, see Figs. 5(a) and 5(b). The first two regions occur around $\varepsilon \approx 0$ for positive bias voltage, while the second larger region develops around $\varepsilon/U \approx -3$ for negative bias. These regions are accompanied with pronounced negative differential conductance (NDC), see Figs. 5(c) and 5(d). Moreover, as

48

can be seen in the figure, this effect does not depend on the magnetic configuration of the system and NDC is present in both parallel and antiparallel alignment. Since the NDC that occurs around $\varepsilon/U \approx -3$ is the most pronounced one, let us now focus on this transport regime and explain the mechanism responsible for the current suppression. Within the mentioned current blockade, the system is predominantly occupied by five electrons. More specifically, the first dot is fully occupied with two electrons (cf. Fig. 1), while the three remaining electrons have wave functions distributed between the second and third dot. In fact, such a state is energetically favorable in a relatively wide range of applied bias voltage within the blockade. Consequently, since the first dot is fully occupied, no more electrons can tunnel from the first lead to this dot and the current becomes suppressed. However, when the voltage is reversed, the electrons from the first dot can escape to the first lead, while electrons from the second and third leads can tunnel to the corresponding dots and then further through the first dot to the first lead. One therefore observes a strong suppression of the current only for one bias polarization, i.e., $eV < 0$. Since this five-electron state is favorable in both magnetic configurations, negative differential conductance develops irrespective of the leads' magnetizations' alignment, see Figs. 5(c) and 5(d).

Furthermore, one can also see another region of negative differential conductance, which occurs for a positive bias voltage around $\varepsilon \approx 0$, see Fig. 5. When the voltage is low, the TQD is occupied by a single electron. Then, by increasing the bias voltage above the threshold, the current starts flowing due to one-electron and two-electron states. However, further increase of the bias voltage decreases the occupation of one-electron states and the system is mainly occupied by two electrons. This two-electron state is a spin triplet, in which the spacial distribution of the wave function is mainly distributed between the second and third dots, cf. Fig. 1. When the system is in this state, it is difficult to make a transition to a one-electron state, as the tunneling rate from the first dot to the first lead is strongly suppressed due to the small electron density on this dot. Moreover, electron tunneling through the second and third lead is also unlikely, as the corresponding dots are already occupied by one electron and the on-site Coulomb interaction U forbids the occupation of three-electron states for the considered bias voltage. All this results in the current suppression and associated negative differential conductance. Further increase of the bias voltage eventually enables three-electron states to participate in transport, which is visible both as a new peak in the conductance plot and a consecutive step in the current-voltage dependence. We would like to note that the unequal spacial distribution of the many-body eigenstates of the system is associated with the fact that the system is not fully symmetric. This is because the hopping between the second and third dot is assumed to be smaller than the hopping between the first dot and the two other dots, $t_{12} = t_{13} \neq t_{23}$.

The bias and gate voltage dependence of the TMR in the case of fork geometry is also much different compared to the case shown in Fig. 2. It does not show symmetry when the bias voltage is applied inversely, likewise the current and the differential conductance. Moreover, we now find transport regions where the current in the parallel configuration becomes smaller than that in the antiparallel configuration, which leads

to a negative TMR, see Fig. 5(f). To understand this behavior, we first note that at equilibrium and for $\varepsilon/U \approx -1.9$, i.e., when negative TMR develops, the ground state of TQD is the four-electron spin triplet. This state is almost degenerate with the four-electron singlet state, which becomes predominantly occupied when the bias voltage increases. In fact, in the transport regime where negative TMR occurs, the singlet state is occupied with the largest probability, while the occupation of the triplet state is relatively small. Moreover, in the antiparallel configuration, the occupation of the triplet state is slightly larger than in the parallel configuration and, due to nonequilibrium spin accumulation, the spin-down component of the triplet is favored. This is generally the reason for the increased current in the antiparallel configuration; the increased occupation of one of the triplet components allows for enhanced tunneling through the system compared to the parallel configuration, in which the overall rate of tunneling is
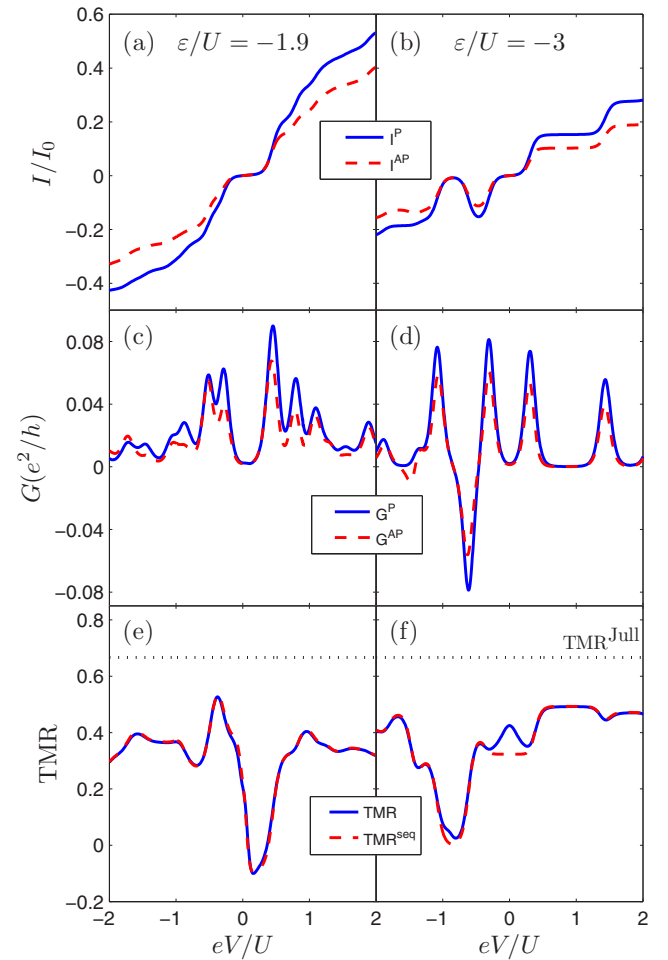

FIG. 6. (Color online) The bias dependence of [(a) and (b)] the current and [(c) and (d)] differential conductance in both magnetic configurations, and [(e) and (f)] the TMR in the case of fork geometry for two values of the TQD level position: $\varepsilon/U = -1.9$ (left) and $\varepsilon/U = -3$ (right). The dashed line in (e) and (f) shows the sequential TMR. The horizontal dotted line in (e) and (f) presents the TMR obtained from the Julliere model. The other parameters are the same as in Fig. 2.

49

smaller due to the small occupation of all components of the triplet state.

By comparing the total TMR with the TMR obtained using only sequential tunneling processes, one can see that cotunneling plays an important role mainly in the Coulomb blockade regime, cf. Figs. 5(e) and 5(f). Similar to the case of mirror configuration, when only elastic cotunneling is present, the TMR reaches the Julliere value, otherwise it is generally suppressed due to inelastic cotunneling.

The effects of negative differential conductance and negative TMR can be explicitly seen in the relevant cross-sections of Fig. 5, which are shown in Fig. 6 for $\varepsilon/U = -1.9$ and $\varepsilon/U = -3$. The differences between the two magnetic configurations can now be directly observed. Moreover, the effects of cotunneling processes can also be inferred. Since the Coulomb blockade regime is relatively narrow, transport is mainly determined by the first-order processes, while higher-order processes play here a minor role. However, their influence is much stronger in other transport regimes, especially when the Coulomb blockade effects are more pronounced, see Fig. 5.

Finally, the bias voltage and level position dependence of the Fano factor F calculated in the case of fork configuration is presented in Fig. 7. The left (right) column corresponds to the parallel (antiparallel) configuration, while the second (first) row shows the results obtained by using both sequential and cotunneling (only sequential) processes. Similar to the case of mirror geometry, we generally find super-Poissonian shot noise ($F > 1$) in Coulomb blockade regimes, where both elastic and inelastic cotunneling processes are possible, and Poissonian shot noise ($F = 1$) when the current is due to elastic cotunneling. Moreover, in the sequential tunneling
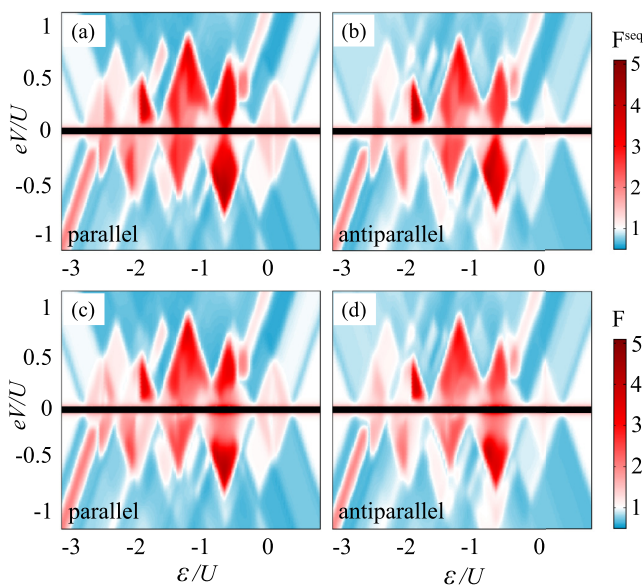
regime, i.e., outside the Coulomb blockade, we again observe sub-Poissonian values ($F < 1$). In addition, one can also see the shot noise enhancement within the current blockade regime where NDC occurs, which occurs for $eV/U < 0$ and $-3.5 \lesssim \varepsilon/U \lesssim -2.5$ and is absent for opposite bias voltage. Super-Poissonian shot noise is also present for positive bias voltage around $-0.5 \lesssim \varepsilon/U \lesssim 0$. The mechanism leading to the super-Poissonian shot noise in both cases is the same. Most time the system is trapped in specific states, which are responsible for the current suppression. As a result, there occurs bunching of tunneling processes through the system. It can be understood by realizing that eventual exit from a blocked state is most likely followed by multiple tunneling events, right before the system returns to the state, where again further tunneling acts have extremely low occurrence. Consequently, the shot noise becomes enhanced leading to $F > 1$.

V. CONCLUDING REMARKS

In this paper, we studied the transport properties of a triangular quantum dot molecule weakly coupled to external ferromagnetic leads. The calculations were performed with the aid of the real-time diagrammatic technique including the sequential and cotunneling processes. We considered two specific configurations of the device: the mirror one, in which the system possesses reflection symmetry with respect to the current flow direction, and the fork one, in which this symmetry is broken. For these two configurations, we determined the dependence of the current, differential conductance, shot noise and TMR on the bias and gate voltages. When the system was in mirror geometry, we found enhanced TMR and super-Poissonian shot noise in certain Coulomb blockade regimes. In the case of fork geometry, on the other hand, we predicted negative TMR and negative differential conductance associated with current suppression due to Coulomb correlations.

Finally, we would like to note that the effects of both enhanced and negative TMR, as well as negative differential conductance are under the strong influence of capacitive correlations between the quantum dots. Such correlations lead to a particular spacial distribution of the wave functions of TQD. By varying the value of the Coulomb correlations between the dots, it is possible to manipulate the shape, range, and magnitude of the aforementioned effects. However, the influence is mainly quantitative and in most cases the above effects are present also when capacitive coupling is negligible.

We also want to notice that in these considerations we focused on spin-dependent transport through TQDs in the case when the system possessed relatively high symmetry. Nevertheless, symmetry breaking, by, e.g., finite detuning of TQD levels, may lead to further interesting effects, such as the spin blockade or coherent population trapping in dark states [42–45]. Detailed analysis of such effects goes, however, beyond the scope of the present paper and will be studied elsewhere [70].

FIG. 7. (Color online) The Fano factor F in the parallel [(a) and (c)] and antiparallel [(b) and (d)] magnetic configuration calculated in the case of fork geometry as a function of bias voltage and TQD's level position. The first row shows the Fano factor calculated using only sequential tunneling processes, F^{seq}, while the second row presents the total Fano factor. The low-voltage regime, where F is divergent, is covered by a thick horizontal line. The parameters are the same as in Fig. 2.

50

APPENDIX: DETAILS OF CALCULATIONS

In this appendix, we present some details of calculations using the real-time diagrammatic technique. The core of calculation is essentially the determination of all irreducible diagrams of a given order. One starts with writing down topologically different irreducible diagrams, in which tunneling lines connect vertices resulting from the expansion of the tunneling Hamiltonian, and estimating their contributions, which can be done with the aid of diagrammatic rules [55,67]. The diagrams of a given order having at their ends the same states are then summed up to find the corresponding self-energy. Having determined all self-energies, one can then solve the appropriate kinetic equations (cf. Sec. II B) for density matrix elements [55,56,67]. The next step is to find the diagrams that contribute to the current and to the shot noise, and determine the self-energy matrices $\mathbf{W}^{\mathrm{I}}$ and $\mathbf{W}^{\mathrm{II}}$ [55,56,67]. These diagrams are given by diagrams contributing to $\mathbf{W}$ with proper prefactors and lead indices, which take into account the direction of current flow and the number of electrons transferred through the system. Below, we show two examples of diagrams of first and second orders and explicitly present the formulas for the first-order self-energies.

1. Examples of first- and second-order diagrams

An exemplary first-order diagram that contributes to the self-energy $W^{(1)}_{\chi(n+1)\chi'(n)}$ between the states $|\chi(n+1)\rangle$ and $|\chi'(n)\rangle$, gives the following contribution:
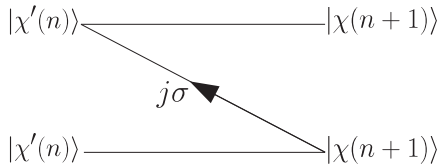
$$= (-i)(-1)^1 \int d\omega \frac{\gamma^+_{j\sigma}(\omega)}{\omega - \varepsilon_\chi + \varepsilon_{\chi'} + i0^+} \left| \langle \chi | d^\dagger_{j\sigma} | \chi' \rangle \right|^2 , \quad \text{(A1)}$$
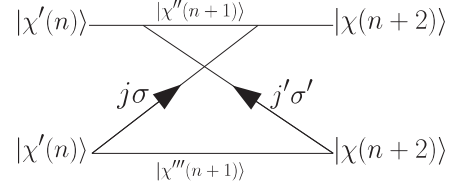
for given spin σ and lead j. Note that to indicate how the number of electrons changes, we have explicitly written the total occupation number next to the states, $n = \sum_{j\sigma} n_{j\sigma}$. In the above formula, the factor $(-1)^1$ is due to the fact that there is one vertex on the backward propagator. The tunneling line carries energy ω and ε_χ ($\varepsilon_{\chi'}$) is the energy of state on the forward (backward) propagator. In addition, each tunneling line carries a factor

$$\gamma^\pm_{j\sigma}(\omega) = \frac{\Gamma^\sigma_j}{2\pi} f^\pm_j(\omega) ,$$

where $f^+_j(\omega)$ denotes the Fermi-Dirac distribution function of lead j and $f^-_j(\omega) = 1 - f^+_j(\omega)$. In Eq. (A1), the direction of tunneling line is backward with respect to the Keldysh

contour, therefore it carries $\gamma^+_{j\sigma}(\omega)$. For tunneling lines going in opposite direction, one would have a factor $\gamma^-_{j\sigma}(\omega)$ [55].

An example of second-order diagram, relevant for the self-energy $W^{(2)}_{\chi(n+2)\chi'(n)}$, is shown below together with its contribution:

$$= (-i)(-1)^3 \sum_{\chi''\chi'''} \iint d\omega_1 d\omega_2 \; \frac{\gamma^+_{j\sigma}(\omega_1)}{-\omega_1 - \varepsilon_{\chi'} + \varepsilon_{\chi''} + i0^+}$$

$$\times \frac{\gamma^+_{j'\sigma'}(\omega_2)}{-\omega_1 + \omega_2 - \varepsilon_{\chi''} + \varepsilon_{\chi'''} + i0^+} \frac{1}{\omega_2 - \varepsilon_\chi + \varepsilon_{\chi'''} + i0^+}$$

$$\times \langle \chi' | d_{j\sigma} | \chi''' \rangle \langle \chi''' | d_{j'\sigma'} | \chi \rangle \langle \chi | d^\dagger_{j\sigma} | \chi'' \rangle \langle \chi'' | d^\dagger_{j'\sigma'} | \chi' \rangle , \quad \text{(A2)}$$

where the prefactor $(-1)^3$ comes from the fact that there are two vertices on the backward propagator and one crossing of tunneling lines, each carrying a minus sign. Note that now one needs to sum over virtual states of the system $|\chi''\rangle$ and $|\chi'''\rangle$ and that there are three resolvents in the double integral. Compared to Eq. (A1), this formula is clearly more complex.

The integrals in the above equations for first- and second-order diagrams can be solved by using the Cauchy's formula. Moreover, in the considered problem, each diagram, say, A has its counterpart B, such that $B = -A^*$. Consequently, since $A + B = 2i\mathrm{Im}\{A\}$, one only needs to calculate the imaginary parts of diagrams. For first-order diagrams, this immediately leads to Fermi functions. On the other hand, for the second-order diagrams, one ends up with single integrals, which can be solved analytically by introducing digamma functions and their derivatives [57,67]. Finally, we note that the formulas obtained using diagrammatic rules [55,67] need to be multiplied by a factor of $(-i)$ to adapt to the matrix notation introduced by A. Thielmann *et al.* [56], which is used in this paper. This factor has already been explicitly included in Eqs. (A1) and (A2).

2. Self-energies

After finding contributions coming from all irreducible diagrams, one can determine the self-energies in a given order of expansion. Here, we explicitly present the first-order self-energies and merely notice that the formulas for second-order self-energies are too lengthly to be presented here [57,67].

The matrix elements of $\mathbf{W}^{(1)}$ are given by

$$W^{(1)}_{\chi(n)\chi'(n-1)} = 2\pi \sum_{j\sigma} \gamma^+_{j\sigma}(\varepsilon_\chi - \varepsilon_{\chi'}) |\langle \chi | d^\dagger_{j\sigma} | \chi' \rangle|^2 ,$$

$$W^{(1)}_{\chi(n)\chi'(n+1)} = 2\pi \sum_{j\sigma} \gamma^-_{j\sigma}(\varepsilon_{\chi'} - \varepsilon_\chi) |\langle \chi | d_{j\sigma} | \chi' \rangle|^2 ,$$

while the diagonal elements are given by $W^{(1)}_{\chi\chi} = -\sum_{\chi' \neq \chi} W^{(1)}_{\chi'\chi}$.

Defining the current operator as $I = (I_R - I_L)/2$, where I_j is the current operator through junction j, the first-order self-energies contributing to the current are given by

$$W^{(1)\mathrm{I}}_{\chi(n)\chi'(n-1)} = \sum_\sigma \left[f_L^+(\varepsilon_\chi - \varepsilon_{\chi'}) \sum_{j=L} \Gamma_j^\sigma \left| \langle \chi | d_{j\sigma}^\dagger | \chi' \rangle \right|^2 - f_R^+(\varepsilon_\chi - \varepsilon_{\chi'}) \sum_{j=R} \Gamma_j^\sigma \left| \langle \chi | d_{j\sigma}^\dagger | \chi' \rangle \right|^2 \right],$$

$$W^{(1)\mathrm{I}}_{\chi(n)\chi'(n+1)} = \sum_\sigma \left[f_R^-(\varepsilon_{\chi'} - \varepsilon_\chi) \sum_{j=R} \Gamma_j^\sigma \left| \langle \chi | d_{j\sigma} | \chi' \rangle \right|^2 - f_L^-(\varepsilon_{\chi'} - \varepsilon_\chi) \sum_{j=L} \Gamma_j^\sigma \left| \langle \chi | d_{j\sigma} | \chi' \rangle \right|^2 \right],$$

with $W^{(1)\mathrm{I}}_{\chi\chi} = 0$. The summation in the above formulas accounts for the fact that more than one lead (out of three), corresponding to either the left or right side of the device, is kept at the same chemical potential. Such situation happens in the fork geometry.

On the other hand, the elements of the first-order self-energy matrix $\mathbf{W}^{(1)\mathrm{II}}$, relevant for the calculation of the shot noise, are given by $W^{(1)\mathrm{II}}_{\chi\chi} = -W^{(1)}_{\chi\chi}/4$ for diagonal elements of $\mathbf{W}^{(1)\mathrm{II}}$ and $W^{(1)\mathrm{II}}_{\chi\chi'} = W^{(1)}_{\chi\chi'}/4$ for $\chi \neq \chi'$.

[1] D. Loss and D. P. DiVincenzo, Phys. Rev. A **57**, 120 (1998).

[2] S. A. Wolf, D. D. Awschalom, R. A. Buhrman, J. M. Daughton, S. von Molnar, M. L. Roukes, A. Y. Chtchelkanova, and D. M. Treger, Science **294**, 1488 (2001).

[3] G. Burkard, Hans-Andreas Engel and D. Loss, *Spintronics, Quantum Computing, and Quantum Communication in Quantum Dots* (Springer-Verlag, Berlin Heidelberg, 2002).

[4] *Semiconductor Spintronics and Quantum Computation*, edited by D. D. Awschalom, D. Loss, and N. Samarth (Springer, Berlin, 2002).

[5] S. Maekawa and T. Shinjo, *Spin Dependent Transport in Magnetic Nanostructures* (Taylor and Francis, New York, 2002).

[6] I. Zutic, J. Fabian, S. Das Sarma, Rev. Mod. Phys. **76**, 323 (2004).

[7] L. P. Kouwenhoven, C. M. Marcus, P. L. McEuen, S. Tarucha, R. M. Westervelt, and N. S. Wingreen: Proceedings of the ASI on *Mesoscopic Electron Transport*, edited by L. L. Sohn, L. P. Kouwenhoven, and G. Schön (Kluwer, 1997)

[8] L. P. Kouwenhoven, D. G. Austing, and S. Tarucha, Rep. Prog. Phys. **64**, 701 (2001).

[9] R. Hanson, L. P. Kouwenhoven, J. R. Petta, S. Tarucha, and L. M. K. Vandersypen, Rev. Mod. Phys. **79**, 1217 (2007).

[10] S. Andergassen, V. Meden, H. Schoeller, J. Splettstoesser, and M. R. Wegewijs, Nanotechnology **21**, 272001 (2010).

[11] K. Ono, D. G. Austing, Y. Tokura, and S. Tarucha, Science **297**, 1313 (2002).

[12] W. G. van der Wiel, S. De Franceschi, J. M. Elzerman, T. Fujisawa, S. Tarucha, and L. P. Kouwenhoven, Rev. Mod. Phys. **75**, 1 (2002).

[13] B. Weber, Y. H. M. Tan, S. Mahapatra, T. F. Watson, H. Ryu, R. Rahman, L. C. L. Hollenberg, G. Klimeck, and M. Y. Simmons, Nat. Nanotechnol. **9**, 430 (2014).

[14] P. Trocha and J. Barnaś, Phys. Rev. B **89**, 245418 (2014); P. Trocha and I. Weymann, *ibid.* **91**, 235424 (2015).

[15] K. P. Wójcik and I. Weymann, Phys. Rev. B **90**, 115308 (2014); **91**, 134422 (2015).

[16] A. J. Keller, S. Amasha, I. Weymann, C. P. Moca, I. G. Rau, J. A. Katine, H. Shtrikman, G. Zaránd, and D. Goldhaber-Gordon, Nat. Phys. **10**, 145 (2014).

[17] A. Vidan, R. M. Westervelt, M. Stopa, M. Hanson, and A. C. Gossard, Appl. Phys. Lett. **85**, 3602 (2004).

[18] L. Gaudreau, S. A. Studenikin, A. S. Sachrajda, P. Zawadzki, A. Kam, J. Lapointe, M. Korkusinski, and P. Hawrylak, Phys. Rev. Lett. **97**, 036807 (2006).

[19] M. L. Ladron de Guevara and P. A. Orellana, Phys. Rev. B **73**, 205303 (2006).

[20] T. Kuzmenko, K. Kikoin, and Y. Avishai, Phys. Rev. B **73**, 235310 (2006).

[21] M. C. Rogge and R. J. Haug, Phys. Rev. B **77**, 193306 (2008).

[22] K. Grove-Rasmussen, H. I. Jørgensen, T. Hayashi, P. E. Lindelof, and T. Fujisawa, Nano Lett. **8**, 1055 (2008).

[23] L. Gaudreau, G. Granger, A. Kam, G. C. Aers, S. A. Studenikin, P. Zawadzki, M. Pioro-Ladriére, Z. R. Wasilewski, and A. S. Sachrajda, Nat. Phys. **8**, 54 (2012).

[24] J. M. Taylor, V. Srinivasa, and J. Medford, Phys. Rev. Lett. **111**, 050502 (2013).

[25] M. Seo, H. K. Choi, S.-Y. Lee, N. Kim, Y. Chung, H.-S. Sim, V. Umansky, and D. Mahalu, Phys. Rev. Lett. **110**, 046803 (2013).

[26] F. R. Braakman, P. Barthelemy, C. Reichl, W. Wegscheider, and L. M. K. Vandersypen, Nat. Nanotechnol. **8**, 432 (2013).

[27] J. Mora, E. Cota, and F. Rojas, Phys. Rev. A **90**, 042323 (2014).

[28] M. Urbaniak, S. B. Tooski, A. Ramsak, and B. R. Bułka, Eur. Phys. J. B **86**, 505 (2013).

[29] J. Łuczak, B. R. Bułka, Phys. Rev. B **90**, 165427 (2014).

[30] C.-Y. Hsieh, A. Rene, and P. Hawrylak, Phys. Rev. B **86**, 115312 (2012).

[31] D. S. Saraga and D. Loss, Phys. Rev. Lett. **90**, 166803 (2003).

[32] S. B. Tooski, B. R. Bułka, R. Žitko, A. Ramsak, Eur. Phys. J. B **87**, 145 (2014).

[33] R. Žitko, J. Bonča, A. Ramšak, and T. Rejec, Phys. Rev. B **73**, 153307 (2006).

[34] A. Oguri, S. Amaha, Y. Nishikawa, T. Numata, M. Shimamoto, and A. C. Hewson, and S. Tarucha Phys. Rev. B **83**, 205304 (2011).

[35] Zhao-tan Jiang, Qing-feng Sun, and Yupeng Wang, Phys. Rev. B **72**, 045332 (2005).

[36] E. Vernek, C. A. Büsser, G. B. Martins, E. V. Anda, N. Sandler, and S. E. Ulloa, Phys. Rev. B **80**, 035119 (2009).

[37] R. Žitko and J. Bonča, Phys. Rev. B **77**, 245112 (2008).

[38] T. Kuzmenko, K. Kikoin, and Y. Avishai, Phys. Rev. Lett. **96**, 046601 (2006).

[39] G. Yoo, J. Park, S.-S. B. Lee, and H.-S. Sim, Phys. Rev. Lett. **113**, 236601 (2014).

52

[40] L. Gaudreau, A. S. Sachrajda, S. Studenikin, A. Kam, F. Delgado, Y. P. Shim, M. Korkusinski, and P. Hawrylak, Phys. Rev. B **80**, 075415 (2009).

[41] G. Granger, L. Gaudreau, A. Kam, M. Pioro-Ladrière, S. A. Studenikin, Z. R. Wasilewski, P. Zawadzki, and A. S. Sachrajda, Phys. Rev. B **82**, 075304 (2010).

[42] C. Emary, Phys. Rev. B **76**, 245319 (2007).

[43] T. Kostyrko and B. R. Bułka, Phys. Rev. B **79**, 075310 (2009).

[44] I. Weymann, B. R. Bułka, and J. Barnaś, Phys. Rev. B **83**, 195302 (2011).

[45] C. Pöltl, C. Emary, and T. Brandes, Phys. Rev. B **80**, 115313 (2009).

[46] R. Sánchez, F. Gallego-Marcos, and G. Platero, Phys. Rev. B **89**, 161402 (2014).

[47] M. Busl, G. Granger, L. Gaudreau, R. Sánchez, A. Kam, M. Pioro-Ladrière, S. A. Studenikin, P. Zawadzki, Z. R. Wasilewski, A. S. Sachrajda, and G. Platero, Nat. Nanotechnol. **8**, 261 (2013).

[48] S. Amaha, W. Izumida, T. Hatano, S. Teraoka, S. Tarucha, J. A. Gupta, and D. G. Austing, Phys. Rev. Lett. **110**, 016803 (2013).

[49] M. Busl, R. Sánchez, and G. Platero, Phys. Rev. B **81**, 121306 (2010).

[50] I. Weymann, J. Phys.: Condens. Matter **22**, 015301 (2010).

[51] D. M. T. Kuo and Y.-c. Chang, Phys. Rev. B **89**, 115416 (2014).

[52] R. Sánchez, G. Granger, L. Gaudreau, A. Kam, M. Pioro-Ladriére, S. A. Studenikin, P. Zawadzki, A. S. Sachrajda, and G. Platero, Phys. Rev. Lett. **112**, 176803 (2014).

[53] L. D. Contreras-Pulido, M. Bruderer, S. F. Huelga, and M. B. Plenio, New J. Phys. **16**, 113061 (2014).

[54] J. Villavicencio, I. Maldonado, E. Cota, and G. Platero, Phys. Rev. B **88**, 245305 (2013).

[55] H. Schoeller and G. Schön, Phys. Rev. B **50**, 18436 (1994); J. König, J. Schmid, H. Schoeller, and G. Schön, *ibid.* **54**, 16820 (1996).

[56] A. Thielmann, M. H. Hettler, J. König, and G. Schön, Phys. Rev. Lett. **95**, 146806 (2005).

[57] I. Weymann, Phys. Rev. B **78**, 045310 (2008).

[58] D. V. Averin and Yu. V. Nazarov, Phys. Rev. Lett. **65**, 2446 (1990); K. Kang and B. I. Min, Phys. Rev. B **55**, 15412 (1997).

[59] U. Fano, Phys. Rev. **124**, 1866 (1961).

[60] Ya. M. Blanter and M. Büttiker, Phys. Rep. **336**, 1 (2000).

[61] J. Kondo, Prog. Teor. Phys. **32**, 37 (1964).

[62] D. Goldhaber-Gordon, H. Shtrikman, D. Mahalu, D. Abusch-Magder, U. Meirav, and M. A. Kastner, Nature (London) **391**, 156 (1998).

[63] S. Cronenwett, T. H. Oosterkamp, and L. P. Kouwenhoven, Science **281**, 540 (1998).

[64] A. C. Hewson, *The Kondo Problem to Heavy Fermions* (Cambridge University Press, Cambridge, 1993).

[65] M. Julliere, Phys. Lett. A **54**, 225 (1975).

[66] J. Barnaś and A. Fert, Phys. Rev. Lett. **80**, 1058 (1998).

[67] I. Weymann, J. König, J. Martinek, J. Barnaś, and G. Schön, Phys. Rev. B **72**, 115334 (2005).

[68] J. Barnaś and I. Weymann, J. Phys.: Condens. Matter **20**, 423202 (2008).

[69] S. Sahoo, T. Kontos, J. Furer, C. Hoffmann, M. Gräber, A. Cottet, and C. Schönenberger, Nat. Phys. **1**, 99 (2005).

[70] K. Wrześniewski and I. Weymann (unpublished).

53

Current Suppression in Transport Through Triple Quantum Dots Coupled to Ferromagnetic Leads

K. Wrześniewski* and I. Weymann

Faculty of Physics, Adam Mickiewicz University, Umultowska 85, 61-614 Poznań, Poland

We consider transport through triple quantum dot system in a triangular geometry weakly coupled to external ferromagnetic leads. The real-time diagrammatic technique in the lowest order perturbation theory is used to calculate the current and Fano factor in the parallel and antiparallel magnetic configuration of the system as well as the resulting tunnel magnetoresistance (TMR). We focus on the transport regime where the current is suppressed and show that it can lead to negative differential conductance and large super-Poissonian shot noise, which are present in both magnetic configurations. Furthermore, we show that for voltages where the system is trapped in a one-particle dark state the TMR becomes suppressed, while for two-particle blockade, the TMR is much enhanced.

1. Introduction

Quantum dots are ideal systems to study various correlations between single charges and spins at the nanoscale [1]. They are also very promising for applications in future nanoelectronics, therefore there is a lot of interest in fully understanding their various properties, including electronic transport. In fact, many phenomena known from different areas of physics can be observed and studied in artificial molecules built from several coupled quantum dots. One prominent example, which comes from atomic physics, is related with coherent population trapping in a dark state, which can also occur in triple quantum dot (TQD) systems [2–4]. The presence of such states reveals itself in current suppression and negative differential conductance. Recently, the role of dark states in transport through coherent TQDs weakly coupled to nonmagnetic leads was analyzed by means of the real-time diagrammatic technique [5]. In this paper we will extend these studies by assuming that the external electrodes are made of ferromagnetic materials. Quantum dots, when attached to ferromagnetic leads, can exhibit a considerable tunnel magnetoresistance (TMR) effect when varying the magnetic configuration between parallel and antiparallel one [6, 7]. The goal is thus to examine the magnetoresistive properties of TQDs and the effect of spin-dependent tunneling on transport through TQDs with a focus on transport regimes where current suppression occurs.

2. Theoretical description

The system consists of three single-level quantum dots in a triangular geometry, coupled to each other via hopping parameter t and attached to external ferromagnetic

leads, see Fig. 1. The first (second) dot is coupled to the left (right) lead with coupling strength Γ^σ and the bias voltage is applied symmetrically to the system. The magnetizations of the leads are assumed to form either parallel or antiparallel magnetic configuration. The Hamiltonian of system is given by, $H = H_{\text{Leads}} + H_{\text{TQD}} + H_{\text{T}}$, with H_{Leads} describing noninteracting electrons in the leads, $H_{\text{Leads}} = \sum_{j=L,R} \sum_{k\sigma} \varepsilon_{jk\sigma} c^\dagger_{jk\sigma} c_{jk\sigma}$, where $c^\dagger_{jk\sigma}, (c_{jk\sigma})$ is the creation (annihilation) operator of an electron with spin σ momentum k in the left ($j = L$) and right ($j = R$) lead, while $\varepsilon_{jk\sigma}$ denotes the corresponding single-particle energy. The TQD Hamiltonian reads

$$H_{\text{TQD}} = \sum_{j\sigma} \varepsilon_j n_{j\sigma} + U \sum_j n_{j\uparrow} n_{j\downarrow} + \frac{U'}{2} \sum_{\langle ij \rangle} \sum_{\sigma\sigma'} n_{i\sigma} n_{j\sigma'}$$
$$+ \sum_{\langle ij \rangle} \frac{t}{2} \sum_\sigma (d^\dagger_{i\sigma} d_{j\sigma} + d^\dagger_{j\sigma} d_{i\sigma}). \qquad (1)$$

Here, $n_{j\sigma} = d^\dagger_{j\sigma} d_{j\sigma}$, where $d^\dagger_{j\sigma}$ creates an electron with spin σ in the jth quantum dot, while ε_j denotes the respective energy. The second and third terms take into account the on-site Coulomb interaction U and the inter-dot Coulomb correlation denoted by U', respectively. The last term of H_{TQD} describes the hopping between the dots with t being the hopping parameter, assumed equal for all dots. The summation $\langle ij \rangle$ is over nearest-neighbor dots and the parameters U' and t are divided by 2 to avoid double counting. Finally, the tunneling Hamiltonian is given by

$$H_{\text{T}} = \sum_{j=L,R} \sum_{k\sigma} (v_j c^\dagger_{jk\sigma} d_{jk\sigma} + \text{H.c.}), \qquad (2)$$

where v_j denotes the tunnel matrix elements between the jth lead and the corresponding dot, see Fig. 1. The respective coupling strength is given by, $\Gamma^\sigma_j = 2\pi |t_j| \rho^\sigma_j$, where ρ^σ_j is the spin-dependent density of states in lead j. With the definition of spin polarization for lead j, $p_j = (\rho^+_j - \rho^-_j)/(\rho^+_j + \rho^-_j)$, the coupling becomes, $\Gamma^{+(-)}_j = \Gamma_j (1 \pm p_j)$, where $\Gamma_j = (\Gamma^+_j + \Gamma^-_j)/2$. Here,

─────────

*corresponding author; e-mail: kacper.wrzesniewski@gmail.com

Γ_j^+ (Γ_j^-) stands for coupling between given dot to the spin-majority (spin-minority) electron band of lead j. In the following we assume, $\Gamma_L = \Gamma_R \equiv \Gamma$ and $p_L = p_R \equiv p$. We also take the limit of $U \to \infty$ and exclude doubly occupied state of each dot from calculations.

To determine the transport characteristics we use the real-time diagrammatic technique [8, 9]. This method is based on a systematic perturbation expansion of the reduced density matrix and the operators of interest with respect to the coupling strength Γ. In this analysis we assume that the coupling is very weak and consider only the lowest order of expansion, which corresponds to sequential tunneling. Moreover, we also assume that the hopping between the dots is relatively large, $t \gg \Gamma$. This leads to significant overlap of the wave functions of the neighboring dots, resulting in the formation of molecular states, $|\chi\rangle$, through which transport takes place.
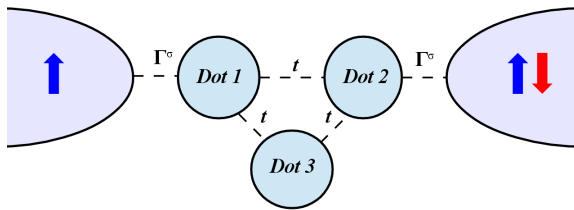

Fig. 1. Schematic of TQD in a triangular geometry. Dot 1 (2) is coupled to the left (right) lead with coupling strength Γ^σ. Each dot is coupled to remaining two dots with hopping parameter t.

Within the real-time diagrammatic technique, the occupation probabilities p_χ can be found from a master-like equation [8, 9]. On the other hand, the current can be calculated from [8, 9], $I = (e/2\hbar)\mathrm{Tr}\{\boldsymbol{W}^I \boldsymbol{p}\}$, where $\boldsymbol{W}^I$ is the self-energy matrix which takes into account the number of particles transferred through the system and $\boldsymbol{p}$ is the probability vector. In the following, we study the bias dependence of the current in the parallel (I^P) and antiparallel (I^{AP}) magnetic configuration and the TMR, defined as [7], TMR = $I^P/I^{AP} - 1$. Moreover, we also analyze the Fano factor, $F = S/(2e|I|)$, where S denotes the shot noise. The formula for S can be found in Ref. [9].

3. Results and conclusions

The currents I^P and I^{AP} as well as the resulting TMR are shown in Fig. 2a for $\varepsilon_1 = \varepsilon_3 \equiv \varepsilon = 1$ meV and $\varepsilon - \varepsilon_2 \equiv \delta = 0.5$ meV. For this level configuration, when $1/2 \lesssim eV/U' \lesssim 3/2$, the system is trapped in a one-particle dark state. The TQD is then in a state, in which the wave function is extended over only two dots, one of which is not directly coupled to the leads. As a result, the transfer of electrons through the system is blocked. Although in the dark state regime the current is suppressed, due to nonzero temperature there is still a finite occupation probability of single-particle states, which are
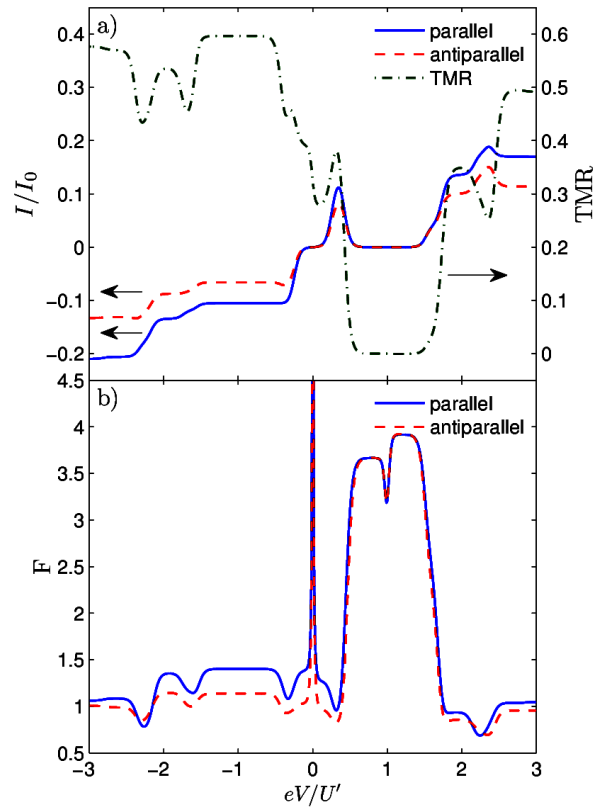

Fig. 2. The bias voltage dependence of (a) the current in the parallel and antiparallel configuration and the resulting TMR, and (b) the Fano factor in both magnetic configurations. The parameters are as follows: $U' = 10$ meV, $\varepsilon_1 = \varepsilon_3 \equiv \varepsilon = 1$ meV, $\varepsilon - \varepsilon_2 \equiv \delta = 0.5$ meV, $t = -1$ meV, $\Gamma = 0.025$ meV, $p = 0.5$, $T = 0.2$ meV and $I_0 = e\Gamma/\hbar$.

extended over all three dots and thus contribute to transport. This gives rise to a thermally-activated nonzero current and to the TMR in the blockade regime. As can be seen in Fig. 2a, for negative bias voltage both currents I^P and I^{AP} display typical Coulomb staircase dependence. However, for positive bias, the current first increases to drop when the system becomes trapped in a dark state, which happens for $1/2 \lesssim eV/U' \lesssim 3/2$. The system exhibits then negative differential conductance, irrespective of magnetic configuration. Moreover, $I^P > I^{AP}$, in the whole range of considered bias voltage, except for $1/2 \lesssim eV/U' \lesssim 3/2$, when one finds $I^P \approx I^{AP}$. As a result, the TMR is always positive and reaches approximately zero, when the system is trapped in one-particle dark state, see Fig. 2a.

The presence of dark states is also revealed in the dependence of the Fano factor on the bias voltage. The Fano factor describes the deviation of the shot noise from the Poissonian noise for uncorrelated events. In the dark state regime, for both parallel and antiparallel configuration, the shot noise becomes super-Poissonian with

Fano factor much larger than unity, see Fig. 2b. For $eV \to 0$, the Fano factor diverges due to the fact that $I \to 0$, while S is dominated by thermal noise. We also note that generally $F^{\mathrm{P}} > F^{\mathrm{AP}}$, this results from the fact that in the parallel configuration there is a larger imbalance between spin-resolved transport channels compared to the antiparallel configuration, which enhances the fluctuations of the current.
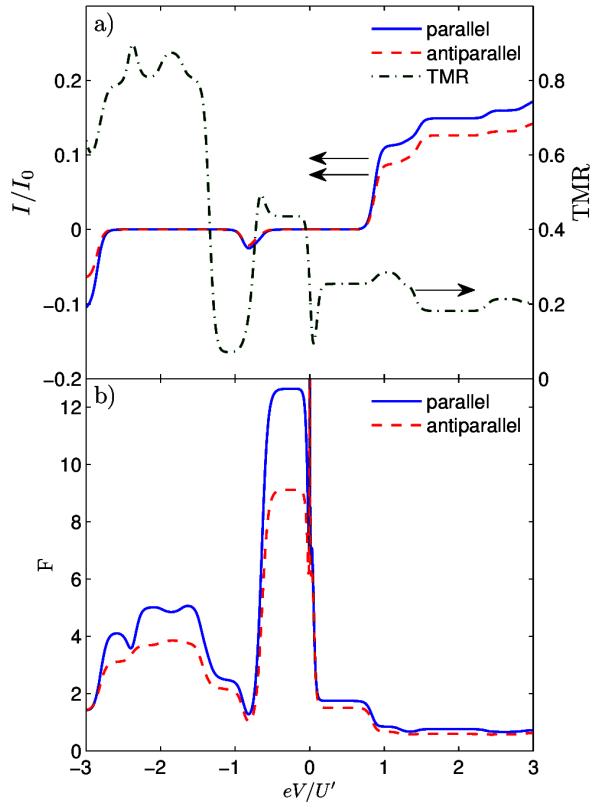

Fig. 3. The bias voltage dependence of (a) the current in the parallel and antiparallel configuration and the resulting TMR, and (b) the Fano factor in both magnetic configurations. The parameters are the same as in Fig. 2 with $\varepsilon = -25$ meV.

By lowering the levels of the dots, the TQD becomes successively occupied with electrons. The transport characteristics for the case when there are three electrons in the TQD for $V = 0$ are shown in Fig. 3. Now, for positive bias the current grows monotonically and shows Coulomb steps, while for negative bias voltage one observes current suppression and negative differential conductance. With increasing negative bias, the current exhibits a small peak for $eV/U' \approx -0.8$, i.e. when the applied bias matches the excitation energy between three and two-particle states. However, for $eV/U' < -0.8$, the system becomes trapped in a two-particle blockade and the current is suppressed in a wide range of negative bias voltage, see Fig. 3a. In this blockade, the occupancy of the second dot is one, while the occupancies of first and third dots are equal to

one half. Because of large on-dot Coulomb interaction, the electrons cannot tunnel from right lead to the second dot and transport is then blocked. Note, that electronic spacial distribution in this blockade is significantly different compared to single-particle dark state where clearly one of the dots was not occupied at all. Now, its occupancy is equal to one, forbidding tunneling from the lead to this dot due to large U. This blockade is thus rather due to finite Coulomb correlations in the dots, contrary to one-particle blockade discussed above, which was due to the trapping in a dark state.

The magnetoresistive properties of the system are also different than those in the case shown in Fig. 2. For two-particle blockade, the TMR is greatly enhanced, see Fig. 3a. This can be attributed to nonequilibrium spin accumulation in triplet states that develops in the antiparallel configuration, leading to large difference between the currents I^{P} and I^{AP}. Moreover, in the blockade regimes due to Coulomb interactions, we find super-Poissonian shot noise, which is enhanced in the parallel configuration compared to the antiparallel one, see Fig. 3b.

In conclusion, we have studied the spin-resolved sequential transport through triple quantum dot in triangular geometry weakly coupled to ferromagnetic leads. We showed that when the system is trapped in one-particle dark state, the TMR is generally suppressed, while for two-particle blockade we predicted an enhancement of TMR. Both blockade regimes are also associated with super-Poissonian shot noise, which is larger in the parallel configuration compared to the antiparallel one.

References

[1] L.P. Kouwenhoven, D.G. Austing, S. Tarucha, *Rep. Prog. Phys.* **64**, 701 (2001).

[2] C. Emary, *Phys. Rev. B* **76**, 245319 (2007).

[3] C. Poltl, C. Emary, T. Brandes, *Phys. Rev. B* **80**, 115313 (2009).

[4] T. Kostyrko, B.R. Bułka, *Phys. Rev. B* **79**, 075310 (2009).

[5] I. Weymann, B. R. Bułka, J. Barnaś, *Phys. Rev. B* **83**, 195302 (2011).

[6] I. Weymann, J. König, J. Martinek, J. Barnaś, G. Schön, *Phys. Rev. B* **72**, 115334 (2005).

[7] J. Barnaś, I. Weymann, *J. Phys.: Condens. Matter* **20**, 423202 (2008).

[8] H. Schoeller, G. Schön, *Phys. Rev. B* **50**, 18436 (1994); J. König, J. Schmid, H. Schoeller, G. Schön, *Phys. Rev. B* **54**, 16820 (1996).

[9] A. Thielmann, M. H. Hettler, J. König, G. Schön, *Phys. Rev. Lett.* **95**, 146806 (2005).

Influence of Magnetic Field on Dark States in Transport through Triple Quantum Dots

K. Wrześniewski* and I. Weymann

Faculty of Physics, Adam Mickiewicz University, Umultowska 85, 61-614 Poznań, Poland

We theoretically study the electronic transport through a triple quantum dot system in triangular geometry weakly coupled to external metallic leads. By means of the real-time diagrammatic technique, the current and Fano factor are calculated in the lowest order of perturbation theory. The device parameters are tuned to such transport regime, in which coherent population trapping of electrons in quantum dots due to the formation of dark states occurs. The presence of such states greatly influences transport properties leading to a strong current blockade and enhanced, super-Poissonian shot noise. We consider both one- and two-electron dark states and examine the influence of magnetic field on coherent trapping in aforementioned states. When the system is in one-electron dark state, we observe a small shift of the blockade's region, whereas in the case of two-electron dark state, we show that strong magnetic field can lift the current blockade completely.

1. Introduction

Coupled quantum dot systems reveal many different quantum phenomena favorable for future applications in nanoelectronics and quantum computation [1, 2]. A prominent class of such systems constitute those built of three quantum dots [3, 4], in which a wide variety of effects, interactions and possible configurations give rise to rich physics and consistently stimulate an extensive theoretical and experimental research. An important example of a quantum-mechanical phenomenon that can emerge in triple quantum dots (TQDs) is associated with the formation of dark states, which lead to coherent electron trapping [5–8]. A dark state forms when destructive interference of electronic wave functions decouples one of the dots from the respective lead and, as a result, the current can no longer flow through the system. This work extends the previous studies on coherent population trapping in TQDs [5–7] by analyzing the role of external magnetic field on the current flowing through a triple quantum dot in triangular geometry in transport regime where dark states form.

2. Model and method

The system is built of three single-level quantum dots (see Fig. 1) arranged in a triangular geometry. The first (second) dot is weakly coupled to the left (right) metallic electrode and the dots are coupled to each other by hopping matrix elements t_{ij}. The total Hamiltonian can be written as $H = H_{\mathrm{Leads}} + H_{\mathrm{TQD}} + H_{\mathrm{T}}$. The first term, $H_{\mathrm{Leads}} = \sum_{j=L,R} \sum_{k\sigma} \varepsilon_{jk\sigma} c^{\dagger}_{jk\sigma} c_{jk\sigma}$, describes noninteracting electrons in the leads, where $c^{\dagger}_{jk\sigma}$ is the creation operator of an electron with spin σ, momentum k and

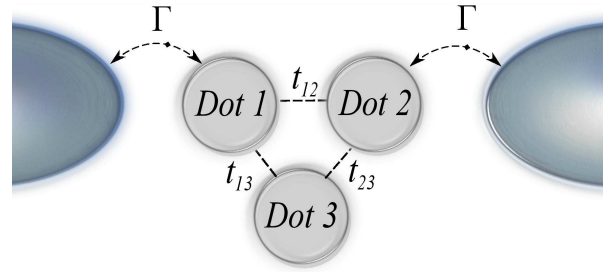————————

*corresponding author; e-mail: wrzesniewski@amu.edu.pl

Fig. 1. Schematic of a triple quantum dot system in triangular geometry. Dot 1 (2) is coupled to the left (right) lead with coupling strength Γ. The dots are coupled to each other via hopping matrix elements t_{ij}.

energy $\varepsilon_{jk\sigma}$ in the left or right ($j = L, R$) electrode. The TQD Hamiltonian reads

$$H_{\mathrm{TQD}} = \tag{1}$$

$$\sum_{j\sigma} \varepsilon_j n_{j\sigma} + U_j \sum_j n_{j\uparrow} n_{j\downarrow} + \frac{U'_{ij}}{2} \sum_{\langle ij \rangle} \sum_{\sigma\sigma'} n_{i\sigma} n_{j\sigma'}$$
$$+ \sum_{\langle ij \rangle} \frac{t_{ij}}{2} \sum_\sigma (d^{\dagger}_{i\sigma} d_{j\sigma} + d^{\dagger}_{j\sigma} d_{i\sigma}) + B \sum_j S_{zj}.$$

The first term describes on-site energy ε_j, with $n_{j\sigma} = d^{\dagger}_{j\sigma} d_{j\sigma}$ and $d^{\dagger}_{j\sigma}$ being the creation operator of an electron with spin σ in j-th quantum dot. The two next terms describe intra- and inter-dot Coulomb interactions, with strength U_j and U'_{ij}, respectively. The fourth term stands for hopping between the dots, while the last one takes into account external magnetic field B in units of $g\mu_B \equiv 1$, with S_{zj} being the z-th component of j-th dot spin.

The last term of total Hamiltonian describes tunneling between TQD and the leads and is given by

$$H_{\mathrm{T}} = \sum_{j=L,R} \sum_{k\sigma} (V_j c^{\dagger}_{jk\sigma} d_{j\sigma} + \mathrm{H.c.}), \tag{2}$$

where V_j is the tunnel matrix element between the j-th

lead and the corresponding dot. The dot-lead coupling strength is then given by $\Gamma_j = 2\pi|V_j|^2\rho_j$, with ρ_j being the density of states of lead j. It is assumed that $\Gamma_L = \Gamma_R \equiv \Gamma$ and that the system is symmetrically biased: $\mu_L = eV/2$ and $\mu_R = -eV/2$.

We calculate the electronic current, shot-noise and Fano factor using the real-time diagrammatic technique [9, 10]. This technique relies on perturbation expansion of the reduced density matrix and corresponding operators with respect to Γ. In this analysis the weak lead-dot coupling is assumed and only the lowest-order of expansion is considered, which describes sequential tunneling processes. Due to relatively large hopping between the dots, $t_{ij} > \Gamma$, there is a significant overlap of the electrons' wave functions of the dots, which results in the formation of molecular states $|\chi\rangle$. Electronic transport takes places through those states and their occupation probabilities p_χ are found from an appropriate kinetic equation [9, 10]. The current is then calculated from $I = (e/2\hbar)\text{Tr}\{\mathbf{W}^I\mathbf{p}\}$, where $\mathbf{W}^I$ is the self-energy matrix, which takes into account electron tunneling through the system, while $\mathbf{p}$ is the vector containing probabilities p_χ. Finally, we also determine the shot noise S and the corresponding Fano factor $F = S/(2e|I|)$ [10].

3. Results and discussion

The current as a function of bias voltage, for indicated values of external magnetic field B, is shown in Fig. 2a. The dots' levels are set to $\varepsilon_j = \varepsilon = U/2$, therefore when no bias is applied, the dots levels are unoccupied and the system is empty. For $B = 0$, around $eV/U \approx 0.8$, there is a peak in the current due to the first one-electron state entering the transport window. However, very close to $eV/U \approx 1$, there is a strong drop of the current and transport through the system is blocked, see Fig. 2a. This current blockade is due to the formation of a one-electron dark state, that entered the transport window. The wave function of this dark state has the following form: $|\Psi_{DS1}\rangle = \frac{1}{\sqrt{2}}(|\sigma, 0, 0\rangle - |0, 0, \sigma\rangle)$, where $|\alpha_1, \alpha_2, \alpha_3\rangle$ is a local state of the system, in which dot j is either empty ($\alpha_j = 0$), occupied by spin-σ electron ($\alpha_j = \sigma$) or doubly-occupied ($\alpha_j = d$). In this one-electron dark state the electron occupies the first and third dot with equal probability, however, due to destructive interference, the occupation of the second dot is equal to zero. This effectively decouples the TQD system from the right lead and blocks tunneling processes through the right junction. As can be seen in Fig. 2a, the system remains in the dark state for a significant range of bias voltage, till the current starts flowing through the system again, around $eV/U \gtrsim 2.5$, when two-electron states enter the bias window. When the magnetic field is turned on, one can clearly see in the current dependence that the energy levels of states taking part in transport are shifted toward lower bias voltage and, consequently, the systems becomes trapped in dark state already for smaller voltages, while the size of this blockade remains almost unchanged. This is due to the Zeeman splitting of the TQD

levels. The one-electron dark state is spin-split and now the lower-energy dark state enters the transport window earlier, which makes the blockade appear faster. On the other hand, the dark state with opposite spin moves toward higher energies. However, this shift does not increase the size of the blockade, because the two-electron triplet states reach the transport window earlier due to the same mechanism, i.e. Zeeman-splitting-induced shift of their energy.
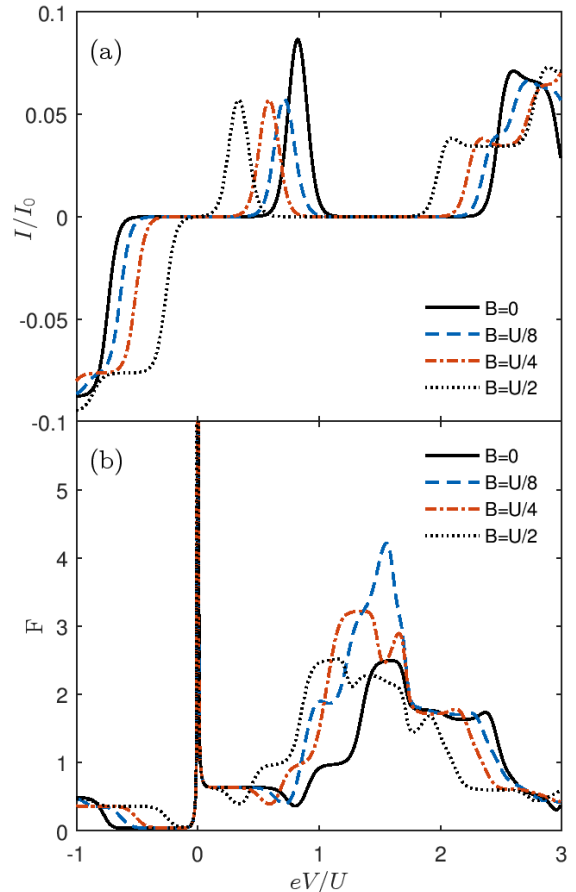

Fig. 2. The bias voltage dependence of (a) the current and (b) the Fano factor for different values of magnetic field B. The parameters are: $U_1 = U_3 = U_{13} = U = 1$, $U_2 = U + \Delta, U_{12} = U_{23} = U - \Delta$, where $\Delta = U/5$. The dots' levels are equal, $\varepsilon_j = 0.5$, $t_{13} = 0.05$, $t_{12} = t_{23} = 0.1$, $\Gamma = 0.01$, and $T = 0.02$ in units of U. The current is plotted in units $I_0 = e\Gamma/\hbar$.

The bias voltage dependence of the Fano factor is presented in Fig. 2b. At zero bias voltage the Fano factor is divergent due to the fact that the current vanishes while the noise is finite due to thermal fluctuations. On the other hand, in the bias range where the system is trapped in the dark state, the shot noise becomes super-Poissonian [7, 8]. For given parameters, the Fano factor reaches $F \approx 2.5$ for $B = 0$, and $F \gtrsim 4$ when the system is in finite magnetic field B.

When the dots' levels are set to $\varepsilon_j = \varepsilon = -U/2$, at zero bias the system is singly occupied. For assumed
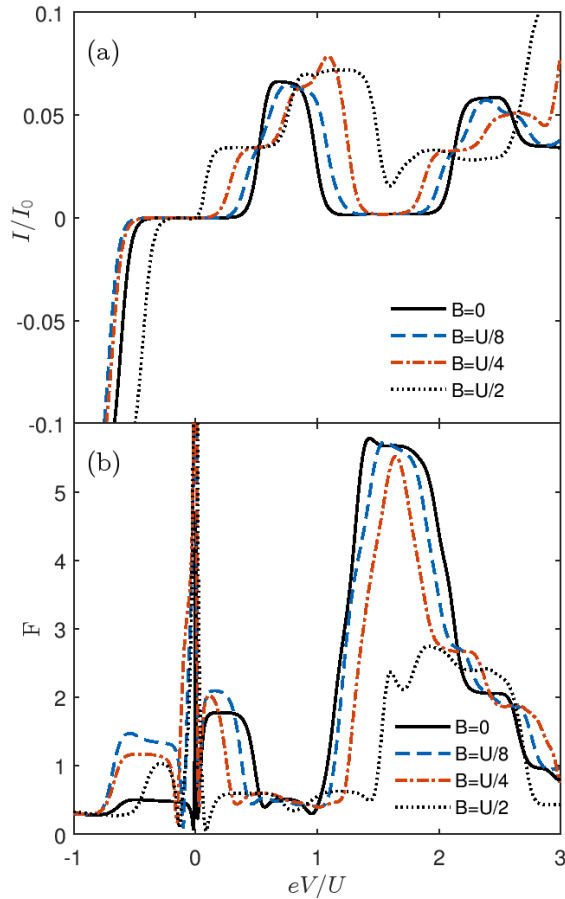
Fig. 3.   The same as in Fig. 2 calculated for $\varepsilon_j = \varepsilon = -U/2$.

of magnetic field, and because of the Zeeman splitting of those levels the current blockade shrinks with increasing B. This is clearly visible in Fig. 3a. The bias voltage range where the two-electron dark state is present gets narrower as the magnetic field becomes stronger. Eventually, for the large enough field ($B = U/2$) the blockade is lifted, however, a significant drop in current is still visible.

The Fano factor dependence on V shown in Fig. 3b again shows strong enhancement of shot-noise within the blockade. The Fano factor for the two-electron dark state is even higher than in previously discussed one-electron case and reaches values $F \gtrsim\!\!> 5$. When the magnetic field is present, due to the reduced size of the blockade, the peak in the Fano factor also gets narrower. When the magnetic field is strong enough to lift the blockade, the Fano factor significantly drops as well ($F < 3$), see Fig. 3b.

To conclude, we have studied the bias voltage dependence of the current and the Fano factor for TQD system in triangular geometry. We have focused on regimes where the transport is blocked due to the presence of one and two-electron dark states, and analyzed how the external magnetic field influences transport in those regimes. We have shown that the blockade's position gets shifted in the case of one-electron dark state, whereas in the two-electron dark state regime, the presence of strong magnetic field can lift the current blockade.

Acknowledgments

References

[1] L.P. Kouwenhoven, D.G. Austing, S. Tarucha, *Rep. Prog. Phys.* **64**, 701 (2001).

[2] D. Loss, D.P. DiVincenzo, *Phys. Rev. A* **57**, 120 (1998).

[3] C.-Y. Hsieh, Y.-P. Shim, M. Korkusinski, P. Hawrylak, *Rep. Prog. Phys.* **75**, 114501 (2012).

[4] K. Wrześniewski, I. Weymann, *Phys. Rev. B* **92**, 045407 (2015).

[5] C. Emary, *Phys. Rev. B* **76**, 245319 (2007).

[6] C. Poltl, C. Emary, T. Brandes, *Phys. Rev. B* **80**, 115313 (2009).

[7] I. Weymann, B.R. Bułka, J. Barnaś, *Phys. Rev. B* **83**, 195302 (2011).

[8] K. Wrześniewski, I. Weymann, *Acta Phys. Pol. A* **127**, 460 (2015).

[9] H. Schoeller, G. Schön, *Phys. Rev. B* **50**, 18436 (1994); J. König, J. Schmid, H. Schoeller, G. Schön, *Phys. Rev. B* **54**, 16820 (1996).

[10] A. Thielmann, M.H. Hettler, J. König, G. Schön, *Phys. Rev. Lett.* **95**, 146806 (2005).

parameters, the TQD can easily reach a two-electron dark state. The current and Fano factor for this case are shown in Fig. 3. For $B = 0$, the current exhibits a plateau for $0.5 \lesssim eV/U \lesssim 1$, which is related to two-electron state entering the transport window, which is not a dark one. Similarly to the previously analyzed case, the dark state has higher energy than the first state participating in transport. Therefore, in both cases we are able to observe a strong peak in the current, followed by sudden current suppression due to trapping the system in a dark state. As can be seen in Fig. 3a, the two-electron dark state enters the transport window around $eV/U \approx 1$ and has the following wave function: $|\Psi_{DS2}\rangle = \frac{1}{2}(|d,0,0\rangle + |\uparrow,0,\downarrow\rangle - |\downarrow,0,\uparrow\rangle + |0,0,d\rangle)$. The occupation of the second dot is again equal to zero, therefore the electrons are not able to reach the right electrode and the current is blocked. However, the behavior of this dark state in magnetic field is quite different from the previous case. The difference results from the fact that the two-electron dark state is formed by two particles of opposing spin, i.e. it is a singlet state. Consequently, this state is not split by external magnetic field. However, the one-electron and three-electron states that are close in energy to this state are under strong influence

Dark states in spin-polarized transport through triple quantum dot molecules

K. Wrześniewski[*] and I. Weymann

Faculty of Physics, Adam Mickiewicz University, Umultowska 85, 61-614 Poznań, Poland

We study the spin-polarized transport through a triple-quantum-dot molecule weakly coupled to ferromagnetic leads. The analysis is performed by means of the real-time diagrammatic technique, including up to the second order of perturbation expansion with respect to the tunnel coupling. The emphasis is put on the impact of dark states on spin-resolved transport characteristics. It is shown that the interplay of coherent population trapping and cotunneling processes results in a highly nontrivial behavior of the tunnel magnetoresistance, which can take negative values. Moreover, a super-Poissonian shot noise is found in transport regimes where the current is blocked by the formation of dark states, which can be additionally enhanced by spin dependence of tunneling processes, depending on the magnetic configuration of the device. The mechanisms leading to those effects are thoroughly discussed.

I. INTRODUCTION

Vast progress in theoretical and experimental studies of artificial molecules, such as those realized in coupled quantum dot systems, ceaselessly brings about many attractive and relevant results and observations [1,2]. On the one side, such nanostructures have promising applications for quantum computation [3–5], where spin-polarized electron encodes a qubit. On the other side, coupled quantum dots exhibit various promising transport phenomena [6,7], which may be important for novel spintronic and nanoelectronic devices. A particularly prominent example of an artificial molecular nanostructure is a system built of three quantum dots (TQD).

The properties of triple quantum dot systems have been extensively studied in various regimes and configurations, exposing rich Kondo physics [8–11], various transport effects, and complex electron structure [12–17], as well as revealing potential for applications in quantum computing [18–22] and for generation of nonlocal, entangled electron pairs [23,24]. When the three quantum dots form a triangular geometry [25–31], the system resembles a simple planar molecule and, due to the interference effects, the formation of dark states is possible [32–37]. This quantum-mechanical phenomenon was first observed in atomic physics [38–41], and then found also in mesoscopic systems, such as, in particular, coupled quantum dots [42,43]. A dark state emerges when destructive interference of electronic wave functions decouples the system from one of the leads. When the system is in a dark state, it results in a coherent electron trapping [42] and, consequently, a strong current suppression, negative differential conductance, and enhanced shot noise [32–35]. Interestingly, the dark states in quantum dot systems are also considered to enable the creation of spatially separated, spin-entangled two-electron states [44] and, thus, open the possibility to build various quantum logic devices as well as quantum memory [45]. It is

important to note that the mechanism of coherent population trapping is very distinct from Coulomb, spin [46–49], and Franck-Condon [50] blockades or Aharonov-Bohm [51] effect on triangular quantum dots, to name a few.

All this provides a strong motivation for further considerations of dark states in transport through triple quantum dots and, in fact, there are still certain aspects that remain unexplored. One of them involves the role of dark states in spin-resolved transport behavior. In fact, spin-dependent phenomena in transport through quantum dot systems are currently intensively studied [52]. This is not only due to expected applications for spintronics and spin nanoelectronics [53], but also because of the possibility to controllably explore the fundamental interactions between single charges and spins [54]. First of all, the presence of ferromagnetic (FM) electrodes introduces many qualitative and quantitative changes in transport, resulting in magnetoresistive or spin diodelike behavior [55–57]. Moreover, the effects, such as the suppression of the Kondo effect with the emergence of an exchange field [58], universal magnetoconductance scaling [59], an enhancement of splitting efficiency of entangled Cooper pairs in QD-based splitters [60,61], or spin thermoelectric effects [62–64] are all among many interesting phenomena arising from the coupling of quantum dots to FM leads. In this context, however, the interplay between the coherent population trapping and spin-resolved tunneling has so far hardly been explored. Therefore, in this paper we address this problem and analyze the spin-dependent transport through triple quantum dots weakly attached to two ferromagnetic electrodes, focusing on the parameter regime where the dark states form.

To determine the nonequilibrium transport characteristics, we use the real-time diagrammatic technique [65], including the first- and second-order diagrams with respect to the tunnel coupling. This allows us to systematically include the sequential and cotunneling processes in the transport analysis. We study the bias and gate voltage dependence of the current, differential conductance and Fano factor in two different magnetic configurations of the device: the parallel and antiparallel one.
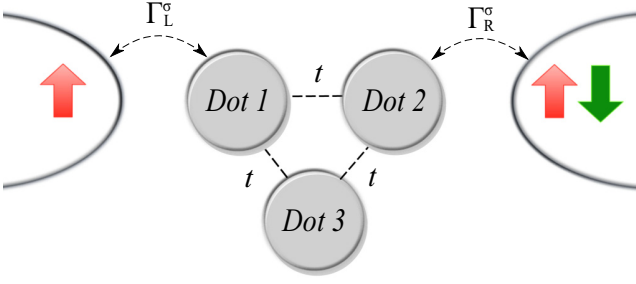
FIG. 1. Schematic of a triangular quantum dot system coupled to ferromagnetic leads. The dot 1 (2) is attached to the left (right) lead with coupling strength Γ_α^σ, while the dots are coupled to each other via the hopping matrix elements t.

Furthermore, by calculating the currents in the two magnetic configurations we also determine the tunnel magnetoresistance (TMR) of the system [55–57,66]. These quantities provide a relevant insight into the spin-dependent transport properties of the considered system and are especially interesting in the regimes where dark states are present. In particular, we focus on the transport regimes where one- and two-particle dark states and their hole counterparts form. We show that when the system is trapped in a dark state, the current flows mainly due to cotunneling processes. Moreover, depending on a particular type of dark state, we find a strong dependence of the current on magnetic configuration of the device, which results in a nontrivial behavior of the TMR. A similarly strong dependence on magnetic configuration is also found in the case of shot noise, which is generally super-Poissonian in the dark state regions.

The paper is structured as follows. Section II consists of a model description and the method used for numerical calculations. In Sec. III we present the numerical results and relevant analysis. This section is divided into four subsections relating to different types of examined dark states. Finally, the work is concluded in Sec. IV.

II. THEORETICAL FRAMEWORK

A. Model

The schematic of the considered system built of three single-level quantum dots forming a triangular geometry is presented in Fig. 1. The dots are coupled to each other via the hopping matrix elements t. The first (second) dot is weakly coupled to the left (right) ferromagnetic electrode with the respective spin-dependent coupling strength Γ_α^σ. We consider two collinear magnetic configurations of the electrodes: the parallel (P) one, where both leads' magnetizations point in the same direction (two red arrows in Fig. 1) and the antiparallel (AP) one, where the magnetizations point in opposite directions (red and green arrows). The change of the system's magnetic configuration can be triggered upon applying a weak external magnetic field, provided the coercive fields of ferromagnets are different. This field is weak enough such that the Zeeman energy associated with this field can be neglected.

The total Hamiltonian of the system is given by

$$H = H_{\text{Leads}} + H_{\text{TQD}} + H_{\text{T}}, \tag{1}$$

where the first term,

$$H_{\text{Leads}} = \sum_{\alpha=L,R} \sum_{k\sigma} \varepsilon_{\alpha k \sigma} c_{\alpha k \sigma}^\dagger c_{\alpha k \sigma}, \tag{2}$$

describes the left and right ferromagnetic leads in the noninteracting quasiparticle approximation. Here, the operator $c_{\alpha k \sigma}^\dagger$ is the creation operator of an electron with spin σ, momentum k, and energy $\varepsilon_{\alpha k \sigma}$ in the left or right ($\alpha = L, R$) electrode. The second term of the Hamiltonian models the triple quantum dot and reads

$$H_{\text{TQD}} = \sum_{j\sigma} \varepsilon_j n_{j\sigma} + U_j \sum_j n_{j\uparrow} n_{j\downarrow} + \frac{U_{ij}}{2} \sum_{\langle ij \rangle} \sum_{\sigma\sigma'} n_{i\sigma} n_{j\sigma}$$
$$+ \sum_{\langle ij \rangle} \frac{t_{ij}}{2} \sum_\sigma (d_{i\sigma}^\dagger d_{j\sigma} + d_{j\sigma}^\dagger d_{i\sigma}). \tag{3}$$

The on-site energy is given by ε_j, with $n_{j\sigma} = d_{j\sigma}^\dagger d_{j\sigma}$ and $d_{j\sigma}^\dagger$ being the creation operator of an electron with spin σ in the jth quantum dot. The intra- and interdot Coulomb interactions are of strength U_j and U_{ij}, respectively. The hopping between the dots t is assumed to be equal between each pair of the dots.

The last term of the Hamiltonian accounts for the tunneling between TQD and the leads, and it takes the standard form

$$H_{\text{T}} = \sum_{k\sigma} (v_L c_{Lk\sigma}^\dagger d_{1\sigma} + v_R c_{Rk\sigma}^\dagger d_{2\sigma} + \text{H.c.}), \tag{4}$$

where v_L and v_R are the tunnel matrix elements between the left and right leads and the corresponding dots. The dot-lead coupling strength is given by $\Gamma_\alpha^\sigma = 2\pi |v_\alpha|^2 \rho_\alpha^\sigma$, with ρ_α^σ being the spin-dependent density of states of lead α. Using the definition of spin polarization of ferromagnetic lead α, $p_\alpha = (\rho_\alpha^+ - \rho_\alpha^-)/(\rho_\alpha^+ + \rho_\alpha^-)$, the couplings can be written as $\Gamma_\alpha^\pm = \Gamma_\alpha(1 \pm p_\alpha)$ for the spin majority ($\sigma = +$) or minority ($\sigma = -$) subband, where $\Gamma_\alpha = (\Gamma_\alpha^+ + \Gamma_\alpha^-)/2$. We assume equal left and right coupling strengths, $\Gamma_L = \Gamma_R \equiv \Gamma$. The applied bias voltage is also assumed to be symmetrical, $\mu_L = eV/2$ and $\mu_R = -eV/2$.

B. Method

The spin-resolved transport properties of the considered system are calculated with the aid of the real-time diagrammatic technique [65,67–69]. This method relies on perturbation expansion of the reduced density matrix and the corresponding operators with respect to the coupling strength Γ. Here we perform all calculations including the first order, accounting for sequential tunneling processes, and the second order of expansion, which describes cotunneling.

The reduced density matrix in the steady state can be found from [65]

$$\mathbf{W}\mathbf{p} = 0, \tag{5}$$

with the normalization condition $\text{Tr}\{\mathbf{p}\} = 1$. In the above equation $\mathbf{W}$ is a matrix, the elements $W_{\chi\chi'}$ of which describe transitions between the TQD many-body states $|\chi\rangle$ and $|\chi'\rangle$, while $\mathbf{p}$ denotes the probability vector. The states $|\chi\rangle$ are the eigenstates of H_{TQD} obtained from the numerical solution of the eigenvalue problem. Note that the triple-dot Hamiltonian H_{TQD} is not diagonal in the local occupation basis. However,

in order to explain the microscopic mechanism of the dark states and the blocking of transport through the system, we will often express the states $|\chi\rangle$ as superpositions of local occupation states. Therefore, we assume that a ket in local occupation basis represents occupation of consecutive dots in the following way: $|\chi_1\chi_2\chi_3\rangle$, where χ_j denotes the allowed $(0, \sigma$ and $d)$ local states, which stand for empty, spin σ, and doubly occupied dot j, respectively. Moreover, to distinguish between different states of the system, we will additionally use the quantum numbers corresponding to the total charge Q and spin zth component S_z of the TQD, $|Q, S_z\rangle$.

The elements of matrix $\mathbf{W}$ are exactly related to self-energies, $\Sigma_{\chi\chi'} = i W_{\chi'\chi}$, which can be determined diagrammatically order by order in Γ [65,67–69]. A given order in Γ corresponds to the respective number of tunneling lines in diagrams; therefore to find the first- and second-order contributions, we consider all topologically different, irreducible diagrams with one and two tunneling lines. An exemplary calculation of two different diagrams can be found in the Appendix. The perturbation expansion of the matrix $\mathbf{W}$ starts in the first order in Γ, while that of $\mathbf{p}$ starts in the zeroth order. The corresponding probabilities can be found from the following kinetic equations [65]:

$$\mathbf{W}^{(1)}\mathbf{p}^{(0)} = 0 \qquad (6)$$

and

$$\mathbf{W}^{(2)}\mathbf{p}^{(0)} + \mathbf{W}^{(1)}\mathbf{p}^{(1)} = 0, \qquad (7)$$

including $\mathrm{Tr}\{\mathbf{p}^{(n)}\} = \delta_{0,n}$.

The current flowing through the system can be calculated from [68]

$$I = \frac{e}{2\hbar}\mathrm{Tr}\{\mathbf{W}^I\mathbf{p}\}, \qquad (8)$$

where $\mathbf{W}^I$ is the self-energy matrix, which accounts for the number of electrons transferred through the TQD system. For the current we again perform the perturbation expansion, such that the current in the first order is given by

$$I^{(1)} = \frac{e}{2\hbar}\mathrm{Tr}\{\mathbf{W}^{I(1)}\mathbf{p}^{(0)}\}, \qquad (9)$$

while the second-order current can be found from

$$I^{(2)} = \frac{e}{2\hbar}\mathrm{Tr}\{\mathbf{W}^{I(2)}\mathbf{p}^{(0)} + \mathbf{W}^{I(1)}\mathbf{p}^{(1)}\}. \qquad (10)$$

The total current, i.e., the first-order (sequential) plus second-order (cotunneling) current, is then simply given by

$$I = I^{(1)} + I^{(2)}. \qquad (11)$$

In addition to the current we also study the tunnel magnetoresistance, which describes the change of system's transport properties when the magnetic configuration of the device is varied. The TMR can be defined as [55–57,66]

$$\mathrm{TMR} = \frac{I^P - I^{AP}}{I^{AP}}, \qquad (12)$$

where $I^P(I^{AP})$ denotes the current flowing through the TQD system in the parallel (antiparallel) magnetic configuration of ferromagnetic leads.

Finally, we also determine the zero-frequency shot noise S and the corresponding Fano factor $\mathrm{F} = S/(2|eI|)$, describing the deviation of the shot noise from the Poissonian value, $S_P = 2|eI|$. A detailed description of how to compute the current fluctuations within the real-time diagrammatic technique in a given order of expansion can be found in Ref. [68]. By comparing the shot noise to the Poissonian noise S_P, one can obtain additional information about the statistics of tunneling processes which is not contained in the average current [70]. In particular, for $F < 1$, the shot noise is sub-Poissonian and its reduction is related to antibunching of tunneling events, which are correlated by the charging effects. On the other hand, when $F > 1$, the noise is super-Poissonian and is associated with some bunching mechanism, e.g., due to the Coulomb blockade [68,70].

We note that in order to perform the perturbation expansion, the coupling strength Γ is assumed to be the smallest energy scale in the problem. Therefore, the approximations made here allow us to study only the weak-coupling limit, while the higher-order correlations, such as those leading to the Kondo physics [71–73], are not captured. Nevertheless, the obtained results are reliable above the exponentially small Kondo temperature in a wide range of finite bias and gate voltage, which makes this analysis relevant for present and future experimental investigations of transport through multi-quantum-dot systems.

III. RESULTS AND DISCUSSION

In this section, we analyze the transport properties of the considered system for a set of parameters, allowing for the formation of one- and two-particle dark states in the TQD. We want to emphasize that there are several possible means to obtain dark states in such systems. An important factor is to distinguish one of the relevant quantum dots by detuning its parameters from the remaining two dots. For instance, this can be obtained by dot-j energy-level detuning $\varepsilon_j = \varepsilon \pm \Delta\varepsilon$, which was already considered [35]. Here, we follow the approach proposed by Pöltl *et al.* [33], where the formation of dark states is conditioned by an appropriate adjustment of Coulomb interactions, while the dots' energy levels are the same, $\varepsilon_j = \varepsilon$, and all the interdot hoppings are also equal. Experimentally, such a setup can be achieved by appropriate tuning of the dot's size and proper position arrangement.

The absolute value of the current in the parallel magnetic configuration with the corresponding differential conductance, as well as the sequential and total (sequential plus cotunneling) TMR, are shown in Fig. 2 as a function of the bias voltage V and the position of the dots' levels $\varepsilon_j = \varepsilon$. Since ε can be tuned experimentally by a gate voltage, this figure effectively presents the gate and bias voltage dependence of transport characteristics. Because a typical transport behavior of TQD systems is already relatively well known [29,31,74,75], we will mainly point out the differences due to the chosen set of parameters of the discussed model and especially focus on the effects related to the formation of dark states.

The triple quantum dot, as a multilevel system, is characterized by a relatively complex Coulomb diamond pattern. A first general observation is that, due to different Coulomb interactions relevant for the second dot ($j = 2$), which is
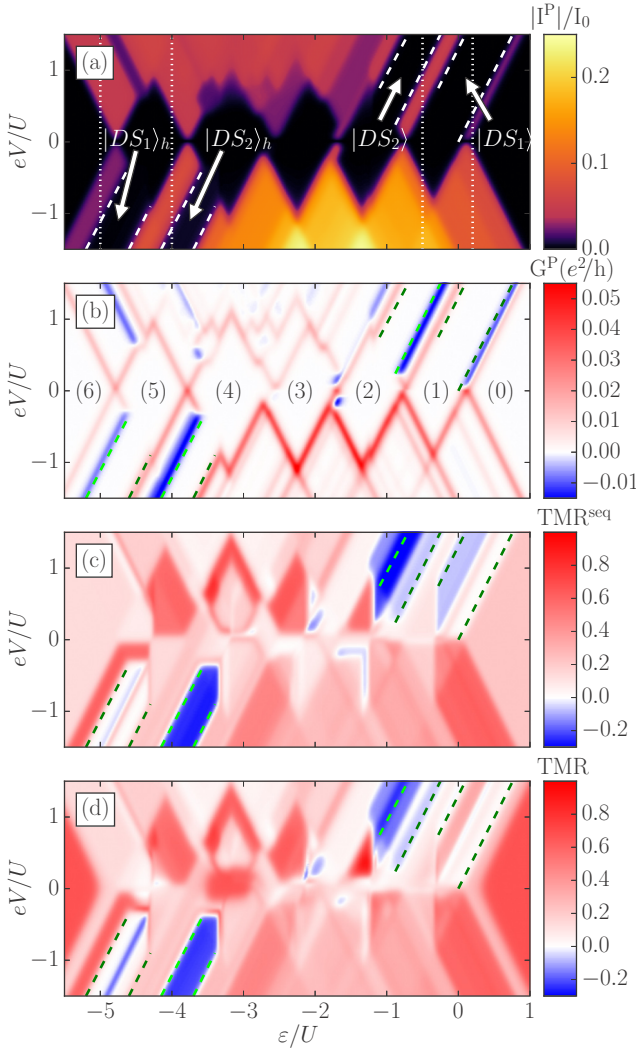
FIG. 2. (a) The absolute value of the current and (b) the differential conductance in the case of parallel configuration, (c) the sequential and (d) total (sequential plus cotunneling) TMR calculated as a function of bias voltage and the position of the dots' levels $\varepsilon_j = \varepsilon$. The parameters are $U_1 = U_2 = U_3 = U_{13} = U, U_{12} = U_{23} = U - \Delta$, where $\Delta = U/5$, $t = 0.1$, $\Gamma = 0.01$, $T = 0.03$ in units of $U \equiv 1$, and $p = 0.5$. The current is plotted in units of $I_0 = e\Gamma/\hbar$. The dotted vertical lines in (a) indicate the cross sections related with dark states discussed in further sections. Dashed lines together with arrows show the ranges of voltages where the current is blocked due to the formation of dark states. The numbers in brackets in (b) indicate the TQD total occupation number in consecutive Coulomb blockade regimes.

coupled to the right lead (cf. Fig. 1), the magnitude of the current is not the same in both directions with respect to the applied bias voltage [see Fig. 2(a)]. The current flowing in the positive bias voltage direction is significantly lower, contrary to the current flowing in the opposite direction. For low bias, the pattern exposes strong Coulomb blockade regimes with an easily distinguishable number of electrons occupying the TQD [see Fig. 2(b)].

Assuming that the hopping between the dots is much smaller than the corresponding inter- and intradot correlations, one can estimate the energies at which the occupation of TQD changes and there is a resonant peak in the linear conductance. In particular, for $\varepsilon \gtrsim 0$ ($\varepsilon \lesssim -5U + 2\Delta$), the TQD system is unoccupied (fully occupied with six electrons). When $-U + \Delta \lesssim \varepsilon \lesssim 0$ there is a single electron on the TQD, for $-2U + \Delta \lesssim \varepsilon \lesssim -U + \Delta$ there are two electrons on the triple dot, and for $-3U + 2\Delta \lesssim \varepsilon \lesssim -2U + \Delta$ the TQD is triply occupied. On the other hand, when $-4U + 2\Delta \lesssim \varepsilon \lesssim -3U + 2\Delta$ ($-5U + 2\Delta \lesssim \varepsilon \lesssim -4U + 2\Delta$), the TQD is occupied by four (five) electrons. The respective electron numbers are indicated in brackets in Fig. 2(b).

The most interesting features visible both in the current and the differential conductance are four extended regions of current blockades, where $I \approx 0$, outgoing from the one-, two-, four-, and five-electron Coulomb blockade regimes. The current is suppressed along the energy levels of formed dark states, as they enter the transport window, and strong negative differential conductance lines visible in Fig. 2(b) are the signatures of that transport phenomena. The presence of dark states also introduces a strong asymmetry in the bias dependence of the current, resulting in substantial rectifying properties of the system.

Two of these dark states are formed for TQD energy levels ε close to the Fermi energy ($\varepsilon = 0$) and are accessible by applying the bias voltage. The dots' occupation numbers in those dark states are respectively equal to 1 and 2. For the following discussion, we therefore label the corresponding states as one- and two-electron dark states: $|DS_1\rangle$ and $|DS_2\rangle$. On the other hand, the two blockades emerging for $\varepsilon \lesssim -4U + 2\Delta$ (see Fig. 2) are related to the formation of two- and one-hole dark states, $|DS_2\rangle_h$ and $|DS_1\rangle_h$, which are symmetric to the aforementioned electron dark states under the particle-hole transformation. The occupation number of the TQD in these states is equal to four and five electrons, respectively; however, it is more convenient to analyze the opposite-direction hole transport in those transport regimes. It is also important to notice that the electron dark states are formed for the opposite sign of the applied voltage bias, as compared to the hole dark states (see Fig. 2). A detailed description of these electron and hole dark states is the main content of the following sections.

In Fig. 2 we present the current and differential conductance only in the case of parallel magnetic configuration. The transport behavior is qualitatively very similar in the antiparallel configuration and the differences are well captured by the TMR, which is shown in Fig. 2(d). To elucidate the role of cotunneling in transport, in Fig. 2(c) we also show the TMR obtained using only the sequential tunneling processes. First of all, one can note that the TMR behavior within the dark state regimes is quite nontrivial. While for a wide range of bias and gate voltages, one observes a typical spin valve behavior with $|I^P| > |I^{AP}|$, resulting in TMR > 0 [57], this is not the case in the dark state regimes. It can be seen that within the one-electron and one-hole dark states, the TMR takes relatively small values in the sequential tunneling approximation and is strongly modified by cotunneling [cf. Figs. 2(c) and 2(d)], which can lead to a sign change of the TMR. On the other hand, both two-electron and two-hole dark state regions are characterized by large negative TMR, TMR ≈ -0.25, which

is much less affected by second-order processes. In fact, these two dark states generate the most significant regions of negative TMR in the system, which implies that, quite counterintuitively, the antiparallel current is exceeding the current flowing in the parallel configuration, $|I^P| < |I^{AP}|$. This behavior is explained in detail in the following sections. Finally, it is also important to note that cotunneling strongly modifies the TMR value for the empty (fully occupied) system, i.e., for low bias and $\varepsilon \gtrsim 0$ ($\varepsilon \lesssim -5U + 2\Delta$). In these transport regions the TMR reaches Julliere's value [66], which is due to the presence of only elastic cotunneling processes [56]. One then finds TMR $=$ TMR$^{\text{Jull}} = 2/3$ for the considered spin polarization $p = 0.5$.

A. One-electron dark state

In this section we analyze in greater detail the system's transport behavior for such gate voltages where the one-electron dark state $|DS_1\rangle$ is formed. Before proceeding with a discussion of distinct transport features, let us first make a comment regarding the choice of parameters. As already mentioned, to observe dark states it is crucial to introduce some asymmetry between the dots. In the present paper this is obtained by allowing for different Coulomb correlations between the dots. However, contrary to multielectron states, the one-electron states are not influenced by Coulomb correlations. Consequently, the assumed asymmetry in Coulomb interactions cannot result in breaking of the symmetry of electronic density distribution in the TQD in the one-electron regime. Therefore, in order to generate an appropriate dark state within the one-electron sector of the TQD Hamiltonian, we introduced a very small detuning to the hopping parameter between the first and third dot, $t_{13} = t - \delta t$, with $\delta t = 10^{-2}t$. This fine tuning of parameters suffices to find a dark state in the one-electron parameter space. We note that in an experimental setup, it is often of great difficulty to prepare such a complex system in perfect symmetry; consequently, it should be possible to satisfy the condition favoring the formation of dark states. We also notice that this small detuning does not affect the other dark states which form due to asymmetry introduced by the difference in corresponding Coulomb correlations.

The bias voltage dependence of the current, differential conductance and the Fano factor in both parallel and antiparallel magnetic configurations as well as the TMR is shown in Fig. 3. In the absence of applied voltage, the system's ground state is given by $|Q = 0, S_z = 0\rangle = |000\rangle$ and the TQD is empty. By increasing the positive bias voltage, $eV > 0$, the first one-electron state enters the transport window. It is the following spin doublet, $|Q = 1, S_z = \pm\frac{1}{2}\rangle = \sqrt{\frac{2}{3}}|0\sigma 0\rangle - \frac{1}{\sqrt{6}}(|\sigma 00\rangle + |00\sigma\rangle)$. This state is a superposition of a single electron delocalized over all three dots. It is important to note here that both the left and right leads are coupled to the dots with finite electron occupation. Therefore the current can flow through the system, and transport takes place by tunneling processes between the above-mentioned excited state $|Q = 1, S_z = \pm\frac{1}{2}\rangle$ and the empty TQD state. As a result, there is a peak in the current for $eV/U \approx 0.25$, i.e., for voltages at which the first excited state enters the transport window, preceded by an associated differential conductance peak [see Fig. 3(c)].
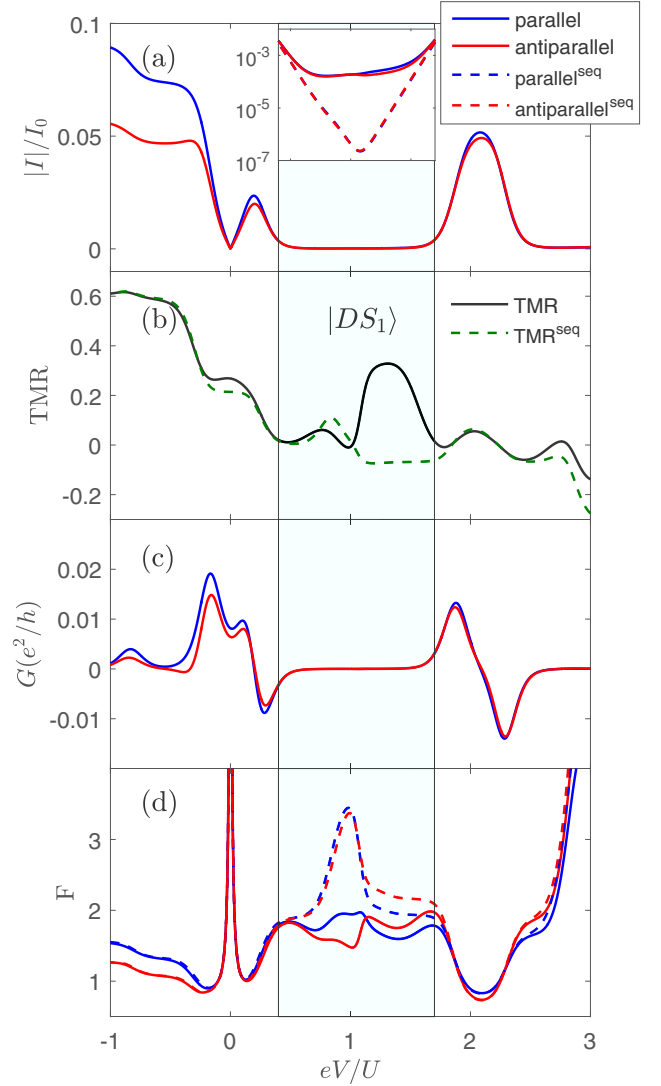

FIG. 3. The bias voltage dependence of (a) the current, (c) the differential conductance, and (d) the Fano factor in the parallel and antiparallel magnetic configurations as well as (b) the TMR in the transport regime where the one-electron dark state $|DS_1\rangle$ forms. The inset in (a) presents the closeup of the system's behavior in the dark state regime, where the sequential and total currents are shown on the logarithmic scale. The dashed (solid) lines correspond to sequential (sequential plus cotunneling) results. The dots' energy levels are $\varepsilon/U = 0.2$, while the other parameters are the same as in Fig. 2. Note that in order to obtain a one-electron dark state we introduced a small detuning in the hopping integral between the first and third dot, $t_{13} = t - \delta t$, with $\delta t = 10^{-2}t$.

Further increase of the applied bias voltage enables the next excited state to enter the transport window, which is, however, the following one-electron dark state doublet:

$$|DS_1\rangle = \left|Q = 1, S_z = \pm\frac{1}{2}\right\rangle_{DS} = \frac{1}{\sqrt{2}}(|\sigma 00\rangle - |00\sigma\rangle).$$

This state is dominating transport in a wide range of bias voltage, $0.4 \lesssim eV/U \lesssim 1.7$, resulting in a strong current suppression and negative differential conductance right before
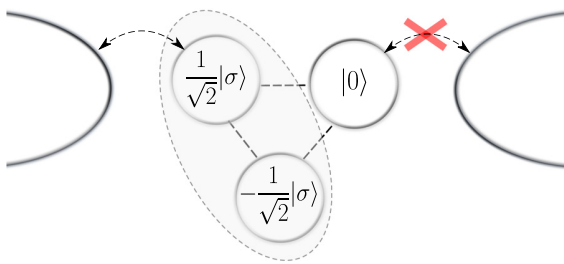
FIG. 4. Graphical representation of the one-electron dark state $|DS_1\rangle$. The electron density is distributed between dots 1 and 3, leaving dot 2 unoccupied and thus blocking the transport through the right junction.

the current plateau [see Figs. 3(a) and 3(c)]. The form of this dark state is as follows: The electron occupies evenly the first and third dots, while the amplitude on the second dot is equal to zero. As the electronic density is completely distributed between dots 1 and 3 (see Fig. 4 for a graphical representation of this dark state), the electron is not able to leave the system through the second dot and further tunnel to the right electrode coupled with that dot. It stays trapped in the TQD system, completely blocking the current. Only if the bias voltage is increased above $eV/U \gtrsim 1.7$ is the blockade lifted as more states enter the transport window.

One can see that the current dependence shows a similar behavior in both magnetic configurations, with generally higher absolute values in the parallel configuration compared to the antiparallel one. In the dark state region, when only sequential tunneling processes are included, TMR^{seq} is relatively low. Despite the leads' spin polarization the system stays in $|DS_1\rangle$ with equal probabilities of both spin components, and in both configurations the current has a similar value. When the system is empty, the tunneling of majority-spin electrons from the left lead is of higher probability. However, the occupation probabilities of both spin directions are balanced by the fact that the tunneling event in the opposing direction, from the TQD back into the left electrode, is also of higher probability for the electron with the spin zth component aligned with the left electrode spin polarization. Nevertheless, as can be clearly seen in the inset of Fig. 3(a), the sequential processes get exponentially suppressed in the dark state region, while the dominant contribution to the current comes from cotunneling, in which electrons can be transferred between the left and right leads through virtual states of the system. Thus, an accurate analysis of the system's spin-resolved transport behavior requires resorting to the second-order processes. One can see that cotunneling enhances the TMR in the dark-state region, which has a maximum around $eV/U \approx 1.3$, indicating that elastic processes are relevant for transport. In such processes the spin of the transferred electron is conserved, which tends to enhance the magnetoresistive properties of the device.

Let us now discuss the behavior of the Fano factor in the considered transport regime. Out of the blockade regime the Fano factor is generally sub-Poissonian due to the fact that the tunneling events are correlated by Coulomb correlations. In the low-bias range, the Fano factor becomes divergent since the current vanishes in the zero-voltage limit, while the noise is still finite due to thermal fluctuations. An interesting behavior

can be observed within the dark-state bias window, where a moderately enhanced super-Poissonian shot noise develops. When only the first-order processes are included, the Fano factor reaches values $F \gtrsim 3$ in both magnetic configurations [see Fig. 3(d)]. However, cotunneling processes reduce this value to $F \approx 2$ in whole blockade range, irrespective of magnetic configuration. The reduction of the shot noise due to cotunneling in the dark-state region is in agreement with numerical results obtained earlier for a similar system, but with nonmagnetic leads [35].

B. Two-electron dark state

When the position of the TQD's energy levels is lowered to $\varepsilon/U = -0.5$, the ground state of the system changes to the one-electron spin doublet state, $|Q=1, S_z = \pm\frac{1}{2}\rangle = \sqrt{\frac{2}{3}}|0\sigma 0\rangle - \frac{1}{\sqrt{6}}(|\sigma 00\rangle + |00\sigma\rangle)$. By applying the bias voltage in the positive direction, it is possible to reach a two-electron dark state, which is responsible for another strong current suppression. This can be seen in Fig. 5, which presents the corresponding transport behavior of the system. First, with increasing the bias voltage, for $eV/U \gtrsim 0.3$, the current exhibits the first Coulomb step associated with a two-electron state entering the transport window. However, around $eV/U \approx 1$, see Fig. 5(a), the current suddenly drops due to the following singlet dark state ($|DS_2\rangle = |Q=2, S_z=0\rangle_{DS}$),

$$|DS_2\rangle \approx \frac{1}{2}(|d00\rangle + |\uparrow 0 \downarrow\rangle - |\downarrow 0 \uparrow\rangle + |00d\rangle),$$

entering the transport window. The distribution of electronic density in this state has a similar feature to the one-electron dark state (cf. Fig. 4), i.e., the occupation of the second dot has a vanishing amplitude. Nonetheless, in the present case, there is a very small but finite amplitude on dot 2, allowing for a current leakage [see the inset of Fig. 5(a)]. The presence of dark state again results in a large negative differential conductance, clearly visible in Fig. 5(c).

On the other hand, the TMR is a very sensitive quantity that helps to identify nontrivial behavior within current blockades. One can see that the TMR behavior in the regime where the system is trapped in the state $|DS_2\rangle$ is different from the one-electron dark state ($|DS_1\rangle$) case. The TMR has a negative sign in almost the whole blockade regime, which also extends slightly above $eV/U \approx 2$, where the consecutive Coulomb step appears and the new states enter the transport window, allowing for current flow. The minimum in TMR is well below $TMR^{seq} \lesssim -0.3$ in the sequential approximation, with cotunneling slightly modifying this value to $TMR \approx -0.2$ [see Fig. 5(b)].

This particular magnetoresistive behavior can be understood by taking a closer look at the transport processes occurring in this regime. First of all, we note that the negative TMR is predicted in the sequential approximation and cotunneling only slightly modifies it.[1] Therefore, in order to identify the most

---

[1]Note that now the role of cotunneling is not that crucial as in the case of a one-electron dark state, since there is a small leakage current due to sequential tunneling processes resulting from extremely small but finite occupation of the second dot.
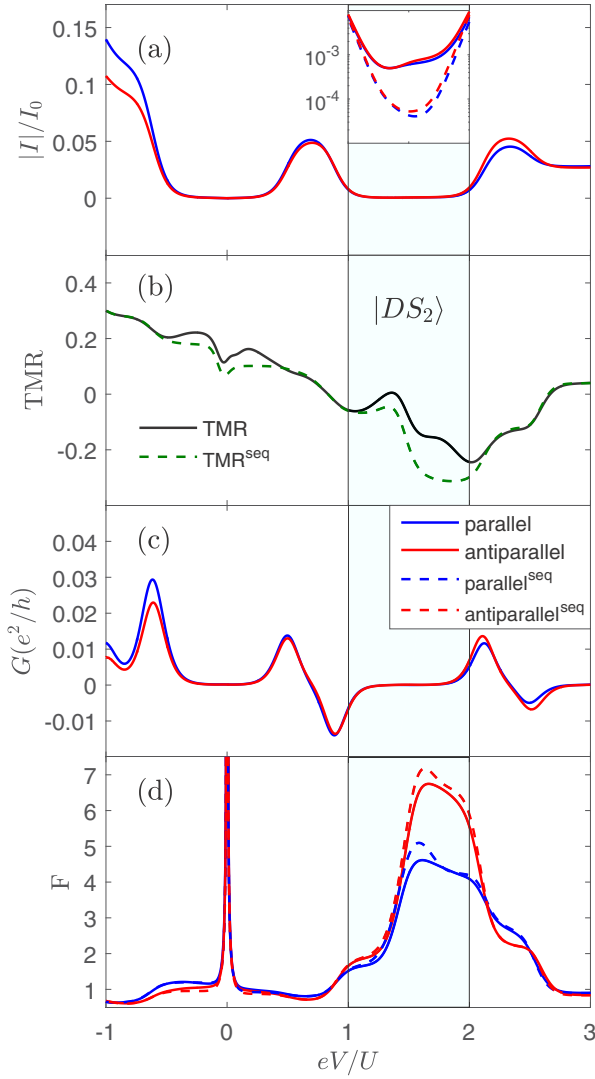
FIG. 5. The bias voltage dependence of (a) the current, (c) the differential conductance, and (d) the Fano factor in the parallel and antiparallel magnetic configurations as well as (b) the TMR in in the two-electron dark state $|DS_2\rangle$ transport regime. The parameters are the same as in Fig. 3 with $\varepsilon/U = -0.5$.

important processes for the effect of negative TMR, let us make a careful analysis of calculated quantities considering sequential tunneling. The most important factor in this case is how the reduced density matrices for both magnetic configurations vary between each other. In the case of parallel configuration, the occupation probability of $|DS_2\rangle$ is close to unity in whole bias range of the blockade, $p_{|DS_2\rangle} \to 1$. However, this is not the case for the antiparallel configuration, where with an increase of the bias voltage, there is another state, $|Q=2, S_z=\pm 1\rangle = \sqrt{\frac{7}{8}}|\sigma 0\sigma\rangle + \frac{1}{4}(|\sigma\sigma 0\rangle - |0\sigma\sigma\rangle)$, that starts to get small nonzero probability. It is a two-electron state, polarized in the same direction as the left electrode, with finite electron density on each quantum dot. We note that the occupation of the second dot is finite in this state, which eventually increases the current in the antiparallel configuration compared to the parallel one.

To find the reason for the difference in probability distributions, we need to consider and compare the dominating processes in both magnetic configurations. In the parallel configuration, when the system leaves the singlet dark state $|DS_2\rangle$ by removing one of the majority-spin electrons, which is a process of finite but very small probability, the TQD remains occupied by a minority-spin electron. The immediate consecutive tunneling event brings another majority-spin electron onto the TQD restoring $|DS_2\rangle$ dark state, such that the system remains trapped in this state for a relatively long time and, as a result, $p_{|DS_2\rangle} \to 1$. In the case of antiparallel configuration, a more complex tunneling sequence defines the dominating scenario. Now, the system leaves the two-electron dark state $|DS_2\rangle$ by tunneling of the electron with spin aligned along the polarization of the right lead; however, in the antiparallel configuration, this is the opposite spin direction to the magnetization of the left lead. This event leaves the TQD with the electron of spin aligned along the magnetization of the left electrode. Consecutive tunneling of another majority-spin electron from the left lead is now preferred, which results in a transition to the state $|Q=2, S_z=\pm 1\rangle$ instead of a transition to $|DS_2\rangle$, which was the case in the parallel configuration. In consequence, the probability of the state $|Q=2, S_z=\pm 1\rangle$ is enhanced, which results in a larger current in the antiparallel configuration compared to the parallel one [see Fig. 5(a)].

The difference in sequences of the most probable transport processes in both magnetic configurations is also visible in the behavior of the shot noise, which is shown in Fig. 5(d). One can see that now the shot noise is enhanced in the dark state region compared to the one-electron dark state case. Moreover, there is a large difference in the Fano factor in both magnetic alignments. The Fano factor reaches $F \approx 7$ in the antiparallel configuration and $F \approx 4$ in the case of parallel configuration. Note also that the influence of cotunneling on the shot noise is now much smaller compared to the case shown in Fig. 3(d), which is due to the reasons discussed above.

C. Two-hole dark state

The transport region with values of TQD's energy levels $\varepsilon/U \lesssim -4$ also displays nontrivial transport characteristics (see Fig. 2). The triple dot is then occupied with a relatively high number of electrons. There are two strong current blockades located on the opposite sign of applied bias voltage (compared to previously discussed cases), which, similarly, are formed due to the presence of the dark states. Moreover, the dark states in those regimes consist of four and five electrons trapped in the system.

Let us first discuss the transport regime where the TQD is occupied by five electrons in the absence of applied bias. The associated transport characteristics calculated for $\varepsilon/U = -4$ are presented in Fig. 6. The ground state of the system is then given by the following (unnormalized) doublet state: $|Q=5, S_z=\pm\frac{1}{2}\rangle = 2t(|\sigma dd\rangle + |dd\sigma\rangle) + (\sqrt{4\Delta^2 + 4t\Delta + 9t^2} - 2\Delta - t)|d\sigma d\rangle$. The first excited state, which is responsible for the first Coulomb step in the direction of negative bias voltage, is $|Q=4, S_z=0\rangle = \frac{1}{\sqrt{6}}(|0dd\rangle - |\uparrow d \downarrow\rangle + |\downarrow d \uparrow\rangle + |dd0\rangle) + \frac{1}{\sqrt{12}}(|d\uparrow\Downarrow\rangle + |\downarrow\uparrow d\rangle - |\uparrow\downarrow d\rangle - |d\downarrow\uparrow\rangle)$. It is a four-electron
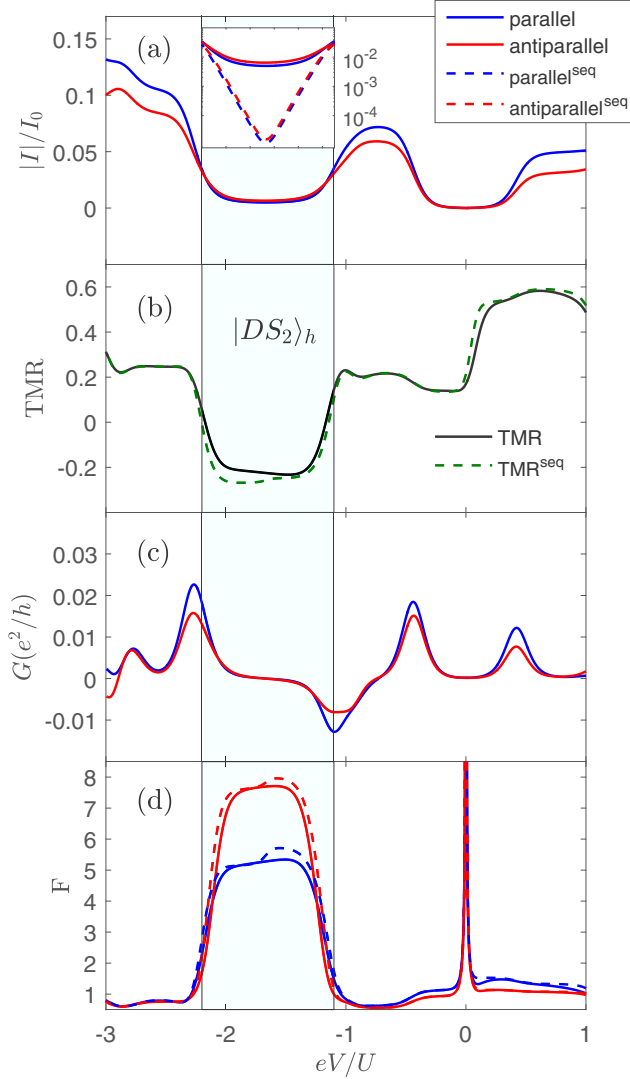
FIG. 6. The bias voltage dependence of (a) the current, (c) the differential conductance, and (d) the Fano factor in the parallel and antiparallel magnetic configurations, as well as (b) the TMR in the transport regime where the two-hole dark state $|DS_2\rangle_h$ occurs. The parameters are the same as in Fig. 3, with $\varepsilon/U = -4$.

state built of an eight-component linear combination of local occupation basis states, which allows for transport together with the five-electron ground state. The crucial factor for the charge transport to happen is that the state $|Q=4, S_z=0\rangle$ allows for transitions to the five-electron state by means of the tunneling process of an electron from the right lead onto the TQD. Such processes can happen when the second dot coupled to the right electrode is not fully occupied in the considered state. This is, however, not the case for the next state, which enters the transport window with further increase of the bias voltage. This state results in the current blockade, which appears for negative bias voltage in the range of $-2.2 \lesssim eV/U \lesssim -1.2$ [see Fig. 6(a)]. The explicit form of this four-electron singlet dark state ($|DS_2\rangle_h = |Q=4, S_z=0\rangle_{DS}$)

is the following:

$$|DS_2\rangle_h \approx \frac{1}{2}(|\downarrow d\uparrow\rangle - |\downarrow d\uparrow\rangle - |dd0\rangle + |0dd\rangle). \quad (13)$$

In this case, when the system is trapped in state $|DS_2\rangle_h$, the possibility of transition to the five-electron state is blocked. Each of the components building this state contains a fully occupied second dot; therefore tunneling of the electron from the lead through the right junction is prohibited. In order to leave this state, the electron has to either tunnel from the TQD through the left junction, however the three-electron states are above the transport window, or tunnel back through the right lead, which is an event of very low probability. Consequently, the system becomes trapped in the two-hole dark state $|DS_2\rangle_h$ and the current blockade develops.

It is convenient and more intuitive to analyze the transport properties in this regime when the TQD states are considered in the hole basis ($h-basis$). With the following electron-hole transformation of local dot's states, $|0\rangle \rightarrow |d\rangle_h$, $|\sigma\rangle \rightarrow |\bar{\sigma}\rangle_h$, and $|d\rangle \rightarrow |0\rangle_h$, we can rewrite $|DS_2\rangle_h$ as

$$|DS_2\rangle_h \approx \frac{1}{2}(|\uparrow 0\downarrow\rangle_h - |\downarrow 0\uparrow\rangle_h - |00d\rangle_h + |d00\rangle_h). \quad (14)$$

Now, the blockade can be understood as the effect of negative interference forming a two-hole dark state, where the second dot is completely unoccupied by holes (doubly occupied by electrons). Then, the second dot is effectively decoupled from the right lead and the hole transport through this junction is suppressed.

Because the structure of the two-hole dark state is quite similar to the two-electron dark state, the transport behavior is qualitatively similar in the two cases, cf. Figs. 5 and 6. First of all, the range of the bias voltage where the dark state dominates transport is of comparable size. Moreover, the behavior of the TMR is also qualitatively similar, i.e., in the whole range of bias where the current is suppressed the TMR has negative values, TMR ≈ -0.2 [see Fig. 6(b)]. The mechanism leading to such behavior is the same as in the case analyzed in Sec. III B. The enhanced Fano factor in the dark state regime reaches $F \approx 8$ in the antiparallel configuration and is reduced to $F \approx 5$ in the case of parallel configuration. A subtle difference when comparing the Fano factor behavior in the case of dark states $|DS_2\rangle$ and $|DS_2\rangle_h$ is that for the latter case the strongly enhanced value is present in the whole range of the current blockade. This is contrary to the two-electron dark state case, where there is a small range of bias voltage in the blockade with significantly lower values of the Fano factor, $F \approx 2$, coincidental with TMR ≈ 0.

D. One-hole dark state

Finally, in this section we discuss the transport regime where one-hole dark states are formed. To realize such a situation, we set the TQD energy levels to $\varepsilon/U = -5$, so that for zero bias the system is fully occupied and the ground state is $|Q=6, S_z=0\rangle = |ddd\rangle$. The corresponding transport characteristics are displayed in Fig. 7. When applying the negative bias voltage, the system starts to conduct the current around $eV/U \approx -0.4$ and then, for larger voltages, there is a wide blockade for $-2.2 \lesssim eV/U \lesssim -1.2$ [see Fig. 7(a)]. The dark state responsible for this current suppression is
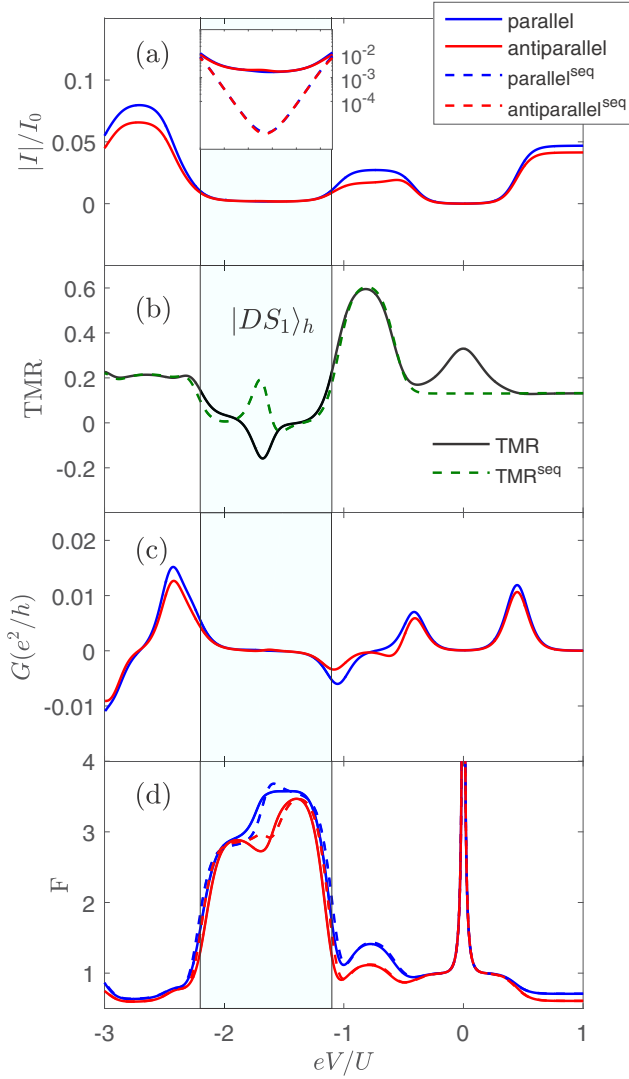
FIG. 7. The bias voltage dependence of (a) the current, (c) the differential conductance, and (d) the Fano factor in the parallel and antiparallel magnetic configurations, as well as (b) the TMR in in the one-hole dark state $|DS_1\rangle_h$ transport regime. The parameters are the same as in Fig. 3 with $\varepsilon/U = -5$.

the following doublet state: $|DS_1\rangle_h = |Q=5, S_z = \pm\frac{1}{2}\rangle_{DS} = \frac{1}{\sqrt{2}}(|\sigma dd\rangle - |dd\sigma\rangle)$. Similarly to the previous case of a two-hole dark state, we again see that the second dot is fully occupied by two electrons. This configuration blocks the electron flow through the right junction onto the TQD, which is the promoted direction by the applied bias. The tunneling processes through the left junction are now also energetically very unfavorable and, as a result, the system remains trapped in the dark state $|DS_1\rangle_h$ blocking the current. The discussed dark state can be also conveniently written in the hole basis as

$$|DS_1\rangle_h = \frac{1}{\sqrt{2}}(|\sigma 00\rangle_h - |00\sigma\rangle_h). \qquad (15)$$

It can be now clearly seen that the above one-hole dark state has a similar form to $|DS_1\rangle$ discussed in Sec. III A (see also

Fig. 4). Consequently, we find that the blocking mechanism and interference effects are analogous in the two cases, with the difference that the holes are considered instead of the electrons.

The TMR behavior in the current blockade regime also has some similarities to the case of the $|DS_1\rangle$ dark state. In both cases the current obtained within the sequential tunneling approximation is relatively low and the transport behavior is predominantly determined by cotunneling processes. Furthermore, in the case of a one-hole dark state, cotunneling results in a sign change of the TMR in the middle of the blockade, where the first-order processes resulted in a maximum [see Fig. 7(b)]. This clearly confirms that the second-order processes are important and dominate in this transport regime. Moreover, these processes strongly enhance the current in the antiparallel configuration. However, the region of negative TMR is now significantly smaller than those predicted in the case of current blockades caused by the formation of two-particle dark states $|DS_2\rangle$ and $|DS_2\rangle_h$. Finally, one can also see that the Fano factor is consistently enhanced in the $|DS_1\rangle_h$ dark state regime, reaching $F \approx 3.5$ in both magnetic configurations [see Fig. 7(d)].

IV. CONCLUSIONS

In this paper we have studied the influence of dark states on the spin-resolved transport properties of a triple quantum dot molecule attached to ferromagnetic contacts. The considerations were performed by using the real-time diagrammatic method and considering both sequential and cotunneling processes. By optimizing the system parameters, we have shown that the current flowing through the device can be blocked due to the coherent population trapping in a dark state. We have analyzed the transport behavior in the case of various dark states in the system, including one- and two-particle (either electron or hole) dark states. In all those cases we have shown that transport is mainly determined by cotunneling processes which result in a great modification of the magnetoresistive properties of the system. In particular, we have demonstrated that the interplay of spin-polarized transport with two-particle dark states can lead to negative tunnel magnetoresistance. Moreover, we have found super-Poissonian shot noise in the current blockade regimes, which can be additionally enhanced by spin dependence of tunneling processes. Finally, we have also indicated that the dark states with high number of electrons can be conveniently understood and analyzed as states formed by interference of holes, and the resulting transport characteristics can be discussed within the hole current framework. In this respect, we have also emphasized some similarities between the transport regions with the electron and hole dark states containing the same numbers of particles.
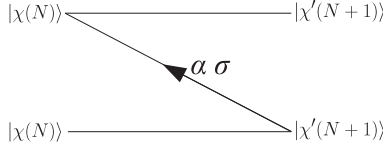
APPENDIX: DETAILS OF CALCULATIONS

In this Appendix we present the details of the performed calculations with the aid of the real-time diagrammatic technique

approach. In order to solve the kinetic equation (5) and obtain the density matrix elements, one has to find the self-energies $\Sigma_{\chi\chi'}$ which are related to the elements of matrix **W** through $\Sigma_{\chi\chi'} = iW_{\chi'\chi}$. The most difficult part of the calculations is to evaluate all irreducible, topologically different diagrams describing tunneling processes, which can be done with the aid of the diagrammatic rules [65,67]. Because in this paper we studied the effects of sequential tunneling and cotunneling, one needs to determine the self-energies up to the second order of perturbation expansion in the tunnel coupling Γ. In practice, it is necessary to consider all the diagrams containing one and two tunneling lines. Below, we present exemplary contributions from the first- and second-order diagrams, as well as their contributions to one specific self-energy.

1. First-order diagrams

The first-order diagrams involve a single tunneling line. Below, we show a diagram contributing to the following first-order self-energy $\Sigma^{(1)}_{\chi(N)\chi'(N+1)}$:

$$= (-1)^1 \sum_j \int d\omega \frac{\gamma_{\alpha\sigma}(\omega)}{\omega - \varepsilon_{\chi'} + \varepsilon_\chi + i\eta} |\langle\chi'|d^\dagger_{j\sigma}|\chi\rangle|^2,$$

where $\gamma_{\alpha\sigma} = \frac{\Gamma^\sigma_\alpha}{2\pi} f_\alpha(\omega)$ is a factor associated with each tunneling line, $f_\alpha(\omega)$ is the Fermi-Dirac distribution of lead α, and $\eta = 0^+$. This diagram corresponds to an electron with spin σ tunneling from the lead α, between $|\chi(N)\rangle$ and $|\chi'(N+1)\rangle$ states, where N indicates total occupation number $N = \sum_{j\sigma} n_{j\sigma}$.

When all the topologically different first-order diagrams are evaluated, the respective self-energies can be determined. In particular, the self-energy $\Sigma^{(1)}_{\chi(N)\chi'(N+1)}$ is given by

$$\Sigma^{(1)}_{\chi(N)\chi'(N+1)} = 2\pi i \sum_{\alpha\sigma} \sum_j \gamma_{\alpha\sigma}(\varepsilon_{\chi'} - \varepsilon_\chi)|\langle\chi'|d^\dagger_{j\sigma}|\chi\rangle|^2.$$

2. Second-order diagrams

The second-order diagrams involve two tunneling lines. Here, as an example we present a contribution from a diagram that contributes to the second-order self-energy $\Sigma^{(2)}_{\chi(N)\chi'(N+2)}$ due to two tunneling events of electrons with spins σ, σ',

tunneling from the leads α, α'. It is given by

$$= (-1)^3 \sum_{\chi''\chi'''} \sum_{jj'} \iint d\omega_1 d\omega_2 \frac{\gamma_{\alpha\sigma}(\omega_1)}{-\omega_1 - \varepsilon_\chi + \varepsilon_{\chi'''} + i\eta}$$

$$\times \frac{\gamma_{\alpha'\sigma'}(\omega_2)}{-\omega_1 + \omega_2 - \varepsilon_{\chi''} + \varepsilon_{\chi'''} + i\eta} \frac{1}{\omega_2 - \varepsilon_{\chi'} + \varepsilon_{\chi'''} + i\eta}$$

$$\times \langle\chi|d_{j\sigma}|\chi'''\rangle\langle\chi'''|d_{j'\sigma'}|\chi'\rangle\langle\chi'|d^\dagger_{j\sigma}|\chi''\rangle\langle\chi''|d^\dagger_{j'\sigma'}|\chi\rangle.$$

An important step simplifying the calculations is to use the mirror rule. By reflecting any diagram horizontally and changing directions of all tunneling lines, one obtains the contribution which is an opposite sign complex conjugate of the initial diagram. The pairs of such symmetric diagrams contribute only with summed imaginary parts, while the real parts cancel out. The integrations in the above formula can be performed analytically by using the Cauchy's principal value theorem and realizing that integrals of the form

$$F^\gamma_{\alpha\sigma} = \int_{-\infty}^\infty d\omega \frac{\gamma_{\alpha\sigma}(\omega)}{(\omega - \varepsilon + i\eta)^\gamma}$$

can be evaluated using the digamma function and its derivatives.

Finally, all contributions to the second-order self-energy $\Sigma^{(2)}_{\chi(N)\chi'(N+2)}$ can be graphically represented as a sum of the following diagrams:

---
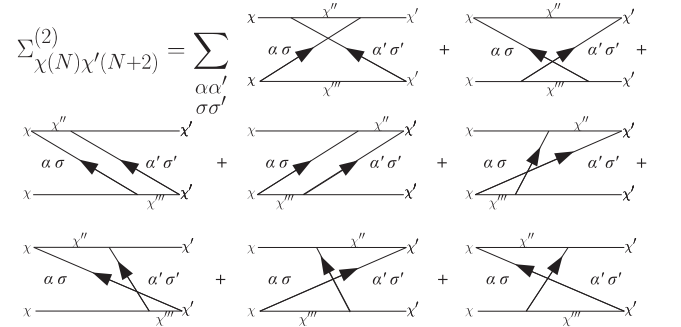
[1] D. G. Austing, L. P. Kouwenhoven, and S. Tarucha, Few-electron quantum dots, Rep. Prog. Phys. **64**, 701 (2001).

[2] S. M. Reimann and M. Manninen, Electronic structure of quantum dots, Rev. Mod. Phys. **74**, 1283 (2002).

[3] A. Barenco, D. Deutsch, A. Ekert, and R. Jozsa, Conditional Quantum Dynamics and Logic Gates, Phys. Rev. Lett. **74**, 4083 (1995).

[4] J. A. Brum and P. Hawrylak, Coupled quantum dots as quantum exclusive-OR gate, Superlatt. Microstruct. **22**, 431 (1997).

[5] D. Loss and D. P. DiVincenzo, Quantum computation with quantum dots, Phys. Rev. A **57**, 120 (1998).

[6] L. P. Kouwenhoven, L. L. Sohn, and G. Schön, *Mesoscopic Electron Transport* (Springer, Netherlands, 1997).

[7] S. Andergassen, V. Meden, H. Schoeller, J. Splettstoesser, and M. R. Wegewijs, Charge transport through single molecules, quantum dots and quantum wires, Nanotechnology **21**, 272001 (2010).

[8] T. Kuzmenko, K. Kikoin, and Y. Avishai, Towards two-channel Kondo effect in triple quantum dot, Europhys. Lett. **64**, 218 (2003).

[9] R. Žitko, J. Bonča, A. Ramšak, and T. Rejec, Kondo effect in triple quantum dots, Phys. Rev. B **73**, 153307 (2006).

[10] T. Numata, Y. Nisikawa, A. Oguri, and A. C. Hewson, Kondo effects in a triangular triple quantum dot: Numerical renormalization group study in the whole region of the electron filling, Phys. Rev. B **80**, 155330 (2009).

[11] R. López, T. Rejec, J. Martinek, and R. Žitko, SU(3) Kondo effect in spinless triple quantum dots, Phys. Rev. B **87**, 035135 (2013).

[12] M. Korkusinski, I. P. Gimenez, P. Hawrylak, L. Gaudreau, S. A. Studenikin, and A. S. Sachrajda, Topological Hunds rules and the electronic properties of a triple lateral quantum dot molecule, Phys. Rev. B **75**, 115301 (2007).

[13] S. Amaha, W. Izumida, T. Hatano, S. Teraoka, S. Tarucha, J. A. Gupta, and D. G. Austing, Two- and Three-Electron Pauli Spin Blockade in Series-Coupled Triple Quantum Dots, Phys. Rev. Lett. **110**, 016803 (2013).

[14] R. Sánchez, G. Granger, L. Gaudreau, A. Kam, M. Pioro-Ladrière, S. A. Studenikin, P. Zawadzki, A. S. Sachrajda, and G. Platero, Long-Range Spin Transfer in Triple Quantum Dots, Phys. Rev. Lett. **112**, 176803 (2014).

[15] Y. X. Cheng, Y. D. Wang, J. H. Wei, Z. G. Zhu, and Y. J. Yan, Long-range exchange interaction in triple quantum dots in the Kondo regime, Phys. Rev. B **95**, 155417 (2017).

[16] S. Głodzik, K. P. Wójcik, I. Weymann, and T. Domański, Interplay between electron pairing and Dicke effect in triple quantum dot structures, Phys. Rev. B **95**, 125419 (2017).

[17] L.-L. Zhang and W.-J. Gong, Transport properties in a non-Hermitian triple-quantum-dot structure, Phys. Rev. A **95**, 062123 (2017).

[18] E. A. Laird, J. M. Taylor, D. P. DiVincenzo, C. M. Marcus, M. P. Hanson, and A. C. Gossard, Coherent spin manipulation in an exchange-only qubit, Phys. Rev. B **82**, 075403 (2010).

[19] L. Gaudreau, G. Granger, A. Kam, G. C. Aers, S. A. Studenikin, P. Zawadzki, M. Pioro-Ladriere, Z. R. Wasilewski, and A. S. Sachrajda, Coherent control of three-spin states in a triple quantum dot, Nat. Phys. **8**, 54 (2012).

[20] J. Łuczak and B. R. Bułka, Readout and dynamics of a qubit built on three quantum dots, Phys. Rev. B **90**, 165427 (2014).

[21] J. Łuczak and B.R. Bułka, Landau-Zener transitions in spin qubit encoded in three quantum dots, Quantum Inf. Process. **16**, 10 (2017).

[22] M. Russ and G. Burkard, Three-electron spin qubits, J. Phys.: Condens. Matter **29**, 393001 (2017).

[23] G. Fülöp, F. Domínguez, S. d'Hollosy, A. Baumgartner, P. Makk, M. H. Madsen, V. A. Guzenko, J. Nygård, C. Schönenberger, A. Levy Yeyati, and S. Csonka, Magnetic Field Tuning and Quantum Interference in a Cooper Pair Splitter, Phys. Rev. Lett. **115**, 227003 (2015).

[24] F. Domínguez and A. L. Yeyati, Quantum interference in a Cooper pair splitter: The three sites model, Phys. E (Amsterdam, Neth.) **75**, 322 (2016).

[25] L. Gaudreau, S. A. Studenikin, A. S. Sachrajda, P. Zawadzki, A. Kam, J. Lapointe, M. Korkusinski, and P. Hawrylak, Stability Diagram of a Few-Electron Triple Dot, Phys. Rev. Lett. **97**, 036807 (2006).

[26] S. Amaha, T. Hatano, T. Kubo, Y. Tokura, D. Guy Austing, and S. Tarucha, Fabrication and characterization of a laterally coupled vertical triple quantum dot device, Phys. E (Amsterdam, Neth.) **40**, 1322 (2008).

[27] A. K. Mitchell, T. F. Jarrold, and D. E. Logan, Quantum phase transition in quantum dot trimers, Phys. Rev. B **79**, 085124 (2009).

[28] B. R. Bułka, T. Kostyrko, and J. Łuczak, Linear and nonlinear Stark effect in a triangular molecule, Phys. Rev. B **83**, 035301 (2011).

[29] C.-Y. Hsieh, Y.-P. Shim, M. Korkusinski, and P. Hawrylak, Physics of lateral triple quantum-dot molecules with controlled electron numbers, Rep. Prog. Phys. **75**, 114501 (2012).

[30] M. Seo, H. K. Choi, S.-Y. Lee, N. Kim, Y. Chung, H.-S. Sim, V. Umansky, and D. Mahalu, Charge Frustration in a Triangular Triple Quantum Dot, Phys. Rev. Lett. **110**, 046803 (2013).

[31] K. Wrześniewski and I. Weymann, Spin effects in transport through triangular quantum dot molecule in different geometrical configurations, Phys. Rev. B **92**, 045407 (2015).

[32] C. Emary, Dark states in the magnetotransport through triple quantum dots, Phys. Rev. B **76**, 245319 (2007).

[33] C. Pöltl, C. Emary, and T. Brandes, Two-particle dark state in the transport through a triple quantum dot, Phys. Rev. B **80**, 115313 (2009).

[34] T. Kostyrko and B. R. Bułka, Symmetry-controlled negative differential resistance effect in a triangular molecule, Phys. Rev. B **79**, 075310 (2009).

[35] I. Weymann, B. R. Bułka, and J. Barnaś, Dark states in transport through triple quantum dots: The role of cotunneling, Phys. Rev. B **83**, 195302 (2011).

[36] Y. Kubo, Turn to the dark side, Nat. Phys. **12**, 21 (2016).

[37] M. Niklas, A. Trottmann, A. Donarini, and M. Grifoni, Fano stability diagram of a symmetric triple quantum dot, Phys. Rev. B **95**, 115133 (2017).

[38] R. M. Whitley and C. R. Stroud, Double optical resonance, Phys. Rev. A **14**, 1498 (1976).

[39] K.-J. Boller, A. Imamoğlu, and S. E. Harris, Observation of Electromagnetically Induced Transparency, Phys. Rev. Lett. **66**, 2593 (1991).

[40] M. Fleischhauer, A. Imamoglu, and J. P. Marangos, Electromagnetically induced transparency: Optics in coherent media, Rev. Mod. Phys. **77**, 633 (2005).

[41] K. Xia, R. Kolesov, Y. Wang, P. Siyushev, R. Reuter, T. Kornher, N. Kukharchyk, A. D. Wieck, B. Villa, S. Yang, and J. Wrachtrup, All-Optical Preparation of Coherent Dark States of a Single Rare Earth Ion Spin in a Crystal, Phys. Rev. Lett. **115**, 093602 (2015).

[42] B. Michaelis, C. Emary, and C. W. J. Beenakker, All-electronic coherent population trapping in quantum dots, Europhys. Lett. **73**, 677 (2006).

[43] M. Bayer, Coherent population trapping: Quantum optics with dots, Nat. Phys. **4**, 678 (2008).

[44] C. Pöltl, C. Emary, and T. Brandes, Spin-entangled two-particle dark state in quantum transport through coupled quantum dots, Phys. Rev. B **87**, 045416 (2013).

[45] E. Aharon, R. Pozner, E. Lifshitz, and U. Peskin, Multi-bit dark state memory: Double quantum dot as an electronic quantum memory, J. Appl. Phys. **120**, 244301 (2016).

70

[46] K. Ono, D. G. Austing, Y. Tokura, and S. Tarucha, Current rectification by Pauli exclusion in a weakly coupled double quantum dot system, Science **297**, 1313 (2002).

[47] J. Fransson and M. Råsander, Pauli spin blockade in weakly coupled double quantum dots, Phys. Rev. B **73**, 205333 (2006).

[48] M. Busl, G. Granger, L. Gaudreau, R. Sanchez, A. Kam, M. Pioro-Ladriere, S. A. Studenikin, P. Zawadzki, Z. R. Wasilewski, A. S. Sachrajda, and G. Platero, Bipolar spin blockade and coherent state superpositions in a triple quantum dot, Nat. Nano **8**, 261 (2013).

[49] A. Noiri, T. Takakura, T. Obata, T. Otsuka, T. Nakajima, J. Yoneda, and S. Tarucha, Cotunneling spin blockade observed in a three-terminal triple quantum dot, Phys. Rev. B **96**, 155414 (2017).

[50] R. Leturcq, C. Stampfer, K. Inderbitzin, L. Durrer, C. Hierold, E. Mariani, M. G. Schultz, F. von Oppen, and K. Ensslin, Franck-Condon blockade in suspended carbon nanotube quantum dots, Nat. Phys. **5**, 327 (2009).

[51] T. Kuzmenko, K. Kikoin, and Y. Avishai, Magnetically Tunable Kondo-Sharonov-Bohm Effect in a Triangular Quantum Dot, Phys. Rev. Lett. **96**, 046601 (2006).

[52] David D. Awschalom, Lee C. Bassett, Andrew S. Dzurak, Evelyn L. Hu, and Jason R. Petta, Quantum spintronics: engineering and manipulating atom-like spins in semiconductors, Science **339**, 1174 (2013).

[53] Igor Žutić, Jaroslav Fabian, and S. Das Sarma, Spintronics: Fundamentals and applications, Rev. Mod. Phys. **76**, 323 (2004).

[54] R. Hanson, L. P. Kouwenhoven, J. R. Petta, S. Tarucha, and L. M. K. Vandersypen, Spins in few-electron quantum dots, Rev. Mod. Phys. **79**, 1217 (2007).

[55] J. Barnaś and A. Fert, Magnetoresistance Oscillations Due to Charging Effects in Double Ferromagnetic Tunnel Junctions, Phys. Rev. Lett. **80**, 1058 (1998).

[56] I. Weymann, J. König, J. Martinek, J. Barnaś, and G. Schön, Tunnel magnetoresistance of quantum dots coupled to ferromagnetic leads in the sequential and cotunneling regimes, Phys. Rev. B **72**, 115334 (2005).

[57] J. Barnaś and I. Weymann, Spin effects in single-electron tunnelling, J. Phys.: Condens. Matter **20**, 423202 (2008).

[58] J. Martinek, Y. Utsumi, H. Imamura, J. Barnaś, S. Maekawa, J. König, and G. Schön, Kondo effect in Quantum Dots Coupled to Ferromagnetic Leads, Phys. Rev. Lett. **91**, 127203 (2003).

[59] M. Gaass, A. K. Hüttel, K. Kang, I. Weymann, J. von Delft, and Ch. Strunk, Universality of the Kondo Effect in Quantum Dots with Ferromagnetic Leads, Phys. Rev. Lett. **107**, 176808 (2011).

[60] I. Weymann and P. Trocha, Superconducting proximity effect and zero-bias anomaly in transport through quantum dots weakly attached to ferromagnetic leads, Phys. Rev. B **89**, 115305 (2014).

[61] K. Wrześniewski, P. Trocha, and I. Weymann, Current cross-correlations in double quantum dot based Cooper pair splitters with ferromagnetic leads, J. Phys.: Condens. Matter **29**, 195302 (2017).

[62] R. Świrkowicz, M. Wierzbicki, and J. Barnaś, Thermoelectric effects in transport through quantum dots attached to ferromagnetic leads with noncollinear magnetic moments, Phys. Rev. B **80**, 195409 (2009).

[63] I. Weymann and J. Barnaś, Spin thermoelectric effects in Kondo quantum dots coupled to ferromagnetic leads, Phys. Rev. B **88**, 085313 (2013).

[64] Ł. Karwacki and P. Trocha, Spin-dependent thermoelectric effects in a strongly correlated double quantum dot, Phys. Rev. B **94**, 085418 (2016).

[65] H. Schoeller and G. Schön, Mesoscopic quantum transport: Resonant tunneling in the presence of a strong Coulomb interaction, Phys. Rev. B **50**, 18436 (1994).

[66] M. Julliere, Tunneling between ferromagnetic films, Phys. Lett. A **54**, 225 (1975).

[67] J. König, J. Schmid, H. Schoeller, and G. Schön, Resonant tunneling through ultrasmall quantum dots: Zero-bias anomalies, magnetic-field dependence, and boson-assisted transport, Phys. Rev. B **54**, 16820 (1996).

[68] A. Thielmann, M. H. Hettler, J. König, and G. Schön, Cotunneling Current and Shot Noise in Quantum Dots, Phys. Rev. Lett. **95**, 146806 (2005).

[69] I. Weymann, Effects of different geometries on the conductance, shot noise, and tunnel magnetoresistance of double quantum dots, Phys. Rev. B **78**, 045310 (2008).

[70] Y. M. Blanter and M. Büttiker, Shot noise in mesoscopic conductors, Phys. Rep. **336**, 1 (2000).

[71] J. Kondo, Resistance minimum in dilute magnetic alloys, Prog. Theor. Phys. **32**, 37 (1964).

[72] D. Goldhaber-Gordon, H. Shtrikman, D. Mahalu, D. Abusch-Magder, U. Meirav, and M. A. Kastner, The Kondo effect in a single-electron transistor, Nature (London) **391**, 156 (1998).

[73] A. C. Hewson, *The Kondo Problem to Heavy Fermions* (Cambridge University Press, Cambridge, 1997).

[74] M. C. Rogge and R. J. Haug, Two-path transport measurements on a triple quantum dot, Phys. Rev. B **77**, 193306 (2008).

[75] G. Granger, L. Gaudreau, A. Kam, M. Pioro-Ladrière, S. A. Studenikin, Z. R. Wasilewski, P. Zawadzki, and A. S. Sachrajda, Three-dimensional transport diagram of a triple quantum dot, Phys. Rev. B **82**, 075304 (2010).

71

Current cross-correlations in double quantum dot based Cooper pair splitters with ferromagnetic leads

Kacper Wrześniewski, Piotr Trocha and Ireneusz Weymann

Faculty of Physics, Adam Mickiewicz University, 61-614 Poznań, Poland

E-mail: wrzesniewski@amu.edu.pl

Abstract

We investigate the current cross-correlations in a double quantum dot based Cooper pair splitter coupled to one superconducting and two ferromagnetic electrodes. The analysis is performed by assuming a weak coupling between the double dot and ferromagnetic leads, while the coupling to the superconductor is arbitrary. Employing the perturbative real-time diagrammatic technique, we study the Andreev transport properties of the device, focusing on the Andreev current cross-correlations, for various parameters of the model, both in the linear and nonlinear response regimes. Depending on parameters and transport regime, we find both positive and negative current cross-correlations. Enhancement of the former type of cross-correlations indicates transport regimes, in which the device works with high Cooper pair splitting efficiency, contrary to the latter type of correlations, which imply negative influence on the splitting. The processes and mechanisms leading to both types of current cross-correlations are thoroughly examined and discussed, giving a detailed insight into the Andreev transport properties of the considered device.

Keywords: quantum dots, Andreev transport, Cooper pair splitter, current cross-correlations

(Some figures may appear in colour only in the online journal)

1. Introduction

Multiterminal quantum dots coupled to superconducting and normal metal leads have recently been under extensive experimental and theoretical research [1–18]. One of very promising applications of such hybrid systems is the possibility to realize a Cooper pair splitter (CPS) [19–30]. In Cooper pair splitting devices the electrons forming a Cooper pair tunnel from superconductor into two separate normal leads, while the tunability of quantum dots embedded in the arms of a CPS enables controlling of the splitting process [20–22]. Cooper pair splitting is most efficient when the applied bias voltage is smaller than the superconducting energy gap Δ, such that transport occurs only through Andreev reflection processes [31]. In fact, the subgap transport properties are determined by the Andreev bound states (ABS) induced by the superconducting proximity effect inside the superconducting energy gap. Such bound states, also referred to as Yu–Shiba–Rusinov

states [32], have recently been investigated by performing the bias spectroscopy experiments [33–36].

The transport properties of hybrid quantum dot systems in the subgap regime with weak coupling to normal leads have already been a subject of extensive theoretical investigations [37–44]. The current flowing through the system inside the superconducting energy gap is dominated by Andreev processes: crossed Andreev reflection (CAR) and direct Andreev reflection (DAR). The former processes take place when split electrons reach two separate normal leads, while the latter ones happen when both electrons enter the same lead. For the realization of an efficient CPS, it is therefore desirable to have dominant CAR processes in the system. Quantifying the relative magnitude of both processes is however not straightforward. It can be done in quantum dot based CPS's with ferromagnetic contacts, in which by varying the magnetic configuration of ferromagnetic leads between the parallel and antiparallel alignment, one can infer the knowledge about the
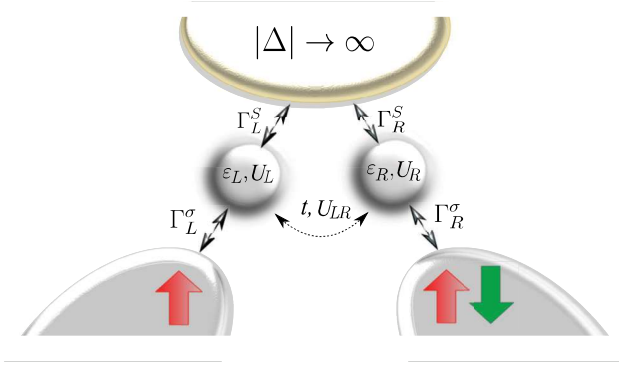
Figure 1. Schematic view of the considered system. It consists of a double quantum dot coupled to two ferromagnetic leads and one superconducting electrode. The spin-dependent coupling between the left (right) dot and the corresponding ferromagnet is denoted by Γ_L^σ (Γ_R^σ), while the coupling to the superconductor is described by Γ_L^S and Γ_R^S for the left and right dot, respectively. Each dot is described by on-site energy ε_i and Coulomb correlation U_i, whereas capacitive coupling between the two dots is denoted by U_{LR} and t is the hopping between the dots. It is assumed that the magnetizations of the leads can form either parallel or antiparallel configuration, as indicated.

amount of CAR processes relative to DAR ones [37, 40, 43, 45]. In an ideal case of half-metallic leads, for bias voltages smaller than the dots' charging energy, the Andreev transport is only due to CAR processes, and the current is maximized in the antiparallel configuration of leads' magnetic moments, while in the case of parallel configuration the Andreev current vanishes. All these indicate that there is a strong motivation to explore the rich physics of such systems.

In this paper we extend the existing studies [43] by analyzing the cross-correlations of the currents flowing due to Andreev reflection in the CPS based on double quantum dots. In our model, we consider a double quantum dot system coupled to an *s*-wave superconductor, with both dots attached to separate ferromagnetic leads forming the arms of CPS, see figure 1. We focus on the zero-frequency cross-correlations between the currents flowing through the left and right ferromagnetic contacts, defined as [46]

$$S_{\mathrm{LR}} = \int_{\infty}^{-\infty} \mathrm{d}t \langle \delta I_{\mathrm{L}}(t)\delta I_{\mathrm{R}}(0) + \delta I_{\mathrm{R}}(0)\delta I_{\mathrm{L}}(t) \rangle, \qquad (1)$$

where $\delta I_\alpha(t) = \hat{I}_\alpha(t) - \langle \hat{I}_\alpha \rangle$ and $\hat{I}_\alpha$ is the current operator for tunneling between the dot and lead α.

The current–current cross-correlations can give a significant insight into the processes taking place in charge and spin transport [46], and have already been successfully measured in various experiments [47–49]. In general, an enhancement of positive cross-correlations, which are strongly present in systems with superconducting electrodes [50–56], results from interactions supporting currents in both junctions. In CPS systems it can be associated with high Cooper pair splitting efficiency. Such positive cross-correlations can be suppressed by interactions, which mutually block the currents, and/or by tunneling processes that occur in opposite directions. On the other hand, negative sign of cross-correlations indicates transport regimes strongly

dominated by aforementioned processes contributing to the total current with different signs.

The present study of spin-dependent transport through double quantum dot system in the subgap regime is accomplished by means of the real-time diagrammatic technique [57, 58]. We consider the first-order expansion with respect to the coupling to ferromagnetic leads, while the coupling to superconductor is arbitrary. In the CAR transport regime we find strong positive current cross-correlations in a wide range of parameters. We show that finite hopping between the dots significantly decreases positive cross-correlations and can result in negative correlations in certain transport regimes. Moreover, when both CAR and DAR processes are allowed, both positive and negative current cross-correlations are present, depending on the transport regime. We show that the sign of cross-correlations depends greatly on the energy of Andreev bound states relevant for transport, which can be tuned by shifting the dots' level positions. In addition, we analyze the influence of spin polarization of ferromagnets, showing that tuning the magnetic properties of electrodes is an important mean to control the splitting efficiency.

We also note that an important application of multiterminal hybrid systems implementing beam splitter architecture is to perform Bell tests. There are nevertheless some considerable issues with predicting entanglement in a straightforward way from current cross-correlations, mainly due to the quasiparticle emission at finite temperatures in detectors [59]. However, there exist theoretical proposals of feasible experimental realizations, with systems involving ferromagnetic contacts [60] or spin filtering due to the spin–orbit interaction in carbon nanotubes [61]. The results presented in this work may thus help in tuning the device into optimal transport regime for such a test experiment, and can be especially relevant for devices with ferromagnetic junctions.

The paper is organized in the following way. Section 2 contains description of the model and method used for calculations, as well as short description of quantities of interest. Section 3 is dedicated to the discussion of numerical results. First, the pure crossed Andreev reflection regime (section 3.1) is analyzed, where we consider the cases of finite level detuning and interdot hopping. Then, in section 3.2 we discuss results for the full parameter space where both CAR and DAR processes are present. The work is concluded in section 4 .

2. Model and method

The schematic of the considered double quantum dot based Cooper pair splitter with ferromagnetic contacts is shown in figure 1. In the central region, two single-level quantum dots are located, each one tunnel-coupled to a separate ferromagnetic electrode and both coupled to an s-wave superconductor (top area). The coupling strength between the αth dot and αth lead is denoted by Γ_α^σ, with $\alpha = L, R$, for the left and right dot and lead. On the other hand, the coupling to superconductor is denoted by Γ_α^S for the left ($\alpha = L$) and right ($\alpha = L$) dot. It is assumed that the device can be in two different magnetic configurations: the parallel (P) and antiparallel (AP) one, as indicated in figure 1.

2.1. Effective hamiltonian

The total Hamiltonian of the system consists of four terms

$$H = H_{DQD} + H_{FM} + H_S + H_T. \tag{2}$$

The first one describes the isolated double quantum dot and is given by

$$H_{DQD} = \sum_{\alpha=L,R} \left(\sum_\sigma \varepsilon_\alpha d_{\alpha\sigma}^\dagger d_{\alpha\sigma} + U_\alpha n_{\alpha\uparrow} n_{\alpha\downarrow} \right) + \sum_{\sigma,\sigma'} U_{LR} n_{L\sigma} n_{R\sigma'} + t \sum_\sigma (d_{L\sigma}^\dagger d_{R\sigma} + d_{R\sigma}^\dagger d_{L\sigma}), \tag{3}$$

where $d_{\alpha\sigma}^\dagger$ ($d_{\alpha\sigma}$) is the creation (annihilation) operator of an electron in dot α with spin σ and energy ε_α. The on-site Coulomb interaction is denoted by U_α, with $n_{\alpha\sigma} = d_{\alpha\sigma}^\dagger d_{\alpha\sigma}$ being the respective occupation number operator. The interdot Coulomb interaction is described by U_{LR} and t is the hopping between the two dots.

The second term of the Hamiltonian describes the ferromagnetic leads in the noninteracting quasiparticle approximation, $H_{FM} = \sum_{\alpha=L,R} \sum_{\mathbf{k}\sigma} \varepsilon_{\alpha\mathbf{k}\sigma} c_{\alpha\mathbf{k}\sigma}^\dagger c_{\alpha\mathbf{k}\sigma}$, where $c_{\alpha\mathbf{k}\sigma}^\dagger$ is the creation operator for an electron with spin σ, wave number $\mathbf{k}$ and energy $\varepsilon_{\alpha\mathbf{k}\sigma}$ in the lead α. The superconductor is modeled by the mean-field BCS Hamiltonian

$$H_S = \sum_{\mathbf{k}\sigma} \varepsilon_{S\mathbf{k}\sigma} c_{S\mathbf{k}\sigma}^\dagger c_{S\mathbf{k}\sigma} + \Delta \sum_\mathbf{k} (c_{S\mathbf{k}\downarrow} c_{S-\mathbf{k}\uparrow} + \text{h.c.}), \tag{4}$$

with $c_{S\mathbf{k}\sigma}^\dagger$ being the respective creation operator for an electron with momentum $\mathbf{k}$, spin σ and energy $\varepsilon_{S\mathbf{k}\sigma}$. The superconducting order parameter is denoted by Δ and assumed to be real and positive.

The tunneling processes between the double dot and the leads are described by the last term of the Hamiltonian (2), which is given by

$$H_T = \sum_{\alpha=L,R} \sum_{\mathbf{k}\sigma} (V_\mathbf{k}^\alpha c_{\alpha\mathbf{k}\sigma}^\dagger d_{\alpha\sigma} + V_{\alpha\mathbf{k}\sigma}^S c_{S\mathbf{k}\sigma}^\dagger d_{\alpha\sigma} + \text{h.c.}), \tag{5}$$

where $V_\mathbf{k}^\alpha$ are the tunnel matrix elements between the respective dot and ferromagnetic lead and $V_{\alpha\mathbf{k}\sigma}^S$ are the elements of tunnel matrix between the dot α and the superconductor. For the considered model, we assume that these matrix elements are momentum and spin independent. Therefore, the coupling strength between given dot and ferromagnetic lead can be expressed as, $\Gamma_\alpha^\sigma = 2\pi |V^\alpha|^2 \rho_\alpha^\sigma$, where ρ_α^σ is the density of states for spin σ in lead α. These couplings can be written as, $\Gamma_\alpha^\sigma = (1 + \sigma p_\alpha) \Gamma_\alpha$, with $\Gamma_\alpha = (\Gamma_\alpha^\uparrow + \Gamma_\alpha^\downarrow)/2$ and p_α being the spin polarization of the lead α. On the other hand, the coupling between superconductor and dot α is given by, $\Gamma_\alpha^S = 2\pi |V_\alpha^S|^2 \rho^S$, where ρ^S is the density of states of superconductor in the normal state.

For precise study of the subgap transport properties, we take the limit of infinite superconducting energy gap $\Delta \to \infty$. With this assumption, we are able to focus exclusively on the Andreev reflection processes, suppressing normal tunneling between superconducting lead and quantum dot system. When Δ is the largest energy scale in the problem, the subsystem consisting of the double quantum dot coupled to superconductor can be modeled by the following effective Hamiltonian [62]

$$H_{DQD}^{eff} = H_{DQD} - \sum_{\alpha=L,R} \frac{\Gamma_\alpha^S}{2} (d_{\alpha\uparrow}^\dagger d_{\alpha\downarrow}^\dagger + \text{h.c.}) + \frac{\Gamma_{LR}^S}{2} (d_{R\uparrow}^\dagger d_{L\downarrow}^\dagger + d_{L\uparrow}^\dagger d_{R\downarrow}^\dagger + \text{h.c.}). \tag{6}$$

The superconducting proximity effect is now accounted for by induced on-dot pairing correlations described by the last two terms. The first term, proportional to Γ_α^S, describes direct Andreev reflection processes. Cooper pairs can be also split, when each of the electrons leaves or enters the superconductor through different dot. Such crossed Andreev reflection processes are accounted for by the last term of the effective Hamiltonian, which is proportional to $\Gamma_{LR}^S = \sqrt{\Gamma_L^S \Gamma_R^S}$.

Although the coupling between each dot and superconductor can be different, here we focus on the symmetric case and assume $\Gamma_L^S = \Gamma_R^S \equiv \Gamma_S$. Moreover, we also assume symmetric couplings to ferromagnetic leads, $\Gamma_L = \Gamma_R \equiv \Gamma/2$ and $p_L = p_R \equiv p$, and symmetric dots, $U_L = U_R \equiv U$. The system is driven out of equilibrium by applying a bias voltage between the superconducting and ferromagnetic leads. The electrochemical potential of superconductor is set to zero, $\mu_S = 0$, while both ferromagnetic leads have the same potential $\mu_L = \mu_R \equiv \mu = eV$. In such setup, for positive bias voltage, $eV > 0$, the electrons tunnel from the normal leads to superconductor, while for negative bias, $eV < 0$, Cooper pairs are extracted from superconductor and electrons tunnel to the normal leads, either in a DAR or in a CAR process. Because the potentials of the ferromagnets are assumed to be equal, the net current between them vanishes.

The effective Hamiltonian (6) is not diagonal in the local states of the dots, $|\chi_L, \chi_R\rangle$, where $\chi_L, \chi_R = 0, \uparrow, \downarrow, d$ for empty, singly occupied with spin-up or spin-down and doubly occupied dot level. This is because the particle-non-conserving on-dot pairing terms mix the states with different electron numbers. Thus, we first diagonalize H_{DQD}^{eff} to find its eigenstates $|\chi\rangle$ and eigenenergies ε_χ. In a general case the analytical formulas for them are however too cumbersome to be presented here, therefore, let us discuss the eigenspectrum for the case when the double occupation of each dot is prohibited and there is no hopping between the dots. In this case there are altogether 9 states relevant for transport, these are: four single-electron doublet states $|\sigma, 0\rangle$, $|0, \sigma\rangle$, three triplet states $|T_0\rangle = (|\downarrow, \uparrow\rangle + |\uparrow, \downarrow\rangle)/\sqrt{2}$ and $|T_\sigma\rangle = |\sigma, \sigma\rangle$, and (due to the proximity effect the empty state $|0\rangle$ is coupled with the singlet state $|S\rangle = (|\downarrow, \uparrow\rangle - |\uparrow, \downarrow\rangle)/\sqrt{2}$) the two states

$$|\pm\rangle = \frac{1}{\sqrt{2}} \left(\sqrt{1 \mp \frac{\delta}{2\varepsilon_A}} \; |0,0\rangle \mp \sqrt{1 \pm \frac{\delta}{2\varepsilon_A}} \; |S\rangle \right), \tag{7}$$

where $\delta = \varepsilon_L + \varepsilon_R + U_{LR}$ is a level detuning parameter and $2\varepsilon_A = \sqrt{\delta^2 + 2\Gamma_S^2}$ is the energy difference between states $|+\rangle$ and $|-\rangle$. The energies of the singly occupied states are simply given by $E_{10} = \varepsilon_L$ and $E_{01} = \varepsilon_R$, the energy of triplet

3

74

states is $E_\text{T} = \varepsilon_\text{L} + \varepsilon_\text{R} + U_\text{LR}$, while the eigenenergy of states $|\pm\rangle$ equals $E_\pm = \delta/2 \pm \varepsilon_A$, respectively. The excitation energies between the singlet and doublet states yield the Andreev bound state (ABS) energies

$$E^\text{ABS}_{\eta\gamma} = \eta\frac{U_\text{LR}}{2} + \frac{\gamma}{2}\sqrt{\delta^2 + 2\Gamma^2_\text{S}}, \qquad (8)$$

with $\eta, \gamma = \pm$.

We would like to emphasize that in our considerations we focus on the pure Andreev reflection regime, for which $\Delta > U$. This condition is however not necessarily satisfied in arbitrary hybrid quantum dot-superconductor systems. For instance, in carbon nanotube quantum dots, the charging energy is typically of the order of 2–4 meV [12], which is higher than the energy gap Δ for superconductors such as Pb ($\sim$1.3 meV) or Nb ($\sim$1.2 meV) [12, 16]. Nevertheless, the ratio of U/Δ can be enhanced in systems with large gap superconductors, for which Δ can reach a few meV [63]. Moreover, for nanowire quantum dots the charging energy is lower than for molecular quantum dots, and typically is of the order of 1 meV. Consequently, there are systems in which the Coulomb correlations are of the order of the superconducting energy gap. Therefore, while our results for bias voltages up to the charging energies are clearly important for current experiments, they also shed light on the Andreev reflection processes at higher voltages, which may be of importance for future experiments.

2.2. Method and quantities of interest

In this paper we focus on the Andreev transport properties of double quantum dot based Cooper pair splitters weakly attached to ferromagnetic leads. We are in particular interested in cross-correlations of the currents flowing through the left and right ferromagnetic junctions S_LR. Moreover, to make the picture complete and be able to identify different transport regimes, we also calculate the Andreev current I_S and associated differential conductance $G_\text{S} = \text{d}I_\text{S}/\text{d}V$. To find the Andreev current, we first need to determine the normal current between the double dot and the left (I_L) and right (I_R) ferromagnetic lead. Then, I_S can be simply found from the Kirchhoff's law, $I_\text{S} = I_\text{L} + I_\text{R}$.

To determine the current and current cross-correlations we use the real-time diagrammatic technique [57, 58, 64–66]. This technique relies on systematic perturbation expansion of the reduced density matrix and relevant operators with respect to the tunneling Hamiltonian. Here, we perform the expansion with respect to the coupling strength Γ to ferromagnetic leads, while the coupling to superconducting electrode is arbitrary. In calculations we take into account the lowest-order terms of expansion, which describe sequential tunneling processes between the dots and ferromagnetic leads. Within the real-time diagrammatic technique, the quantities of interest can be expressed in terms of self-energies, which can be calculated by collecting contributions from relevant diagrams. Once the self-energies are determined, the stationary occupation probability p^st_χ of the eigenstate $|\chi\rangle$ of effective DQD Hamiltonian can be found from [57, 58]

$$\mathbf{W}\mathbf{p}^\text{st} = 0, \qquad (9)$$

together with the normalization condition. Here, $\mathbf{p}^\text{st}$ is the vector containing probabilities p^st_χ and the elements $W_{\chi\chi'}$ of self-energy matrix $\mathbf{W}$ account for transitions between the states $|\chi\rangle$ and $|\chi'\rangle$. The current flowing through the junction with ferromagnetic lead α can be found from [57, 58]

$$I_\alpha = \frac{e}{2\hbar}\text{Tr}\{\mathbf{W}^{I_\alpha}\mathbf{p}^\text{st}\}, \qquad (10)$$

where the self-energy matrix $\mathbf{W}^{I_\alpha}$ is similar to $\mathbf{W}$, but it takes into account the number of electrons transferred through a given junction.

In order to determine the cross-correlations of the currents flowing through the left and right junctions, first, we have to calculate both matrices $\mathbf{W}^{I_\text{L}}$ and $\mathbf{W}^{I_\text{R}}$. The current–current correlation function has contributions from two current operators which appear either in one irreducible block or in two distinct blocks. For the cross-correlations in the sequential tunneling approximation, the former auto-correlation term vanishes, which leads to the following expression for S_LR [57, 58]

$$S_\text{LR} = \frac{e^2}{\hbar}\text{Tr}\{[\mathbf{W}^{I_\text{L}}\mathbf{P}\mathbf{W}^{I_\text{R}} + \mathbf{W}^{I_\text{R}}\mathbf{P}\mathbf{W}^{I_\text{L}}]\mathbf{p}^\text{st}\}, \qquad (11)$$

where the propagator $\mathbf{P}$ is determined from $\tilde{\mathbf{W}}\mathbf{P} = \mathbf{p}^\text{st}\mathbf{e}^T - \mathbf{1}$, with $\tilde{\mathbf{W}}$ being identical to matrix $\mathbf{W}$ with arbitrary one row replaced by $(\Gamma, \Gamma, \dots, \Gamma)$ and $\mathbf{e}^T = (1, 1, \dots, 1)$.

The perturbation expansion with respect to the coupling to ferromagnetic leads limits us to the weak coupling regime, with Γ being the smallest energy scale. Therefore, it is important to notice that within this approximation, it is not possible to grasp higher-order correlations, such as for instance those leading to the Kondo effect [67–69].

3. Results and discussion

In this section we present and discuss the transport properties of the considered system for various parameters of the model. First, we examine the transport characteristics assuming infinite on-site Coulomb correlations. With this assumption we are able to focus exclusively on the CAR transport regime. We analyze the current cross-correlations both in the absence and presence of detuning between the dots' levels, as well as in the presence of hopping between the dots. Although both finite detuning and hopping lead to a similar splitting of Andreev bound states [43], we show that they have a completely different influence on the current cross-correlations. We then allow for double occupation of both dots, and study the transport behavior in the presence of both DAR and CAR processes. Before proceeding, let us recall that the bias voltage in all considered cases is applied in the same way, with superconducting lead grounded and equal potential $\mu = eV$ applied to ferromagnetic leads.

3.1. Crossed Andreev reflection regime

When the on-site interaction in the dots is assumed to be infinite ($U \to \infty$), the double occupancy of each dot is prohibited. There are then 9 states relevant for transport in this limit, as discussed in section 2.1. As a result, the current
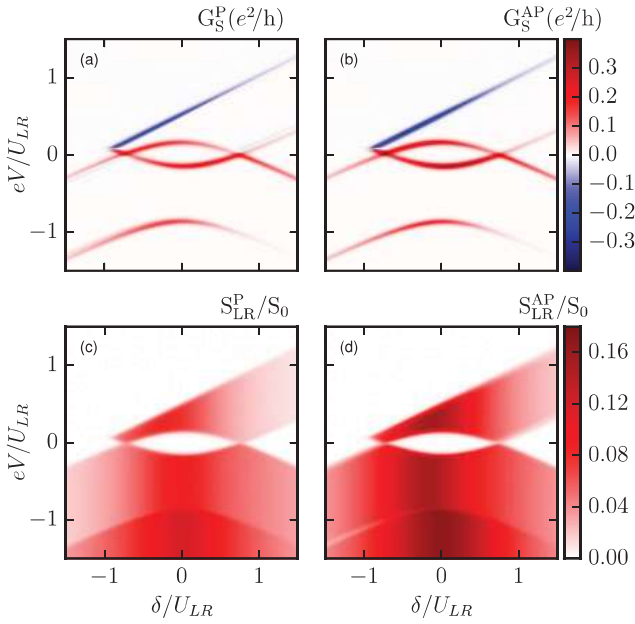
4

Figure 2. ((a) and (b)) The differential conductance $G_S = dI_S/dV$ of the Andreev current and ((c) and (d)) the current–current cross-correlations in the parallel (left column) and antiparallel (right column) magnetic configuration as a function of detuning parameter $\delta = 2\varepsilon + U_{LR}$ and the applied bias voltage eV. The parameters are: $\Gamma_S = 0.5$, $T = 0.015$, $\Gamma = 0.01$, $p = 0.5$, $t = 0$, $U = \infty$, with $U_{LR} \equiv 1$ the energy unit, and $S_0 = e^2\Gamma/\hbar$.

flows exclusively due to crossed Andreev reflection processes, while direct processes are not allowed. In figure 2 we show the Andreev differential conductance and cross-correlations of Andreev currents as a function of applied bias voltage eV and level detuning parameter $\delta = 2\varepsilon + U_{LR}$, assuming $\varepsilon_L = \varepsilon_R = \varepsilon$. The left column presents the density plots for the parallel magnetic configuration of ferromagnetic leads, while the right column corresponds to the antiparallel configuration.

Let us first discuss the behavior of the Andreev differential conductance. The current starts flowing, when the energy of Andreev bound state lies within the window provided by the bias voltage. Consequently, at the threshold voltage there is a peak in differential conductance for both positive and negative bias voltages. In the low bias voltage regime, for wide range of detuning parameter we observe the Coulomb blockade where the current is strongly suppressed. When approaching $|\delta| = \sqrt{U_{LR}^2 - 2\Gamma_S^2}$ ($\delta/U_{LR} \approx 0.7$ in figure 2), the Andreev bound states enter the resonance, resulting in a maximum in the differential conductance. As can be seen in figure 2, independently of magnetic configuration, we can identify both positive and negative differential conductance (NDC) peaks. When the first bound state becomes active in transport, the Andreev current starts flowing and there is a positive peak in the differential conductance. However, the next peak in G_S when increasing the bias voltage can be either positive or negative, depending on the sign of eV. The NDC forms for positive bias voltage, starting from $eV/U_{LR} \approx 0$ for detuning parameter $\delta/U_{LR} \approx -1$, and progressing along the higher values of eV/U_{LR} and δ/U_{LR} according to $eV \approx (\delta + U_{LR})/2$, see figures 2(a) and (b). At this bias voltage, the triplet state occupation becomes strongly enhanced, which leads to the

suppression of the Andreev current, since it is forbidden to tunnel from a triplet state into an *s*-wave superconductor. This phenomenon is known as the triplet blockade of the Andreev current [37, 43]. When the bias voltage is reversed, the electrons from the triplet state can always tunnel to normal ferromagnetic leads and the triplet blockade is not present.

Contrary to the differential conductance, the current cross-correlations are non-negative in the whole range of bias voltage and detuning parameter δ, irrespective of magnetic configuration, see figures 2(c) and (d). Positive sign of S_{LR} is characteristic of crossed Andreev reflection processes [51, 53]. When the double occupancy of each dot is forbidden, extracting/injecting Cooper pairs from/into superconductor is always associated with the current flowing through both left and right junction, since this can happen only in a CAR process. Consequently, the Andreev current flowing through one junction has positive influence on the Andreev current flowing through the right junction, and one thus finds $S_{LR} \geqslant 0$. We also note that the current cross-correlations are nonzero only when the sequential current flows through the system. Therefore, similarly to the current, the cross-correlations are suppressed in the triplet blockade regime. Moreover, as can be seen in figure 2, enhanced cross-correlations occur around the particle-hole symmetry point, $\delta = 0$, since then the energy of doubly occupied and empty DQD states is minimum and the Andreev reflection is maximized.

The main difference between the results in the parallel and antiparallel magnetic configuration of the device is related with the magnitude of the considered quantities. Both the differential conductance and the current–current cross-correlations have higher absolute values in the antiparallel configuration compared to the parallel one. This observation indicates that spin-dependent tunneling from and into ferromagnetic leads has a strong impact on the Andreev transport properties [43]. To understand enhanced transport in the antiparallel configuration, it is desirable to take a look at the most important processes active in transport. Transferring a Cooper pair through the system involves two electrons of opposite spins. Consequently, in the antiparallel configuration, there is a fast transport channel, which involves majority spins of both ferromagnets. In the parallel configuration, on the other hand, one of the electrons is always a minority spin, which results in a smaller overall rate for tunneling processes. The difference in the currents reveals in the associated difference in the current cross-correlations, which are generally enhanced for the antiparallel leads' alignment compared to the parallel one, $S_{LR}^{AP} > S_{LR}^{P}$.

Assuming the zero temperature limit, it is possible to derive some approximate analytical formulas for both I_S and S_{LR}. For $eV < 0$ and $\delta \approx 0$, the first step in the current appears between $-1 \lesssim eV/U_{LR} \lesssim -0.2$. In this regime, in the parallel configuration, the current reaches

$$I^P/I_0 = \frac{p^2 - 1}{p^2 + 3}, \qquad (12)$$

where $I_0 = e\Gamma/\hbar$ and the current–current cross-correlations can be approximated by
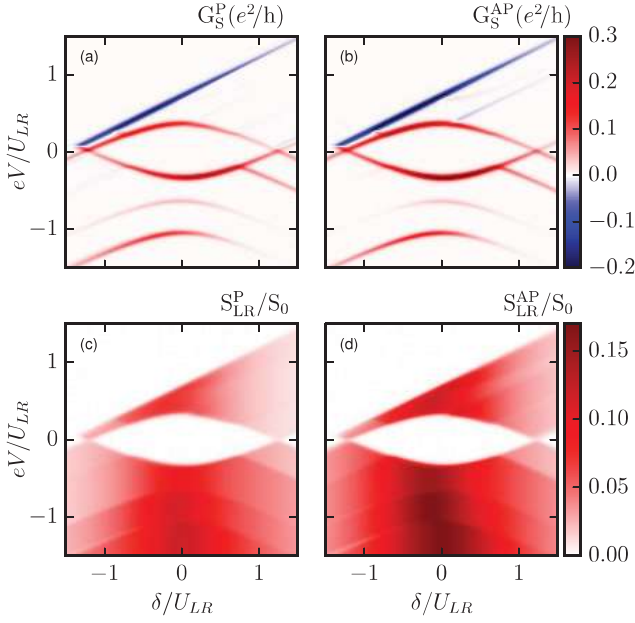
Figure 3. The detuning and bias voltage dependence of ((a) and (b)) the Andreev differential conductance and ((c) and (d)) the current cross-correlations calculated in the case of parallel (left column) and antiparallel (right column) magnetic configuration. The other parameters are the same as in figure 2 with finite level detuning $\Delta\varepsilon = \varepsilon_L - \varepsilon_R = 0.4 U_{LR}$.

$$S_{LR}^P = \frac{(-3+p)(-1+p)(1+p)(3+p)(1+3p^2)}{4(3+p^2)^3} \frac{e^2 \Gamma}{\hbar}. \tag{13}$$

In antiparallel configuration, the current is given by $I_S^{AP}/I_0 = -1/3$, while for the current–current cross-correlations one finds

$$S_{LR}^{AP} = \frac{(9+7p^2)}{108(1-p^2)} \frac{e^2 \Gamma}{\hbar}. \tag{14}$$

For parameters where the current is maximized and exhibits a plateau, the current–current cross-correlations also retain a finite and constant value. The current in the parallel configuration for the plateau at $eV/U_{LR} \lesssim -1$ and $\delta \approx 0$ is given by, $I_S^P/I_0 = p^2 - 1$, while the current–current cross-correlations are given by

$$S_{LR}^P = \frac{1}{32}[4 - p^2(1+p^2)^2]\frac{e^2 \Gamma}{\hbar}. \tag{15}$$

On the other hand, in the case of antiparallel configuration the current is maximized with $I_S^{AP}/I_0 = -1$, and the cross-correlations can be expressed as

$$S_{LR}^{AP} = \frac{1}{8-8p^2}\frac{e^2 \Gamma}{\hbar}. \tag{16}$$

When the double dot levels are detuned by a gate voltage, $\varepsilon_L \neq \varepsilon_R$, the Andreev bound states become split [43]. Figure 3 displays the differential conductance and current–current cross-correlations as a function of eV and δ in the presence of finite level detuning $\Delta\varepsilon/U_{LR} = 0.4$, with $\Delta\varepsilon = \varepsilon_L - \varepsilon_R$. The main difference between the system's transport properties in
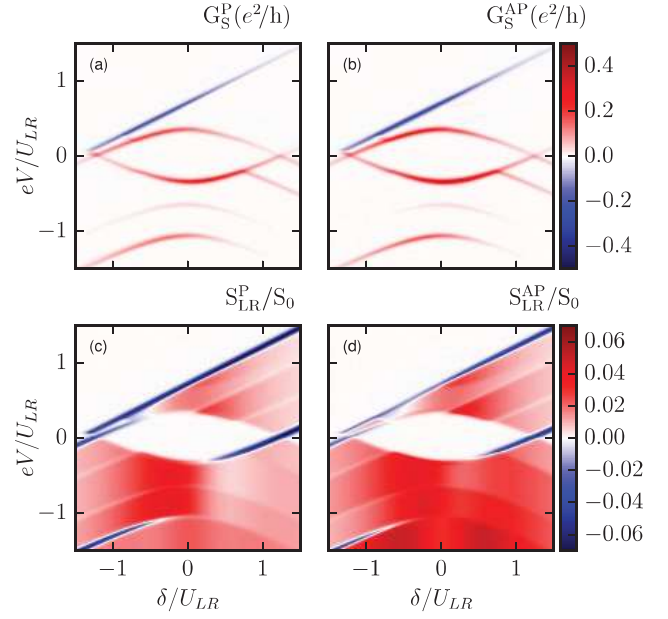

Figure 4. ((a) and (b)) The Andreev differential conductance G_S and ((c) and (d)) the current cross-correlations S_{LR} in the case of parallel (left column) and antiparallel (right culomn) magnetic configuration calculated as a function of detuning δ and applied bias voltage eV. The parameters are the same as in figure 2 with $t = 0.2/U_{LR}$.

the absence and presence of detuning is related to new peaks visible in the Andreev differential conductance and corresponding new plateaus in S_{LR}. Except for that, the general behavior of the current cross-correlations is similar to the case of $\varepsilon_L = \varepsilon_R$; S_{LR} are positive in the whole range considered in figure 3 and show an enhancement around the particle-hole symmetry point.

The Andreev bound states become also split when there is a finite hopping between the dots. In figure 4 we show the same transport characteristics as in figure 3, however now, instead of finite level detuning, we investigate the influence of the interdot hopping by assuming $t/U_{LR} = 0.2$. A good point to start the analysis is by comparing the Andreev differential conductance in the case with finite hopping and with finite level detuning, see figures 3 and 4. The results are qualitatively very similar, i.e. the number of conductance peaks and their position are the same for $t = \Delta\varepsilon/2$, and the main difference is only related to slightly different values of the conductance in both cases.

Contrary to the Andreev current, the cross-correlations display a nontrivial change once $t \neq 0$. As can be seen in figures 4(c) and (d), there is a range of parameters where S_{LR} becomes negative. This important difference visible in current cross-correlations is related to the bonding and antibonding states that form due to finite t. The four single-electron states, $|\sigma, 0\rangle, |0, \sigma\rangle$, which were present in the case of $t = 0$, now form the following doublets

$$|\sigma_\pm\rangle = \frac{1}{\sqrt{2}}(|\sigma, 0\rangle \pm |0, \sigma\rangle). \tag{17}$$

These states are delocalized over both quantum dots and tunneling from/into these states is now possible through both

left and right junctions. Although this fact has a rather small impact on the steady-state current, it may result in a more dramatic change in S_{LR}, which is determined by time-dependent correlations between the currents. As in the case of $t = 0$, each split electron entered different dot and tunneled further to different ferromagnetic lead, in the case of finite t, when one of the two electrons leaves the double dot through one junction, the other electron, which is now delocalized, can leave the system through the same junction. Consequently, the two electrons forming a Cooper pair are no longer forced to tunnel into separate leads. More specifically, due to the above-mentioned single-electron states, non-CAR processes are possible, with electrons sequentially tunneling through the same junction, one after another. Such scenario has now a finite probability and such processes take in fact significant part in transport. As a result, we observe a drop of positive cross-correlations in a wide range of transport parameters compared to the previous case and, more importantly, we find regimes where S_{LR} changes sign and becomes negative.

As can be seen in figures 4(c) and (d), three strong negative cross-correlation lines emerge, having the same value of a positive slope in the (δ, eV)-plane, aligned along conductance peaks and parallel to each other. Negative cross-correlations appear for both directions of applied bias voltage. They result from the tunneling processes in distinct junctions that contribute to the current with opposite signs. This sequence of tunneling events is now possible for certain transport parameters, contrary to the case with vanishing interdot hopping t. Due to the finite t, the one-electron states are no longer localized on single quantum dots, therefore the effect of the infinite Coulomb interaction $U \to \infty$ is not critical for the type of allowed processes, as it does not block the tunneling of consecutive electrons through the same junction. Now, from any of single-electron states, there is a possibility to tunnel through either left or right junction, which was forbidden in the case of negligible hopping. For each of the three negative cross-correlation peaks, the energy of the states $|\pm\rangle$ is such that most tunneling processes occur between them and single-electron states, but in opposite directions, as the relevant states are near resonance with electrochemical potential of ferromagnetic leads. The single-electron states are most likely to change into one of the $|\pm\rangle$ states by an electron tunneling through the normal junction. However, from the former state, it is energetically more favorable for an electron to tunnel back to the ferromagnetic lead. These two processes are dominant for this narrow set of transport parameters, eV and δ, and when they happen through distinct ferromagnetic junctions negative cross-correlations emerge.

It is also important to note that negative cross-correlations may be accompanied by vanishing current $I_S \approx 0$, which is understandable, as most processes occur in opposite directions, canceling out the contribution to the average current. This is however not the case for $eV/U_{LR} \lesssim -1$ and $\delta/U_{LR} \lesssim -0.5$ where negative S_{LR} appears despite finite current flowing through the system. In this case, there are two one-electron doublets, well separated energetically. One of them is inside the window provided by the transport voltage and contributes strongly to the current, however its contribution
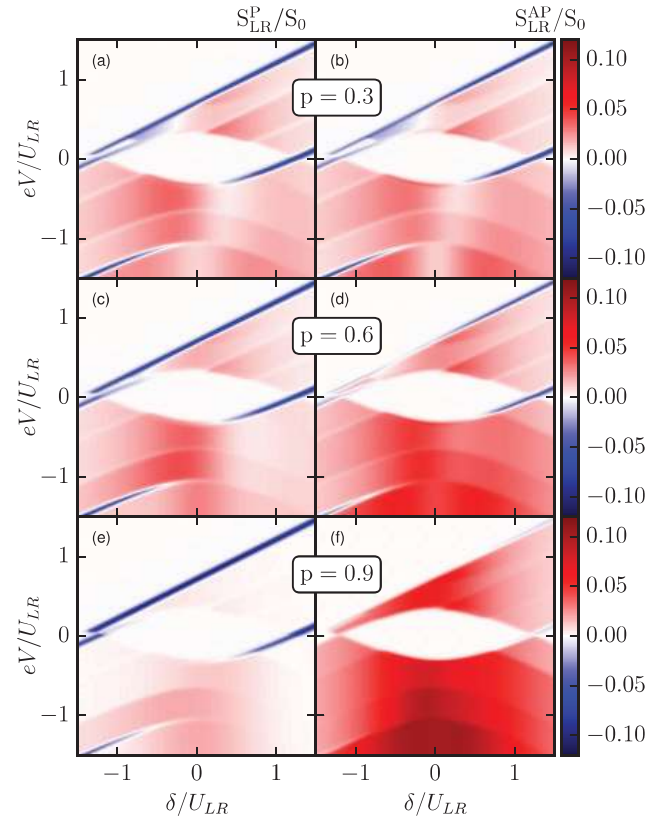

Figure 5. The current cross-correlations in the parallel S_{LR}^P and antiparallel S_{LR}^{AP} magnetic configurations as a function of detuning δ and applied bias voltage eV. Parameters are the same as in figure 2 with $t = 0.2/U_{LR}$ and different values of spin polarization p of ferromagnetic leads, as indicated.

to cross-correlations is relatively low. On the other hand, the second doublet is around the electrochemical potential of ferromagnetic leads, and transport processes between these states and Andreev bound states are negatively correlated, which results in $S_{LR} < 0$. Final important observation is that negative cross-correlation peak occurring around the triplet blockade is additionally enhanced by the fact that from the triplet state, the only possible tunneling processes are in opposite direction, back into ferromagnetic leads.

Let us now analyze how the magnitude of the electrodes' spin polarization influences the current cross-correlations. Figure 5 presents the bias voltage and level detuning dependence of S_{LR} calculated for both the parallel (left column) and antiparallel (right column) magnetic configurations of ferromagnetic leads. The spin polarization p varies from relatively small $p = 0.3$ up to $p = 0.9$, as indicated. When $p \lesssim 0.3$, one can see that, both qualitatively and quantitatively, current cross-correlations show similar dependence in both configurations, with slightly higher absolute values in the antiparallel configuration. However, when the spin polarization increases, clear differences appear in S_{LR}^P and S_{LR}^{AP}, involving not only quantitative, but also qualitative changes. In particular, one can see for $p = 0.9$ (figure 5(e)) that in the parallel configuration positive cross-correlations are strongly diminished, while negative ones have a sharper dependence and higher absolute values. In the antiparallel configuration, on the other hand, the

behavior is quite opposite. Positive cross-correlations are significantly enhanced, while the negative ones are almost completely suppressed, see figure 5(f).

The mechanism explaining the above behavior is strictly associated with the magnitude of leads' spin polarization and the resulting spin-dependent couplings. When the magnetizations of the leads form the antiparallel configuration, the DQD states are strongly coupled to two separate reservoirs with opposite majority states. Thus, there are high tunneling rates for both majority spins, taking place in distinct junctions, which results in strong positive current cross-correlations. The decrease of spin polarization p lowers the dominant coupling strengths, which in consequence weakens positive cross-correlations. Switching the magnetic configuration to the parallel one, increases this effect even further. Now, only electrons with spin aligned with leads' polarization have high tunneling rates, and the electrons with opposite spin are weakly coupled to whichever ferromagnetic lead. Therefore, the escaping processes for one of the electrons forming a Cooper pair into the ferromagnetic lead is enhanced by relatively high coupling strength, but the rate for the associated process of the other electron with opposite spin is relatively low.

The coupling imbalance also strongly influences negative cross-correlations, but in a reverse way, i.e. the strongest negative cross-correlations occur in the parallel polarized setup, see figure 5. In this configuration, for parameters for which negative cross-correlations occur, the processes giving opposite contributions to the current most likely take place through distinct leads. This is completely opposite to the case of strongly-polarized antiparallel configuration when the negative values of S_{LR} are almost completely suppressed, see figure 5(f). This is because for consecutive processes in opposite directions, due to strong polarization of the leads, an electron of majority spin which tunnels to the DQD, will most probably tunnel back through the same junction, as the electron of opposite spin is very weakly coupled. Such processes do not contribute to cross-correlations because both tunneling events happen through the same junction.

Once again, we look for analytical approximations of the current and the current cross-correlations in the current plateaus in the particle-hole symmetric case. In both magnetic configurations, the current for $eV/U_{LR} \lesssim -1$ and $\delta \approx 0$ has approximately the same value as the current in the aforementioned case without hopping. However, the current cross-correlations are strongly reduced and given by

$$S_{LR}^{P} = \frac{p^2}{32}(3 - 2p^2 - p^4)\frac{e^2\Gamma}{\hbar} \qquad (18)$$

for the parallel and

$$S_{LR}^{AP} = \frac{p^2}{8}\frac{e^2\Gamma}{\hbar} \qquad (19)$$

for the antiparallel magnetic configuration.

By a simple comparison with already discussed case of infinite U, we expect that experimental measurement of cross-correlations can help to estimate how well both quantum dots are separated from each other. Lack of negative cross-correlations may suggest that dots are not tunnel coupled.
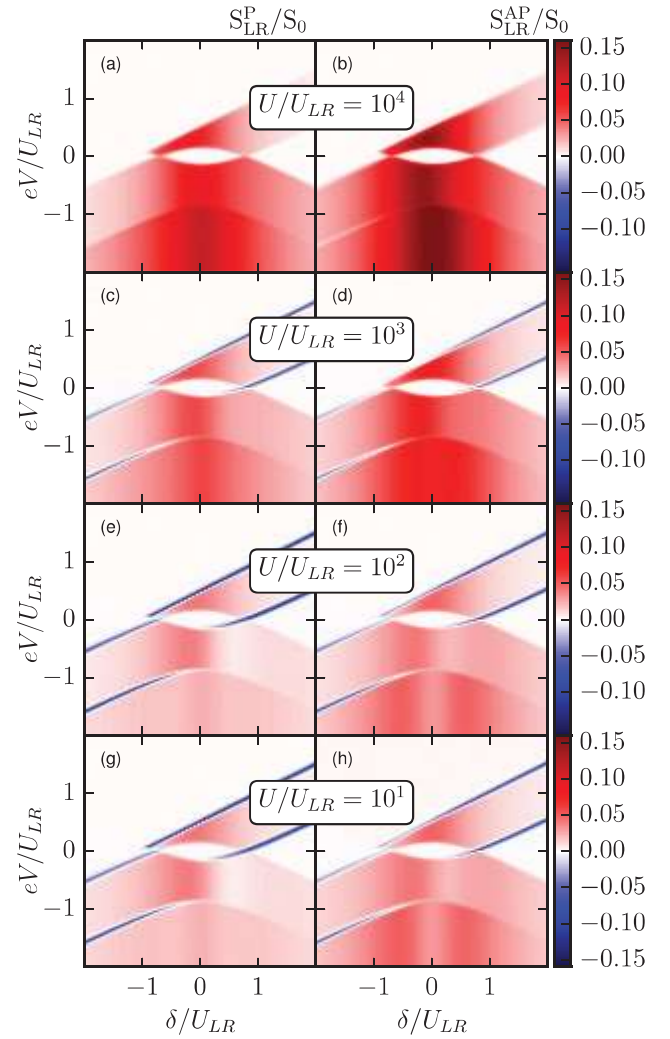

Figure 6. The current cross-correlations in the parallel S_{LR}^{P} and antiparallel S_{LR}^{AP} magnetic configurations as a function of detuning δ and applied bias voltage eV calculated for different values of on-site Coulomb correlation parameter U. The other parameters are the same as in figure 2.

There are already experimental realizations of Cooper pair splitters using distant graphene quantum dots, such that no direct hopping between the dots is possible [25]. Examining the current cross-correlations might be then a good indicator, if the device is well-fabricated and has desired properties. On the other hand, by detecting negative values of cross-correlations, one can assume significant finite hopping influencing transport properties and decreasing splitting efficiency. However, we would like to note, that this conclusion is only valid when strong charging energy is present on the dots. In the following section, we will show that, despite vanishing hopping, negative current cross-correlations can be measured when the charging energy is finite and comparable to the applied voltage.

3.2. Crossed and direct Andreev transport regime

In this section we analyze the effect of finite on-site Coulomb correlation U and its influence on the current cross-correlations. Figure 6 presents S_{LR} in both magnetic configurations as a
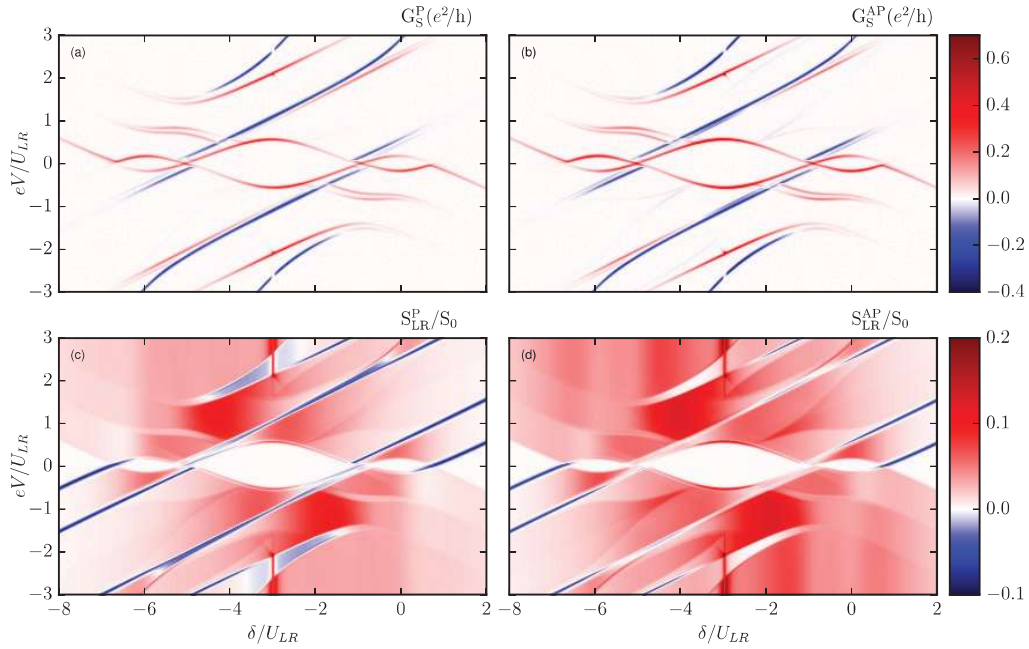
Figure 7. The differential conductance $G_S = dI_S/dV$ of the Andreev current in the parallel (G_S^P) and antiparallel (G_S^{AP}) magnetic configurations and current cross-correlations for the parallel (S_{LR}^P) and antiparallel (S_{LR}^{AP}) magnetic configurations as a function of detuning $\delta = 2\varepsilon + U_{LR}$ and the applied bias eV. The parameters are the same as in figure 2 with $U/U_{LR} = 2$.

function of δ and eV for different values of U. Starting with an extremely high value of on-site correlations, see the case of $U/U_{LR} = 10^4$ in figure 6, we observe strong positive cross-correlations in the range where the current is expected to flow through the system, suggesting significant presence of CAR processes in transport, while negative cross-correlations are not present. This fact supports the statement that one should expect the behavior of the system with very high U to be essentially the same as that predicted in the case of $U \to \infty$, see figure 2. However, one needs to be careful with the above conclusion. As can be seen in figures 6(c) and (d), which present results for $U/U_{LR} = 10^3$, despite U being still the highest, finite energy scale in the problem, greatly exceeding both bias voltage and thermal energy, negative cross-correlations can appear. With lowering the strength of Coulomb correlations, we observe further increase of negative cross-correlations and decrease of positive ones, see figure 6.

To explain this behavior it is important to realize that the presence of Coulomb correlations strongly influences the states forming in double quantum dot system. Again, in the considered transport regime especially important are the single-electron states. Let us recall that in the case of $U \to \infty$ ($t = 0$) the singly occupied states are $|\sigma, 0\rangle$, $|0, \sigma\rangle$. When U is finite this is however not the case due to on-site pairing correlations in the double dot generated by the superconducting proximity effect. For finite value of U, those states have the following general form, $|\sigma_\pm\rangle = \alpha|\sigma, 0\rangle \pm \beta|0, \sigma\rangle$, with α and β being parameter-dependent amplitudes. When U is very large only one of those amplitudes is relevant, however, for lower values of correlations, both amplitudes are becoming important and comparable. As a result, single-electron delocalized states start playing a role similar to the bonding and antibonding states in the case of finite t, giving rise to negative

correlations between the left and right currents. As can be seen in figure 6, lowering the value of U results in an enhancement of negative cross-correlations. It is important to emphasize that the above mechanism of hybridization is due to superconducting correlations and Coulomb interaction U is a parameter controlling these effects, as for lower and lower values, it allows to form more delocalized states in the system.

Finally, let us analyze the behavior of cross-correlations in the full parameter space assuming $U/U_{LR} = 2$. Figure 7 shows the differential conductance and current cross-correlations in both magnetic configurations, for a wide range of applied bias voltage and detuning parameter δ. All quantities exhibit now symmetry with respect to the particle-hole symmetry point $\varepsilon_{ph} = -U_{LR} - U/2$ under the replacement $eV \to -eV$ and $\delta \to -\delta$. For the detuning parameter used in the figure it has the following value, $\delta_{ph} = -U_{LR} - U = -3U_{LR}$, see figure 7. With lowering the detuning parameter δ, the double dot becomes consecutively occupied with electrons. More precisely, the charge in DQD changes when $\delta \approx U_{LR}$, $\delta \approx -U_{LR}$, $\delta \approx -2U - U_{LR}$ and $\delta \approx -2U - 3U_{LR}$. In between those points, at low bias voltage the system is in the Coulomb blockade. The blockade can be lifted when the applied voltage becomes larger than a certain threshold voltage, such that Andreev bound states enter the transport window. Due to more states relevant for transport as compared to the case of infinite U, the differential conductance shows now more peaks corresponding to additional Andreev bound states [43].

As far as cross-correlations are concerned, one can clearly identify the regimes where negative S_{LR} occur. They appear as four lines across the wide range of bias voltage and detuning parameter, with a positive slope in the (δ, eV)-plane, each one parallel to another one, see figure 7. Moreover, they are aligned along the strongest conductance peaks related to new quantum

dots' states entering the transport window with higher occupancy. The mechanism responsible for the formation of these negative cross-correlation lines is similar to that discussed in the case of finite hopping t. In present case, despite $t = 0$, the states with odd electron number, which are delocalized over the two dots, are responsible for negative cross-correlations between the currents.

In addition, an important difference in cross-correlations as compared to the case of large U can be seen around the triplet blockade regimes, which are near $\delta = 0$ for $eV/U_{LR} \gtrsim 1$, as well as $\delta/U_{LR} = -6$ for $eV/U_{LR} \lesssim -1$, see figures 7(c) and (d). In the case of infinite on-site Coulomb interactions, the current was fully suppressed due to the triplet blockade, and so were the current cross-correlations. In the case of finite U, the cross-correlations have a positive sign in this regime, indicating a current leakage through the states with doubly occupied dots.

4. Conclusions

In this paper we have analyzed the current–current cross-correlations in a double quantum dot based Cooper pair splitter with ferromagnetic leads. We focused on the transport regime where the current flows due to Andreev reflection processes and the calculations were performed by using the real-time diagrammatic technique. First, we considered the case of infinite Coulomb on-site correlations on the dots, when the current is purely due to crossed Andreev reflection processes. We showed that the cross-correlations are then positive in the full range of bias voltage and DQD detuning parameter, and are larger in the case of antiparallel magnetic configuration compared to the parallel one. Moreover, we analyzed the effect of finite hopping between the dots and demonstrated that it can induce negative current cross-correlations that greatly depend on the degree of spin polarization of the leads and magnetic configuration of the device.

We also considered the case of finite Coulomb correlations on the dots and analyzed the transport behavior in the full parameter space. It turned out that there are regimes of negative cross-correlations even in the absence of hopping between the dots. The mechanism responsible for negative correlations between the currents flowing through both junctions is generally associated with odd-electron states that are delocalized over the two quantum dots. Because positive current cross-correlations can be related to high Cooper pair splitting efficiency, the presented results point out the important conditions and parameters for optimizing the operation of Cooper pair splitters based on double quantum dots.

Acknowledgments

References

[1] Choi M S, Bruder C and Loss D 2000 *Phys. Rev.* B **62** 13569
[2] Recher P, Sukhorukov E V and Loss D 2001 *Phys. Rev.* B **63** 165314
[3] Feng J F and Xiong S J 2003 *Phys. Rev.* B **67** 045316
[4] Cao X F, Shi Y, Song X, Zhou S and Chen H 2004 *Phys. Rev.* B **70** 235341
[5] Zhang P and Li Y X 2009 *J. Phys.: Condens. Matter.* **21** 095602
[6] De Franceschi S, Kouwenhoven L, Schönenberger C and Wernsdorfer W 2010 *Nat. Nanotechnol.* **5** 703
[7] Hofstetter L, Geresdi A, Aagesen M, Nygård J, Schönenberger C and Csonka S 2010 *Phys. Rev. Lett.* **104** 246804
[8] Siqueira E C and Cabrera G G 2010 *Phys. Rev.* B **81** 094526
[9] Sothmann B, Futterer D, Governale M and König J 2010 *Phys. Rev.* B **82** 094514
[10] Martín-Rodero A and Yeyati A L 2011 *Adv. Phys.* **60** 899
[11] Braggio A, Governale M, Pala M G and König J 2011 *Solid State Commun.* **151** 155
[12] Gramich J, Baumgartner A and Schönenberger C 2015 *Phys. Rev. Lett.* **115** 216801
[13] Droste S, Splettstoesser J and Governale M 2015 *Phys. Rev.* B **91** 125401
[14] Weymann I and Wójcik K P 2015 *Phys. Rev.* B **92** 245307
[15] Su Z, Tacla A B, Hocevar M, Car S, Plissard S R, Bakkers E, Daley A J, Pekker D and Frolov S M 2016 arXiv:1611.00727v3
[16] Gramich J, Baumgartner A and Schönenberger C 2016 *Appl. Phys. Lett.* **108** 172604
[17] Hwang S-Y, López R and Sánchez D 2016 *Phys. Rev.* B **94** 054506
[18] Głodzik S, Wójcik K P, Weymann I and Domański T 2017 *Phys. Rev.* B **95** 125419
[19] Russo S, Kroug M, Klapwijk T M and Morpurgo A F 2005 *Phys. Rev. Lett.* **95** 027002
[20] Hofstetter L, Csonka S, Nygard J and Schönenberger C 2009 *Nature* **461** 960
[21] Herrmann L G, Portier F, Roche P, Yeyati A L, Kontos T and Strunk C 2010 *Phys. Rev. Lett.* **104** 026801
[22] Hofstetter L, Csonka S, Baumgartner A, Fülöp G, d'Hollosy S, Nygård J and Schönenberger C 2011 *Phys. Rev. Lett.* **107** 136801
[23] Schindele J, Baumgartner A and Schönenberger C 2012 *Phys. Rev. Lett.* **109** 157002
[24] Fülöp G, d'Hollosy S, Baumgartner A, Makk P, Guzenko V A, Madsen M H, Nygard J, Schönenberger C and Csonka S 2014 *Phys. Rev.* B **90** 235412
[25] Tan Z B, Cox D, Nieminen T, Lahteenmaki P, Golubev D, Lesovik G B and Hakonen P J 2015 *Phys. Rev. Lett.* **114** 096602
[26] Fülöp G *et al* 2015 *Phys. Rev. Lett.* **115** 227003
[27] Domínguez F and Yeyati A L 2016 *Physica* E **75** 322–9
[28] Gramich J, Baumgartner A and Schönenberger C 2016 arXiv:1612.01201
[29] Hussein R, Braggio A and Governale M 2016 arXiv:1609.01902v1
[30] Hussein R, Jaurigue L, Governale M and Braggio A 2016 *Phys. Rev.* B **94** 235134
[31] Andreev A F 1964 *Sov. Phys.—JETP* **19** 1228
[32] Yu L 1965 *Acta Phys. Sin.* **21** 75
Shiba H 1968 *Prog. Theor. Phys.* **40** 435
Rusinov A I 1969 Containing paramagnetic impurites *Sov. Phys.—JETP* **29** 1101

[33] Lee E J H, Jiang Z, Aguado R, Katsaros G, Lieber C M and De Franceschi S 2012 *Phys. Rev. Lett.* **109** 186802

[34] Lee E J H, Jiang X, Houzet M, Aguado R, Lieber C M and De Franceschi S 2014 *Nat. Nanotechnol.* **9** 79

[35] Schindele J, Baumgartner A, Maurand R, Weiss M and Schönenberger C 2014 *Phys. Rev. B* **89** 045422

[36] Kumar A, Gaim M, Steininger D, Yeyati A L, Martin-Rodero A, Hüttel A K and Strunk C 2014 *Phys. Rev. B* **89** 075428

[37] Futterer D, Governale M, Pala M G and König J 2009 *Phys. Rev. B* **79** 054505

[38] Eldridge J, Pala M G, Governale M and König J 2010 *Phys. Rev. B* **82** 184507

[39] Bocian K and Rudziński W 2013 *Eur. Phys. J. B* **86** 439

[40] Weymann I and Trocha P 2014 *Phys. Rev. B* **89** 115305

[41] Wójcik K P and Weymann I 2014 *Phys. Rev. B* **89** 165303

[42] Trocha P and Barnaś J 2014 *Phys. Rev. B* **89** 245418

[43] Trocha P and Weymann I 2015 *Phys. Rev. B* **91** 235424

[44] Michałek G, Domański T and Wysokiński K I 2017 *J. Supercond. Nov. Magn.* **30** 135

[45] Beckmann D, Weber H B and Löhneysen H V 2004 *Phys. Rev. Lett.* **93** 197003

[46] Blanter Y M and Büttiker M 2000 *Phys. Rep.* **336** 1–66

[47] Sukhorukov E V, Jordan A N, Gustavsson S, Leturcq R, Ihn T and Ensslin K 2007 *Nat. Phys.* **3** 243

[48] McClure D T, DiCarlo L, Zhang Y, Engel H A, Marcus C M, Hanson M P and Gossard A C 2007 *Phys. Rev. Lett.* **98** 056801

[49] Das A, Ronen Y, Heiblum M, Mahalu D, Kretinin A V and Shtrikman H 2012 *Nat. Commun.* **3** 1165

[50] Bignon G, Houzet M, Pistolesi F and Hekking F W J 2004 *Europhys. Lett.* **67** 110

[51] Mélin R, Benjamin C and Martin T 2008 *Phys. Rev. B* **77** 094512

[52] Dong B, Lei X L and Horing N J M 2009 *Phys. Rev. B* **80** 153305

[53] Freyn A, Flöser M and Mélin R 2010 *Phys. Rev. B* **82** 014510

[54] Chevallier D, Rech J, Jonckheere T and Martin T 2011 *Phys. Rev. B* **83** 125421

[55] Rech J, Chevallier D, Jonckheere T and Martin T 2012 *Phys. Rev. B* **85** 035419

[56] Riwar R P, Badiane D M, Houzet M, Meyer J S and Nazarov Y V 2016 *Physica* E **76** 231–7

[57] Schoeller H and Schön G 1994 *Phys. Rev. B* **50** 18436
König J, Schmid J, Schoeller H and Schön G 1996 *Phys. Rev. B* **54** 16820

[58] Thielmann A, Hettler M H, König J and Schön G 2005 *Phys. Rev. Lett.* **95** 146806

[59] Hannes W-R and Titov M 2008 *Phys. Rev. B* **77** 115323

[60] Kłobus W, Grudka A, Baumgartner A, Tomaszewski D, Schönenberger C and Martinek J 2014 *Phys. Rev. B* **89** 125404

[61] Braunecker B, Burset P and Yeyati A L 2013 *Phys. Rev. Lett.* **111** 136806

[62] Rozhkov A V and Arovas D P 2000 *Phys. Rev. B* **62** 6687

[63] Heinrich B W, Braun L, Pascual J I and Franke K J 2013 *Nat. Phys.* **9** 765

[64] Pala M G, Governale M and König J 2007 *New J. Phys.* **9** 278

[65] Governale M, Pala M G and König J 2008 *Phys. Rev. B* **77** 134513

[66] Weymann I 2009 *Phys. Rev. B* **78** 045310

[67] Glazman L I and Matveev K A 1989 *JETP Lett.* **49** 659

[68] Avishai Y, Golub A and Zaikin A D 2003 *Phys. Rev. B* **67** 041301

[69] Yeyati A L, Martin-Rodero A and Vecino E 2003 *Phys. Rev. Lett.* **91** 266802

82

Cross-correlations in a quantum dot Cooper pair splitter with ferromagnetic leads

Piotr Trocha and Kacper Wrześniewski

Faculty of Physics, Adam Mickiewicz University, 61-614 Poznań, Poland

E-mail: ptrocha@amu.edu.pl

CrossMark

Abstract

We investigate Andreev transport through a quantum dot attached to two external ferromagnetic leads and one superconducting electrode. The transport properties of the system are studied by means of the real-time diagrammatic technique in the sequential tunneling regime. To distinguish various contributions to Andreev current we calculate the current cross-correlations, i.e. correlations between currents flowing through two junctions with normal leads. We analyze dependence of current cross-correlations on various parameters of the considered model, both in linear and nonlinear transport regimes. The processes and mechanisms leading to enhancement, suppression or sign change of current cross-correlations are examined and discussed. Interestingly, our results show that for specific transport regimes splitted Cooper pair results in two uncorrelated electrons. However, utilizing ferromagnetic leads instead of non-magnetic electrodes can result in positive current cross-correlations.

Keywords: Cooper pair splitters, current cross-correlations, quantum dot, Andreev transport

(Some figures may appear in colour only in the online journal)

1. Introduction

Electronic transport phenomena in hybrid quantum dot (QD) systems have recently attracted great attention [1–12]. Particularly, QD systems with one superconducting lead and two normal metal electrodes enable creation of nonlocal entangled electron pairs [13–17]. Moreover, the splitting of Cooper pairs into two spatially separated electrodes has been demonstrated experimentally in a carbon nanotube double quantum dot system [18–20]. These investigations are important both from the fundamental point of view and also for future applications in quantum computing [21].

When the applied bias voltage window is in the superconducting gap, the current flows mainly due to Andreev reflection processes [22] while the quasiparticle tunneling becomes negligible in the low temperature limit. Generally, in-gap tunneling processes can occur via direct Andreev reflection (DAR), crossed Andreev reflection (CAR), or elastic cotunneling (EC). Under certain conditions, by properly changing device parameters, one can tune the contributions due to CAR and DAR, or EC processes or even suppress one of them. Thus, a tool which allows to distinguish these contributions is

sought. An important one seems to be given by current cross-correlations, i.e. correlations calculated between currents flowing through two junctions with normal leads [23, 24].

The current cross-correlations deliver a deeper insight into tunneling processes contributing to electronic transport [25] and has been reported experimentally [26–28] in various setups. Generally, positive current cross-correlations can be attributed with interactions supporting currents in both junctions. Especially, they are present in systems with superconducting electrodes [29–38], like Cooper pair splitters, in which enhancement of positive current cross-correlations can be associated with high Cooper pair splitting efficiency. On the other hand, positive current cross-correlations can be suppressed by interactions, which mutually block the currents flowing through two junctions. The tunneling processes that occur in opposite directions are associated with negative sign of cross-correlations.

Interestingly, negative current cross-correlations in electron beam splitter device have been observed experimentally in a Hanbury Brown–Twiss setup [39, 40]. Moreover, in a paramagnetic multiterminal quantum dot current cross-correlations have been found to be negative [41]. However, in

a three-terminal QD system coupled to ferromagnetic leads some positive cross-correlations between output currents can appear as a result of dynamical spin blockade on the dot not observed in the paramagnetic case [42].

The current cross-correlations are also useful for determining the efficiency and fidelity of an electron-entangler device and allow to formulate Bell-type inequalities [43, 44]. Their violation provides an evidence of nonlocality of split pairs of electrons.

One should also bear in mind that positive current cross-correlations noticed in hybrid superconducting structures are not always due to CAR processes [33, 45]. For instance, such situation has been predicted for normal metal-superconductor-normal metal hybrid structures with highly transparent interfaces [45].

In hybrid QD's systems being in proximity to superconductor the formation of entangled electrons' pairs seems to be rather natural. Therefore, superconducting lead acts as a source of entangled pairs of electrons as its ground state is occupied by Cooper pairs in a spin-singlet state. Furthermore, these Cooper pairs can be extracted from a superconductor by tunneling through the dot's states into the normal metal leads. However, two Andreev tunneling processes have to be distinguished: direct Andreev reflection (DAR) and crossed Andreev reflection (CAR). The former process occurs when Cooper pair extracted from superconductor is transmitted to the same normal lead, whereas in the latter one, entangled pair of electrons leaving the superconductor is split into its individual electrons which end in two spatially-separated leads. A minimal condition to assure the split electrons stay correlated is that the coherence length of Cooper pair has to exceed the width of the superconducting source contact. In an efficient electron entangler, which converts a charge current to a flux of spin-entangled electron pairs, the CAR processes have to be enforced. By analyzing current cross-correlations one is able to distinguish regions in device's parameters space with high and low Cooper pairs splitting efficiency. Particulary, large positive cross-correlations can be associated with enhancement in Cooper pair splitting efficiency, while small values of the aforementioned quantity indicate low splitter's efficiency.

In this paper, we study dependence of current cross-correlations on various parameters of the considered model focusing on the in-gap transport regime. The processes and mechanisms leading to enhancement or suppression of current cross-correlations are examined and discussed. Moreover, the influence of external magnetic field and ferromagnetism of external leads on current cross-correlations is also investigated. We use the real-time diagrammatic technique to calculate transport characteristics. In general, the external weakly coupled leads are assumed to be metallic ferromagnetic electrodes. We consider collinear magnetic configurations i.e. when magnetic moments of both leads are aligned in the same directions (parallel) or oppositely (antiparallel).

The paper is organized in the following way: in section 2 we introduce the model of the system and present theoretical background. This includes description of the model and also description of the method used to calculate quantities
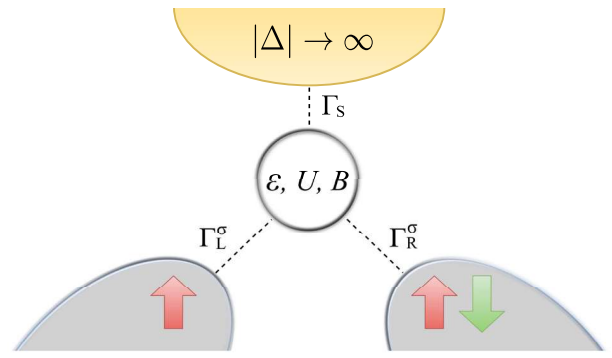

Figure 1. Schematic picture of the QD system coupled to two normal metal and one superconducting leads.

of interest. In section 3, numerical results are presented and discussed. In this section we distinguish the cases of leads with and without spin polarization. Additionally, the cases of system with and without external magnetic field are considered separately. Finally, section 4 includes a brief summary and general conclusions.

2. Theoretical description

The system taken into consideration consists of single-level quantum dot attached to two normal metal and one superconducting lead as shown in figure 1.

The Hamiltonian of the system acquires the following form:

$$H = \sum_{\beta=L,R} H_\beta + H_S + H_{\mathrm{QD}} + H_T, \tag{1}$$

where the first term, H_β for $\beta = L, R$, describes the left (L) and right (R) electrodes in the noninteracting quasiparticle approximation, $H_\beta = \sum_{\mathbf{k}\sigma} \varepsilon_{\mathbf{k}\beta\sigma} c_{\mathbf{k}\beta\sigma}^\dagger c_{\mathbf{k}\beta\sigma}$ with $\varepsilon_{\mathbf{k}\beta\sigma}$ denoting the single particle energy.

The second term in equation (1) describes the s-wave BCS superconducting lead in the mean field approximation

$$H_S = \sum_{\mathbf{k},\sigma} \varepsilon_{\mathbf{k}S} c_{\mathbf{k}S}^\dagger c_{\mathbf{k}S} + \sum_{\mathbf{k}} \left(\Delta^* c_{\mathbf{k}S\downarrow} c_{-\mathbf{k}S\uparrow} + \Delta c_{-\mathbf{k}S\uparrow}^\dagger c_{\mathbf{k}S\downarrow}^\dagger \right), \tag{2}$$

with $\varepsilon_{\mathbf{k}S}$ denoting the relevant single-particle energy and Δ, assumed real and positive, standing for the order parameter of the superconductor.

The third term of Hamiltonian describes single-level quantum dot and acquires the following form:

$$H_{\mathrm{QD}} = \sum_\sigma \varepsilon_\sigma d_\sigma^\dagger d_\sigma + U n_\uparrow n_\downarrow, \tag{3}$$

where ε_σ and U denote the spin dependent dot's energy level and the corresponding Coulomb integral. Applying external magnetic field dot's energy level becomes split, $\varepsilon_\sigma = \varepsilon \pm B/2$ with B denoting Zeeman splitting energy.

Finally, tunneling of electrons between the leads (L, R, S) and the quantum dot can be modelled by the Hamiltonian

$$H_T = \sum_{\mathbf{k}\sigma} \sum_{\beta=L,R,S} (V^{\beta}_{\mathbf{k}\sigma} c^{\dagger}_{\mathbf{k}\beta\sigma} d_{\sigma} + \text{h.c.}) \quad (4)$$

with $V^{\beta}_{\mathbf{k}\sigma}$ denoting the relevant tunneling matrix elements.

In the wide band approximation dot's coupling to the normal metal electrodes can be assumed to be energy independent and constant, $\Gamma^{\sigma}_L = \Gamma_L(1 + \tilde{\sigma}p)$, and $\Gamma^{\sigma}_R = \Gamma_R(1 + \eta\tilde{\sigma}p)$ with $\tilde{\sigma} = 1$ for $\sigma = \uparrow$ and $\tilde{\sigma} = -1$ for $\sigma = \downarrow$. Here, p denotes the spin polarization of magnetic leads assumed the same for the left and right electrodes, whereas $\eta = \pm 1$ for parallel (upper sign) and antiparallel (lower sign) magnetic alignment of ferromagnetic leads. Furthermore, we assume symmetric couplings, $\Gamma_L = \Gamma_R \equiv \Gamma/2$.

As we are interested in Andreev transport regime we can take the limit of an infinite superconducting gap, $\Delta \to \infty$. Then the quantum dot coupled to the superconducting lead is described by an effective Hamiltonian [46]:

$$H^{\text{eff}}_{\text{QD}} = \sum_{\sigma} \varepsilon_{\sigma} d^{\dagger}_{\sigma} d_{\sigma} + U n_{\uparrow} n_{\downarrow} - \frac{\Gamma_S}{2} \left(d^{\dagger}_{\uparrow} d^{\dagger}_{\downarrow} + d_{\downarrow} d_{\uparrow} \right) \quad (5)$$

where the effective pair potential Γ_S is the coupling strength between the dot and superconducting electrode and acquires the form $\Gamma_S = 2\pi |V^S|^2 \rho_S$ with ρ_S denoting BCS density of states in the normal state.

The eigenstates of the effective dot's Hamiltonian are as follows: $|\sigma\rangle$, and $|\pm\rangle = 1/\sqrt{2} \left(\sqrt{1 \mp \delta/(2\varepsilon_A)}|0\rangle \mp \sqrt{1 \pm \delta/(2\varepsilon_A)}|2\rangle \right)$, while the corresponding eigen-energies are: $E_{\uparrow} = \varepsilon_{\uparrow}$, $E_{\downarrow} = \varepsilon_{\downarrow}$, and $E_{\pm} = \delta/2 \pm \varepsilon_A$, with $\delta = \varepsilon_{\uparrow} + \varepsilon_{\downarrow} + U$. Here, $\varepsilon_A = \sqrt{\delta^2 + \Gamma^2_S}/2$ measures the energy difference between the states $|+\rangle$ and $|-\rangle$.

The Andreev bound states' energies are defined as:

$$E^{\Lambda}_{\alpha,\beta} = \alpha\frac{U}{2} + \frac{\beta}{2}\sqrt{\delta^2 + \Gamma^2_S}, \quad (6)$$

where $\alpha, \beta = \pm$. These energies are the excitation energies of the dot decoupled from the normal metal leads.

In order to determine the transport properties of the system we employ the real-time diagrammatic technique [47–49]. The stationary occupation probability p^{st}_{χ} of a state $|\chi\rangle$ can be found from:

$$\mathbf{W}\mathbf{p}^{\text{st}} = 0, \quad (7)$$

where $\mathbf{p}^{\text{st}}$ is the vector containing probabilities p^{st}_{χ} and the elements $W_{\chi\chi'}$ of self-energy matrix $\mathbf{W}$ account for transitions between the states $|\chi\rangle$ and $|\chi'\rangle$.

The current flowing through the junction with lead $\alpha = (L, R)$ can be found from:

$$I_{\alpha} = \frac{e}{2\hbar}\text{Tr}\left\{\mathbf{W}^{I_{\alpha}}\mathbf{p}^{\text{st}}\right\}, \quad (8)$$

where the self-energy matrix $\mathbf{W}^{I_{\alpha}}$ is similar to $\mathbf{W}$, but it takes into account the number of electrons transferred through a given junction.

The current cross-correlations in the sequential tunneling approximation, S_{LR}, are defined as [48]:

$$S_{\text{LR}} = \frac{e^2}{\hbar}\text{Tr}\left\{\left[\mathbf{W}^{I_L}\mathbf{P}\mathbf{W}^{I_R} + \mathbf{W}^{I_R}\mathbf{P}\mathbf{W}^{I_L}\right]\mathbf{p}^{\text{st}}\right\}, \quad (9)$$

where the propagator $\mathbf{P}$ is determined from $\mathbf{W}\mathbf{P} = \mathbf{p}^{\text{st}}\mathbf{e}^T - \mathbf{1}$, with $\mathbf{e}^T = (1, 1, \dots, 1)$.

3. Numerical results

We present the numerical results for Andreev transport assuming large superconducting-gap limit. Here, we show the differential conductance associated with current injected/extracted into/from superconductor and the corresponding current cross-correlations. The differential conductance, G_S, is calculated as $G_S = dI_S/dV$ with I_S denoting Andreev current. The Andreev current is simply obtained from Kirchoff's law as $I_S = I_L + I_R$.

The section is divided into two parts. In the first part of the section the case of nonmagnetic external electrodes $(p = 0)$ is considered, whereas in the second part we investigate the case of magnetic leads $(p \neq 0)$. Moreover, throughout the sections we consider two distinct cases, with and without external magnetic field leading to finite or no Zeeman splitting.

3.1. Nonmagnetic leads (p = 0)

In this section the transport properties of QD coupled to one superconducting electrode and two nonmagnetic metallic leads are considered. The differential conductance and corresponding current cross-correlations are calculated for two cases. The former case corresponds to situation when no external magnetic field is applied, whereas in the latter one the influence of magnetic field is taken into account.

3.1.1. No external magnetic field, B = 0. The differential conductance G_S corresponding to Andreev current and the respective current cross-correlations S_{LR} calculated for zero magnetic field, $B = 0$, are shown in figure 2 as a function of bias voltage applied to the two normal leads. The system is biased in the following way: $\mu_L = \mu_R = eV$ and grounding the superconducting electrode $\mu_S = 0$. We introduce detuning parameter, $\delta = 2\varepsilon + U$, for spin-degenerate dot's level, i.e. for $\varepsilon_{\uparrow} = \varepsilon_{\downarrow} \equiv \varepsilon$.

First of all, one can notice that differential conductance obeys the symmetry, $G_S(\delta, eV) = G_S(-\delta, -eV)$. Due to the fact that the Andreev current (not shown) is optimized when particle-hole symmetry holds, it becomes significant only for small detuning δ. As a result, G_S acquires the largest values for δ close to zero. The differential conductance, G_S, reveals a peak each time the electrochemical potential of normal metal leads crosses one of the Andreev levels. Generally, for zero magnetic field, G_S exhibits four peaks associated with four Andreev levels. However, for $|\delta| = \sqrt{U^2 - \Gamma^2_S}$ only three peaks appear as the states E^{+-}_A and E^{-+}_A become degenerate. Moreover, G_S is asymmetric with respect to the bias reversal for finite detuning $\delta \neq 0$, which is directly related with the behavior of the Andreev current.
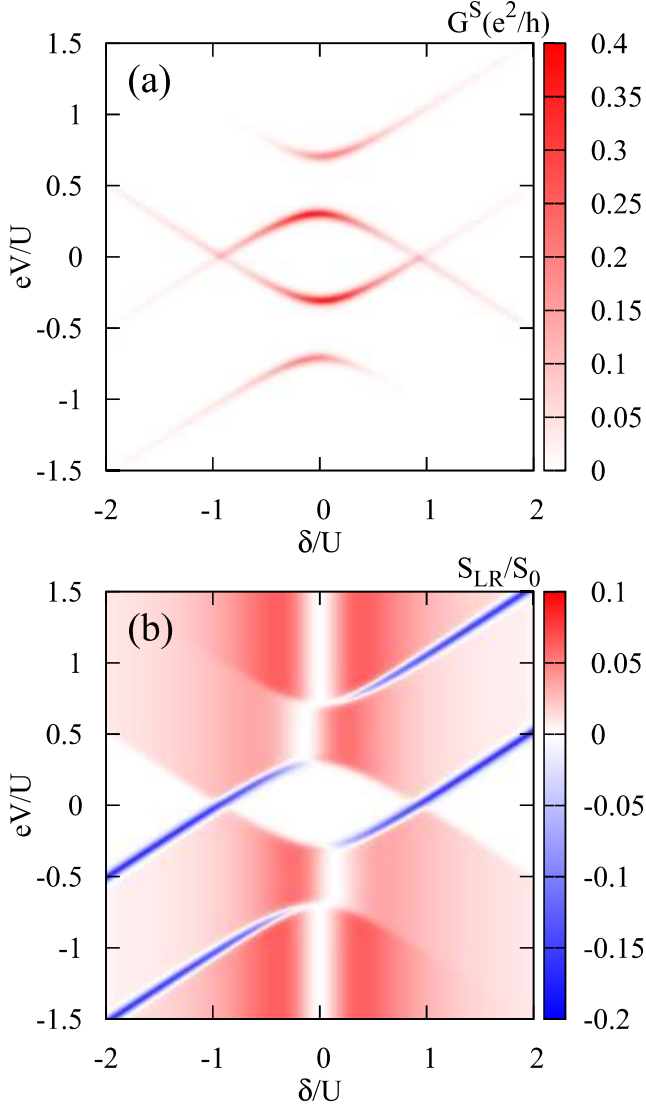
Figure 2. Differential conductance G_S (a) and corresponding current cross-correlations (b) as a function of bias voltage and detuning δ calculated for magnetic field, $B = 0$. The other parameters are: $U = 1$ (used as energy unit), $\Gamma_S = 0.4$, $\Gamma = 0.01$ and $T = 0.015$, with $S_0 = e^2\Gamma/\hbar$.

In figure 2(b) the corresponding current cross-correlations, S_{LR}, are shown. One can notice that S_{LR} vanishes in the Coulomb blockade regime when the dot is occupied by single electron, i.e. for $E_{+-} < eV < E_{-+}$ and for $|\delta| < \sqrt{U^2 - \Gamma_S^2}$. This is the result of vanishing current in the Coulomb blockade regime as two electrons are required to form Cooper pair. The current cross-correlations also vanish for $|\delta| > \sqrt{U^2 - \Gamma_S^2}$ and for small bias voltage, $E_A^{+-} < eV < E_A^{-+}$, when no current flows. These regions corresponds to empty or doubly occupied dot regime. For most regions, where the current can flow, S_{LR} acquires positive values, which indicates that CAR processes give main contribution to the current. Interestingly, S_{LR} exhibits also negative values. Specifically, S_{LR} becomes negative when bias voltage passes through E_{-+}^A for $\delta \gtrsim 0$ and for $\delta \lesssim 0$ when $eV \approx E_{+-}^A$. Another two regions of negative

current cross-correlations appear for $\delta > 0$ when $eV \approx E_{++}^A$ and for $\delta < 0$ when $eV \approx E_{--}^A$. This happens each time the bias voltage eV approaches dot's level ε or $\varepsilon + U$. Then, single electron can tunnel from the left lead onto the dot and re-tunnel into the right lead. Reverse tunneling processes $(R \to L)$ occur with the same probability. Hence, there is no net charge current, but these processes give contribution to the current cross-correlation, specifically to its negative values, indicating that tunneling processes by left and right junctions occur in opposite directions and compensate each other.

It is worth noting that S_{LR} vanishes in the vicinity of particle-hole symmetry point ($\delta \approx 0$) for $eV > E_{++}^A$ and for $eV < E_{--}^A$, irrespective of the presence of magnetic field. However, it can not be stated that Andreev current flows only due to DAR processes although S_{LR} vanishes. According to symmetry of the system, both DAR and CAR processes equally contribute to the Andreev transport. It is enough to consider positive bias case with $eV > E_{++}^A$ as for negative bias voltage with $eV < E_{--}^A$ an analogous discussion can be applied. Due to strong coupling between the dot and super-conducting lead ($\Gamma_S \gg \Gamma$) fast coherent oscillations of Cooper pairs occur between QD and superconductor. These coherent oscillations are occasionally interrupted by tunneling of single electron from normal lead (left or right). The average interval of time between tunneling of an electron from normal lead into the dot is relatively large ($2\hbar/\Gamma$) comparing with the Cooper pairs oscillations' period ($2\hbar/\Gamma_S$). Thus, from the point of view of normal leads, single electrons tunnel into the dot inde-pendently (of the oscillations) [50]. Thus, such uncorrelated single-electron tunneling events of two subsequent electrons originating from different normal leads can not give impact to S_{LR}. To support the above explanation let us present more formal considerations. The zero-frequency cross-correlations between the currents flowing through the left and right junc-tions can be defined as follows:

$$S_{LR} = \int_{-\infty}^{\infty} dt \langle \delta I_L(t) \delta I_R(0) + \delta I_R(0) \delta I_L(t) \rangle, \quad (10)$$

with $\delta I_\alpha(t) = \hat{I}_\alpha(t) - \langle \hat{I}_\alpha \rangle$ and $\hat{I}_\alpha$ being the current operator.

For bias voltages $eV > E_{++}^A$ and for $eV < E_{--}^A$ in the particle-hole symmetry point ($\delta/U = 0$) the Andreev current is maximized, but simultaneously the current cross-correla-tions are completely suppressed, i.e. $S_{LR} = 0$. This behavior can be explained by analysing the states' probabilities of the quantum dot and matrix elements of current matrices W^{I_α} for discussed transport parameters. The probability of occupation of each available states, i.e. $|+\rangle, |-\rangle, |\uparrow\rangle$ and $|\downarrow\rangle$ is the same and equals to $p_\chi = 1/4$ with $\chi = +, -, \uparrow, \downarrow$. Moreover, all non-zero matrix W^{I_α} elements for both left and right junctions are equal as well, which means that all possible tunneling events have equal and maximal rates, with left/right junction indifference. This results in a constant average current in each (left/right) junction of equal value. Moreover, it turns out that the currents through both junctions are constant in time. This has been checked by solving rate equation $\dot{\mathbf{p}}(t) = \mathbf{W}\mathbf{p}(t)$ and calculating time evolution of currents through left and right junction. As a result, there are no fluctuations of the current
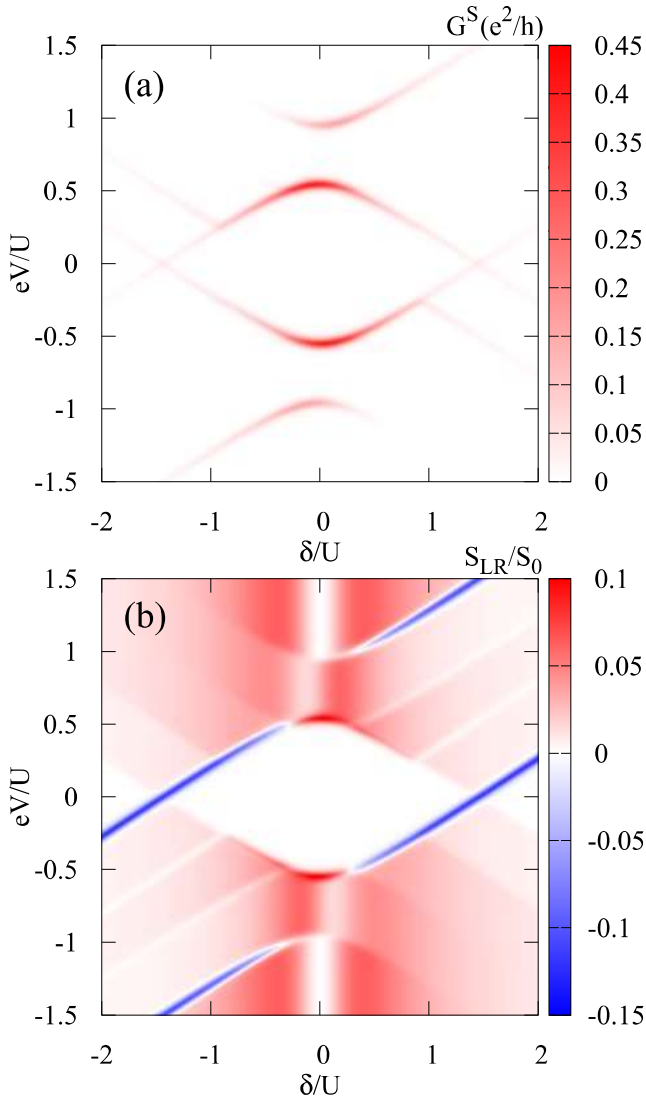
Figure 3. Differential conductance G_S (a) and corresponding current cross-correlations (b) as a function of bias voltage and detuning δ calculated for magnetic field, $B/U = 0.5$. The other parameters are as in figure 2.

away from the average value, i.e. $\delta I_\alpha(t) = \hat{I}_\alpha(t) - \langle \hat{I}_\alpha \rangle = 0$, and thus, $S_{LR} = 0$.

Similar considerations can be applied for bias voltage $E^A_{-+} < eV < E^A_{++}$ as well as for $E^A_{--} < eV < E^A_{+-}$. However, now the zero current cross-correlations are realized for slightly shifted δ from particle-hole symmetry point. In the former case, $S_{LR} = 0$ is noticed around $\delta = -\frac{\sqrt{2}}{4}\Gamma_S$, whereas for the latter one, current cross-correlations vanish for $\delta = \frac{\sqrt{2}}{4}\Gamma_S$.

3.1.2. Finite external magnetic field, $B \neq 0$. Applying finite magnetic field leads to the splitting of the Andreev bound states and to doubling of corresponding excitation energies. Now, Andreev excitation energies acquire the following form, $E^A_{\alpha,\beta,\gamma} = E^A_{\alpha,\beta} + \gamma\frac{B}{2}$ with $\gamma = \pm 1$. As a result, more peaks appear in the differential conductance, see e.g. figure 3(a) calculated for $B/U = 0.5$. One can notice that the range of

Coulomb blockade becomes enlarged, as filling the dot with second electron cost the energy $\varepsilon_\uparrow + U$.

In the case of finite magnetic field the current cross-correlations reveal rather minor qualitative and quantitative differences disregarding the effect due to Andreev bound states splitting. First of all, the maximal positive values of current cross-correlations are of the same order as these corresponding to zero magnetic field case. In turn, the negative values of current cross-correlations become slightly increased. Due to additional Andreev bound states originating from Zeeman splitting S_{LR} exhibits more steps. However, the number of regions where S_{LR} is negative becomes independent of magnetic field. In the remaining regions between the steps S_{LR} vanishes instead of acquiring negative values. The most striking qualitative difference in S_{LR} generated by magnetic field is associated an enhancement of positive current cross-correlations when eV crosses through E^A_{+-+} (E^A_{-+-}) for $\delta \in (-\sqrt{B^2 - \Gamma_S^2}, \sqrt{U^2 - \Gamma_S^2})$ ($\delta \in (-\sqrt{U^2 - \Gamma_S^2}, \sqrt{B^2 - \Gamma_S^2},)$), i.e. for bias voltages for which QD passes from singly occupied state to doubly or empty state, respectively, allowing for CAR processes to occur. The widths of these peaks in S_{LR} becomes smaller with decreasing temperature and disappear in the limit $T \to 0$.

3.2. Magnetic leads ($p > 0$)

So far, the calculations have been performed for QD Cooper pair beam splitters with nonmagnetic leads. However, because using ferromagnetic leads can be important to estimate entanglement between split electrons [51], here, we provide comprehensive study of transport properties of the QD Cooper beam splitters with ferromagnetic contacts.

In this section, the effects arising due to magnetism of external weakly coupled leads are considered. Now, the left and right electrodes are spin polarized and the strength of the external leads' polarization is described by spin polarization factor, p, assumed equal for both ferromagnetic electrodes. Here, we consider collinear magnetic configurations of ferromagnetic leads: parallel (P) and antiparallel (AP). The former one corresponds to the situation when magnetic moments of ferromagnetic leads are aligned in the same direction, whereas in the latter one they align in the opposite directions.

Let us first consider parallel magnetic configuration. In this case the differential conductance (figure 4(a)) reveals several differences comparing with nonmagnetic situation (figure 2(a)). One can notice that maximal intensity of differential conductance becomes suppressed as the minority carriers determine the Andreev current. Accordingly, in the parallel magnetic configuration the density of states of minority carriers rules the rate of injecting/extracting electron pairs, which becomes the *bottleneck* for the Andreev transport. However, more striking difference is appearance of negative values in the differential conductance. Specifically, negative values of the differential conductance emerge for $|\delta| > \sqrt{U^2 - \Gamma_S^2}$ in the vicinity of Andreev levels E^A_{-+} (E^A_{+-}) for positive (negative) electrochemical potential shift, see figure 4(a). The physical
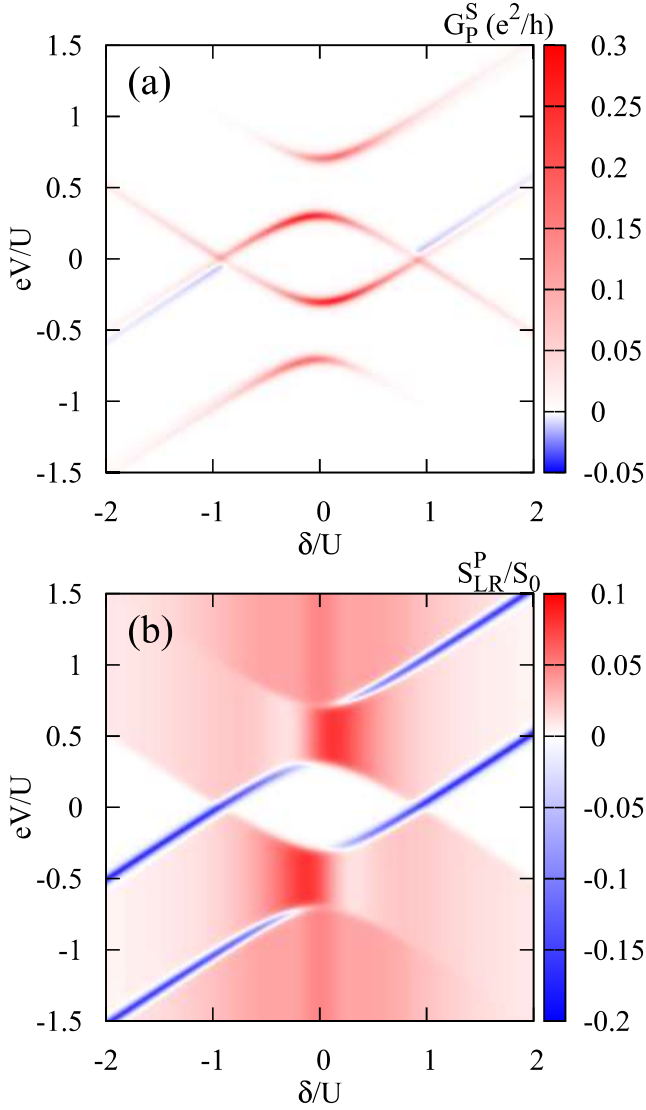
Figure 4. Differential conductance G_S (a) and corresponding current cross-correlations (b) as a function of bias voltage and detuning δ in parallel magnetic configuration P calculated for spin polarization $p = 0.5$. The other parameters are as in figure 2.

Figure 5. Differential conductance G_S (a) and corresponding current cross-correlations (b) as a function of bias voltage and detuning δ in antiparallel magnetic configuration AP calculated for spin polarization $p = 0.5$. The other parameters are as in figure 2.

mechanism leading to negative differential conductance in hybrid three-terminal QD system is due to the nonequilibrium spin accumulation in the dot and has been explained in details in [8].

In turn, in the antiparallel magnetic configuration (figure 5) the differential conductance G_S^{AP} behaves similarly to that one obtained for $p = 0$ because total population of electrons with a given spin direction in both leads remains constant disregarding of the value of p.

On the other hand, current cross-correlations exhibit both qualitative and quantitative differences in both magnetic configurations comparing with $p = 0$ case. First of all, the current cross-correlations become enhanced in the vicinity of particle-hole symmetry point for $eV > E_{++}^A$ and for $eV < E_{--}^A$ in both magnetic configurations (compare figures 4 and 5 with figure 2).
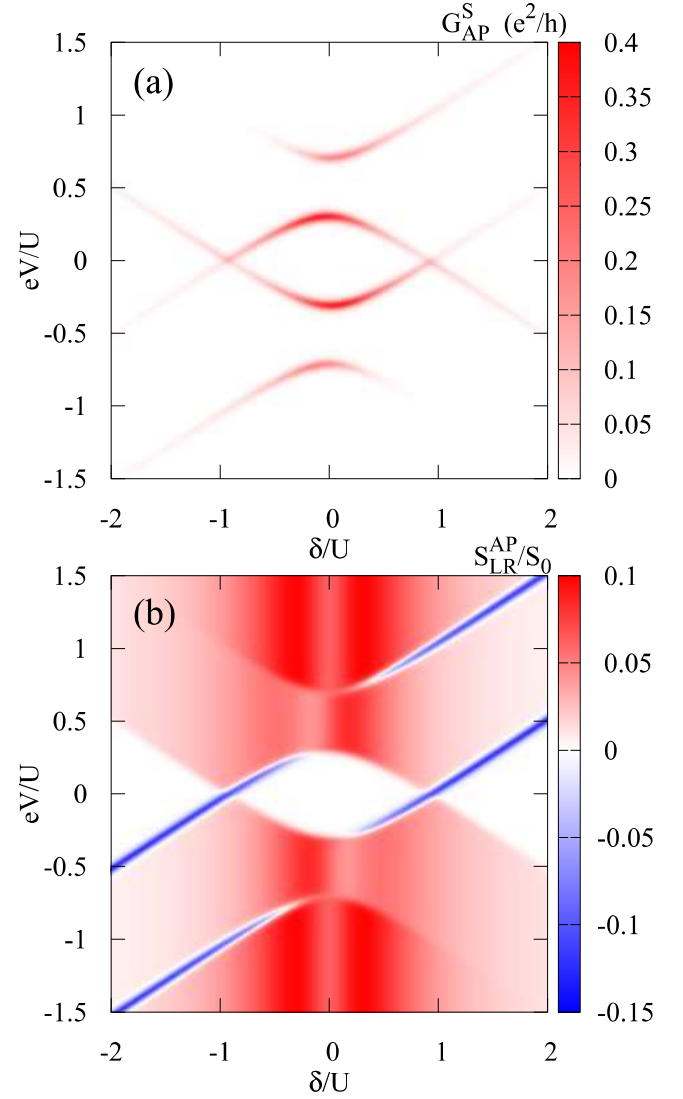
However, maximal positive values of S_{LR} in the P-alignment become suppressed, whereas negative values are slightly increased (in the sense of absolute values) which can be clearly seen in figure 4. In turn, S_{LR} in AP configuration differs significantly from that in P configuration and also from that in the nonmagnetic case. One can notice that current cross-correlations for antiparallel magnetic configuration reach larger maximal values comparing with S_{LR} for both parallel alignment and $p = 0$ case.

To provide a deeper insight into p dependence of Andreev current (I_S) and corresponding current cross-correlation S_{LR}, in both magnetic configurations, we derive some approximative analytical formulas assuming low temperature limit. Here, we concentrate on the particle-hole limit, i.e. $\delta \approx 0$ as for $\delta \neq 0$ the obtained formulas become cumbersome. The corresponding formulas for $\delta \approx 0$ and for $\frac{1}{2}[U - \Gamma_S] \lesssim eV \lesssim \frac{1}{2}[U + \Gamma_S]$ are:

$$I_S^P = \frac{4(1-p^2)}{3+p^2}I_0$$

$$S_{LR}^P = \frac{1+21p^2-29p^4+7p^6}{2(3+p^2)^3}S_0 \qquad (11)$$

for parallel (*P*), and

$$I_S^{AP} = \frac{4}{3}I_0$$

$$S_{LR}^{AP} = \frac{1+9p^2}{54}S_0 \qquad (12)$$

for antiparallel (AP) alignment, where $I_0 = e\Gamma/\hbar$. The analytical formulas for S_{LR} at negative bias voltage $eV < 0$ in the corresponding regions are the same as for $eV > 0$, whereas that for current are obtained from the relation, $I_S(\delta, eV) = -I_S(-\delta, -eV)$.

The above formulas confirm the deduced *p*-dependence of current cross-correlations. Specifically, S_{LR} in parallel magnetic configuration changes nonmonotonically with increasing *p*. For small values of polarization factor S_{LR} grows with increasing *p* until achieving maximum at $p = \sqrt{1/23(27 - 8\sqrt{6})} \approx 0.57$. It is worth noting that such a value of spin polarization is observed for typical ferromagnets. With further increase of *p*, S_{LR} decreases with increasing *p*. Finally, for half-metallic leads ($p = 1$) current cross-correlations vanish and so does the current. In turn, current–current cross-correlations in AP alignment monotonically grow with increasing *p* achieving maximum for half-metallic leads ($p = 1$).

The next step in the current, for $\delta \approx 0$, appears at $eV \gtrsim \frac{1}{2}[U + \Gamma_S]$. In this regime, in the parallel magnetic configuration, the current and the corresponding current cross-correlations are described by the following formulas:

$$I_S^P = 2(1-p^2)I_0$$

$$S_{LR}^P = \frac{p^4(1-p^2)}{4}S_0. \qquad (13)$$

The above formula shows that S_{LR} is non-negative for all values of polarization factor and nonmonotonically depends on *p* achieving maximum at $p = 1/\sqrt{2}$. In AP alignment current becomes independent from spin polarization factor *p* and reaches its maximal value $I_S^{AP} = 2I_0$, while for the current–current cross-correlations one finds $S_{LR}^{AP} = p^2/4$. Increase of S_{LR}^{AP} is a result of enhanced CAR processes at the expense of DAR processes, which become suppressed while increasing *p*.

Moreover, an applied magnetic field influences current and corresponding current cross-correlations. At the first step in the current one finds the following formulas for I_S and S_{LR} calculated for $B/U = 0.5$:

$$I_S^P = \frac{(p-1)(p+1)(p+3)}{2}I_0$$

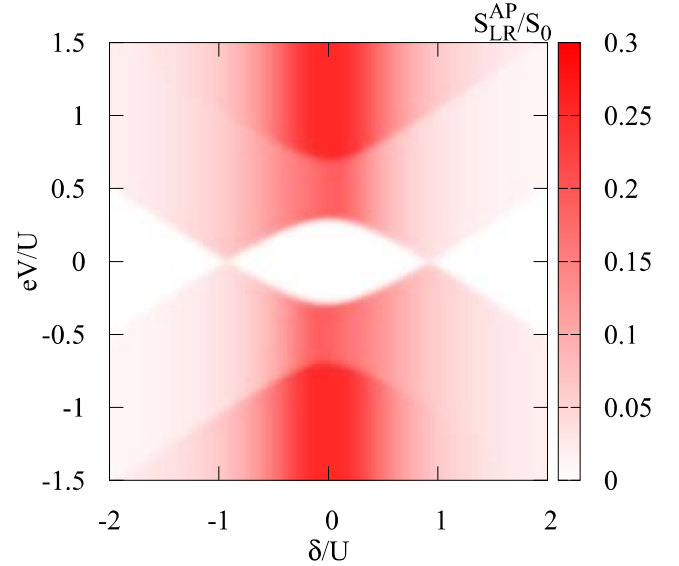$$S_{LR}^P = \frac{(1-p)(1+p)(2-10p+5p^2+12p^3+3p^4)}{64}S_0 \qquad (14)$$

Figure 6. Current cross-correlations as a function of bias voltage and detuning δ in antiparallel magnetic configuration AP calculated for spin polarization $p = 1$. The other parameters are as in figure 2.

in *P* configuration, and

$$I_S^{AP} = \frac{3}{2}I_0$$

$$S_{LR}^{AP} = \frac{2+13p^2}{64}S_0, \qquad (15)$$

in AP configuration. Accordingly, for bias voltages at which the second step in the current occurs both I_S and S_{LR} are not influenced by magnetic field and resulting formulas remain the same as in the absence of magnetic field.

Finally, in the case of half-metallic leads in AP alignment current–current cross-correlations acquire non-negative values in the whole range of bias voltage and detuning parameter δ (see figure 6). This is a result of total blockage of tunneling processes through the left and right junctions in opposite directions, as there are no available states in a given ferromagnetic lead for electrons incoming to the other ferromagnetic electrode. Moreover, both current and current cross-correlations become maximized. Maximization of current cross-correlations is well understood as for half-metallic leads in the AP alignment only CAR processes can contribute to Andreev current, whereas DAR processes are completely blocked, since in given electrode only electrons with one spin orientation are available. From the experimental point of view, such a device can be used for verification of the presence and role of CAR processes. Although, ideal half-metallic leads are rather unaccessible in real systems, one can utilize the change in magnetic configuration of magnetic electrodes from antiparallel to parallel alignment in order to quantify the role of CAR comparing to DAR. Such protocol can be used because any switch of magnetic alignment of the system affects only CAR, whereas DAR processes are not influenced. By comparing the transport properties of the system in both magnetic configurations, some information on CAR can be extracted.

4. Conclusions

In this paper, we have analyzed the current cross-correlations and differential conductance corresponding to the Andreev current flowing in single quantum dot based Cooper pair splitters. We have shown that finite magnetic field leads to the splitting of Andreev bound states, which can be clearly seen in the differential conductance characteristics. The current cross-correlations exhibit both positive and negative values in zero and finite magnetic field. However, finite magnetic field tends to suppress negative values (in the sense of absolute value) of the current cross-correlations and simultaneously it enhances the positive values of this quantity at least in specified regions of transport parameters. Moreover, we have found that in the vicinity of particle-hole symmetry point the current cross-correlations are suppressed to zero and the splitting pairs of electrons ending in two separate normal metal leads become uncorrelated. However, using ferromagnetic leads, in place of nonmagnetic ones, can restore entanglement of pair of split electrons in this transport regime. This finding is important as one wants to obtain large current of entanglement split pairs of electrons and as the Andreev current achieves maximum values in the particle-hole symmetry point.

When external weakly coupled leads are ferromagnetic the behavior of transport properties become more interesting. Especially, we have found negative differential conductance in the parallel magnetic configuration. Moreover, significantly different behavior of current cross-correlations has been found in both magnetic configurations compared to the nonmagnetic case. Furthermore, the dependence of current cross-correlations on leads' polarization factor p has been addressed for both magnetic alignments. Specifically, in the parallel magnetic configuration the current cross-correlations exhibit nonmonotonic behavior with varying p; they reach maximal value for finite polarization factor suggesting that competition between CAR and DAR processes in P alignment is not trivial. On the other hand, in the antiparallel magnetic configuration contribution of CAR processes gradually grows with increasing p, and finally for half-metallic leads $p = 1$, CAR becomes the only source of Andreev current. We have also indicated possible experimental utilization of the considered system in order to quantify the different processes contributed to the transport.

Acknowledgments

ORCID iDs

Piotr Trocha https://orcid.org/0000-0001-7765-8538

References

[1] Martin-Rodero A and Levy Yeyati A 2011 *Adv. Phys.* **60** 899
[2] Futterer D, Governale M, Pala M G and König J 2009 *Phys. Rev. B* **79** 054505
[3] Sothmann B, Futterer D, Governale M and König J 2010 *Phys. Rev. B* **82** 094514
[4] Eldridge J, Pala M G, Governale M and König J 2010 *Phys. Rev. B* **82** 184507
[5] Hofstetter L, Geresdi A, Aagesen M, Nygård J, Schönenberger C and Csonka S 2010 *Phys. Rev. Lett.* **104** 246804
[6] Sadovskyy I A, Lesovik G B, Blatter G, Jonckheere T and Martin T 2012 *Phys. Rev. B* **85** 125442
[7] Wójcik K P and Weymann I 2014 *Phys. Rev. B* **89** 165303
[8] Weymann I and Trocha P 2014 *Phys. Rev. B* **89** 115305
[9] Trocha P and Barnaś J 2014 *Phys. Rev. B* **89** 245418
[10] Trocha P and Weymann I 2015 *Phys. Rev. B* **91** 235424
[11] Feinberg D, Jonckheere T, Rech J, Martin T, Douçot B and Mélin R 2015 *Eur. Phys. J. B* **88** 99
[12] Mélin R, Sotto M, Feinberg D, Caputo J-G and Douçot B 2016 *Phys. Rev. B* **93** 115436
[13] Zhu Y, Sun Q-F and Lin T-H 2001 *Phys. Rev. B* **65** 024516
[14] Sauret O, Feinberg D and Martin T 2004 *Phys. Rev. B* **70** 245313
[15] Chen Z, Wang B, Xing D Y and Wang J 2004 *Appl. Phys. Lett.* **85** 2553
[16] Feng J-F, Wua X-S and Jiang S-S 2006 *J. Appl. Phys.* **99** 08F713
[17] Golubev D S and Zaikin A D 2007 *Phys. Rev. B* **76** 184510
[18] Hofstetter L, Csonka S, Nygård J and Schönenberger C 2010 *Nature* **461** 960
[19] Herrmann L G, Portier F, Roche P, Levy Yeyati A, Kontos T and Strunk C 2010 *Phys. Rev. Lett.* **104** 026801
[20] Hofstetter L, Csonka S, Baumgartner A, Fülöp G, d'Hollosy S, Nygård J and Schönenberger C 2011 *Phys. Rev. Lett.* **107** 136801
[21] de Franceschi S, Kouwenhoven L P, Schönenberger C and Wernsdorfer W 2011 *Nat. Nanotechnol.* **5** 703
[22] Andreev A F 1964 *Zh. Eksp. Teor. Fiz.* **46** 1823
Andreev A F 1964 *Sov. Phys.—JETP* **19** 1228
[23] Chevallier D, Rech J, Jonckheere T and Martin T 2011 *Phys. Rev. B* **83** 125421
[24] Rech J, Chevallier D, Jonckheere T and Martin T 2012 *Phys. Rev. B* **85** 035419
[25] Blanter Ya M and Büttiker M 2000 *Phys. Rep.* **336** 1–166
[26] Sukhorukov E V, Jordan A N, Gustavsson S, Leturcq R, Ihn T and Ensslin K 2007 *Nat. Phys.* **3** 243
[27] McClure D T, DiCarlo L, Zhang Y, Engel H-A, Marcus C M, Hanson M P and Gossard A C 2007 *Phys. Rev. Lett.* **98** 056801
[28] Das A, Ronen Y, Heiblum M, Mahalu D, Kretinin A V and Shtrikman H 2012 *Nat. Commun.* **3** 1165
[29] Martin T 1996 *Phys. Lett.* A **220** 137
[30] Torrès J and Martin T 1999 *Eur. Phys. J. B* **12** 319
[31] Lesovik G B, Martin T and Blatter G 2001 *Eur. Phys. J. B* **24** 287
[32] Bignon G, Houzet M, Pistolesi F and Hekking F W J 2004 *Europhys. Lett.* **67** 110
[33] Mélin R, Benjamin C and Martin T 2008 *Phys. Rev. B* **77** 094512
[34] Dong B and Lei X L 2009 *Phys. Rev. B* **80** 153305
[35] Freyn A, Flöser M and Mélin R 2010 *Phys. Rev. B* **82** 014510
[36] Freyn A, Douçot B, Feinberg D and Mélin R 2011 *Phys. Rev. Lett.* **106** 257005

[37] Riwar R-P, Badiane D M, Houzet M, Meyer J S and
     Nazarov Y V 2016 *Physica* E **76** 231
[38] Wrześniewski K, Trocha P and Weymann I 2017 *J. Phys.:
     Condens. Matter* **29** 195302
[39] Henny M, Oberholzer S, Strunk C, Heinzel T, Ensslin K,
     Holland M and Schönenberger C 1999 *Science* **284** 296
[40] Oliver W D, Kim J, Liu R C and Yamamoto Y 1999 *Science*
     284 299
[41] Bagrets D A and Nazarov Y W 2003 *Phys. Rev.* B **67** 085316
[42] Cottet A, Belzig W and Bruder C 2004 *Phys. Rev. Lett.*
     92 206801
[43] Chtchelkatchev N M, Blatter G, Lesovik G B and Martin T
     2002 *Phys. Rev.* B **66** 161320
[44] Sauret O, Martin T and Feinberg D 2005 *Phys. Rev.* B
     72 024544

[45] Flöser M, Feinberg D and Mélin R 2013 *Phys. Rev.* B
     88 094517
[46] Rozhkov A V and Arovas D P 2000 *Phys. Rev.* B **62** 6687
[47] Schoeller H and Schön G 1994 *Phys. Rev.* B **50** 18436
     König J, Schmid J, Schoeller H and Schön G 1996 *Phys. Rev.*
     B **54** 16820
[48] Thielmann A, Hettler M H, König J and Schön G 2005 *Phys.
     Rev. Lett.* **95** 146806
[49] Governale M, Pala M G and König J 2008 *Phys. Rev.* B
     77 134513
[50] Braggio A, Governale M, Pala M G and König J 2011 *Solid
     State Commun.* **151** 155
[51] Kłobus W, Grudka A, Baumgartner A, Tomaszewski D,
     Schönenberger C and Martinek J 2014 *Phys. Rev.* B
     89 125404

91

Kondo physics in double quantum dot based Cooper pair splitters

Kacper Wrześniewski and Ireneusz Weymann[*]

Faculty of Physics, Adam Mickiewicz University, ul. Umultowska 85, 61-614 Poznań, Poland

The Andreev transport properties of double quantum dot based Cooper pair splitters with one superconducting and two normal leads are studied theoretically in the Kondo regime. The influence of the superconducting pairing correlations on the local density of states, Andreev transmission coefficient, and Cooper pair splitting efficiency is thoroughly analyzed. It is shown that finite superconducting pairing potential quickly suppresses the SU(2) Kondo effect, which can however reemerge for relatively large values of coupling to superconductor. In the SU(4) Kondo regime, a crossover from the SU(4) to the SU(2) Kondo state is found as the coupling to superconductor is enhanced. The analysis is performed by means of the density-matrix numerical renormalization group method.

I. INTRODUCTION

Creation, manipulation, and detection of entangled pairs of electrons is an important requirement for engineering quantum information and computation protocols in solid state systems [1–3]. As a natural source of entangled electrons one can consider superconductors, in which two electrons with opposite spins form spin singlet states—the Cooper pairs [4–6]. It has been demonstrated experimentally that it is possible to extract and split Cooper pairs in a double quantum dot (DQD) setup involving one superconductor (SC) and two normal (N) leads, each attached to a different quantum dot [7–14]. In such a Cooper pair splitter (CPS), when the bias voltage eV applied between the SC and N leads is smaller than the superconducting energy gap Δ, the current flows through the system due to the Andreev reflection processes [15]. One can generally distinguish two types of such processes: (i) direct Andreev reflection (DAR), in which the Cooper pair electrons tunnel through one arm of the device, and (ii) crossed Andreev reflection (CAR), when the Cooper pair electrons become split and each electron leaves the superconductor through a different arm of the device [16,17]. Since the latter processes are crucial for the creation of entangled electrons, it is important to optimize the splitting efficiency η of the device, i.e., to enhance the rate of CAR processes as compared to the DAR processes. This can be obtained, for example, by tuning the position of the DQD's energy levels and setting the system in an appropriate transport regime [7,10].

Transport properties of double quantum dots with superconducting contacts have been recently explored both experimentally [7–14,18] and theoretically [19–27]. The theoretical investigations were however mostly devoted to transport properties in a relatively weak coupling regime. Various geometries of the system were considered, with the two dots attached to the leads forming either serial [19], T-shaped [22], or CPS fork configurations [24,25]. In particular, the emergence of the triplet blockade and its influence on transport were analyzed, as well as various Andreev bound states (ABS) splitting mechanisms [20,25]. Moreover, unconventional pairing [24] in the presence of inhomogeneous magnetic field was predicted and the role of the spin-orbit interaction on nonlocal entanglement was demonstrated [26]. Other important aspects of transport

in such systems, such as the current and noise correlations [21,27] and spin dependence of transport controlled by means of ferromagnetic contacts [23,25,27], were also thoroughly discussed.

In this paper we extend those studies by focusing on the Andreev transport in the strong coupling regime, where electronic correlations can give rise to the Kondo effect [28,29]. When a spin one-half impurity is coupled to the conduction band of a metallic host, for temperatures T lower than the Kondo temperature T_K, the conduction electrons screen the impurity's spin and a delocalized singlet state is formed. Its emergence results in the formation of an additional peak at the Fermi energy in the local density of states [29]. For single quantum dots, in the case of spin SU(2) Kondo effect, this leads to an enhancement of the conductance to its maximum value of $2e^2/h$ [30,31]. For double quantum dots, depending on the DQD occupation, one can observe different types of the Kondo effect. In particular, when both the spin and orbital degrees of freedom are degenerate, an SU(4) Kondo state is formed in the system [32,33].

When the leads are superconducting the situation becomes much more interesting [34–38]. First of all, for dot coupled to superconductor, the occurrence of the Kondo phenomenon is conditioned by the ratio of the Kondo temperature to the superconducting energy gap T_K/Δ, and a quantum phase transition occurs as this ratio is varied [35,39–42]. Furthermore, for two-terminal hybrid junctions involving quantum dot and N and SC leads, the Kondo state can be formed by screening the dot's spin by the normal lead [34,35], while finite coupling to SC lead can result in an enhancement of the Kondo temperature [43].

From the theoretical side, the accurate studies of transport properties of nanostructures in nonperturbative regime require resorting to sophisticated numerical methods. One of them is the density-matrix numerical renormalization group (DM-NRG) method [44,45], which allows for obtaining results of very high accuracy on the transport behavior of the considered system [46]. In these considerations we employ DM-NRG to address the problem of the Kondo effect and Andreev transport in double quantum dot based Cooper pair splitters. In particular, we study the DQD energy level dependence of the local density of states as well as the Andreev transmission coefficient, together with the splitting efficiency of the device. We then focus on the two transport regimes when the system in the absence of coupling to superconductor exhibits either the SU(2) or the SU(4) Kondo effect, and study the influence

[*]weymann@amu.edu.pl

of superconducting pairing correlations on these two types of Kondo state. We show that, contrary to single quantum dots [43,47], the SU(2) Kondo state becomes quickly suppressed by even small superconducting pairing potential. On the other hand, the pairing correlations result in a crossover from the SU(4) to the SU(2) Kondo effect.

The paper is organized as follows. In Sec. II we present the model, Hamiltonian, and method used in calculations, and describe the main quantities of interest. Section III is devoted to numerical results and their discussion. In Secs. III A and III B we analyze the DQD level dependence of the local density of states and the Andreev transmission coefficient, together with splitting efficiency, respectively. The SU(2) [SU(4)] Kondo regime is thoroughly discussed in Sec. III C (Sec. III D). Finally, the conclusions can be found in Sec. IV.

II. THEORETICAL DESCRIPTION

A. Model and parameters

The considered system consists of two single level quantum dots attached to an s-wave superconductor (SC) and coupled to two normal (N) electrodes; see Fig. 1. The Hamiltonian of isolated double quantum dot has the form

$$H_{DQD} = \sum_{j\sigma} \varepsilon_j d^{\dagger}_{j\sigma} d_{j\sigma} + \sum_j U_j n_{j\uparrow} n_{j\downarrow} + \sum_{\sigma\sigma'} U_{LR} n_{L\sigma} n_{R\sigma'},$$

$$(1)$$

with $d^{\dagger}_{j\sigma}$ creating a spin-σ electron in dot j of energy ε_j. The on-dot Coulomb correlations are denoted by U_j, with $n_{j\sigma} = d^{\dagger}_{j\sigma} d_{j\sigma}$, while the interdot Coulomb interactions are described by U_{LR}. The normal electrodes are modeled as free quasiparticles by the Hamiltonian, $H_N = \sum_{j\mathbf{k}\sigma} \varepsilon_{j\mathbf{k}} c^{\dagger}_{j\mathbf{k}\sigma} c_{j\mathbf{k}\sigma}$, where $c^{\dagger}_{j\mathbf{k}\sigma}$ is the creation operator for an electron with spin σ, wave number $\mathbf{k}$, and energy $\varepsilon_{j\mathbf{k}}$ in the jth lead. The BCS superconductor is modeled by $H_S = \sum_{\mathbf{k}\sigma} \xi_{\mathbf{k}} a^{\dagger}_{\mathbf{k}\sigma} a_{\mathbf{k}\sigma} + \Delta \sum_{\mathbf{k}} (a_{\mathbf{k}\downarrow} a_{-\mathbf{k}\uparrow} + \text{H.c.})$, where $a^{\dagger}_{\mathbf{k}\sigma}$ creates an electron with momentum $\mathbf{k}$, spin σ, and energy $\xi_{\mathbf{k}}$. The superconducting order parameter, assumed to be real, is denoted by Δ. The double dot is coupled to external leads by the tunneling
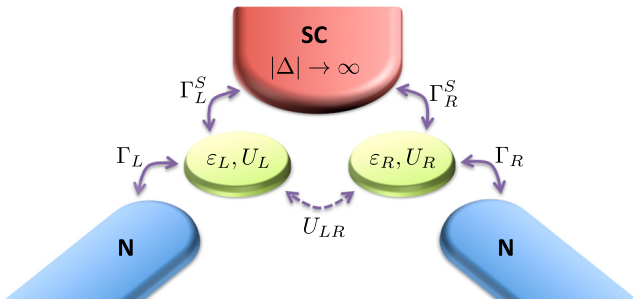

FIG. 1. Schematic of the considered system. Two single-level quantum dots, described by on-site energy ε_j ($j = L$ for left and $j = R$ for right dot) and Coulomb correlations U_j are coupled to a common s-wave superconductor (SC), with coupling strength Γ_j^S, and attached to two separate normal (N) electrodes, with coupling strength Γ_j. The two dots are coupled capacitively by U_{LR}.

Hamiltonian

$$H_T = \sum_{j\mathbf{k}\sigma} \left(V_{j\mathbf{k}} c^{\dagger}_{j\mathbf{k}\sigma} d_{j\sigma} + V^S_{j\mathbf{k}} a^{\dagger}_{\mathbf{k}\sigma} d_{j\sigma} + \text{H.c.} \right), \quad (2)$$

where the tunnel matrix elements between the dot j and the normal lead j (superconductor) are denoted by $V_{j\mathbf{k}}$ ($V^S_{j\mathbf{k}}$). Assuming momentum independent tunnel matrix elements, the coupling between the dot j and the corresponding normal electrode is described by $\Gamma_j = \pi |V_j|^2 \rho_j$, where ρ_j is the density of states of lead j. On the other hand, the coupling between the dot j and superconductor is given by $\Gamma_j^S = \pi |V_j^S|^2 \rho_S$, with ρ_S the density of states of the superconductor in the normal state.

In our considerations we focus on the Andreev transport regime; therefore, to exclude the normal tunneling processes, in the following we take the limit of infinite superconducting energy gap. In this limit the double dot coupled to superconductor can be described by the effective Hamiltonian of the form [20,25,48]

$$H_{DQD}^{\text{eff}} = H_{DQD} - \sum_j \Gamma_j^S (d^{\dagger}_{j\uparrow} d^{\dagger}_{j\downarrow} + d_{j\downarrow} d_{j\uparrow}) + \Gamma_{LR}^S (d^{\dagger}_{L\uparrow} d^{\dagger}_{R\downarrow}$$

$$+ d^{\dagger}_{R\uparrow} d^{\dagger}_{L\downarrow} + d_{R\downarrow} d_{L\uparrow} + d_{L\downarrow} d_{R\uparrow}). \quad (3)$$

Now, the proximity effect is included through pairing potential induced in the DQD, where the first term, proportional to Γ_j^S, describes the direct Andreev reflection (DAR) processes, while the last term, proportional to $\Gamma_{LR}^S = \sqrt{\Gamma_L^S \Gamma_R^S}$, corresponds to the crossed Andreev reflection (CAR) processes. In DAR processes Cooper pairs are transferred through one arm of the splitter. On the other hand, in CAR processes Cooper pair electrons become split and each electron leaves the superconductor through a different junction with normal lead.

The effective double dot Hamiltonian is not diagonal in the local basis defined by the states $|\chi_L \chi_R\rangle = |\chi_L\rangle |\chi_R\rangle$, in which the left (right) dot is in state $|\chi_L\rangle$ ($|\chi_R\rangle$), with $\chi_j = 0, \sigma, d$, for empty, singly occupied, and doubly occupied dot j. Because the effective Hamiltonian commutes with the total spin operator, H_{DQD}^{eff} has a block-diagonal form in the corresponding spin quantum number. As we show in the Appendix, the spin triplet space is quite trivial because it is not affected by the superconducting correlations due to symmetry reasons. In the spin doublet subspace we present a general solution to the eigenproblem. However, in the singlet subspace it is in general not possible to find simple analytical formulas for the eigenstates and eigenenergies; therefore, in this subspace we discuss the eigenspectrum only in some limiting situations. The first one is the particle-hole symmetry point of the model, $\varepsilon = -U/2 - U_{LR}$, and the second one is the fully symmetric SU(4) Kondo regime, $\varepsilon = -U_{LR}/2$ with $U_{LR} = U$. The analytical formulas presented in the Appendix will be crucial to understanding the complex behavior of the system in the considered transport regimes. Moreover, the eigenenergies will help to relate the position of peaks observed in transport quantities to energies of Andreev bound states (ABS), which can be inferred from excitation energies between the corresponding molecular states of the double quantum dot proximized by SC lead.

In our analysis we assume that the system is symmetric, i.e., we set $\Gamma_L = \Gamma_R \equiv \Gamma$ and $\Gamma_L^S = \Gamma_R^S \equiv \Gamma_S$. For the two

quantum dots we also assume $U_L = U_R \equiv U$ and $\varepsilon_L = \varepsilon_R \equiv \varepsilon$. To perform the calculations, we set $U \equiv 1$ and take $U_{LR} = U/2$ and $\Gamma = U/20$. We note that since both the couplings and the position of the DQD levels can be tuned individually by applied gate voltages [33], the chosen set of parameter is of relevance for current and future experiments. We also notice that a weak left-right asymmetry would induce rather quantitative changes to the results we present and discuss in the following, while qualitatively we expect our predictions to be relevant. However, the assumption of the superconducting energy gap being the largest energy scale in the problem needs to be treated with a certain care. While this assumption allows us to focus exclusively on the behavior of Andreev reflection processes, and for that reason it was adapted in many previous theoretical works [19,20,24,25,49–59], from an experimental point of view, the condition $\Delta > U$ does not need to be fulfilled in any Cooper pair splitting device. Nevertheless, there are superconductors, in which the gap is of the order of a couple of meV [60]; consequently, experimental realizations of splitters with large Δ should be possible.

B. Quantities of interest and method

The main quantity of interest is the transmission coefficient for Andreev reflection processes, $T_A(\omega)$, which can be written as

$$T_A(\omega) = T_A^{\text{DAR}}(\omega) + T_A^{\text{CAR}}(\omega), \qquad (4)$$

where the first term describes the transmission due to DAR processes, which is explicitly given by

$$T_A^{\text{DAR}}(\omega) = 4 \sum_{j\sigma} \Gamma_j^2 \left| \langle\!\langle d_{j\sigma} | d_{j\bar{\sigma}} \rangle\!\rangle_\omega^r \right|^2, \qquad (5)$$

while the last term denotes the transmission coefficient due to CAR processes and is described by

$$T_A^{\text{CAR}}(\omega) = 4 \Gamma_L \Gamma_R \sum_\sigma \left[|\langle\!\langle d_{L\sigma} | d_{R\bar{\sigma}} \rangle\!\rangle_\omega^r|^2 + |\langle\!\langle d_{R\sigma} | d_{L\bar{\sigma}} \rangle\!\rangle_\omega^r|^2 \right]. \qquad (6)$$

Here, $\langle\!\langle A | B \rangle\!\rangle_\omega^r$ is the Fourier transform of the retarded Green's function, $\langle\!\langle A | B \rangle\!\rangle_t^r = -i\Theta(t)\langle\{A(t), B(0)\}\rangle$. The DAR and CAR transmission coefficients can be used to define the Cooper pair splitting efficiency of the device as

$$\eta = \frac{T_A^{\text{CAR}}(\omega)}{T_A^{\text{CAR}}(\omega) + T_A^{\text{DAR}}(\omega)}. \qquad (7)$$

When $\eta \to 1$, transport is exclusively due to CAR processes, which means that each Cooper pair leaving the superconductor becomes split into two separate leads. On the other hand, if only DAR processes are responsible for Andreev transport, $\eta \to 0$.

With the Andreev transmission coefficient, it is possible to determine the Andreev current flowing between the superconductor and the normal leads [23]

$$I_A(V) = \frac{e}{h} \int d\omega [f(\omega - eV) - f(\omega + eV)] T_A(\omega), \qquad (8)$$

where $f(\omega)$ denotes the Fermi-Dirac distribution function and it is assumed that the chemical potential of the left and right lead is equal to eV, while the superconductor is grounded. From the above formula it is easy to find the Andreev

differential conductance, which in the limit of vanishing temperature can be approximated by

$$G_A(V) \approx \frac{e^2}{h} [T_A(\omega = eV) + T_A(\omega = -eV)]. \qquad (9)$$

Consequently, the measurement of differential conductance allows one to probe the energy dependence of the Andreev transmission coefficient.

Another interesting quantity is the local density of states, which is given by the total normalized spectral function

$$\mathcal{A} = \sum_{ij} \mathcal{A}_{ij} = -\sum_{ij} \sqrt{\Gamma_i \Gamma_j} \, \text{Im} \langle\!\langle d_{i\sigma} | d_{j\sigma}^\dagger \rangle\!\rangle_\omega^r. \qquad (10)$$

Thus $\mathcal{A}_i \equiv \mathcal{A}_{ii}$ corresponds to the local density of states of one of the quantum dots, while $\mathcal{A}_{ij}$ describes the cross correlations between the two quantum dots generated by proximity-induced interdot pairing potential Γ_{LR}^S. Because we consider a symmetric situation, $\mathcal{A}_L = \mathcal{A}_R$, and $\mathcal{A}_{LR} = \mathcal{A}_{RL}$.

To determine the relevant correlation functions we use the density-matrix numerical renormalization group method [44–46]. This nonperturbative method allows for obtaining very accurate results on the static and dynamic properties of the system. In NRG, the initial Hamiltonian is transformed to an NRG Hamiltonian, in which the leads are modeled as tight-binding chains with appropriate hopping integrals [44]. The calculations are performed in an iterative fashion by keeping an assumed number N_K of the lowest-energy eigenstates. Here, we exploited the full spin symmetry of the system and kept at least $N_K = 2000$ states per iteration. The imaginary parts of the Green's functions were determined from discrete NRG data by performing appropriate broadening [61] and averaging over $N_z = 2$ shifted discretization meshes [62]. The real parts of the Green's functions were obtained from the Kramers-Kronig relation.

C. Stability diagram and transport regimes

The linear Andreev conductance plotted as a function of the position of each dot level assuming a weak coupling between the double dot and normal leads is shown in Fig. 2. The numbers in brackets indicate approximate expectation values of the occupation number of each dot, $(\langle n_L \rangle, \langle n_R \rangle)$, with $n_j = \sum_\sigma n_{j\sigma}$. The conductance was calculated using the rate equations within the sequential tunneling approximation [25]. We note that although this method is not suitable for capturing the correlation effects studied here, it allows us to indicate the considered transport regimes in the phase diagram of the device. In this paper we in particular focus on the symmetric case, $\varepsilon_L = \varepsilon_R \equiv \varepsilon$, a cross section of Fig. 2 marked with a dashed line. By sweeping ε, which can be experimentally done with gate voltages [33], the device can be tuned from the empty or fully occupied orbital regime to the SU(4) and SU(2) Kondo regimes, respectively.[1] The SU(4)

---

[1]Note that the SU(2) and SU(4) Kondo regimes can be greatly modified by finite coupling to superconductor, such that the Kondo effect can even become fully suppressed. Therefore, referring to the appropriate Kondo regime should be considered as a guide to estimate the corresponding parameter space in the phase diagram of the device in the limit of weak coupling to superconductor.
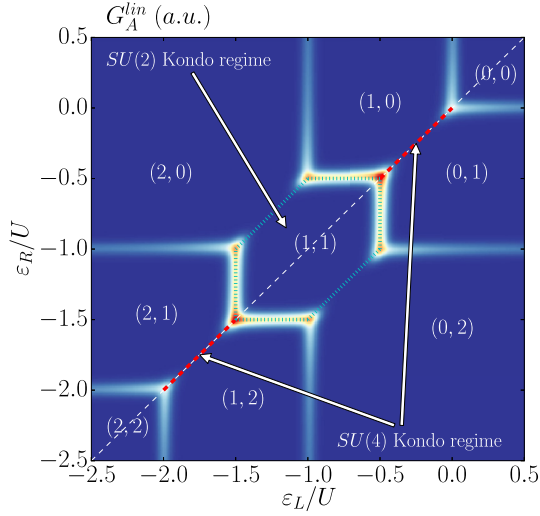
FIG. 2. Linear Andreev conductance G_A^{lin} calculated as a function of the position of each dot level, ε_L and ε_R, using the rate equations. The parameters are $U = 1$, $U_{LR} = U/2$, $\Gamma = U/100$, and $\Gamma_S = U/10$. The numbers in brackets indicate the average occupation of each dot, $(\langle n_L \rangle, \langle n_R \rangle)$, with $n_j = \sum_\sigma n_{j\sigma}$.

Kondo regime is marked with a thick dashed line, while the SU(2) Kondo regime is surrounded by dotted lines in Fig. 2. These transport regimes will be studied in detail in the next sections, and the influence of the proximity-induced pairing potential on the corresponding Kondo states will be thoroughly analyzed.

III. RESULTS AND DISCUSSION

In this section we present and discuss the main results on the local density of states and the Andreev transmission coefficient. We will first study the general gate voltage dependence of transport characteristics assuming $\varepsilon_L = \varepsilon_R \equiv \varepsilon$, i.e., along the dashed line marked in Fig. 2. Then, we shall focus on some more relevant transport regions, including the SU(2) and SU(4) Kondo regimes.

A. Local density of states

The normalized spectral function plotted as a function of energy ω and DQD level position $\varepsilon_L = \varepsilon_R \equiv \varepsilon$ is shown in Fig. 3. This figure is calculated for different values of the coupling to superconductor, as indicated, and it demonstrates the evolution of local density of states with increasing Γ_S. When $\Gamma_S = 0$, one observes the transport behavior typical for a double quantum dot system [63]; see Fig. 3(a). When the position of the DQD energy levels is lowered, the DQD becomes consecutively occupied with electrons. For $\varepsilon \gtrsim 0$ ($\varepsilon \lesssim -U - 2U_{LR}$), the DQD is empty (fully occupied). When $-U_{LR} \lesssim \varepsilon \lesssim 0$ ($-U - 2U_{LR} \lesssim \varepsilon \lesssim -U - U_{LR}$), the double dot is singly occupied (occupied with three electrons), while for $-U - U_{LR} \lesssim \varepsilon \lesssim -U_{LR}$, the DQD is occupied by two electrons, each located on a different quantum dot. The above energies also specify when the charge on the DQD
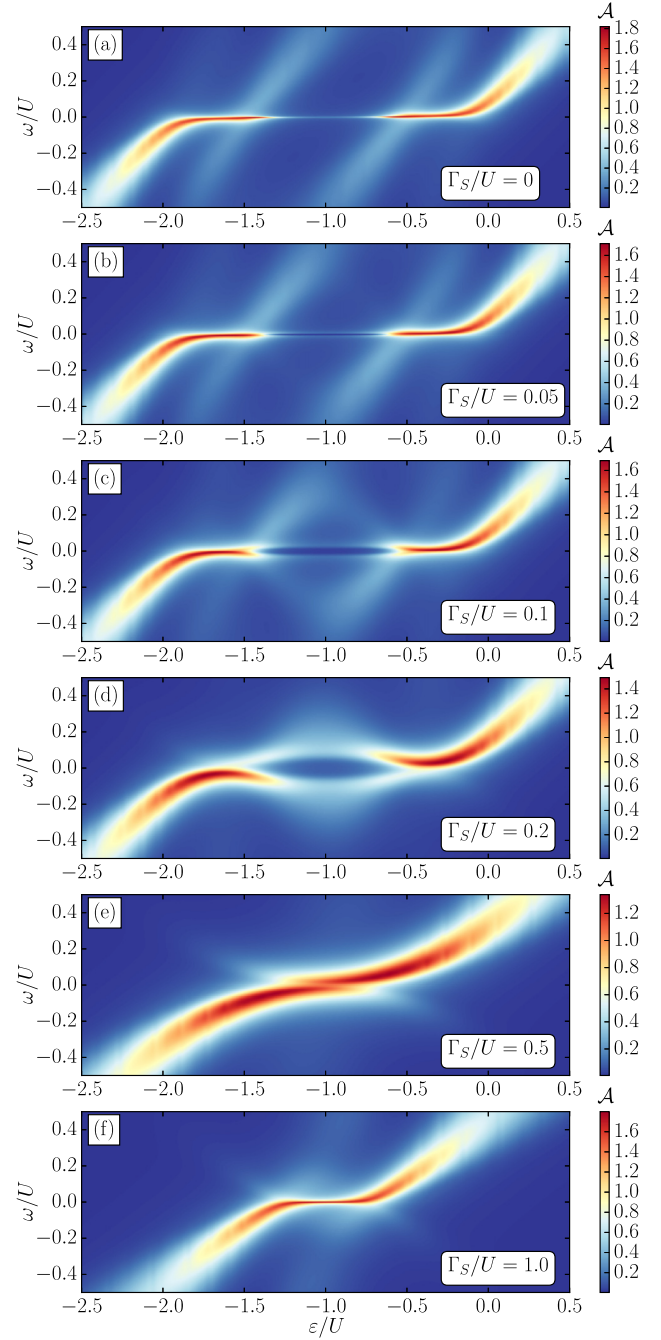

FIG. 3. Total normalized spectral function $\mathcal{A}$ of DQD-based Cooper pair splitter plotted as a function of energy ω and double dot level position, $\varepsilon_L = \varepsilon_R \equiv \varepsilon$, calculated for different values of coupling to superconductor Γ_S, as indicated. The parameters are $U = 1$, $U_{LR} = U/2$, $\Gamma = U/20$, and $T = 0$.

changes and the local density of states exhibits a resonance. In between those resonant energies, the system's spectral function exhibits an enhancement due to the Kondo effect. In the odd occupation regime, i.e., when DQD hosts either one or three electrons, the system exhibits the SU(4) Kondo effect resulting from orbital and spin degeneracies [32,33].

One can estimate the SU(4) Kondo temperature, $T_K^{SU(4)}$, from the half width at half maximum (HWHM) of the Kondo peak in the total spectral function for $\varepsilon = -U_{LR}/2$, which for assumed parameters yields $T_K^{SU(4)}/U \approx 0.017$. On the other hand, when the DQD is occupied by two electrons, each dot exhibits the spin SU(2) Kondo resonance [29,30]. The corresponding Kondo temperature, $T_K^{SU(2)}$, estimated from HWHM of the Kondo resonance in the spectral function for $\varepsilon = -U/2 - U_{LR}$, is equal to $T_K^{SU(2)}/U \approx 10^{-4}$. Note that for the parameters assumed in calculations $T_K^{SU(2)} \ll T_K^{SU(4)}$. This is why in Fig. 3(a) the SU(2) Kondo peak is much less pronounced as compared to the SU(4) Kondo resonance.

When the coupling to superconductor becomes finite, the behavior of the spectral function starts changing. First, one observes the suppression and splitting of the Kondo resonance in the doubly occupied transport regime; see Figs. 3(b)–3(d). This splitting increases with Γ_S; however, when $\Gamma_S \gtrsim U/2$, a single resonance starts forming; see Figs. 3(e) and 3(f). This resonance is again due to the Kondo effect, since for $\Gamma_S \gtrsim U/2$, the doublet state becomes the ground state of the system. On the other hand, the SU(4) Kondo resonance looks much less affected, at least for small values of coupling to superconductor. This is, however, not entirely true, since with increasing Γ_S, the SU(4) Kondo resonance merges with resonance resulting from the formation of Andreev bound states. A thorough discussion of the influence of strength of coupling to superconductor on the corresponding Kondo resonances will be presented in the next sections.

Let us now analyze the behavior of separate contributions, $\mathcal{A}_L$ and $\mathcal{A}_{LR}$, to the total spectral function $\mathcal{A}$. Their energy and DQD energy level dependence is shown in Fig. 4 for $\Gamma_S = U/10$. At first sight, one can notice that the qualitative behavior of $\mathcal{A}$ is mainly determined by the spectral function of single quantum dot $\mathcal{A}_L$. For the considered value of Γ_S, $\mathcal{A}_L$ exhibits a pronounced split Kondo resonance for $-U - U_{LR} \lesssim \varepsilon \lesssim -U_{LR}$ and the SU(4) Kondo resonance when $-U_{LR} \lesssim \varepsilon \lesssim 0$ ($-U - 2U_{LR} \lesssim \varepsilon \lesssim -U - U_{LR}$), similar to the total spectral function; cf. Figs. 4(a) and 4(b).

On the other hand, the off-diagonal spectral function, which accounts for the cross correlations between transport processes through the two dots, behaves in a clearly different manner. First of all, we note that finite value of $\mathcal{A}_{LR}$ results solely from proximity-induced interdot pairing, and it vanishes if CAR processes are not allowed in the system. One can see that $\mathcal{A}_{LR}$ takes considerable values for energies corresponding to resonances in $\mathcal{A}$; cf. Figs. 4(a) and 4(c). Moreover, if on one side of the resonance $\mathcal{A}_{LR}$ is positive, on the other side it changes sign. This effect is most pronounced for $-U_{LR} \lesssim \varepsilon \lesssim 0$ ($-U - 2U_{LR} \lesssim \varepsilon \lesssim -U - U_{LR}$), i.e., when DQD hosts an odd number of electrons; see Fig. 4(c). Positive sign of $\mathcal{A}_{LR}$ can be associated with processes that occur in the same direction through both normal junctions, while negative sign of $\mathcal{A}_{LR}$ indicates that the two processes are anticorrelated [27].

B. Andreev transmission and splitting efficiency

The energy and DQD level dependence of the Andreev transmission coefficient calculated for different values of
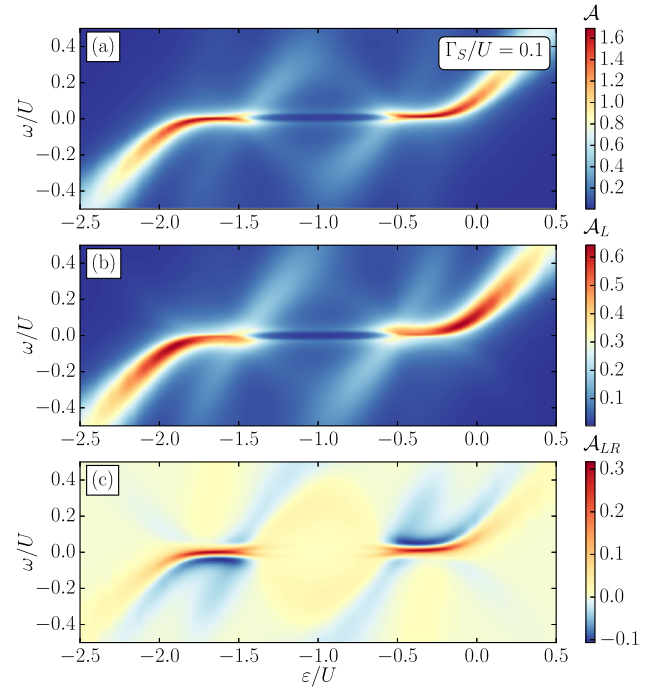

FIG. 4. Normalized spectral function: (a) $\mathcal{A}$, (b) $\mathcal{A}_L$, and (c) $\mathcal{A}_{LR}$, plotted versus energy ω and double dot energy level position ε. The parameters are the same as in Fig. 3 with $\Gamma_S = U/10$.

coupling to superconductor is presented in Fig. 5. When the coupling Γ_S is relatively small, one can see that $T_A(\omega)$ becomes finite in the low-energy regime and it is considerably enhanced for $\varepsilon \approx -U_{LR}$ and $\varepsilon \approx -U - U_{LR}$; see Fig. 5(a). The area when the maximum occurs grows with increasing Γ_S and, at the same time, the maximum value slightly decreases. Moreover, for $\Gamma_S = U/5$, $T_A(\omega)$ becomes finite in almost the whole energy range considered in the figure, with maximum values occurring still for $\varepsilon \approx -U_{LR}$ and $\varepsilon \approx -U - U_{LR}$; see Fig. 5(c). Note that $T_A(\omega)$ exhibits a similar split structure as that visible in the local density of states; cf. Figs. 3(d) and 5(c). Further increase of the coupling strength results in a decrease of the size of the Coulomb blockade regime, which is seen as merging of the two maxima at the particle-hole symmetry point $\varepsilon = -U/2 - U_{LR}$ [Fig. 5(d)]. For even larger Γ_S the transmission coefficient drops and the energy range where $T_A(\omega)$ is enhanced shrinks; see Fig. 5(e).

The different contributions to the transmission coefficient coming from DAR and CAR processes are presented in Fig. 6 for $\Gamma_S = U/10$. The first general observation is that the total Andreev transmission is mainly determined by crossed Andreev reflection processes. This can be expected because the rate of direct Andreev reflection is conditioned by the value of on-site Coulomb correlations, while the rate of CAR processes depends on the interdot correlations. Because $U_{LR} < U$, as in typical experimental realizations [7], one finds more CAR processes compared to DAR ones. This is in fact a very desired situation for Cooper pair splitting experiments, in which one would like to suppress DAR processes and maximize CAR ones.

From the application point of view, it is thus interesting to analyze the Cooper pair splitting efficiency η of the device.
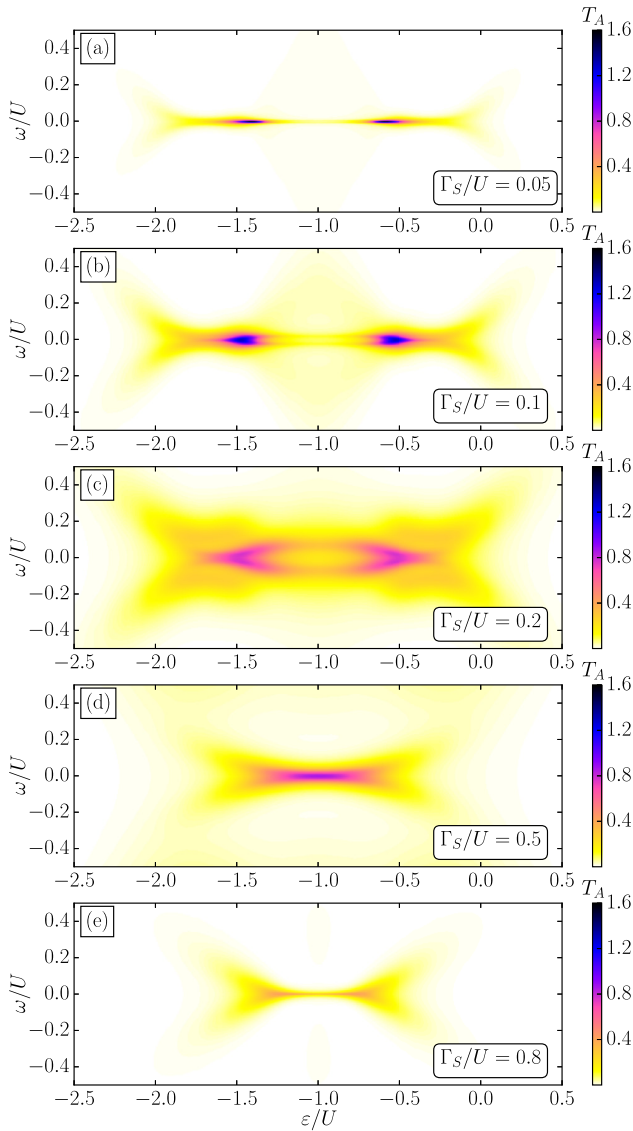
FIG. 5. Andreev transmission coefficient plotted versus energy ω and double dot energy level position ε, and calculated for different values of Γ_S, as indicated. The other parameters are the same as in Fig. 3.
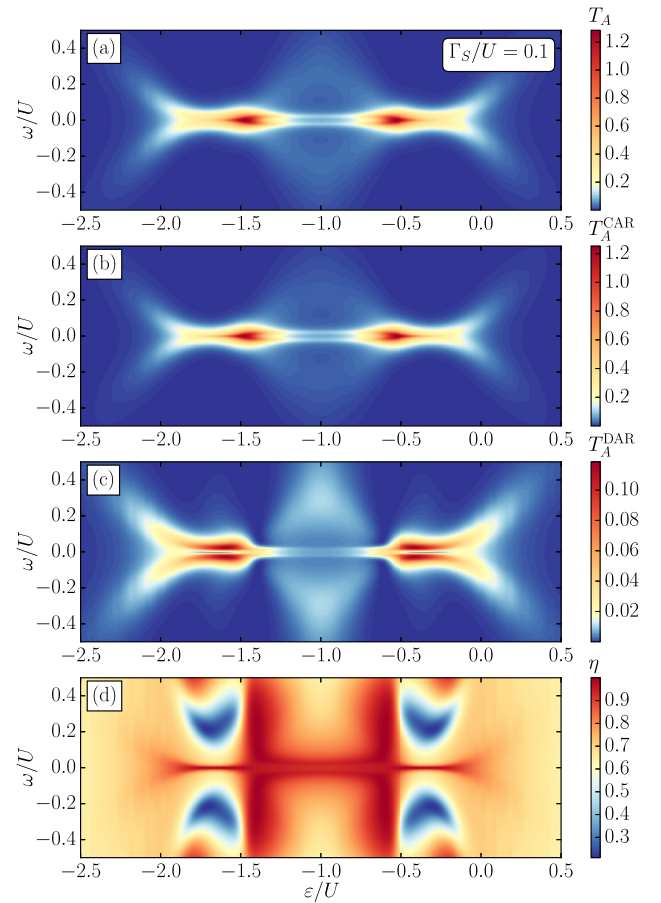

FIG. 6. (a) Total Andreev transmission coefficient and its contributions due to (b) CAR and (c) DAR processes, as well as (d) Cooper pair splitting efficiency η plotted as function of energy ω and double dot energy level position ε. The parameters are the same as in Fig. 3 with $\Gamma_S = U/10$.

The splitting efficiency greatly depends on the strength of coupling to superconductor. This dependence is explicitly demonstrated in Fig. 7, which shows the energy and DQD level dependence of η calculated for different values of Γ_S corresponding to those considered in Fig. 5. In this figure one can identify optimal parameters, for which the process of Cooper pair splitting is most efficient in the considered transport regime.

Finally, we would like to emphasize that the splitting efficiency also strongly depends on the ratio of interdot and intradot Coulomb correlations U/U_{LR}. In typical experimental realizations, $U \gg U_{LR}$, which is desired to enhance CAR processes and suppress DAR ones, obtaining thus large values of η. The splitting efficiency however generally decreases when the ratio of U/U_{LR} becomes smaller. In particular, the amount of DAR and CAR processes becomes equal when $U = U_{LR}$, such that $\eta = 1/2$ in the whole parameter space.

C. SU(2) Kondo regime

We now focus in greater detail on the SU(2) Kondo regime, where for $\Gamma_S = 0$ the DQD is occupied by two electrons, each on a different quantum dot; see Fig. 2. To simplify the

This is presented in Fig. 6(d). One can see that the splitting efficiency, depending on DQD energy level position ε and energy ω, takes values ranging from very low ($\eta \approx 0.2$) to its maximum value of $\eta = 1$. We recall that for $\eta = 1$ transport is exclusively due to CAR processes, while for $\eta = 0$, only DAR processes contribute to Andreev conductance; cf. Eq. (7). Clearly, large splitting efficiency is observed at low energies and for $-U - 2U_{LR} \lesssim \varepsilon \lesssim 0$; see Fig. 6(d). Moreover, a region of enhanced η is present in the Coulomb blockade regime with two electrons. Then, mainly CAR processes are responsible for Andreev transport. Note also that there are transport regimes where the splitting efficiency is rather poor and mainly DAR processes are responsible for transport; see the transport regime with odd number of electrons for elevated energies $|\omega|$ in Fig. 6(d).
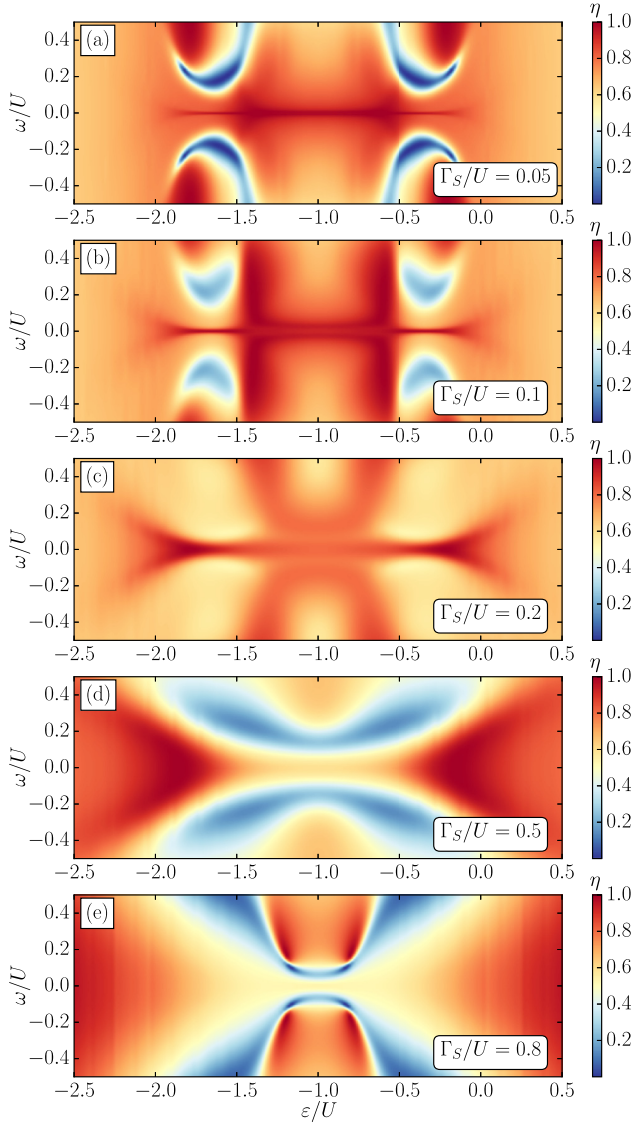
FIG. 7. Splitting efficiency η calculated for different values of coupling strength to superconducting lead, as indicated, and for parameters the same as in Fig. 3.
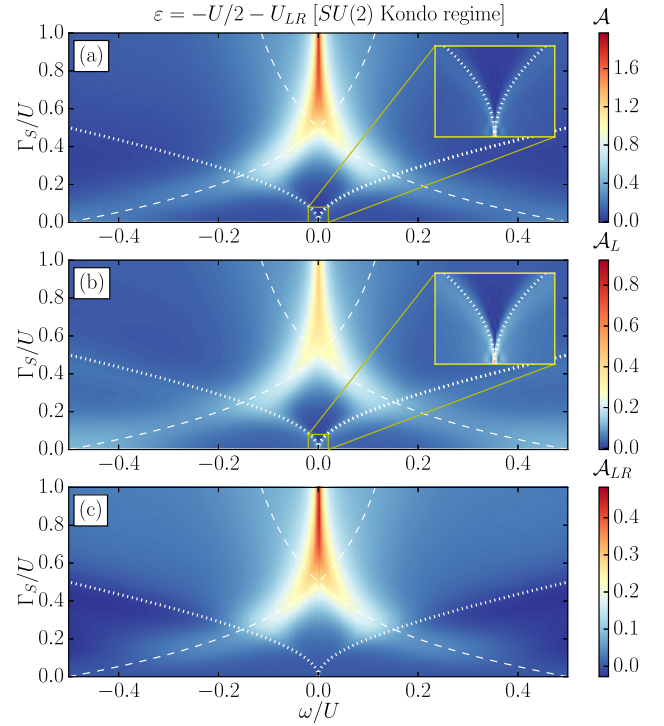

FIG. 8. Energy dependence of (a) the total normalized spectral function $\mathcal{A}$ and its contributions: (b) $\mathcal{A}_L$ and (c) $\mathcal{A}_{LR}$ calculated as a function of the coupling to superconductor Γ_S and for $\varepsilon = -U/2 - U_{LR}$. The insets show the zoom into the suppression of the SU(2) Kondo resonance with increasing Γ_S. The dashed lines indicate the energies of the Andreev bound states, cf. Eq. (12), while the dotted lines present the excitation energies between corresponding singlet and triplet states; cf. Eq. (13). The other parameters are as in Fig. 3.

discussion, we consider the particle-hole symmetry point of the model, $\varepsilon = -U/2 - U_{LR}$. Nevertheless, the conclusions drawn here shall apply to the whole two-electron Coulomb blockade regime where the spin SU(2) Kondo effect can develop.

The total normalized spectral function in the SU(2) Kondo regime, together with its contributions $\mathcal{A}_L$ and $\mathcal{A}_{LR}$, calculated as a function of Γ_S for $\varepsilon = -U/2 - U_{LR}$, is shown in Fig. 8. The dashed lines indicate the energies of the Andreev bound states, while the insets present the zooms into the low-energy behavior of the spectral function, where the suppression of the Kondo resonance with increasing Γ_S is clearly visible. The general behavior is as follows: finite coupling to superconductor results in the splitting and suppression of the Kondo resonance, which, however, emerges again for $\Gamma_S \approx U/2$. In fact, for this value of Γ_S, the system exhibits a phase transition

and the ground state changes from spin singlet to spin doublet. Consequently, the Kondo resonance develops once $\Gamma_S \gtrsim U/2$; see Fig. 8.

Let us shed more light on the system's behavior by using some analytical arguments. For the particle-hole symmetry point, it is easy to find the eigenspectrum of the effective Hamiltonian (3). We will consider the lowest-energy singlet ($|S\rangle$), doublet ($|D_\sigma\rangle$), and triplet ($|T_\delta\rangle$) states. The first two states have the following explicit form:

$$|S\rangle = \alpha(|dd\rangle - |00\rangle) - \beta(|\uparrow\downarrow\rangle - |\downarrow\uparrow\rangle),$$
$$|D_\sigma\rangle = \tfrac{1}{2}(|\sigma 0\rangle + |0\sigma\rangle + |\sigma d\rangle + |d\sigma\rangle),$$

where the coefficients are given by $\alpha = \sqrt{(\gamma - U - U_{LR})/(4\gamma)}$, $\beta = 2\Gamma_S/\sqrt{\gamma(\gamma - U - U_{LR})}$, and $\gamma = \sqrt{(U + U_{LR})^2 + 16\Gamma_S^2}$. Note that these states correspond to the states $|D_\sigma^2\rangle$ and $|S_4\rangle$ presented in the Appendix. The triplet state is threefold degenerate with components $|T_+\rangle = |\uparrow\uparrow\rangle$, $|T_-\rangle = |\downarrow\downarrow\rangle$, and $|T_0\rangle = (|\uparrow\downarrow\rangle + |\downarrow\uparrow\rangle)/\sqrt{2}$. The energies of the above states are given by

$$E_S = -\tfrac{1}{2}\big[U + U_{LR} + \sqrt{(U + U_{LR})^2 + 16\Gamma_S^2}\big],$$
$$E_D = -\tfrac{1}{2}(U + 2U_{LR} + 4\Gamma_S),$$
$$E_T = -U - U_{LR}, \tag{11}$$

respectively. Note that the energy of the triplet state does not depend on Γ_S. This is to be expected since the triplet state does not match the symmetry of the s-wave superconductor. The excitation energies between singlet and doublet states define the relevant ABS's energies

$$E_{ABS} = \pm \frac{U_{LR}}{2} \pm 2\Gamma_S \mp \frac{1}{2}\sqrt{(U + U_{LR})^2 + 16\Gamma_S^2}, \quad (12)$$

which are marked with dashed lines in Fig. 8.

In the case of $\Gamma_S = 0$, the singlet and triplet state are degenerate and the system exhibits the SU(2) Kondo effect on each quantum dot; see the insets in Figs. 8(a) and 8(b). However, when Γ_S becomes finite, the induced interdot pairing relevant for crossed Andreev reflection results in the singlet-triplet splitting and causes the singlet state $|S\rangle$ to be the ground state of the system. Because of that, the Kondo resonance gets very quickly suppressed when Γ_S increases and only split Kondo peaks are visible; see the insets in Fig. 8. The position of the split Kondo peaks is determined by the excitation energy between the singlet and triplet states, such that the peaks occur for

$$\omega \approx \pm\frac{1}{2}\big[U + U_{LR} - \sqrt{(U + U_{LR})^2 + 16\Gamma_S^2}\big]. \quad (13)$$

Thus, for small values of Γ_S, the position of side peaks depends in a parabolic way on the coupling to superconductor, $\omega \approx \pm 4\Gamma_S^2/(U + U_{LR})$. This parabolic dependence can be seen in Figs. 8(a) and 8(b) and the corresponding insets.

The value of Γ_S at which the Kondo resonance becomes suppressed can be estimated by comparing the characteristic energy scales, i.e., the Kondo temperature and the singlet-triplet excitation energy. One can then find the value of the coupling to superconductor, Γ_S^{TS}, at which the suppression of the Kondo resonance develops

$$\Gamma_S^{TS} \approx \frac{1}{2}\sqrt{T_K^{SU(2)}(U + U_{LR})}. \quad (14)$$

For assumed parameters and recalling that $T_K^{SU(2)}/U \approx 10^{-4}$, one gets $\Gamma_S^{TS}/U \approx 0.006$. This estimate is validated by NRG calculations of the total normalized spectral function for small values of Γ_S, which is plotted as a function of energy on logarithmic scale in Fig. 9(a). One can clearly see the Kondo peak for $\Gamma_S \ll \Gamma_S^{TS}$ and a gradual decrease of its height with increasing Γ_S, until the peak becomes completely suppressed for $\Gamma_S \gtrsim \Gamma_S^{TS}$. The vertical dashed lines in Fig. 9(a) mark the energy of the side Kondo peak as estimated from Eq. (13). The agreement between this analytical formula and full numerical calculations is quite satisfactory.

For $\Gamma_S \gtrsim \Gamma_S^{TS}$ and such values of Γ_S that the ground state is spin singlet, the system does not exhibit the Kondo effect at all. The spectral function reveals then just peaks at energies corresponding to the Andreev bound states; see Fig. 8. When, however, the energies of Andreev bound states cross the zero energy for $\Gamma_S \approx \Gamma_S^{SD}$, with

$$\Gamma_S^{SD} = \frac{U(U + 2U_{LR})}{8U_{LR}} \quad (15)$$

(for assumed parameters this happens when $\Gamma_S^{SD} = U/2$), the doublet state $|D_\sigma\rangle$ becomes the ground state of the system. Then, one observes the reemergence of the Kondo resonance. This is explicitly presented in Fig. 9(b), which shows the total
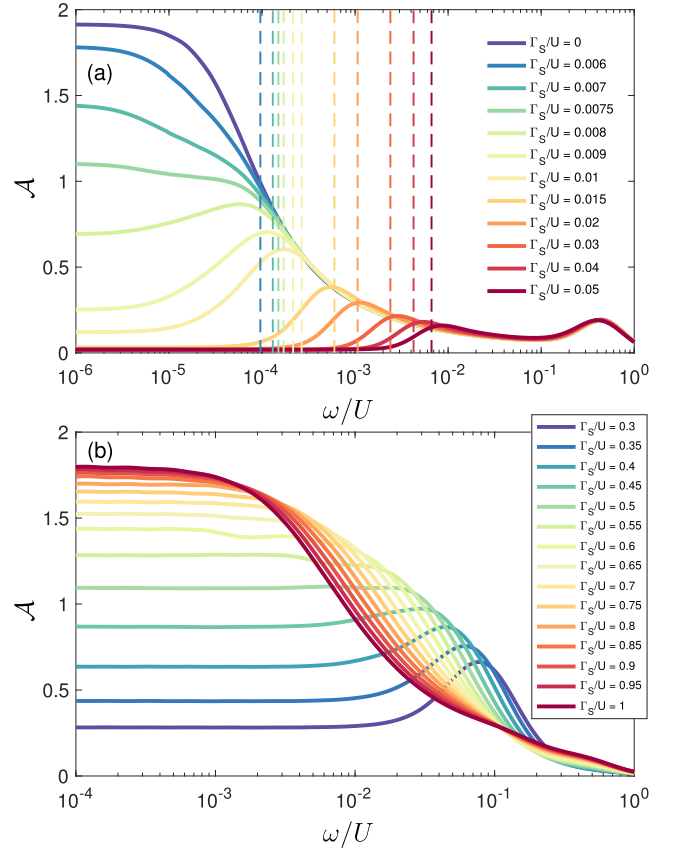

FIG. 9. Total normalized spectral function $\mathcal{A}$ plotted vs energy on logarithmic scale for selected values of Γ_S. Panel (a) presents the suppression of the Kondo resonance with Γ_S, which occurs for the critical value of $\Gamma_S = \Gamma_S^{TS} \approx 0.006U$; cf. Eq. (14). The vertical dashed lines in (a) show the excitation energies between the singlet and triplet states for given Γ_S; cf. Eq. (13). At these excitation energies side Kondo peaks occur. Panel (b) presents the restoration of the Kondo effect when $\Gamma_S \gtrsim \Gamma_S^{SD}$. The parameters are the same as in Fig. 8.

normalized spectral function plotted on logarithmic energy scale for the corresponding values of Γ_S. Note that the Kondo temperature is now clearly larger compared to the case of $\Gamma_S = 0$; cf. Figs. 9(a) and 9(b). This basically results from the difference in excitation energies to virtual states allowing for spin-flip processes driving the Kondo effect. For $\Gamma_S = 0$, the energy is given by the charging energy of each dot, while for $\Gamma_S \gtrsim \Gamma_S^{SD}$, it is given by the doublet-singlet excitation energy, which is smaller than U. Consequently, there is a larger exchange interaction in the latter case, which explains the observed difference in Kondo temperatures.

It is also interesting to notice that the maximum value of $\mathcal{A}$ at $\omega = 0$ is comparable for $\Gamma_S = 0$ and $\Gamma_S = U$, and approaches 2; see Fig. 9. In the former case this limit can be easily understood since each of the two quantum dots contributes with the Kondo resonance, such that $\mathcal{A}_L = \mathcal{A}_R \to 1$. In the latter case, on the other hand, one finds $\mathcal{A}_L = \mathcal{A}_R \to 1/2$ and $\mathcal{A}_{LR} = \mathcal{A}_{RL} \to 1/2$, cf. Fig. 8, which implies that the off-diagonal spectral function, that encompasses cross correlations between the two dots, contributes $1/(\pi\Gamma)$ to the height of the Kondo peak in the total spectral function.
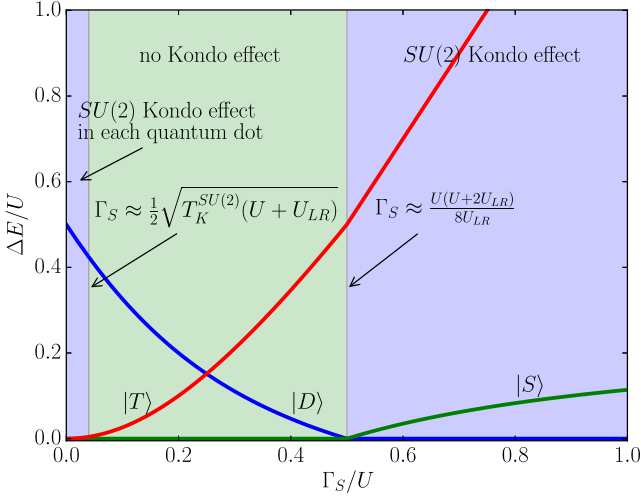
FIG. 10. Excitation energies ΔE between the singlet, doublet, and triplet states plotted as a function of the coupling to superconductor for parameters the same as in Fig. 8. The excitation energies are measured relative to the ground state energy, which is set to zero. The evolution of the ground state from the singlet ($|S\rangle$) to the doublet ($|D\rangle$) state is clearly visible. The values of Γ_S at which the Kondo effect becomes suppressed or emerges are indicated. $T_K^{SU(2)}$ denotes the SU(2) Kondo temperature for $\Gamma_S = 0$. Note that for $\Gamma_S = 0$ the singlet and triplet ($|T\rangle$) states are degenerate.

The low-energy behavior of the system in the two-electron transport regime is summarized in Fig. 10, which shows the evolution of the excitation energies ΔE between the relevant states, cf. Eq. (11), when Γ_S is varied. For two indicated values of Γ_S, the transport behavior of the system greatly changes. When $\Gamma_S \lesssim \Gamma_S^{TS}$, the Kondo singlet is the ground state of the system and the electrons experience a $\pi/2$ phase shift [29]. At $\Gamma_S \approx \Gamma_S^{TS}$, there is a crossover, such that for $\Gamma_S^{TS} \lesssim \Gamma_S \lesssim \Gamma_S^{SD}$, the interdot pairing-induced singlet becomes the ground state of the system. Consequently, there is no Kondo effect (phase shift is equal to zero). On the other hand, when $\Gamma_S \approx \Gamma_S^{SD}$, the system exhibits a phase transition and for $\Gamma_S \gtrsim \Gamma_S^{SD}$ the doublet state becomes the ground state of the splitter. This results in the reemergence of the Kondo effect.

Note that the system's behavior as a function of Γ_S is completely different from the case of a single quantum dot. In single quantum dots attached to superconducting and normal leads, in the subgap transport regime, the increase of Γ_S results in an enhancement of the Kondo temperature [43]. Since in the case of DQD for $\Gamma_S = 0$ the Kondo effect develops on each quantum dot, one could naively expect that for finite Γ_S the behavior will be qualitatively the same as in the single quantum dot case. The above-presented analysis clearly demonstrates that such conjecture is completely unjustified. The proximity-induced interdot pairing potential spoils this picture and, once $\Gamma_S \gtrsim \Gamma_S^{TS}$, it immediately results in the suppression of the Kondo resonance on both quantum dots. Thus the coupling to superconductor has a strong *destructive* influence on the SU(2) Kondo effect in DQD-based Cooper pair splitters. Note also that a very large value of the coupling Γ_S, i.e., $\Gamma_S \gtrsim \Gamma_S^{SD}$, can induce the Kondo effect again.
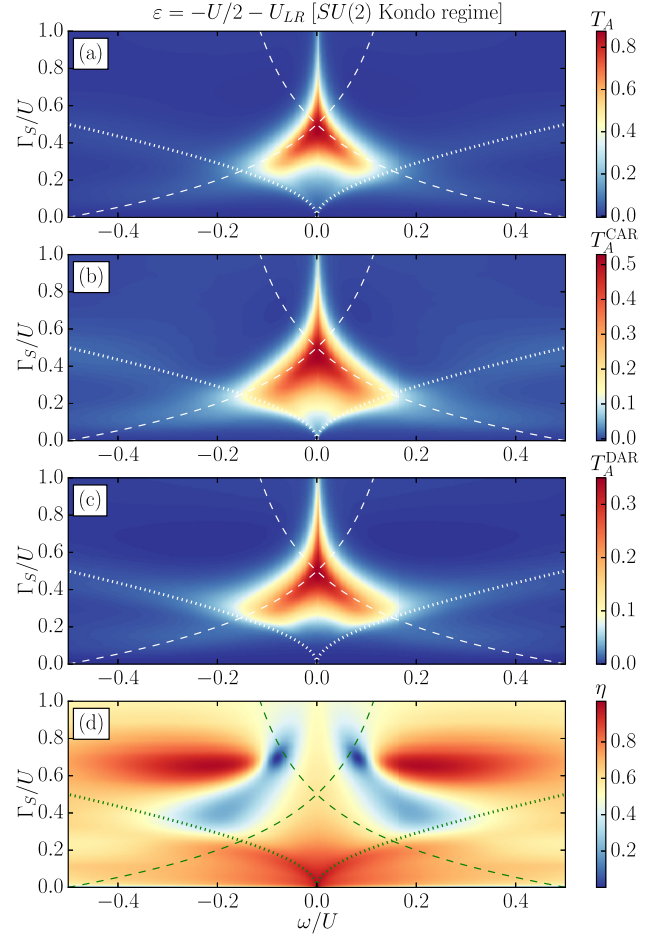

FIG. 11. (a) Total Andreev transmission coefficient and its contributions due to (b) CAR and (c) DAR processes, as well as (d) the Cooper pair splitting efficiency η plotted as function of energy ω and the strength of coupling to superconductor Γ_S. The dashed lines indicate the energies of the Andreev bound states given by Eq. (12), while the dotted lines present the excitation energies between corresponding singlet and triplet states given by Eq. (13). The parameters are the same as in Fig. 8.

Let us now analyze the behavior of the Andreev transmission, its contributions due to DAR and CAR processes, and the splitting efficiency in the SU(2) Kondo regime. The dependence of these quantities on energy and strength of coupling to superconductor is presented in Fig. 11. First of all, one can see that the transmission coefficient achieves considerable values mainly in the low-energy regime, in between the Andreev bound states. Moreover, an enhancement of transmission can be also seen along the energies of Andreev bound states; see Fig. 11. Interestingly, we note that for small values of Γ_S and low energies, mainly CAR processes dominate transport, which results in almost perfect splitting efficiency; see Fig. 11(d). We recall that this is the regime of suppressed and split Kondo resonance, which now we can clearly associate with the interdot pairing generated by crossed Andreev reflection. Note that despite suppression of the Kondo effect, in this transport regime $T_A^{CAR}(\omega)$ is still considerable and extends to energy regions greater than $T_K^{SU(2)}$. When
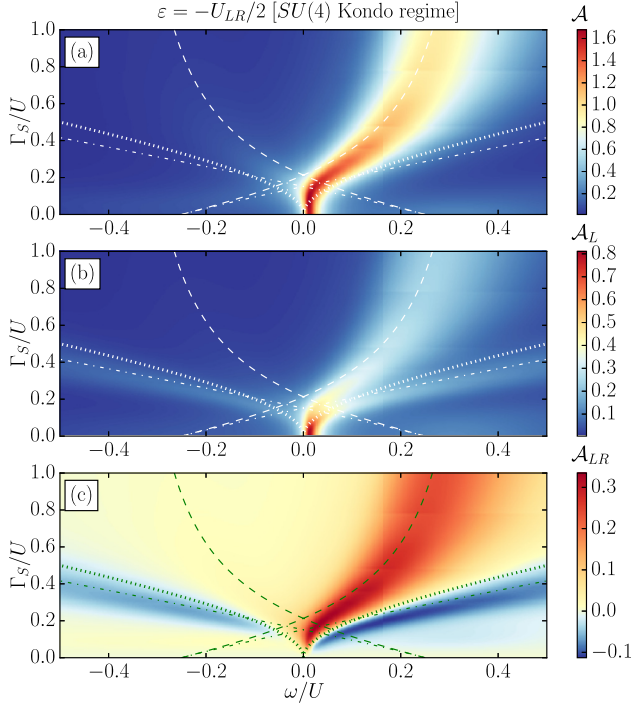
FIG. 12. Energy dependence of (a) the total normalized spectral function $\mathcal{A}$ and its contributions: (b) $\mathcal{A}_L$ and (c) $\mathcal{A}_{LR}$ calculated as a function of the coupling to superconductor Γ_S and for $\varepsilon = -U_{LR}/2$. The dashed and dotted-dashed lines indicate the energies of the Andreev bound states, while the dotted line shows the splitting of the doublet states, as given by Eq. (18). The other parameters are as in Fig. 3.
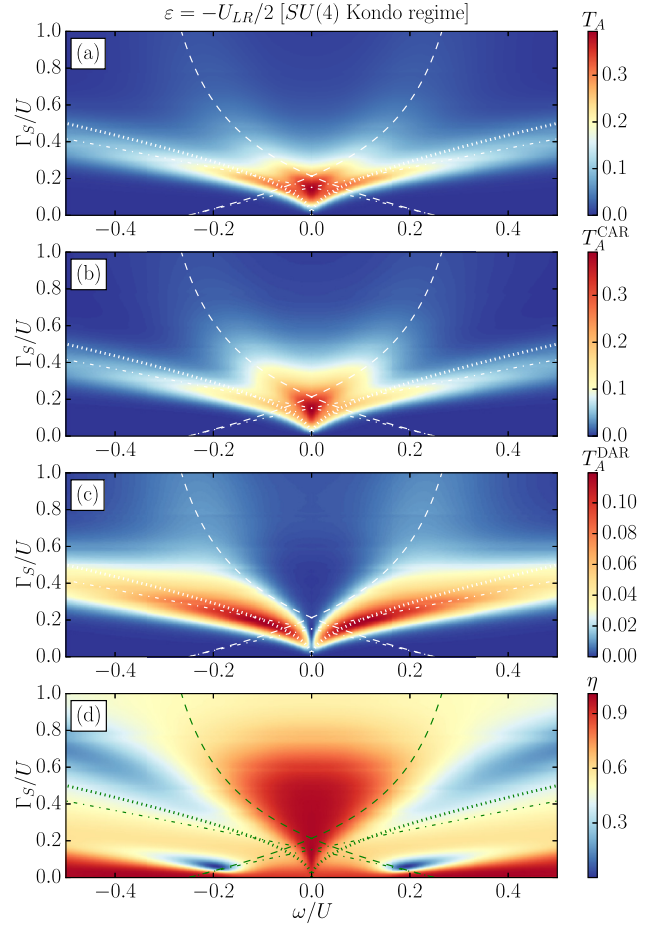

FIG. 13. (a) Total Andreev transmission coefficient and its contributions due to (b) CAR and (c) DAR processes, as well as (d) the Cooper pair splitting efficiency η plotted as function of energy ω and the strength of coupling to superconductor Γ_S for parameters the same as in Fig. 12. The dashed and dotted-dashed lines indicate the energies of the Andreev bound states, and the dotted line shows the splitting of the doublet states, as described by Eq. (18).

$\Gamma_S \gtrsim \Gamma_S^{SD}$, at low energies the splitting efficiency is smaller and it indicates that CAR and DAR processes contribute to Andreev transport on an equal footing. On the other hand, for larger energies, η first becomes suppressed and then increases again. However, in this transport regime the total transmission is relatively low; see Fig. 11.

D. SU(4) Kondo regime

In this section we consider more thoroughly the behavior of the spectral function and Andreev transmission in the SU(4) Kondo regime; see also Fig. 2. For $\Gamma_S = 0$ and when the DQD is singly occupied, the system exhibits the SU(4) Kondo effect resulting from the spin and orbital degeneracies. For the present analysis we thus assume $\varepsilon = -U_{LR}/2$. The normalized spectral function calculated as a function of energy and the strength of coupling to superconductor is shown in Fig. 12. At first sight, one can deduce that for relatively low values of Γ_S, i.e., $\Gamma_S \lesssim U/5$, the SU(4) Kondo resonance is hardly affected by the superconducting proximity effect. Only when the coupling to superconductor becomes larger ($\Gamma_S \gtrsim U/5$) does the Kondo phenomenon get suppressed—the resonance in the spectral function becomes then broadened and departs to larger energies. In fact, for $\Gamma_S \approx U/5$, the ground state of the system changes from the spin doublet to spin singlet state, and this is the reason for vanishing of the Kondo effect. For $\Gamma_S \gtrsim U/5$, $\mathcal{A}$ exhibits only resonances at larger energies

corresponding to the Andreev bound state energies; see the dashed and dotted-dashed lines in Fig. 12, which mark the energies of Andreev bound states. The ABS's energies were determined from the excitation energies between appropriate singlet and doublet states obtained from numerical solution of the eigenvalue problem. The resonances associated with excitations due to Andreev bound states are also clearly visible in the spectral function of individual quantum dots $\mathcal{A}_L$ as well as in $\mathcal{A}_{LR}$, shown in Figs. 12(b) and 12(c), respectively.

At energies corresponding to Andreev bound states, the Andreev transmission coefficient also becomes enhanced. This can be seen in Fig. 13, which presents the energy ω and Γ_S dependence of $T_A(\omega)$ and its contributions due to CAR and DAR processes, together with the splitting efficiency η. We again notice that generally $T_A^{CAR}(\omega) > T_A^{DAR}(\omega)$ [cf. Figs. 13(b) and 13(c)], which leads to large splitting efficiency, especially visible for low energies [Fig. 13(d)]. In fact, for $\Gamma_S \approx U/5$, i.e., when the doublet-singlet transition occurs, the total transmission coefficient has a local maximum, which
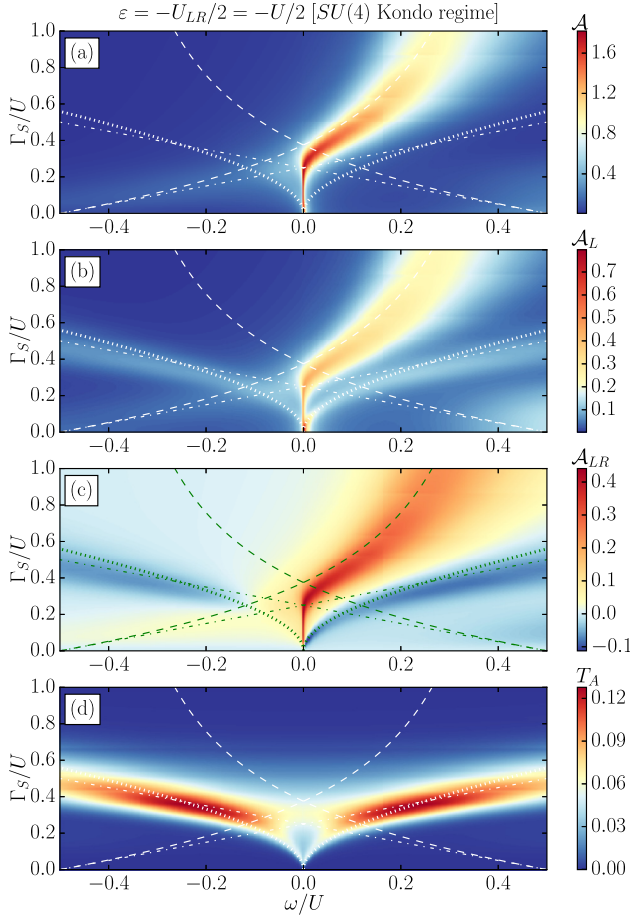
$\varepsilon = -U_{LR}/2 = -U/2$ [$SU(4)$ Kondo regime]

FIG. 14. Energy dependence of (a) the total normalized spectral function $\mathcal{A}$, its contributions (b) $\mathcal{A}_L$ and (c) $\mathcal{A}_{LR}$, and (d) the total Andreev transmission coefficient $T_A(\omega)$ plotted as a function of energy ω and Γ_S in the $SU(4)$ Kondo regime for the symmetric case with $U_{LR} = U$. The dotted-dashed (dashed) lines indicate the energies of the Andreev bound states E^1_{ABS} (E^2_{ABS}), cf. Eq. (22), while the dotted lines show the doublet splitting energy; cf. Eq. (18). The other parameters are the same as in Fig. 3.

results mainly from CAR processes; see Fig. 13. Consequently, the splitting efficiency becomes then very close to unity. On the other hand, there are also transport regimes where η is very much suppressed, which indicates that DAR processes are dominant; see the transport region for $|\omega| \approx U/5$ and low values of Γ_S ($\Gamma_S \approx U/10$) in Fig. 13(d). The transmission coefficient in these transport regimes is however relatively low.

To shed more light on the influence of superconducting pairing correlations on the $SU(4)$ Kondo regime, let us now assume a fully symmetric situation, namely $U_{LR} = U$. For this case, the dependence of the relevant spectral functions and the total Andreev transmission coefficient on ω and Γ_S is shown in Fig. 14. In the symmetric case, one can find the eigenenergies and eigenstates in the spin singlet subspace explicitly. These are presented in Table III in the Appendix, while the eigenspectrum in the doublet subspace can be found in Table I. Note that in the doublet subspace we can find the eigenspectrum for arbitrary parameters; therefore, if only

TABLE I. Eigenvalues and unnormalized eigenvectors of the effective DQD Hamiltonian in the doublet subspace. Here, $\Delta_D = [(2\varepsilon + 2U_{LR} + U)^2 + 16\Gamma_S^2]^{\frac{1}{2}}$ and $\alpha = (2\varepsilon + 2U_{LR} + U + \Delta_D)/(4\Gamma_S)$.

State	Eigenenergy	Eigenvector
$\lvert D^1_\sigma \rangle$	ε	$\lvert \sigma 0 \rangle - \lvert 0\sigma \rangle$
$\lvert D^2_\sigma \rangle$	$2\varepsilon + U_{LR} + \frac{U - \Delta_D}{2}$	$\alpha(\lvert \sigma 0 \rangle + \lvert 0\sigma \rangle) + \lvert \sigma d \rangle + \lvert d\sigma \rangle$
$\lvert D^3_\sigma \rangle$	$2\varepsilon + U_{LR} + \frac{U + \Delta_D}{2}$	$\lvert \sigma 0 \rangle + \lvert 0\sigma \rangle - \alpha(\lvert \sigma d \rangle + \lvert d\sigma \rangle)$
$\lvert D^4_\sigma \rangle$	$3\varepsilon + 2U_{LR} + U$	$\lvert \sigma d \rangle - \lvert d\sigma \rangle$

the doublet states are considered we will present the analytical formulas for the general case of $U_{LR} \neq U$. From the inspection of the spectrum of H^{eff}_{DQD} one can see that for $\Gamma_S \to 0$ the ground state is indeed fourfold degenerate and given by the doublet states

$$\lvert D^1_\sigma \rangle = \frac{1}{\sqrt{2}}(\lvert \sigma 0 \rangle - \lvert 0\sigma \rangle) \qquad (16)$$

with energy $E^1_D = -U_{LR}/2$ and

$$\lvert D^2_\sigma \rangle = \frac{1}{\sqrt{16\Gamma_S^2 + \alpha^2}}[\alpha(\lvert \sigma 0 \rangle + \lvert 0\sigma \rangle) + 4\Gamma_S(\lvert \sigma d \rangle + \lvert d\sigma \rangle)], \qquad (17)$$

with $\alpha = U + U_{LR} + \sqrt{(U + U_{LR})^2 + 16\Gamma_S^2}$, and the energy, $E^2_D = U/2 - \sqrt{(U + U_{LR})^2 + 16\Gamma_S^2}/2$. With increasing Γ_S, the two doublet states become split and the ground state is given by the state $\lvert D^2_\sigma \rangle$. The doublet splitting energy is given by

$$\omega = \pm \frac{1}{2}\left[U + U_{LR} - \sqrt{(U + U_{LR})^2 + 16\Gamma_S^2}\right]. \qquad (18)$$

This energy difference is marked with dotted lines in Figs. 12, 13, and 14. It coincides with the resonances in the spectral function $\mathcal{A}_L$ obtained from NRG calculations. These resonances are however not visible in the total spectral function, since the peak in $\mathcal{A}_L$ is counterbalanced by an associated minimum in $\mathcal{A}_{LR}$; see, e.g., Figs. 12(b) and 12(c). Pronounced maxima can be also observed in the Andreev transmission coefficient shown in Figs. 13 and 14(d). Note that while around the Fermi energy both the spectral function and Andreev transmission show features at the doublet-doublet excitation energy [Eq. (18)], for larger ω, the resonances occur at energies corresponding rather to the Andreev bound states.

The influence of the superconducting pairing correlations on the $SU(4)$ Kondo state can be better resolved in the spectral function plotted versus energy on logarithmic scale. This is presented in Fig. 15. Now, one can clearly see that the maximum in the spectral function strongly depends on Γ_S. For very small pairing correlations, $\mathcal{A}$ exhibits a resonance at finite ω; see Fig. 15. Now for assumed parameters and $\Gamma_S = 0$ one finds $T^{SU(4)}_K/U \approx 0.004$. However, with increasing Γ_S, this resonance becomes suppressed and moves towards the Fermi energy. This is a clear indication of a crossover from the $SU(4)$ to the $SU(2)$ Kondo effect. Finite pairing correlations break the fourfold degeneracy of the ground state and reduce it to twofold degeneracy due to only the spin degrees of freedom. Because
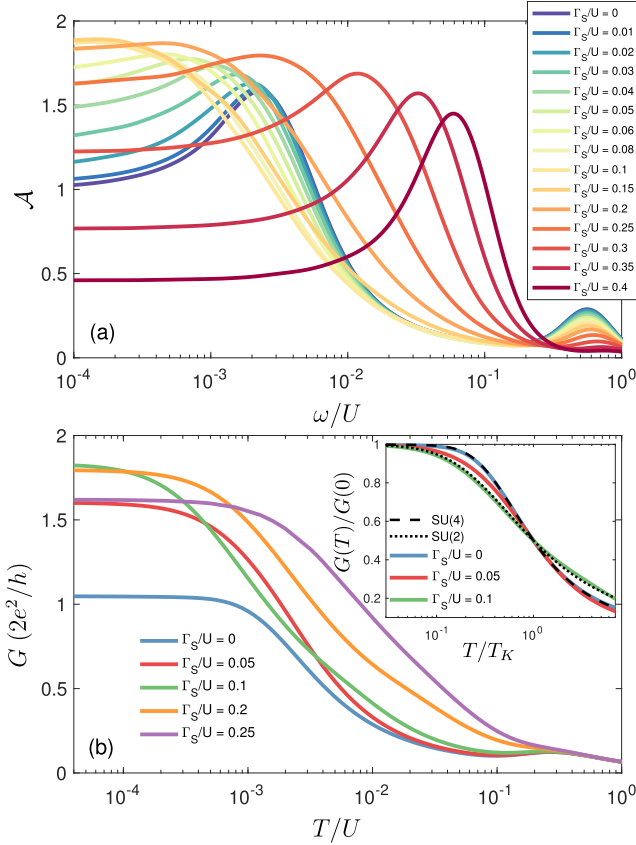
FIG. 15. (a) Total spectral function plotted vs energy on logarithmic scale and (b) the temperature dependence of the linear-response normal conductance for different values of Γ_S, as indicated in the legends. The inset in (b) presents the crossover of the universal scaling of the conductance vs T/T_K from the SU(4) to the SU(2) Kondo regime. The other parameters are the same as in Fig. 14. For $\Gamma_S = 0$ and assumed parameters $T_K^{SU(4)}/U \approx 0.004$.

of that, the SU(4) Kondo effect becomes suppressed. One can estimate the strength of coupling Γ_S when this crossover takes place (Γ_S^{DD}) by comparing the doublet splitting energy with the corresponding Kondo temperature. This leads to

$$\Gamma_S^{DD} \approx \frac{1}{2}\sqrt{T_K^{SU(4)}(U + U_{LR})}. \quad (19)$$

For parameters assumed in Fig. 15 one then finds $\Gamma_S^{DD} \approx 0.045U$. This estimate agrees reasonably well with the numerical data shown in Fig. 15(a).

Moreover, we corroborate the SU(4)-SU(2) crossover by calculating the temperature dependence of the normal conductance, which for potential drop between the left and right leads in the linear response regime can be expressed as [23,64]

$$G = \frac{2e^2}{h} \int d\omega \left(-\frac{\partial f(\omega)}{\partial \omega} \right) \mathcal{A}, \quad (20)$$

where $f(\omega)$ is the Fermi-Dirac distribution function. We note that, since the total conductance may contain contributions from Andreev reflection processes, the normal conductance G should be considered as a theoretical tool to gain information about the type of scaling and, thus, the type of the Kondo

effect in the system. The temperature dependence of G is shown in Fig. 15(b). For $\Gamma_S = 0$, $G(T)$ exhibits the SU(4) universal scaling; see the inset in Fig. 15(b). However, with increasing Γ_S, e.g., for $\Gamma_S = 0.05U \gtrsim \Gamma_S^{DD}$, the scaling does not collapse onto the SU(4) universal function any more. Instead, for $\Gamma_S > \Gamma_S^{DD}$, one finds that the SU(2) Kondo effect becomes responsible for the conductance enhancement. The conductance reveals the SU(2) universal scaling for Γ_S up to $\Gamma_S \approx 3U/10$ (not shown), since for larger Γ_S the doublet is not the ground state of the system any more and the Kondo effect is not present in the system.

Note also that the maximum value of the low-temperature conductance, which corresponds directly to $\mathcal{A}$ at $\omega = 0$, depends in a nonmonotonic fashion on Γ_S. For $\Gamma_S = 0$, $G = 2e^2/h$, while for $\Gamma_S^{DD} \lesssim \Gamma_S$, G is clearly larger than $2e^2/h$ and approaches almost $4e^2/h$; see Fig. 15(b). This can be understood by realizing that finite coupling to a superconductor leads to an enhancement of the average occupation of each dot, such that the occupation of the double dot becomes larger than one. Moreover, finite coupling to a superconductor results in a large enhancement of $\mathcal{A}_{LR}$, such that the total conductance reaches $G \approx 4e^2/h$.

When the coupling to superconductor is enhanced further, a doublet-singlet transition occurs for $\Gamma_S = 3U/8$. For $\Gamma_S > 3U/8$, the ground state of the system is given by the following singlet state (cf. state $|S_2\rangle$ in Table III):

$$|S\rangle = \frac{1}{\sqrt{2}}\left[|00\rangle + \frac{1}{2}(|d0\rangle + |0d\rangle) + \frac{1}{2}(|\uparrow\downarrow\rangle - |\downarrow\uparrow\rangle) \right], \quad (21)$$

with the energy $E_S = -2\Gamma_S$. The excitations between the singlet and the two doublet states allow us to estimate the analytical formulas for the energies of the relevant Andreev bound states, which are given by

$$E_{ABS}^1 = \pm\frac{U}{2} \mp 2\Gamma_S,$$

$$E_{ABS}^2 = \pm\frac{U}{2} \pm 2\Gamma_S \mp \sqrt{U^2 + 4\Gamma_S^2}. \quad (22)$$

The energies of those Andreev bound states are presented in Fig. 14 with dotted-dashed and dashed lines, respectively. In fact, for $\Gamma_S > 3U/8$, the resonances present in the spectral function for positive energies are exactly due to the Andreev bound states; see Fig. 14. At the ABS energy E_{ABS}^1 an enhancement of the Andreev transmission is also clearly present; see Fig. 14(d).

Summing up, in the SU(4) Kondo regime, i.e., for $\varepsilon = -U/2$ with $U_{LR} = U$, the SU(4) Kondo effect is present for $\Gamma_S \lesssim \Gamma_S^{DD}$. At $\Gamma_S \approx \Gamma_S^{DD}$, there is an SU(4)-SU(2) crossover, and for $\Gamma_S^{DD} \lesssim \Gamma_S \lesssim 3U/8$ the system exhibits the SU(2) Kondo resonance. When $\Gamma_S \approx 3U/8$, there is a phase transition and the ground state changes from the spin doublet to the spin singlet state, such that for larger values of Γ_S the system does not exhibit the Kondo effect any more. These findings are schematically summarized in Fig. 16, which shows the evolution of the ground state when the strength of coupling to superconductor increases.
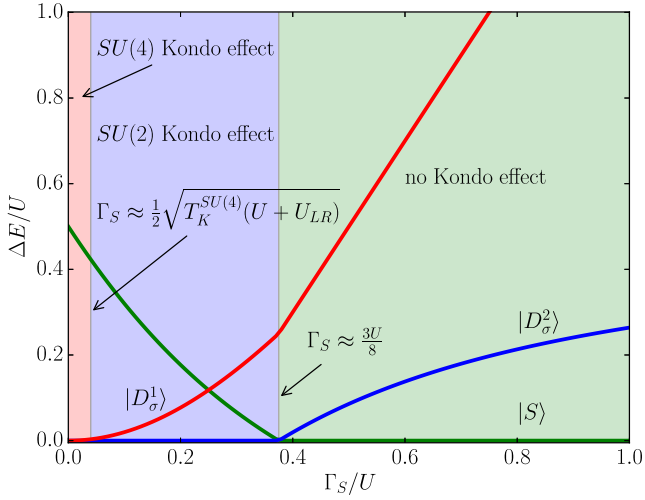
FIG. 16. Excitation energies ΔE between the corresponding singlet and two doublet states plotted as a function of the coupling to superconductor for parameters the same as in Fig. 14. The excitation energies are measured relative to the ground state energy, which is set to zero. The values of Γ_S at which the symmetry of the Kondo state or the ground state of the system changes are indicated.

IV. CONCLUSIONS

We have analyzed the transport properties of double quantum dot based Cooper pair splitters strongly coupled to external electrodes, focusing on the Kondo regime. The two dots were attached to a common s-wave superconductor and each dot was coupled to a separate metallic electrode. The considerations were performed in the subgap transport regime, where transport was driven by direct and crossed Andreev reflection processes. By using the density-matrix numerical renormalization group method, we determined the behavior of the local density of states of DQD and the Andreev transmission coefficient, together with Cooper-pair splitting efficiency. First, we have analyzed the dependence of the transport properties on the position of the DQD energy levels and then we have focused on the SU(2) and SU(4) Kondo regimes.

We have shown that the superconducting pairing correlations can greatly influence the Kondo effect in the system. In the SU(2) Kondo regime, we predict a very quick suppression of the Kondo resonance with increasing the strength of coupling to superconductor. This effect is in stark contrast to the single quantum dot case, where increase of pairing correlations resulted in an enhancement of the Kondo temperature [43,47]. The disappearance of the SU(2) Kondo peak is directly associated with the formation of a spin singlet state between the two quantum dots triggered by proximity-induced interdot pairing potential. With increasing the strength of coupling to superconductor further, we demonstrate that the system undergoes a transition to the doublet state. In this transport regime, the Kondo effect reemerges and the total spectral function shows a pronounced Kondo peak. The occurrence of this resonance is associated with contributions coming from both individual quantum dots $\mathcal{A}_i$, as well as from cross correlations described by the off-diagonal part of the spectral function $\mathcal{A}_{ij}$.

In the SU(4) Kondo regime, on the other hand, the impact of superconducting pairing correlations on the Kondo state is less abrupt and now the Kondo effect persists for larger couplings to superconductor as compared to the SU(2) case. More specifically, we predict that, in the fully symmetric situation, the SU(4) Kondo effect becomes first reduced to the SU(2) Kondo effect, which becomes then fully suppressed once $\Gamma_S > 3U/8$. For this value of coupling to superconductor, the ground state changes from the spin doublet to the proximity-induced singlet state and, consequently, there is no Kondo effect. The spectral function exhibits then only resonances at energies corresponding to energies of Andreev bound states. Interestingly, in the SU(4) Kondo regime, when $U_{LR} < U$, we find that the Andreev current is mainly due to CAR processes, which yields almost perfect Cooper pair splitting efficiency.

Finally, we would like to note that most of our findings, and especially the suppression or reemergence of the Kondo state as the coupling to superconductor is varied, could be tested with the present-day experimental technology. We hope that our research will stimulate further efforts in this direction.

APPENDIX: SPECTRUM OF THE EFFECTIVE DOUBLE DOT HAMILTONIAN

Here we present the eigenvalues and eigenvectors of isolated double quantum dot with proximity-induced pairing potentials, as modeled by the effective Hamiltonian (3). Because the Hamiltonian possesses the full spin SU(2) symmetry, we can write $H_{DQD}^{\rm eff}$ in blocks labeled by the spin quantum number. Moreover, it is enough to use 10 spin multiplets instead of 16 local states. Let us first start from the trivial triplet subspace. The triplet state $|T_\delta\rangle$ has the components: $|T_+\rangle = |\uparrow\uparrow\rangle$, $|T_-\rangle = |\downarrow\downarrow\rangle$, $|T_0\rangle = (|\uparrow\downarrow\rangle + |\downarrow\uparrow\rangle)/\sqrt{2}$, and the energy $E_T = 2\varepsilon + U_{LR}$.

The Hamiltonian block in the spin doublet subspace is explicitly given by

$$H_{DQD}^{{\rm eff},S=\frac{1}{2}} = \begin{pmatrix} \varepsilon & 0 & -\Gamma_S & -\Gamma_S \\ 0 & \varepsilon & -\Gamma_S & -\Gamma_S \\ -\Gamma_S & -\Gamma_S & \varepsilon_3 & 0 \\ -\Gamma_S & -\Gamma_S & 0 & \varepsilon_3 \end{pmatrix}, \quad (A1)$$

with $\varepsilon_3 = 3\varepsilon + 2U_{LR} + U$. This matrix is written in the following states: $|\sigma 0\rangle$, $|0\sigma\rangle$, $|\sigma d\rangle$, and $|d\sigma\rangle$, respectively, and its eigenvalues together with unnormalized eigenvectors are listed in Table I.

Now, let us consider the singlet subspace which is spanned by the following five states: $|00\rangle$, $|d0\rangle$, $|0d\rangle$, $|S_0\rangle = (|\uparrow\downarrow\rangle - |\downarrow\uparrow\rangle)/\sqrt{2}$, and $|dd\rangle$. The effective DQD Hamiltonian in this

TABLE II. Eigenvalues and unnormalized eigenvectors of the effective DQD Hamiltonian in the singlet subspace for the particle-hole symmetry point, $\varepsilon = -U/2 - U_{LR}$. Here, $\Delta_S = (U_{LR}^2 + 4\Gamma_S^2)^{\frac{1}{2}}$, $\alpha = (U_{LR} + \Delta_S)/(2\Gamma_S)$, and $\tilde{\Delta}_S = [(U + U_{LR})^2 + 16\Gamma_S^2]^{\frac{1}{2}}$.

State	Eigenenergy	Eigenvector
$|S_1\rangle$	$-2U_{LR}$	$|d0\rangle - |0d\rangle$
$|S_2\rangle$	$-U_{LR} - \Delta_S$	$|dd\rangle + |00\rangle + \alpha(|d0\rangle + |0d\rangle)$
$|S_3\rangle$	$-U_{LR} + \Delta_S$	$\alpha(|dd\rangle + |00\rangle) - |d0\rangle - |0d\rangle$
$|S_4\rangle$	$-\frac{U+U_{LR}+\tilde{\Delta}_S}{2}$	$|dd\rangle - |00\rangle + \frac{U+U_{LR}+\tilde{\Delta}_S}{2\sqrt{2}\Gamma_S}|S_0\rangle$
$|S_5\rangle$	$-\frac{U+U_{LR}-\tilde{\Delta}_S}{2}$	$|dd\rangle - |00\rangle + \frac{U+U_{LR}-\tilde{\Delta}_S}{2\sqrt{2}\Gamma_S}|S_0\rangle$

TABLE III. Eigenvalues and unnormalized eigenvectors of the effective DQD Hamiltonian in the singlet subspace in the SU(4) Kondo regime, that is for $\varepsilon = -U/2$ and $U_{LR} = U$. Here, $\Delta_S = (U^2 + \Gamma_S^2)^{\frac{1}{2}}$ and $\alpha = (U + \Delta_S)/(2\Gamma_S)$.

State	Eigenenergy	Eigenvector
$|S_1\rangle$	0	$|d0\rangle - |0d\rangle$
$|S_2\rangle$	$-2\Gamma_S$	$|S_0\rangle - \sqrt{2}|00\rangle - \frac{1}{\sqrt{2}}(|d0\rangle + |0d\rangle)$
$|S_3\rangle$	$2\Gamma_S$	$|S_0\rangle + \sqrt{2}|00\rangle - \frac{1}{\sqrt{2}}(|d0\rangle + |0d\rangle)$
$|S_4\rangle$	$2U - 2\Delta_S$	$\alpha(|d0\rangle + |0d\rangle + \sqrt{2}|S_0\rangle) + |dd\rangle$
$|S_5\rangle$	$2U + 2\Delta_S$	$\alpha|dd\rangle - (|d0\rangle + |0d\rangle + \sqrt{2}|S_0\rangle)$

subspace is given by

$$H_{DQD}^{\text{eff},S=0}$$

$$= \begin{pmatrix} 0 & -\Gamma_S & -\Gamma_S & \sqrt{2}\Gamma_S & 0 \\ -\Gamma_S & 2\varepsilon+U & 0 & 0 & -\Gamma_S \\ -\Gamma_S & 0 & 2\varepsilon+U & 0 & -\Gamma_S \\ \sqrt{2}\Gamma_S & 0 & 0 & 2\varepsilon+U_{LR} & -\sqrt{2}\Gamma_S \\ 0 & -\Gamma_S & -\Gamma_S & -\sqrt{2}\Gamma_S & \varepsilon_4 \end{pmatrix},$$

(A2)

where $\varepsilon_4 = 4\varepsilon + 2U + 4U_{LR}$ is the energy of the fully occupied double dot. The first eigenstate is $|S_1\rangle = (|d0\rangle - |0d\rangle)/\sqrt{2}$ and its eigenenergy reads $2\varepsilon + U$. The next eigenenergies are given by polynomials of various Hamiltonian parameters and do not have simple analytical structure; therefore, we will not present them here. Instead, let us consider some limiting situations. The first one is relevant to the SU(2) Kondo regime, $\varepsilon = -U/2 - U_{LR}$, and the second one is associated with the SU(4) Kondo regime, when $\varepsilon = -U_{LR}/2$ and $U = U_{LR}$. The eigenspectrum in the former case is presented in Table II, while the states and energies in the latter case are listed in Table III.

[1] D. Loss and D. P. DiVincenzo, Quantum computation with quantum dots, Phys. Rev. A **57**, 120 (1998).

[2] B. Ruggiero, P. Delsing, C. Granata, Y. A. Pashkin, and P. Silvestrini, *Quantum Computing in Solid State Systems* (Springer-Verlag, New York, 2006).

[3] M. A. Nielsen and I. L. Chuang, *Quantum Computation and Quantum Information: 10th Anniversary Edition* (Cambridge University Press, Cambridge, UK, 2011).

[4] P. Recher, E. V. Sukhorukov, and D. Loss, Andreev tunneling, Coulomb blockade, and resonant transport of nonlocal spin-entangled electrons, Phys. Rev. B **63**, 165314 (2001).

[5] M. Tinkham, *Introduction to Superconductivity: Second Edition (Dover Books on Physics) (Vol. I)* (Dover Publications, Mineola, NY, 2004).

[6] D. Ciudad, Superconductivity: Splitting Cooper pairs, Nat. Mater. **14**, 463 (2015).

[7] L. Hofstetter, S. Csonka, J. Nygård, and C. Schönenberger, Cooper pair splitter realized in a two-quantum-dot y-junction, Nature (London) **461**, 960 (2009).

[8] L. G. Herrmann, F. Portier, P. Roche, A. L. Yeyati, T. Kontos, and C. Strunk, Carbon Nanotubes as Cooper-Pair Beam Splitters, Phys. Rev. Lett. **104**, 026801 (2010).

[9] L. Hofstetter, S. Csonka, A. Baumgartner, G. Fülöp, S. d'Hollosy, J. Nygård, and C. Schönenberger, Finite-Bias Cooper Pair Splitting, Phys. Rev. Lett. **107**, 136801 (2011).

[10] J. Schindele, A. Baumgartner, and C. Schönenberger, Near-Unity Cooper Pair Splitting Efficiency, Phys. Rev. Lett. **109**, 157002 (2012).

[11] A. Das, Y. Ronen, M. Heiblum, D. Mahalu, A. V. Kretinin, and H. Shtrikman, High-efficiency Cooper pair splitting demonstrated by two-particle conductance resonance and positive noise cross-correlation, Nat. Commun. **3**, 1165 (2012).

[12] G. Fülöp, S. d'Hollosy, A. Baumgartner, P. Makk, V. A. Guzenko, M. H. Madsen, J. Nygård, C. Schönenberger, and S. Csonka, Local electrical tuning of the nonlocal signals in a Cooper pair splitter, Phys. Rev. B **90**, 235412 (2014).

[13] G. Fülöp, F. Domínguez, S. d'Hollosy, A. Baumgartner, P. Makk, M. H. Madsen, V. A. Guzenko, J. Nygård, C. Schönenberger, A. Levy Yeyati, and S. Csonka, Magnetic Field Tuning and Quantum Interference in a Cooper Pair Splitter, Phys. Rev. Lett. **115**, 227003 (2015).

[14] Z. B. Tan, D. Cox, T. Nieminen, P. Lähteenmäki, D. Golubev, G. B. Lesovik, and P. J. Hakonen, Cooper Pair Splitting by Means of Graphene Quantum Dots, Phys. Rev. Lett. **114**, 096602 (2015).

[15] A. F. Andreev, The Thermal conductivity of the intermediate state of superconductors, Zh. Eksp. Teor. Fiz. **46**, 1823 (1964) [Sov. Phys. JETP **19**, 1228 (1964)].

[16] D. Beckmann, H. B. Weber, and H. v. Löhneysen, Evidence for Crossed Andreev Reflection in Superconductor-Ferromagnet Hybrid Structures, Phys. Rev. Lett. **93**, 197003 (2004).

[17] J. Gramich, A. Baumgartner, and C. Schönenberger, Resonant and Inelastic Andreev Tunneling Observed on a Carbon Nanotube Quantum Dot, Phys. Rev. Lett. **115**, 216801 (2015).

[18] D. Sherman, J. S. Yodh, S. M. Albrecht, J. Nygård, P. Krogstrup, and C. M. Marcus, Normal, superconducting and topological

105

regimes of hybrid double quantum dots, Nat. Nanotechnol. **12**, 212 (2017).

[19] Y. Tanaka, N. Kawakami, and A. Oguri, Correlated electron transport through double quantum dots coupled to normal and superconducting leads, Phys. Rev. B **81**, 075404 (2010).

[20] J. Eldridge, M. G. Pala, M. Governale, and J. König, Superconducting proximity effect in interacting double-dot systems, Phys. Rev. B **82**, 184507 (2010).

[21] D. Chevallier, J. Rech, T. Jonckheere, and T. Martin, Current and noise correlations in a double-dot Cooper-pair beam splitter, Phys. Rev. B **83**, 125421 (2011).

[22] J. Barański and T. Domański, Decoherence effect on fano line shapes in double quantum dots coupled between normal and superconducting leads, Phys. Rev. B **85**, 205451 (2012).

[23] P. Trocha and J. Barnaś, Spin-polarized Andreev transport influenced by Coulomb repulsion through a two-quantum-dot system, Phys. Rev. B **89**, 245418 (2014).

[24] B. Sothmann, S. Weiss, M. Governale, and J. König, Unconventional superconductivity in double quantum dots, Phys. Rev. B **90**, 220501 (2014).

[25] P. Trocha and I. Weymann, Spin-resolved Andreev transport through double-quantum-dot Cooper pair splitters, Phys. Rev. B **91**, 235424 (2015).

[26] R. Hussein, L. Jaurigue, M. Governale, and A. Braggio, Double quantum dot Cooper-pair splitter at finite couplings, Phys. Rev. B **94**, 235134 (2016).

[27] K. Wrześniewski, P. Trocha, and I. Weymann, Current cross-correlations in double quantum dot based Cooper pair splitters with ferromagnetic leads, J. Phys.: Condens. Matter **29**, 195302 (2017).

[28] J. Kondo, Resistance minimum in dilute magnetic alloys, Prog. Theor. Phys. **32**, 37 (1964).

[29] A. C. Hewson, *The Kondo Problem to Heavy Fermions* (Cambridge University Press, Cambridge, UK, 1997).

[30] D. Goldhaber-Gordon, H. Shtrikman, D. Mahalu, D. Abusch-Magder, U. Meirav, and M. A. Kastner, The Kondo effect in a single-electron transistor, Nature (London) **391**, 156 (1998).

[31] S. M. Cronenwett, T. H. Oosterkamp, and L. P. Kouwenhoven, A tunable Kondo effect in quantum dots, Science **281**, 540 (1998).

[32] L. Borda, G. Zaránd, W. Hofstetter, B. I. Halperin, and J. von Delft, SU(4) Fermi Liquid State and Spin Filtering in a Double Quantum Dot System, Phys. Rev. Lett. **90**, 026602 (2003).

[33] A. J. Keller, S. Amasha, I. Weymann, C. P. Moca, I. G. Rau, J. A. Katine, H. Shtrikman, G. Zaránd, and D. Goldhaber-Gordon, Emergent SU(4) Kondo physics in a spin-charge-entangled double quantum dot, Nat. Phys. **10**, 145 (2014).

[34] S. De Franceschi, L. Kouwenhoven, C. Schonenberger, and W. Wernsdorfer, Hybrid superconductor-quantum dot devices, Nat. Nanotechnol. **5**, 703 (2010).

[35] A. Martin-Rodero and A. Levy Yeyati, Josephson and Andreev transport through quantum dots, Adv. Phys. **60**, 899 (2011).

[36] E. J. H. Lee, X. Jiang, R. Aguado, G. Katsaros, C. M. Lieber, and S. De Franceschi, Zero-Bias Anomaly in a Nanowire Quantum Dot Coupled to Superconductors, Phys. Rev. Lett. **109**, 186802 (2012).

[37] J.-D. Pillet, P. Joyez, R. Žitko, and M. F. Goffman, Tunneling spectroscopy of a single quantum dot coupled to a superconductor: From Kondo ridge to Andreev bound states, Phys. Rev. B **88**, 045101 (2013).

[38] E. J. H. Lee, X. Jiang, M. Houzet, R. Aguado, C. M. Lieber, and S. De Franceschi, Spin-resolved Andreev levels and parity crossings in hybrid superconductor-semiconductor nanostructures, Nat. Nanotechnol. **9**, 79 (2014).

[39] J. Bauer, A. Oguri, and A. C. Hewson, Spectral properties of locally correlated electrons in a Bardeen-Cooper-Schrieffer superconductor, J. Phys.: Condens. Matter **19**, 486211 (2007).

[40] R. Maurand and C. Schönenberger, Viewpoint: To screen or not to screen, that is the question! Physics **6**, 75 (2013).

[41] K. J. Franke, G. Schulze, and J. I. Pascual, Competition of superconducting phenomena and Kondo screening at the nanoscale, Science **332**, 940 (2011).

[42] B.-K. Kim, Y.-H. Ahn, J.-J. Kim, M.-S. Choi, M.-H. Bae, K. Kang, J. S. Lim, R. López, and N. Kim, Transport Measurement of Andreev Bound States in a Kondo-Correlated Quantum Dot, Phys. Rev. Lett. **110**, 076803 (2013).

[43] T. Domański, I. Weymann, M. Barańska, and G. Górski, Constructive influence of the induced electron pairing on the Kondo state, Sci. Rep. **6**, 23336 (2016).

[44] K. G. Wilson, The renormalization group: Critical phenomena and the Kondo problem, Rev. Mod. Phys. **47**, 773 (1975).

[45] Ö. Legeza, C. P. Moca, A. I. Tóth, I. Weymann, and G. Zaránd, Manual for the flexible DM-NRG code, arXiv:0809.3143v1 (the open access Budapest code is available at http://www.phy.bme.hu/~dmnrg/).

[46] R. Bulla, T. A. Costi, and T. Pruschke, Numerical renormalization group method for quantum impurity systems, Rev. Mod. Phys. **80**, 395 (2008).

[47] R. Žitko, J. S. Lim, R. López, and R. Aguado, Shiba states and zero-bias anomalies in the hybrid normal-superconductor Anderson model, Phys. Rev. B **91**, 045441 (2015).

[48] A. V. Rozhkov and D. P. Arovas, Interacting-impurity Josephson junction: Variational wave functions and slave-boson mean-field theory, Phys. Rev. B **62**, 6687 (2000).

[49] T. Yoichi, K. Norio, and O. Akira, Numerical renormalization group approach to a quantum dot coupled to normal and superconducting leads, J. Phys. Soc. Jpn. **76**, 074701 (2007).

[50] T. Meng, S. Florens, and P. Simon, Self-consistent description of Andreev bound states in Josephson quantum dot devices, Phys. Rev. B **79**, 224521 (2009).

[51] D. Futterer, M. Governale, M. G. Pala, and J. König, Nonlocal Andreev transport through an interacting quantum dot, Phys. Rev. B **79**, 054505 (2009).

[52] B. Sothmann, D. Futterer, M. Governale, and J. König, Probing the exchange field of a quantum-dot spin valve by a superconducting lead, Phys. Rev. B **82**, 094514 (2010).

[53] J. Barański and T. Domański, Fano-type interference in quantum dots coupled between metallic and superconducting leads, Phys. Rev. B **84**, 195424 (2011).

[54] D. Futterer, J. Swiebodzinski, M. Governale, and J. König, Renormalization effects in interacting quantum dots coupled to superconducting leads, Phys. Rev. B **87**, 014509 (2013).

[55] K. P. Wójcik and I. Weymann, Proximity effect on spin-dependent conductance and thermopower of correlated quantum dots, Phys. Rev. B **89**, 165303 (2014).

[56] I. Weymann and P. Trocha, Superconducting proximity effect and zero-bias anomaly in transport through quantum dots weakly attached to ferromagnetic leads, Phys. Rev. B **89**, 115305 (2014).

[57] I. Weymann and K. P. Wójcik, Andreev transport in a correlated ferromagnet-quantum-dot-superconductor device, Phys. Rev. B **92**, 245307 (2015).

[58] R. Chirla and C. P. Moca, Fingerprints of Majorana fermions in spin-resolved subgap spectroscopy, Phys. Rev. B **94**, 045405 (2016).

[59] S. Głodzik, K. P. Wójcik, I. Weymann, and T. Domański, Interplay between electron pairing and Dicke effect in triple quantum dot structures, Phys. Rev. B **95**, 125419 (2017).

[60] B. W. Heinrich, L. Braun, J. I. Pascual, and K. J. Franke, Protection of excited spin states by a superconducting energy gap, Nat. Phys. **9**, 765 (2013).

[61] A. Freyn and S. Florens, Optimal broadening of finite energy spectra in the numerical renormalization group: Application to

[62] W. C. Oliveira and L. N. Oliveira, Generalized numerical renormalization-group method to calculate the thermodynamical properties of impurities in metals, Phys. Rev. B **49**, 11986 (1994).

[63] W. G. van der Wiel, S. De Franceschi, J. M. Elzerman, T. Fujisawa, S. Tarucha, and L. P. Kouwenhoven, Electron transport through double quantum dots, Rev. Mod. Phys. **75**, 1 (2002).

[64] K. Bocian and W. Rudziński, Photon-assisted tunneling in a hybrid junction based on a quantum dot coupled to two ferromagnets and a superconductor, Phys. Status Solidi B **254**, 1600206 (2017).

dissipative dynamics in two-level systems, Phys. Rev. B **79**, 121102 (2009).

Chapter 3

Appendix

3.1 Academic achievements

3.1.1 List of publications

[1] K. Wrześniewski, I. Weymann,

Spin effects in transport through triangular quantum dot molecule in different geometrical configurations,

Phys. Rev. B **92**, 045407 (2015).

[2] K. Wrześniewski, I. Weymann,

Current Suppression in Transport Through Triple Quantum Dots Coupled to Ferromagnetic Leads,

Acta Phys. Pol. A **127**, 460 (2015).

[3] K. Wrześniewski, I. Weymann,

Influence of Magnetic Field on Dark States in Transport through Triple Quantum Dots,

Acta Phys. Pol. A **132**, 109 (2017).

[4] K. Wrześniewski, P. Trocha, I. Weymann,

Current cross-correlations in double quantum dot based Cooper pair splitters with ferromagnetic leads,

J. Phys.: Cond. Matter **29**, 195302 (2017).

[5] K. Wrześniewski, I. Weymann,

Kondo physics in double quantum dot based Cooper pair splitters,

Phys. Rev. B **96**, 195409 (2017).

[6] K. Wrześniewski, I. Weymann,

Dark states in spin-polarized transport through triple quantum dot molecules,

Phys. Rev. B **97**, 075425 (2018).

[7] P. Trocha, K. Wrześniewski,

Cross-correlations in a quantum dot Cooper pair splitter with ferromagnetic leads,

J. Phys.: Cond. Matter **30**, 305303 (2018).

[8] K. Wrześniewski, I. Weymann,

Quench dynamics in quantum dots coupled to ferromagnetic leads,

(in preparation).

3.1.2 List of conferences

[1] Deutsche Physikalische Gesellschaft Spring meeting 2015, Berlin, 15-20.03.2015

Delivered poster *The tunnel magnetoresistance and shot noise of triple quantum dots in the sequential and cotunneling regimes*.

[2] SpinTech VIII, Basel, 10-13.08.2015.

Delivered poster *Spin dependent Andreev transport through triple quantum dot system*.

[3] Deutsche Physikalische Gesellschaft Spring meeting 2016, Regensburg, 6-12.03.2015.

Delivered talk *Current cross-correlations in double quantum dot Cooper pair splitter*.

[4] 12th International Workshop on Magnetism and Superconductivity at the Nanoscale, Coma-Ruga, 2016.

Delivered poster *Spin-Resolved Andreev transport in Quantum-Dot-Based Cooper Pair Splitters*.

[5] The Twelfth International School on Theoretical Physics Symmetry and Structural Properties of Condensed Matter, Rzeszów, 5-10.09.2016.

Delivered poster *Dark states in spin-polarized transport through triple quantum dots*.

[6] Konferencja użytkowników KDM, Poznań, 2017.

Delivered talk *Zastosowanie sieci tensorowych w obliczeniach procedura numerycznej grupy renormalizacji*.

[7] Physics of Magnetism, Poznań, 26-30.06.2017.

Delivered poster *Quench dynamics in quantum dots with ferromagnetic contacts*.

[8] 12th International Workshop on Magnetism and Superconductivity at the Nanoscale, Coma-Ruga, 2017.

Delivered poster *Andreev transport through quantum-dot-based Cooper pair splitters with ferromagnetic leads*.

[9] Low Temperature 28, Gotebörg, 8.08.2017.

Delivered poster *Kondo effect in transport through quantum dot based Cooper pair splitters*.

[10] The Arnold Sommerfeld Center for Theoretical Physics, *Numerical methods for correlated many-body systems*, Monachium, 11.09.2017.

Delivered poster *Quench dynamics in quantum dots with ferromagnetic contacts*.

[11] Deutsche Physikalische Gesellschaft Spring meeting, Berlin, 2018.

Delivered talk *Quench dynamics in correlated quantum dots coupled to ferromagnetic leads*.

[12] Konferencja użytkowników KDM, Poznań, 2018.

Delivered talk *Quench dynamics of spin in quantum dots*.

3.1.3 List of awards

[1] 2017 - Best Poster Award at conference Low Temperature 28 in Sweden, Goteborg

[2] 2017 - Rector's scholarship for best PhD students at Adam Mickiewicz University.

[3] 2016 - Rector's award for scientific research at Adam Mickiewicz University in Poznań - as a member of awarded team.

[4] 2015 - Rector's scholarship for best PhD students at Adam Mickiewicz University.

3.1.4 Scientific projects

[1] Co-investigator in Polish National Science Centre grant Sonata Bis no. 2013/10/E/ST3/00213. Project title: Teoretyczne badania transportu w nanostrukturach magnetycznych (*Theoretical studies of transport in magnetic nanostructures*). Project leader: dr hab. Ireneusz Weymann, prof UAM.

[2] Submitted a project *Current fluctuations and interference effects in transport through hybrid triangular quantum dot systems* as the Principal Investigator to Polish National Science Centre under the call Preludium 15.

3.1.5 Other scientific activities

[1] Helping in organization of the conference Physics of Magnetism, Poznań, 26-30.06.2017.

[2] Conducting a lab course for North Carolina State University students visiting Poznań, Global STEM Semester (Outgoing Program), 2017.

[3] Helping in organization of *Science on Stage - Poland*, Poznań, 21-22.09.2018.

3.2 Statements concerning authors' contributions

Hereby, I declare my contribution to the following papers:

1. K. Wrześniewski, I. Weymann,
   Dark states in spin-polarized transport through triple quantum dot molecules,
   Phys. Rev. B **97**, 075425 (2018).
   I performed most of the calculations, interpreted the results and prepared figures and manuscript. I estimate my contribution as 70%.

2. P. Trocha, K. Wrześniewski,
   Cross-correlations in a quantum dot Cooper pair splitter with ferromagnetic leads,
   J. Phys.: Cond. Matter 30, 305303 (2018).
   I performed part of the calculations and contributed to the interpretation of the results. I estimate my contribution as 40%.

3. K. Wrześniewski, P. Trocha, I. Weymann,
   Current cross-correlations in double quantum dot based Cooper pair splitters with ferromagnetic leads,
   J. Phys.: Cond. Matter **29**, 195302 (2017).
   I performed all numerical calculations, interpreted the results and prepared figures and manuscript. I estimate my contribution as 70%.

4. K. Wrześniewski, I. Weymann,
   Influence of Magnetic Field on Dark States in Transport through Triple Quantum Dots,
   Acta Phys. Pol. A **132**, 109 (2017).
   I performed all calculations, interpreted the results and prepared figures and manuscript. I estimate my cotribution as 80%.

5. K. Wrześniewski, I. Weymann,
   Kondo physics in double quantum dot based Cooper pair splitters,
   Phys. Rev. B **96**, 195409 (2017).
   I performed part of the calculations (Linear Andreev conductance) and analysis of the eigenstates, contributed to the interpretation of the results and prepared figures. I estimate my contribution as 50%.

6. K. Wrześniewski, I. Weymann,
   Current Suppression in Transport Through Triple Quantum Dots Coupled to Ferromagnetic Leads,
   Acta Phys. Pol. A **127**, 460 (2015).
   I performed all calculations, interpreted the results and prepared figures and manuscript. I estimate my contribution as 80%.

7. K. Wrześniewski, I. Weymann,
   Spin effects in transport through triangular quantum dot molecule in different geometrical configurations,
   Phys. Rev. B **92**, 045407 (2015).
   I performed most of the calculations, interpreted the results and prepared figures and manuscript. I estimate my contribution as 70%.

Kacper Wrześniewski

Poznań, September 20, 2018

Prof. UAM dr hab. Ireneusz Weymann
Mesoscopic Physics Division
Faculty of Physics
Adam Mickiewicz University in Poznań

Hereby, I declare that my contribution to the following publications:

1. K. Wrześniewski, I. Weymann
   Dark states in spin-polarized transport through triple quantum dot molecules
   Phys. Rev. B **97**, 075425 (2018)

2. K. Wrześniewski, P. Trocha, I. Weymann
   Current cross-correlations in double quantum dot based Cooper pair splitters with ferromagnetic leads
   J. Phys.: Cond. Matter **29**, 195302 (2017)

3. K. Wrześniewski, I. Weymann
   Influence of Magnetic Field on Dark States in Transport through Triple Quantum Dots
   Acta Phys. Pol. A **132**, 109 (2017)

4. K. Wrześniewski, I. Weymann
   Kondo physics in double quantum dot based Cooper pair splitters
   Phys. Rev. B **96**, 195409 (2017)

5. K. Wrześniewski, I. Weymann
   Current Suppression in Transport Through Triple Quantum Dots Coupled to Ferromagnetic Leads
   Acta Phys. Pol. A **127**, 460 (2015)

6. K. Wrześniewski, I. Weymann
   Spin effects in transport through triangular quantum dot molecule in different geometrical configurations
   Phys. Rev. B **92**, 045407 (2015)

relied on proposing the research topic, supervising and assisting in performing calculations, helping in the interpretation of results and in finalizing the manuscripts for publication.

dr Piotr Trocha
Mesoscopic Physics Division
Faculty of Physics
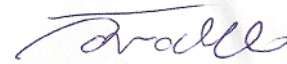Adam Mickiewicz University in Poznań

Poznań, September 17, 2018

Hereby, I declare my contribution to the following publications:

(1)
K. Wrześniewski, P. Trocha, I. Weymann,
Current cross-correlations in double quantum dot based Cooper pair splitters with ferromagnetic leads,
J. Phys.: Cond. Matter 29, 195302 (2017).

I performed the analytical approximations of the relevant formulas and contributed to the interpretations of results.

(2)
P. Trocha, K. Wrześniewski,
Cross-correlations in a quantum dot Cooper pair splitter with ferromagnetic leads,
J. Phys.: Cond. Matter 30, 305303 (2018).

I formulated the project, performed part of the calculations, prepared the manuscript and figures.

Piotr Trocha

Bibliography

[1] M. A. Reed, R. T. Bate, K. Bradshaw, W. M. Duncan, W. R. Frensley, J. W. Lee, and H. D. Shih, *Spatial quantization in GaAs-AIGaAs multiple quantum dots*, J. Vac. Sci. Technol. B **4**, 358 (1986).

[2] D.G.Austing, L. P.Kouwenhoven, and S. Tarucha, *Few-electron quantum dots*, Rep. Prog. Phys. **64**, 701 (2001).

[3] S. M. Reimann and M. Manninen, *Electronic structure of quantum dots*, Rev. Mod. Phys. **74**, 1283 (2002).

[4] I. Žutić, J. Fabian, and S. Das Sarma, *Spintronics: Fundamentals and applications*, Rev. Mod. Phys. **76**, 323 (2004).

[5] D. D. Awschalom, L. C.Bassett, A. S. Dzurak, E. L. Hu, and J. R. Petta, *Quantum spintronics: engineering and manipulating atom-like spins in semiconductors*, Science **339**, 1174 (2013).

[6] D. Loss and D. P. DiVincenzo, *Quantum computation with quantum dots*, Phys. Rev. A **57**, 120 (1998).

[7] R. Hanson, L. P. Kouwenhoven, J. R. Petta, S. Tarucha, and L. M. K. Vandersypen, *Spins in few-electron quantum dots*, Rev. Mod. Phys. **79**, 1217 (2007).

[8] H. Haug, A.-P. Jauho, *Quantum Kinetics in Transport and Optics of Semiconductors* (Springer-Verlag, Berlin Heidelberg, 2008).

[9] Y. V. Nazarov, Y. M. Blanter, *Quantum Transport* (Cambridge University Press, New York, 2009).

[10] L. P. Kouwenhoven, L. L. Sohn, and G. Schön, *Mesoscopic Electron Transport* (Springer, Netherlands, 1997).

[11] S. Andergassen, V. Meden, H. Schoeller, J. Splettstoesser, and M. R. Wegewijs, *Charge transport through single molecules, quantum dots and quantum wires*, Nanotechnology **21**, 272001 (2010).

[12] G. D. Mahan, *Many-particle physics* (Kulwer Academic, New York, 2000).

[13] B. Michaelis, C. Emary, and C. W. J. Beenakker, *All-electronic coherent population trapping in quantum dots*, Europhys. Lett. **73**, 677 (2006).

[14] C. Emary, *Dark states in the magnetotransport through triple quantum dots*, Phys. Rev. B **76**, 245319 (2007).

[15] C. Pöltl, C. Emary, and T. Brandes, *Two-particle dark state in the transport through a triple quantum dot*, Phys. Rev. B **80**, 115313 (2009).

[16] I.Weymann, B. R. Bułka, and J. Barnaś, *Dark states in transport through triple quantum dots: The role of cotunneling*, Phys. Rev. B **83**, 195302 (2011).

[17] L. Hofstetter, S. Csonka, J. Nygård, and C. Schönenberger, *Cooper pair splitter realized in a two-quantum-dot y-junction*, Nature (London) **461**, 960 (2009).

[18] L.G. Herrmann, F. Portier, P. Roche, A. L.Yeyati, T.Kontos, and C. Strunk, *Carbon Nanotubes as Cooper-Pair Beam Splitters*, Phys. Rev. Lett. **104**, 026801 (2010).

[19] L. Hofstetter, S. Csonka, A. Baumgartner, G. Fülöp, S. d'Hollosy, J.Nygård, and C. Schönenberger, *Finite-Bias Cooper Pair Splitting*, Phys. Rev. Lett. **107**, 136801 (2011).

[20] A. Das, Y.Ronen, M. Heiblum, D. Mahalu, A.V.Kretinin, and H. Shtrikman, *High-efficiency Cooper pair splitting demonstrated by two-particle conductance resonance and positive noise crosscorrelation*, Nat. Commun. **3**, 1165 (2012).

[21] A. F. Andreev, *The Thermal conductivity of the intermediate state of superconductors*, Zh. Eksp. Teor. Fiz. **46**, 1823 (1964) [Sov. Phys. JETP 19, 1228 (1964)].

[22] Y. M. Blanter and M. Büttiker, *Shot noise in mesoscopic conductors*, Phys. Rep. **336**, 1 (2000).

[23] J. Kondo, *Resistance minimum in dilute magnetic alloys*, Prog. Theor. Phys. **32**, 37 (1964).

[24] A. C. Hewson, *The Kondo Problem to Heavy Fermions* (Cambridge University Press, Cambridge, UK, 1997).

[25] D. Goldhaber-Gordon, H. Shtrikman, D. Mahalu, D. Abusch- Magder, U. Meirav, and M. A. Kastner, *The Kondo effect in a single-electron transistor*, Nature (London) **391**, 156 (1998).

[26] A. J. Keller, S. Amasha, I.Weymann, C. P. Moca, I. G. Rau, J. A. Katine, H. Shtrikman, G. Zaránd, and D. Goldhaber-Gordon, *Emergent SU(4) Kondo physics in a spin-charge-entangled double quantum dot*, Nat. Phys. **10**, 145 (2014).

[27] M. C. Rogge and R. J. Haug, *Two-path transport measurements on a triple quantum dot*, Phys. Rev. B **77**, 193306 (2008).

[28] A. Donarini, M. Niklas, M. Schafberger, N. Paradiso, C. Strunk, M. Grifoni, *Dark states in a carbon nanotube quantum dot*, arXiv:1804.02234 (2018).

[29] A. Noiri, T. Takakura, T. Obata, T. Otsuka, T. Nakajima, J. Yoneda, and S. Tarucha, *Co-tunneling spin blockade observed in a three-terminal triple quantum dot*, Phys. Rev. B **96**, 155414 (2017).

[30] G. Fülöp, F. Domínguez, S. d'Hollosy, A. Baumgartner, P. Makk, M. H. Madsen, V. A. Guzenko, J. Nygård, C. Schönenberger, A. Levy Yeyati, and S. Csonka, *Magnetic Field Tuning and Quantum Interference in a Cooper Pair Splitter*, Phys. Rev. Lett. **115**, 227003 (2015).

[31] P. W. Anderson, *Localized magnetic states in metals*, Phys. Rev. **124**, 41 (1961).

[32] J. Bardeen, L. N. Cooper, J. R. Schrieffer, *Microscopic theory of superconductivity*, Phys. Rev. **106**, 162 (1957).

[33] A. V. Rozhkov and D. P. Arovas, *Interacting-impurity Josephson junction: Variational wave functions and slave-boson mean-field theory*, Phys. Rev. B **62**, 6687 (2000).

[34] M. Governale, M. G. Pala and J. König, *Real-time diagrammatic approach to transport through interacting quantum dots with normal and superconducting leads*, Phys. Rev. B **77**, 134513 (2008).

[35] I. Weymann and P. Trocha, *Superconducting proximity effect and zero-bias anomaly in transport through quantum dots weakly attached to ferromagnetic leads*, Phys. Rev. B **89**, 115305 (2014).

[36] T. Domański, I. Weymann, M. Barańska and G. Górski, *Constructive influence of the induced electron pairing on the Kondo state*, Sci. Rep. **6**, 23336 (2016).

[37] J. Eldridge, M, G. Pala, M, Governale and J. König, *Superconducting proximity effect in interacting double-dot systems*, Phys. Rev. B **82**, 184507 (2010).

[38] P. Trocha and I. Weymann, *Spin-resolved Andreev transport through double-quantum-dot Cooper pair splitters*, Phys. Rev. B **91**, 235424 (2015).

[39] J. Schmid, J. Weis, K. Eberl and K. von Klitzing, *A Quantum Dot in the Limit of Strong Coupling to Reservoirs*, Physica B **256**, 182 (1998).

[40] R. Landauer, *Spatial Variation of Currents and Fields Due to Localized Scatterers in Metallic Conduction*, IBM J. Res. Dev. **1**, 233 (1957).

[41] S. Datta, *Electronic Transport in Mesoscopic Systems* (Cambridge University Press, 1995).

[42] D. Haldane, *Scaling Theory of the Asymmetric Anderson Model*, Phys. Rev. Lett. **40**, 416 (1978).

[43] P. W. Anderson, *A poor man's derivation of scaling laws for the Kondo problem*, J. Phys. C **3**, 2436 (1970).

[44] H. Schoeller and G. Schön, *Mesoscopic quantum transport: Resonant tunneling in the presence of a strong Coulomb interaction*, Phys. Rev. B **50**, 18436 (1994).

[45] J. König, J. Schmid, H. Schoeller, and G. Schön, *Resonant tunneling through ultrasmall quantum dots: Zero-bias anomalies, magnetic-field dependence, and boson-assisted transport*, Phys. Rev. B **54**, 16820 (1996).

[46] A. Thielmann, M. H. Hettler, J. König, and G. Schön, *Shot noise in tunneling transport through molecules and quantum dots*, Phys. Rev. B **68**, 115105 (2003).

[47] K. G. Wilson, *The renormalization group: Critical phenomena and the Kondo problem*, Rev. Mod. Phys. **47**, 773 (1975).

[48] R. Bulla, T. A. Costi, and T. Pruschke, *Numerical renormalization group method for quantum impurity systems*, Rev. Mod. Phys. **80**, 395 (2008).

[49] W. Hofstetter, *Generalized Numerical Renormalization Group for Dynamical Quantities*, Phys. Rev. Lett. **85**, 1508 (2000).

[50] F. B. Anders and A. Schiller, *Real-Time Dynamics in Quantum-Impurity Systems: A Time-Dependent Numerical Renormalization-Group Approach*, Phys. Rev. Lett. **95**, 196801 (2005).

[51] A. Weichselbaum and J. von Delft, *Sum-Rule Conserving Spectral Functions from the Numerical Renormalization Group*, Phys. Rev. Lett. **99**, 076402 (2007).

[52] Ö. Legeza, C. P. Moca, A. Tóth, I. Weymann and G. Zaránd,
Manual for the flexible DM-NRG code: arXiv:0809.3143v1
(the open access Budapest code is available at http://www.phy.bme.hu/~dmnrg/).

[53] M. Misiorny, I. Weymann, J. Barnaś, *Spin effects in transport through single-molecule magnets in the sequential and cotunneling regimes*, Phys. Rev. B **79**, 224420 (2009).

[54] B. Sothmann and J. König, *Transport through quantum-dot spin valves containing magnetic impurities*, Phys. Rev. B **82**, 245319 (2010).

[55] M. Misiorny, I. Weymann, and J. Barnaś, *Interplay of the Kondo Effect and Spin-Polarized Transport in Magnetic Molecules, Adatoms, and Quantum Dots*, Phys. Rev. Lett. **106**, 126602 (2011).

[56] M. Misiorny, M. Hell and M. R. Wegewijs, *Spintronic magnetic anisotropy* Nat. Phys. **9**, 801 (2013).

[57] S. Sapmaz, P. Jarillo-Herrero, L. P. Kouwenhoven, and H. S. J. van der Zant, *Quantum dots in carbon nanotubes*, Semicond. Sci. Technol. **21**, S52 (2006).

[58] I. Weymann, J. Barnaś, S. Krompiewski, *Transport through single-wall metallic carbon nanotubes in the cotunneling regime*, Phys. Rev. B **78**, 035422 (2008).

[59] M. R. Galpin, F. W. Jayatilaka, D. E. Logan, F. B. Anders, *Interplay between Kondo physics and spin-orbit coupling in carbon nanotube quantum dots*, Phys. Rev. B **81**, 075437 (2010).

[60] H. Grabert, M. H. Devoret (ed.), *Single charge tunneling: Coulomb blockade phenomena in nanostructures*, NATO ASI Series B: Physics 294 (Plenum, New York 1992).

[61] D. V. Averin and Yu. V. Nazarov, *Virtual electron diffusion during quantum tunneling of the electric charge*, Phys. Rev. Lett. **65**, 2446 (1990).

[62] L. P. Kouwenhoven, N. C. van der Vaart, A. T. Johnson, W. Kool, C. J. P. M. Harmans, J. G. Williamson, A. A. M. Staring and C. T. Foxon, *Single electron charging effects in semiconductor quantum dots*, Z. Phys. B - Condensed Matter **85**, 367 (1991).

[63] D. V. Averin and K. K. Likharev, *Coulomb blockade of single-electron tunneling, and coherent oscillations in small tunnel junctions*, J. Low Temp. Phys **62**, 345 (1986).

[64] M. Seo, H. K. Choi, S.-Y. Lee, N. Kim, Y. Chung, H.-S. Sim, V. Umansky, and D. Mahalu, *Charge Frustration in a Triangular Triple Quantum Dot*, Phys. Rev. Lett. **110**, 046803 (2013).

[65] A. Noiri, K. Kawasaki, T. Otsuka, T. Nakajima, J. Yoneda, S. Amaha, M. R. Delbecq, K. Takeda, G. Allison, A. Ludwig, *A triangular triple quantum dot with tunable tunnel couplings*, Semicond. Sci. Technol. **32**, 084004 (2017).

[66] J. Barnaś and A. Fert, *Magnetoresistance Oscillations due to Charging Effects in Double Ferromagnetic Tunnel Junctions*, Phys. Rev. Lett. **80**, 1058 (1998).

[67] S. Takahashi and S. Maekawa, *Effect of Coulomb Blockade on Magnetoresistance in Ferromagnetic Tunnel Junctions*, Phys. Rev. Lett. **80**, 1758 (1998).

[68] W. Rudziński and J. Barnaś, *Tunnel magnetoresistance in ferromagnetic junctions: Tunneling through a single discrete level*, Phys. Rev. B **64**, 085318 (2001).

[69] R. Świrkowicz, J. Barnaś, M. Wilczyński, *Electron tunneling in a double ferromagnetic junction with a magnetic dot as a spacer*, J. Phys.: Cond. Matter **14**, 2011 (2002).

[70] M. Julliére, *Tunneling between ferromagnetic films*, Phys. Lett. A **54**, 225 (1975).

[71] I. Weymann, J. König, J. Martinek, J. Barnaś and G. Schön, *Tunnel magnetoresistance of quantum dots coupled to ferromagnetic leads in the sequential and cotunneling regimes*, Phys. Rev. B **72**, 115334 (2005).

[72] R. Landauer, *The noise is the signal*, Nature **392**, 658 (1998).

[73] W. Schottky, *Über spontane Stromschwankungen in verschiedenen Elektrizitätsleitern*, Annalen der Physik (in German) **57**, 541 (1918).

[74] U. Fano, *Ionization Yield of Radiations. II. The Fluctuations of the Number of Ions*, Phys. Rev. **72**, 26 (1947).

[75] A. Thielmann, M. H. Hettler, J. König, and G. Schön, *Cotunneling Current and Shot Noise in Quantum Dots*, Phys. Rev. Lett. **95**, 146806 (2005).

[76] I. Weymann and J. Barnaś, *Shot noise and tunnel magnetoresistance in multilevel quantum dots: Effects of cotunneling*, Phys. Rev. B **77**, 075305 (2008).

[77] E.V. Sukhorukov, A. N. Jordan, S. Gustavsson, R. Leturcq, T. Ihn and K. Ensslin, *Conditional statistics of electron transport in interacting nanoscale conductors*, Nat. Phys. **3**, 243 (2007).

[78] D. T. McClure, L. DiCarlo, Y. Zhang, H. A. Engel, C.M. Marcus, M. P. Hanson and A. C. Gossard, *Tunable Noise Cross Correlations in a Double Quantum Dot*, Phys. Rev. Lett. **98**, 056801 (2007).

[79] A. Das, Y. Ronen, M. Heiblum, D. Mahalu, A. V. Kretinin and H. Shtrikman, *High-efficiency Cooper pair splitting demonstrated by two-particle conductance resonance and positive noise cross-correlation*, Nat. Commun. **3**, 1165 (2012).

[80] A. Thielmann, *Co-tunneling Current and Shot Noise in Molecules and Quantum Dots*, Wissenschaftliche Berichte, FZKA 7167, Forschungszentrum Karlsruhe (2005).

[81] M. Bayer, *Coherent population trapping: Quantum optics with dots*, Nat. Phys. **4**, 678 (2008).

[82] T. Kostyrko and B. R. Bułka, *Symmetry-controlled negative differential resistance effect in a triangular molecule*, Phys. Rev. B **79**, 075310 (2009).

[83] R. M. Whitley and C. R. Stroud, Jr. *Double optical resonance*, Phys. Rev. A **14**, 1498 (1976).

[84] K.-J. Boller, A. Imamoğlu, and S. E. Harris, *Observation of Electromagnetically Induced Transparency*, Phys. Rev. Lett. **66**, 2593 (1991).

[85] M. Fleischhauer, A. Imamoğlu, and J. P.Marangos, *Electromagnetically induced transparency: Optics in coherent media*, Rev. Mod. Phys. **77**, 633 (2005).

[86] L. Gaudreau, S. A. Studenikin, A. S. Sachrajda, P. Zawadzki, A. Kam, J. Lapointe, M. Korkusinski, and P. Hawrylak, *Stability Diagram of a Few-Electron Triple Dot*, Phys. Rev. Lett. **97**, 036807 (2006).

[87] C.-Y. Hsieh, Y.-P. Shim, M. Korkusinski, and P. Hawrylak, *Physics of lateral triple quantum-dot molecules with controlled electron numbers*, Rep. Prog. Phys. **75**, 114501 (2012).

[88] Y. Aharonov and D. Bohm, *Significance of Electromagnetic Potentials in the Quantum Theory*, Phys. Rev. **115**, 485 (1959).

[89] R. A. Webb, S. Washburn, C. P. Umbach, and R. B. Laibowitz, *Observation of $\frac{h}{e}$ Aharonov-Bohm Oscillations in Normal-Metal Rings*, Phys. Rev. Lett. **54**, 2696 (1985).

[90] C. Pöltl, C. Emary, and T. Brandes, *Spin-entangled two-particle dark state in quantum transport through coupled quantum dots*, Phys. Rev. B **87**, 045416 (2013).

[91] E. Aharon, R. Pozner, E. Lifshitz, and U. Peskin, *Multi-bit dark state memory: Double quantum dot as an electronic quantum memory*, J. Appl. Phys. **120**, 244301 (2016).

[92] W. J. De Haas, G. J. Van Den Berg, *The electrical resistance of gold and silver at low temperatures*, Physica **3**, 440 (1936).

[93] L. I. Glazman and M. E. Raikh, *Resonant Kondo transparency of a barrier with quasilocal impurity states*, JETP Lett. **47**, 452 (1988).

[94] T. K. Ng and P. A. Lee, *On-site Coulomb repulsion and resonant tunneling*, Phys. Rev. Lett. **61**, 1768 (1988).

[95] S. M. Cronenwett, T. H. Oosterkamp, L. P. Kouwenhoven, *A Tunable Kondo Effect in Quantum Dots*, Science **281**, 540 (1998).

[96] D. Goldhaber-Gordon, J. Göres, M.A. Kastner, H. Shtrikman, D. Mahalu and U. Meirav, *From the Kondo Regime to the Mixed-Valence Regime in a Single-Electron Transistor*, Phys. Rev. Lett. **81**, 5225 (1998).

[97] W.G. van der Wiel, S. de Francheschi, T. Fujisawa, J.M. Elzerman, S. Tarucha and L.P. Kouwenhoven, *The Kondo Effect in the Unitary Limit*, Science **289**, 2105 (2000).

[98] Andrey V. Kretinin, H. Shtrikman, D. Goldhaber-Gordon, M. Hanl, A. Weichselbaum, J. von Delft, T. Costi, and D. Mahalu, *Spin-1/2 Kondo effect in an InAs nanowire quantum dot: Unitary limit, conductance scaling, and Zeeman splitting*, Phys. Rev. B **84**, 245316 (2011).

[99] K. J. G. Götz, D. R. Schmid, F. J. Schupp, P. L. Stiller, Ch. Strunk, and A. K. Hüttel, *Nanomechanical Characterization of the Kondo Charge Dynamics in a Carbon Nanotube*, Phys. Rev. Lett. **120**, 246802 (2018).

[100] L. E. Bruhat, J. J. Viennot, M. C. Dartiailh, M. M. Desjardins, A. Cottet, and T. Kontos, *Scaling laws of the Kondo problem at finite frequency*, Phys. Rev. B **98**, 075121 (2018).

Oświadczenie

Ja, niżej podpisany Kacper Wrześniewski doktorant Wydziału Fizyki Uniwersytetu im. Adama Mickiewicza w Poznaniu oświadczam, że przedkładaną rozprawę doktorską pt.:

Correlation effects in transport through quantum dot systems

napisałem samodzielnie. Oznacza to, że przy pisaniu pracy, poza niezbędnymi konsultacjami, nie korzystałem z pomocy innych osób, a w szczególnosci nie zlecałem opracowania rozprawy lub jej istotnych części innym osobom, ani nie odpisywałem tej rozprawy lub jej istotnych części od innych osób.

Równocześnie wyrażam zgodę na to, że gdyby powyższe oświadczenie okazało się nieprawdziwe, decyzja o nadaniu mi stopnia naukowego doktora zostanie cofnięta.

Kacper Wrześniewski